

Reduction properties of doped hematite pellets.

MALLAH, Abdul H.

Available from the Sheffield Hallam University Research Archive (SHURA) at:

<http://shura.shu.ac.uk/20005/>

A Sheffield Hallam University thesis

This thesis is protected by copyright which belongs to the author.

The content must not be changed in any way or sold commercially in any format or medium without the formal permission of the author.

When referring to this work, full bibliographic details including the author, title, awarding institution and date of the thesis must be given.

Please visit <http://shura.shu.ac.uk/20005/> and <http://shura.shu.ac.uk/information.html> for further details about copyright and re-use permissions.

POLYTECHNIC LIBRARY
POND STREET
SHEFFIELD S1 1WB

6870

Sheffield City Polytechnic Library

REFERENCE ONLY

793290701 2

TELEPEN



ProQuest Number: 10697312

All rights reserved

INFORMATION TO ALL USERS

The quality of this reproduction is dependent upon the quality of the copy submitted.

In the unlikely event that the author did not send a complete manuscript and there are missing pages, these will be noted. Also, if material had to be removed, a note will indicate the deletion.



ProQuest 10697312

Published by ProQuest LLC (2017). Copyright of the Dissertation is held by the Author.

All rights reserved.

This work is protected against unauthorized copying under Title 17, United States Code
Microform Edition © ProQuest LLC.

ProQuest LLC.
789 East Eisenhower Parkway
P.O. Box 1346
Ann Arbor, MI 48106 – 1346

REDUCTION PROPERTIES OF DOPED

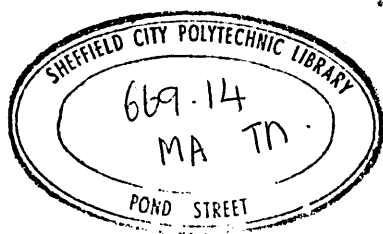
HEMATITE PELLETS

by

Abdul Hakim Mallah BE(Sind), MMet(Sheff)

This thesis is submitted for the degree of Doctor of Philosophy to the Council for National Academic Awards. The work was carried out in the Department of Metallurgy, at Sheffield City Polytechnic, in collaboration with the Teesside Laboratories of the British Steel Corporation.

September 1984



7932907-01

*
*
* IN THE NAME OF *
*
* ALLAH *
*
* THE MOST GRACIOUS *
*

PREFACE

This thesis is submitted for the degree of Doctor of Philosophy of the Council for National Academic Awards, the research work described having been carried out in the Department of Metallurgy of Sheffield City Polytechnic. No part of the research work described has ever been submitted by the undersigned for the award of any other degree.

In addition to the research, the following courses were attended and the course booklet described below studied:

- (i) Post-graduate courses: Department of Metallurgy
Sheffield City Polytechnic
 - (a) Process Metallurgy. 64 hrs.
 - (b) Electric Arc Steel Making. 24 hrs.
- (ii) Directed Study using course booklet "Direct Reduction of Iron Ore" by Dr A W D Hills.
- (iii) Course booklet - "multi-component diffusion on porous media" by Dr A W D Hills

ACKNOWLEDGEMENTS

I would like to thank my Polytechnic supervisor, Mr T J J Smith and Dr A W D Hills for all the guidance they have given me during the period of this work.

Sincere thanks are also expressed to my industrial supervisor Dr G J Hassall from the Teesside Laboratories of the British Steel Corporation for his valuable discussions. I am also grateful to Dr G Briggs for his recommendations and advice given during this work.

I would like to thank all those departmental technical staff members who have supported me with special thanks to Mr D Latimer and Dr B Lewis for their assistance.

Finally I would like to express my sincere thanks to the Mehran University of Engineering and Technology, Jamshoro, Sind, Pakistan for leave of absence and their financial support.

ABSTRACT

The objective of the present work was to study the reduction properties of doped hematite pellets, with special reference to the properties demanded by direct reduction (DR) processes, viz: high reducibility coupled with low dimensional changes and high strength during reduction. Iron oxide ores doped with lime, silica and alumina were studied microstructurally using optical and scanning electron microscopy after compaction and sintering. A reduction-under-load apparatus has been designed comprising a strain-gauged cantilver beam at the bottom and a scaled screw-jack at the top which allows the dimensional changes of the doped iron oxide pellets to be followed during reduction under a range of different initial stresses.

The reducibility of doped iron oxide pellets has been determined in hydrogen and in a hydrogen/carbon monoxide gas mixture using a thermogravimetric spring balance. The results showed that the reduction of iron oxide pellets in hydrogen follows three different modes of reduction, viz: homogeneous, mixed mode and topochemical. These modes are associated with varying degrees of dimensional stability and reducibility. The topochemical mode of reduction exhibits the highest dimensional stability but lower reducibility than the homogeneous mode. On the other hand, the homogeneous mode gives better reducibility but less dimensional stability. In general, lime improves dimensional stability but decreases reducibility, whereas silica and alumina both increase reducibility and decrease dimensional stability.

The variation in these properties have been related in this work to the phases present in the pellet microstructure and to their morphology. Reduction in a mixture of hydrogen and carbon monoxide showed that doping agents have similar effects on reducibility as in pure hydrogen but with overall slower rates of reduction.

PREFACE

ACKNOWLEDGEMENTS

ABSTRACT

CHAPTER 1

INTRODUCTION	1
--------------	---

CHAPTER 2

LITERATURE SURVEY

2. Introduction	3
2.1 Nature of the oxides of iron	3
2.2 Pelletization of iron oxides	5
2.2.1 Feed preparation and firing of iron oxide pellets	5
2.2.2 Influence of slag-forming constituents on the structure and phase formation in iron oxide pellets during sintering	7
2.3 Reduction of iron oxides by reducing gases	11
2.3.1 Direct reduction processes	13
2.3.2 Use of direct reduced iron in Electric Arc Furnaces	16
2.4 Reducibility of iron oxide pellets	18
2.4.1 Mechanism of iron oxide reduction	18
2.4.2 Influence of chemical constituents of iron oxide pellets on reducibility	25
2.4.3 Influence of physical characteristics of iron oxide pellets on reducibility	29
2.4.4 Influence of operating variables on reducibility	30
2.5 Dimensional changes of iron oxide pellets during reduction	33
2.5.1 Influence of chemical constituents on the dimensional changes of iron oxide pellets	36
2.5.2 Effect of physical characteristics of iron oxide pellets on dimensional changes	40
2.5.3 Effect of operating variables on the dimensional changes	40

2.6	Strength of iron oxide pellets during reduction	42
2.6.1	Influence of chemical composition and mineralogy on strength of iron oxide pellets	43
2.6.2	Effect of operating variables on the strength of iron oxide pellets during reduction	45

CHAPTER 3

EXPERIMENTAL PROCEDURE

3.1	Introduction	47
3.2	Preparation of iron oxide pellets	47
3.3	Development of reduction-under-load apparatus	49
3.3.1	Calibration of strain-gauged cantilever beam system	53
3.3.2	Temperature control in the reduction furnace	54
3.3.3	Gas purification	55
3.3.4	Critical flow rate	
3.3.5	Blank test and reproducibility of reduction-under-load apparatus	56
3.4	Thermogravimetric spring balance	57
3.4.1	Temperature control	60
3.4.2	Calibration of the glass spring	60
3.4.3	Reduction procedure	61
3.5	Porosity and true density determinations	63
3.6	Metallography	64
3.6.1	Optical microscopy	64
3.6.2	Scanning electron microscopy (SEM)	65
3.7	Gas boundary mass transfer determination experiments	66
3.7.1	Naphthalene sample preparation	66
3.7.2	Temperature determination	66
3.7.3	Sublimation of naphthalene pellets	67

CHAPTER 4

EXPERIMENTAL RESULTS

4.1	Introduction	69
4.2	Density and porosity of iron oxide pellets	69
4.2.1	Density of base material and doped hematite pellets	70
4.2.2	Porosity of base material and doped hematite pellets	71

4.3	The microstructure and constituents of sintered iron oxide pellets	72
4.3.1	Variation in microstructure with the addition of different amounts of doping agent	72
4.3.1.1	The microstructure of iron oxide pellets sintered at 1250°C for 3 hours	73
4.3.1.2	The microstructure of iron oxide pellets sintered at 1325°C for 30 minutes	77
4.3.1.3	The microstructure of iron oxide pellet sintered at 1250°C for 12 hours	77
4.3.2	Analysis of microstructural constituents of iron oxide pellets	78
4.3.2.1	Analysis of microstructural constituents of iron oxide pellets sintered at 1250°C for 3 hours	78
4.3.2.2	Analysis of the microstructural constituents of iron oxide pellets sintered at 1325°C for 30 minutes	82
4.3.2.3	Analysis of the microstructural constituents of iron oxide pellet sintered at 1250°C for 12 hours	82
4.4	Results of mass transfer experimentation	83
4.5	The reducibility of iron oxide pellets	85
4.5.1	Reducibility in hydrogen gas at 830°C of different iron oxide pellets sintered at 1250°C for 3 hours	85
4.5.2	Reducibility of doped iron oxide pellets produced by sintering at 1250°C for 3 hours and reduced in a gas mixture of hydrogen + carbon monoxide at 830°C	87
4.5.3	The reducibility in hydrogen at 850°C of iron oxide pellets sintered at 1325°C for 30 minutes	88
4.5.4	The reducibility in hydrogen at 850°C of iron oxide pellets sintered at 1250°C for 12 hours	88
4.6	Dimensional stability and strength of iron oxide pellets during reduction in hydrogen at 830°C	88
4.6.1	Dimensional changes	89
4.6.2	Relationships between reduction properties (reducibility and linear change) of iron oxide pellets containing varying amounts of doping agents at different stresses	90
4.6.3	Relationship relating peak expansion to pellet composition at different stresses	92
4.6.4	Relationship at different stresses between the terminal expansion and composition of iron oxide pellets containing varying amounts of doping agents	95

4.7	The density and porosity of unreduced and reduced iron oxide pellets, reduced in hydrogen at 830°C	98
4.8	Microscopic observation of partially reduced pellets	98

CHAPTER 5

DISCUSSION

5.1	Commercial importance of reduction properties	101
5.2	Discussion of experimental accuracy and mass transfer through gas boundary layer	103
5.2.1	Assessment of experimental errors	103
5.2.2	Comparison of mass transfer across gas boundary layer in reduction-under-load apparatus and spring balance	106
5.3	Presentation of results in ternary diagram form	110
5.4	The designation of the different reduction modes and their influence on dimensional stability	114
5.5	Influence of doping agents on the microstructure of the sintered pellets	120
5.5.1	Identification of phases	120
5.5.2	Incidence of phases	122
5.5.3	Comparison with previous work	125
5.6	Influence of microstructure of sintered pellets on the speed of reduction of hematite to magnetite and hence on the mode of reduction	128
5.7	Influence of doping agents and a hydrogen/carbon monoxide gas mixture on reducibility.	140
5.8	Influence of doping agents on the reduction properties of iron oxide pellets reduced at 850°C	143
5.9	Relevance of present findings to industrial DR processes and use of DRI	144

CHAPTER 6

CONCLUSIONS AND SUGGESTIONS FOR FURTHER WORK	149
REFERENCES	152

	<u>Page No.</u>
APPENDIX 1: Determination of the true density of the iron ore concentrate	160
APPENDIX 2: Calculation of the diffusion coefficient in binary gas mixture	162
APPENDIX 3: Calculation of the kinematic viscosity of gases	164
TABLES	166
PLATES	184
FIGURES	212

1. INTRODUCTION

The reduction properties of hematite pellets are of vital interest because of the abundant availability of hematite ores and their use as a basic source for producing iron. At the present time two such processes are in commercial use. These are the Blast Furnace and the Direct Reduction processes in which iron oxide in the form of lumps, fines and agglomerates are reduced. These processes can be differentiated on the basis, that the iron produced in the former is in liquid form, while iron produced in the latter process is in solid form.

The demand for iron oxide pellets has increased with the development in the last two decades of the DRI-EAF route, because of the availability of natural gas, the shortage or high price of good quality cooking coal, and also the high capital cost of the BF-BOF route.

Iron oxide pellets were initially produced for the blast furnace process, but are now also used as a major burden material for DR processes. The ideal reduction properties of such pellets are (i) high reducibility, (ii) resistance to degradation during heating and reduction, (iii) minimum amount of swelling during reduction, (iv) low tendency to stick and form clusters at reduction temperature, (v) high strength of reduced product, (vi) resistance to reoxidation of reduced pellets. The first three properties quoted are common requirements for both processes but the other properties are required particularly in DR processes.

The main objective of this work is to study the reduction behaviour of iron oxide pellets to be used in DR processes, eg Midrex and HYL, with reference to the above requirements. These required properties are dependent on the gangue minerals, ie silica, alumina and lime, which are usually contained in iron oxides as impurities and also on the operating variables eg reducing temperature, reductant composition and load on the pellets. In practice the reduction temperature in DR processes cannot be raised significantly due to the problem of sticking of iron oxide pellets during reduction. The emphasis must therefore be on the preparation of suitable iron oxide pellets in order to meet the above requirements. Hence it was decided to dope hematite pellets using different amounts of above gangue minerals, bearing in mind that the DRI consumers demand low gangue contents especially with regard to acid constituents.

This work was carried out to study the reduction properties of doped hematite pellets. The second chapter of this thesis covers the basic concepts of reduction of iron oxides and the influence of initial constituents and operating variables on reduction properties. The third chapter describes the various experimental techniques including doping and sintering of the pellets, thermogravimetric studies using hydrogen gas and a $\text{CO} + \text{H}_2$ gas mixture, study of the dimensional changes occurring during reduction with and without load, and the microscopy of initial and reduced materials. The fourth and fifth chapters present respectively the experimental results and discussion.

This chapter provides a commentary on the available technical literature dealing with the nature and pelletization of iron oxides, and the reduction behaviour of iron oxides and pellets based on such oxides. Full details of the references quoted are given in the reference section to be found on Page 152.

2.1 NATURE OF THE OXIDES OF IRON

Iron oxides are compounds of iron and oxygen which appear at the compositions shown in the binary phase diagram given in Fig.2.1 as developed by Darken and Gurry⁽¹⁾. This figure shows that iron and oxygen form three stable oxides containing differing amounts of oxygen as follows:

- a) Wustite Fe_xO (23.1 to 25.1 mass % of oxygen)
- b) Magnetite Fe_3O_4 (27.6 mass % of oxygen)
- c) Hematite Fe_2O_3 (30.1 mass % of oxygen)

Wustite has a cubic lattice of the NaCl type, that is a close-packed oxygen lattice with the iron ions arranged in the octahedral interstices between the larger oxygen ions. Wustite is unstable below 560°C , it decomposes eutectoidally into iron and magnetite ($4 \text{ FeO} \longrightarrow \text{Fe}_3\text{O}_4 + \text{Fe}$). Wustite has a variable composition between $\text{Fe}_{0.95}\text{O}$ and $\text{Fe}_{0.84}\text{O}$, depending on the oxygen potential and temperature. Its variable composition arises because vacancies can occur in the iron sub-lattice of its crystal structure. To maintain electro-neutrality two iron ions become trivalent for each vacancy present in the structure. The specific gravity is between 5.6 and 5.7 as the oxygen content increases over the above range.

Magnetite, sometimes referred to as magnetic iron oxide, is strongly magnetic, its colour varies from grey to black and it has a specific gravity of about 5.0. Magnetite is an oxide of the 2-3 spinel type, for which the general chemical formula is $Me^{2+}_2Me^{3+}_2O_4$. The oxygen ions form a close-packed cubic lattice structure with the divalent and trivalent ions occupying specific sites between the oxygen ions. In the case of magnetite, divalent ions are ferrous ions Fe^{2+} and its trivalent ions are ferric ions Fe^{3+} . Magnetite is of variable composition since its lattice can accept an excess of trivalent ions. However, the range of variable composition is much smaller than that for wustite and is only significant at high temperature.

Hematite of ferric oxide is the most important mineral of iron. The colour of the naturally occurring ores can vary from red to black and steel grey. Hematite ores have values of specific gravity in the range 4.9 to 5.3. There are two types of hematite:

- a) Hexagonal α - Fe_2O_3 which is the most common type found in iron ores. The oxygen ions are arranged in a close-packed hexagonal lattice with two-thirds of the octahedral interstices occupied by Fe^{3+} ions. The oxide has a small oxygen deficit due to vacancies on the oxygen sub-lattice.
- b) γ - Fe_2O_3 which has a structure similar to that of magnetite and is generally regarded as unstable. It is only formed under very specific conditions, e.g. by low temperature oxidation of magnetite.

Pelletization (pellet-forming) is a technique in which iron ore fines are converted to a regular and smooth shape^(2,3). The pelletizing process became industrially significant in the U.S.A. using magnetite fines, but today hematite is also used as a feed material. There are three well-known methods used to produce pellets on a commercial basis⁽⁴⁾, viz. (i) the straight grate, (ii) the circular grate, (iii) the grate-kiln process. The earliest pellets formed in these processes were for feeding to the blast furnace and were acid in nature. These processes are now also used for producing pellets of a wider range of compositions for reduction in DR processes, with the straight grate being the most popular.

The main steps involved in pelletising are, (i) feed preparation, (ii) balling, (iii) drying, (iv) preheating and (v) firing. The properties of the end-product are strongly dependent on the feed preparation and firing conditions used, together with the chemistry and mineralogy of the initial material and any additions made.

2.2.1. Feed Preparation and Firing of Iron Oxide Pellets

It has been broadly accepted that the quality of pellets is largely influenced by the degree of fineness of the initial feed particles. Finer particles make an important contribution to the interlocking of the grains in the green balls and hence increase the strength and ease the balling kinetics^(2,4). It has been recommended that feed material should have a specific surface (Blaine index) of 1500 - 2000 cm²/g⁽⁵⁾. Urich and Ban⁽⁶⁾ demonstrate that the

quality of fired pellet can be controlled by the degree of fineness of the initial particles. A specular hematite was ground to give products with the $-44\mu\text{m}$ content ranging from 45 to 100% as given below:

% $-44\mu\text{m}$ in Feed Material	Green ball strength	
	lb	kg
45	1.5	0.7
75	2.9	1.3
100	8.6	3.9

It was found that the green pellet strength increased with degree of fineness, and that the balling rate increased as the fineness of the feed material increased. It was also found by Sandoval⁽⁵⁾ that increasing fineness of the feed material resulted in higher compressive strength and decrease of porosity. A fineness of ⁽⁵⁾ 80% $-44\mu\text{m}$ was recommended by Sandoval for optimum results.

During firing pellets are heated to different temperatures, depending on the type of ore and the gangue content. Usually pellets are fired in an oxidizing atmosphere at temperatures of up to $1250 - 1350^{\circ}\text{C}$. As a result, oxide bonding, grain growth and some slag bonding occur, thereby improving the strength⁽⁷⁾.

During firing the strength of hematite pellets is developed by oxide bridging, recrystallization and slag formation. Grain growth has been found to be directly related to the firing temperature up to 1350°C . During firing small particles lose their identity and recrystallize into rounded Fe_2O_3 granules which act as bridges and bond together the large particles.

On the other hand, large particles are subjected to varying degrees of superficial migration, forming humps. Above 1350°C temperature reversion of $\text{Fe}_2\text{O}_3 \longrightarrow \text{Fe}_3\text{O}_4$ takes place, and slag occurs as inclusions in the Fe_3O_4 formed and as intergranular films between the Fe_2O_3 grains, replacing oxide bridges. As a result the strength is decreased. It has also been reported that this reversion can take place at a temperature as low as 1358°C in the presence of lime⁽³⁾.

Magnetite pellets are oxidized during firing to Fe_2O_3 and their strength is developed by recrystallization and grain growth of the Fe_2O_3 ⁽⁸⁾. As a result, a duplex structure consisting essentially of Fe_2O_3 at the shell and Fe_3O_4 in the core is found. The relative proportions of these phases present depends on the heating rate and firing temperature. In the presence of gangue, slag formation starts at $1100 - 1150^{\circ}\text{C}$. Only a small quantity of gangue is sufficient to envelope the iron oxide particles in a film of slag and if the viscosity of this film is high, the oxidation of Fe_3O_4 can be inhibited. Melting of slag at temperatures above 1150°C assists crystallization and grain growth, and hence aids the development of strength.

2.2.2. Influence of Slag-forming Constituents on the Structure and Phase Formation in Iron Oxide Pellets During Sintering

The main slag-forming constituents in iron oxides are calcium oxide, silica and alumina. Extensive work has been carried out on laboratory-made as well as on commercial pellets, and also on sinters, in order to examine the influence of slag-forming constituents on micro-structure and phase formation during sintering.

A phase diagram for the $\text{Fe}_2\text{O}_3 - \text{CaOSiO}_2$ system as reproduced by Philips and Muan⁽⁹⁾ is shown in Figure 2.2 (a). From this figure it is clear that there is no compound formation between hematite and silica. On the other hand, it will be seen that compounds are formed between CaO and Fe_2O_3 and between CaO and SiO_2 .

Lime reacts with Fe_2O_3 to form the ferrites, i.e. $\text{CaO} \cdot \text{Fe}_2\text{O}_3$, $2\text{CaO} \cdot \text{Fe}_2\text{O}_3$ and $\text{CaO} \cdot 2\text{Fe}_2\text{O}_3$ as shown in Fig. 2.2 (b). Besides these ferrites, Ahsan et al⁽¹⁰⁾ have found hematite containing 7.0% of lime which they named as calcium ferrite.

Matsune⁽¹¹⁾ reported that calcium ferrite is formed by solid state diffusion at $950 - 1000^\circ\text{C}$ and melts at about 1200°C . Calcium ferrite liquid, due to its low viscosity, disseminates very easily throughout the pores in the pellet and result in a close-pored microstructure⁽¹²⁾. In the literature there is disagreement about the presence of calcium diferrite (CF_2) at ambient temperature. According to Philips et al⁽⁹⁾ CF_2 is thermodynamically unstable below 1155°C and decomposes during cooling into calcium monoferrite (CF) and hematite. However, the presence of this phase has been mentioned by many workers - Turkdogan et al⁽¹³⁾, Moon et al⁽¹⁴⁾, Friel et al⁽¹⁵⁾, Lu et al⁽¹²⁾ and recently by Staia⁽¹⁶⁾.

Moon and Walker⁽¹⁴⁾ and Lu et al⁽¹²⁾ attribute the presence of CF_2 at low temperatures to cooling rates high enough to suppress the decomposition of calcium diferrite. On the other hand, Ahsan et al⁽¹⁰⁾ have found a wide range of calcium ferrites present in sinter in addition to C_2F and CF . They found phases containing 7.6 - 13.0 m/o calcium and 47.2 - 62.3 m/o iron including those with a composition corresponding to the stoichiometric values for CF_2 . At the same

time they have found the phases present to be of variable morphology including the presence of needles and laths. Shehata et al⁽¹⁷⁾ have also reported the formation of all calcium ferrite phases (CF , CF_2 and C_2F) in lime doped pellets.

Phases are also formed between calcium oxide and silica as shown in Fig. 2.2 (a). The extent of their formation depends upon their contact and on the sintering temperature. Kunii et al⁽¹⁸⁾ studied the mineral phases in self-fluxing pellets with various basicities (ratio of acid to basic $\frac{CaO}{Al_2O_3 + SiO_2}$) and found that, if the basicity is lower than 0.5, most of the siliceous constituents react with constituents containing calcium oxide to form pseudo-wollastonite ($CaO \cdot SiO_2$) in the solid state. At higher basicity values greater than 0.5, pseudo-wollastonite ($CaO \cdot SiO_2$), as well as some calcium ferrite, is formed because excess calcium oxide reacts with hematite. Similarly, Friel et al⁽¹⁵⁾ found that calcium silicates of formulae $CaO \cdot SiO_2$ and $3CaO \cdot 2SiO_2$ are formed at a basicity of 0.6 whereas at an increased basicity of 1.3, they found $3CaO \cdot 2SiO_2$ together with calcium diferrite containing dissolved silica. The presence of glass in silica-added pellets has also been reported by Turkdogan and Vinter⁽¹³⁾, Shehata et al⁽¹⁷⁾ and Frazer et al⁽¹⁹⁾.

Mamuro et al⁽²⁰⁾ studied the phases present in commercial acid and basic pellets by X-Ray microanalysis and found slags mainly composed of calcium oxide and silica with a smaller proportion of hematite. They classified such slags on the basis of CaO/SiO_2 ratio as of high, middle or low basicity. As well as the slag they found calcium ferrites, some of them containing significant amounts of silica and alumina. These showed similar chemical composition to

those mentioned by Ahsan et al⁽¹⁰⁾ for silico-ferrites of calcium aluminate (SFCA). Ahsan et al⁽¹⁰⁾ also found a wide range of silicates present in fluxed sinters.

Further phase formation possible in the $\text{CaO-SiO}_2\text{-Fe}_2\text{O}_3$ system is between calcium ferrites and silica, e.g. where a CF melt reacts with SiO_2 to form glassy ferrites. Such phases have been referred to by Turkdogan and Vinter⁽¹³⁾, Kaneko and Narita⁽²¹⁾ and Matsuno⁽¹¹⁾.

Hamilton's⁽²²⁾ work has shown the effect of lime and firing temperature on hematite pellets containing alumina and silica. Different phases to those reported above were found due to the presence of alumina. In the temperature range $800 - 1000^\circ\text{C}$, this worker found that calcium alumino-silicate (gehlenite and anorthite) and calcium ferrites ($2 \text{CaO} \cdot \text{Fe}_2\text{O}_3$ and $\text{CaO} \cdot \text{Fe}_2\text{O}_3$) were formed by solid state attack of lime on meta-kaolinite. Minor amounts of mullite and cristobalite were also formed in lime-deficient regions. At $1000 - 1200^\circ\text{C}$ calcium alumino-silicates and ferrites are replaced by a silico-ferrite of calcium and aluminium (SFCA) and a pyroxene mineral. Formation of SFCA has also been reported by Coheur⁽²³⁾, Ahsan et al⁽¹⁰⁾, Hancart⁽²⁴⁾ and Mukherjee and Whiteman⁽²⁵⁾. Hancart⁽²⁴⁾ found two complex crystallized phases. The first is deficient in iron and is an alumino-silicate of the Fe-gehlenite type having the stoichiometric formula $\text{Ca}_2\text{Fe}^{3+}(\text{AlSi})\text{O}_7$ which he designated by the symbol GH. The second phase is rich in iron and calcium, and contains a little silica and alumina. Its structure derives from $2 \text{Fe}_2\text{O}_3 \cdot \text{CaO}$ and this phase is symbolized by SFCA. Other phases in the $\text{Al}_2\text{O}_3\text{-CaO-SiO}_2\text{-Fe}_2\text{O}_3$ system mentioned by Mazanek and Jasienska⁽²⁶⁾ include $\text{CaO} \cdot \text{Al}_2\text{O}_3 \cdot 2\text{Fe}_2\text{O}_3$ and $4 \text{CaO} \cdot \text{Al}_2\text{O}_3 \cdot \text{Fe}_2\text{O}_3$.

The reduction of iron oxides can only take place when the oxygen potential above the iron oxides has been adequately reduced by the presence of reducing gases, e.g. hydrogen, carbon monoxide or hydrogen/carbon monoxide gas mixtures.

Four solid phases may exist during the reduction of hematite

(Fe_2O_3) to iron except below 570°C , when wustite is not stable.

Below 570°C iron is directly formed from Fe_2O_3 in two stages^(27, 28),

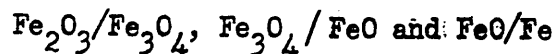
viz. $\text{Fe}_2\text{O}_3 \xrightarrow{\text{Stage I}} \text{Fe}_3\text{O}_4 \xrightarrow{\text{Stage II}} \text{Fe}$. However, above 570°C ,

when wustite is a stable phase, the reaction takes place in the

following three stages:



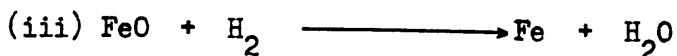
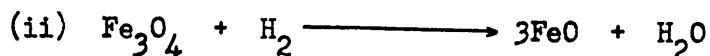
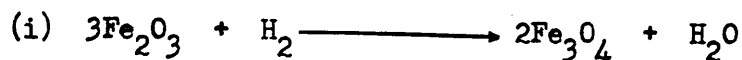
During reduction, the following phase boundaries exist:



The reduction of iron oxides by hydrogen is the net result of two

or more gas-solid reactions. Above 570°C the reduction of Fe_2O_3

takes place through the following sequence of chemical reaction:

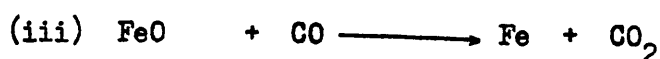


The values of enthalpy changes (ΔH°) for these reactions are given

in Table 2.1. The reduction of hematite to magnetite liberates

heat, whilst heat is absorbed in the reduction of magnetite to wustite and wustite to iron. The net result of reduction of Fe_2O_3 to Fe by H_2 is heat absorption.

The reduction of iron oxides by carbon monoxide follows similar steps to those using H_2 , viz.



At low temperatures (below 800°C) carbon deposition is increasingly favoured by the Boudouard reaction $2\text{CO} \rightleftharpoons \text{CO}_2 + \text{C}$ as shown in Fig. 2.3⁽²⁸⁾.

Carbon deposition is believed to be catalysed by the presence of freshly reduced iron⁽²⁸⁾. It can be seen from Table 2.1 and Fig. 2.3 that the reductions by carbon monoxide of Fe_2O_3 to Fe_3O_4 and of wustite to iron are both exothermic, whereas that from magnetite to wustite is endothermic. The overall reduction of hematite to iron is exothermic.

The reduction of iron oxides using $\text{H}_2 + \text{CO}$ gas mixture is now widespread with the development of DR processes. The composition of such reducing gas mixtures varies widely with respect to the hydrogen/carbon ratio depending upon the source and method of gas manufacture⁽²⁸⁾.

2.3.1 Direct Reduction Processes

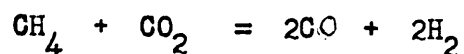
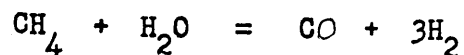
Direct reduction is a process to produce iron without melting, and as a smelting process can compete with the blast furnace. Up to now more than one hundred techniques have been suggested to produce Direct Reduced Iron (DRI), but the two processes of commercial significance currently are the Midrex and HyL processes^(28,29). In view of the demands placed on the pellets charged for reduction in such processes and on the recent rapid expansion of DR processes, it is proposed to include a short description of each technique.

Midrex Process

This process basically consists of a gas reforming system for the production of reducing gas, and a shaft furnace in which reduction takes place in a similar manner to the upper region of a blast furnace. These two main stages are shown clearly in Fig. 2.4⁽²⁸⁾.

In the gas reformer natural gas is converted to the reducing gas.

The oxygen removed from iron oxides as CO_2 and H_2O provides the oxygen required to reform the natural gas, as shown by chemical reactions:



Therefore, part of the exit gas from the reduction furnace is re-circulated to the reformers including heat, the remainder being

burned to provide the necessary heat for gas-reforming and preheating of the combustion air, or being used to prevent re-oxidation of metallized product on cooling.

In the shaft furnace, iron oxide, generally in the form of pelletised ore, descends and is heated and reduced by a rising stream of hot reducing gas at a temperature of about 860°C. After reduction the charged material enters the conically-shaped bottom section, where it is cooled before discharge.

The Midrex process is attractive because it is continuous and consumes about 20% less energy than other process utilizing natural gas. It gives a product of reasonable quality with respect to degree of metallization and controlled carbon content, and has a high production rate. At the present time furnaces which produce up to 1 million tonnes per year of DRI are in operation.

The DRI product from this process has a typical composition which makes it an ideal charge material for the electric arc furnace. By careful control, the Midrex process can give degrees of metallization in the range 85-98% and carbon contents of between 0.7 to 2%. The gangue and sulphur contents depend largely on the initial composition of iron ore used, but products containing 5% gangue and 0.005% sulphur are typical.

This process has been in commercial operation for more than 25 years, and is a batch-type process in which iron oxides in the form of either lumps or pellets are converted to DRI with a mixture of $\text{CO} + \text{H}_2$ reducing gas.

The reducing gas is prepared by catalytic conversion of natural gas and steam in a reformer. A gas of composition (by volume) 75% H_2 , 14% CO , 8% CO_2 and 3% CH_4 is obtained, and this flows through the reducing units in series where preheating, reduction and cooling occur. In the reduction units, reducing gases at about $1000 - 1200^\circ\text{C}$ are introduced to reduce iron oxides and subsequently cooling of the DRI product and carburization to the desired level are performed.

In 1980, this process was modified to a continuous gas-based direct reduction process with many inherent advantages. The features of this modified plant, designed to produce 750,000 tonnes per year are given in Fig. 2.5⁽³⁰⁾.

Compared to the previous batch-type HyL process, the continuous plant has the following advantages⁽³⁰⁾:

- (i) Less energy consumption.
- (ii) Independent control of degree of metallization and carbon content.

- (iii) Lower capital investment.

There is still much more research required to improve the productivity of these DR processes. Productivity can be improved by using highly reducible, strong, non-sticking and non-swelling iron oxide pellets. Good reducibility is related to the gangue content and porosity of the pellets, low gangue content and highly porous pellets favouring high reducibility but giving less strength, more swelling and more sticking. On the other hand, higher gangue contents improve all the other properties at the expense of reducibility, but the users of DRI prefer low gangue contents which are consistent with lower energy consumption in the EAF. Hence, further work is required to optimize the chemical composition of iron oxide pellets as feed for DR processes and for DRI consumers.

2.3.2 Use of Direct Reduced Iron in Electric Arc Furnace

At the present time about 95% of DRI produced is used in the electric arc furnace (EAF), where it provides the complete or partial source of iron units. The main reasons for its use are⁽²⁸⁾:

- (i) The chemical composition of DRI is uniform and known exactly,
- (ii) DRI contains very low levels of undesirable metallic impurities,
- (iii) use of DRI permits dilution with low cost scrap,

- (iv) DRI is easy to transport and handle and can be continuous charged,
- (v) DRI increases furnace productivity.

In contrast to these advantages, DRI has an adverse effect on energy consumption in the EAF. This is related to the characteristics of DRI including, (i) the amount of gangue, (ii) the composition of the gangue and (iii) the degree of metallization defined as the ratio of metallic iron to total iron expressed as a percentage.

The gangue content of DRI influences the slag weight as illustrated in Fig. 2.6⁽³¹⁾ for various percentages of DRI in charge. The weight of slag produced in the EAF depends on the gangue content and the amount of lime required to balance the acid constituents, alumina and silica. Consumers are normally prepared to accept reduced pellets containing an acid gangue content of up to 4%.

Additional energy is also required in the EAF to allow the endothermic reduction of wustite present in reduced pellets of low degree of metallization. The joint influences of gangue content, gangue composition and degree of metallization are shown in Fig. 2.7⁽³¹⁾.

Reducibility is arguably the most important characteristic of iron oxide pellets, and is the ease with which oxygen can be removed from iron oxide pellets. Very simply defined, reducibility is a measure of the mass percentage of oxygen removed from iron oxides per unit time for a selected degree of reduction (% oxygen removal/minute or oxygen milligram removed/minute). Values for reducibility by laboratory and other conventional testing methods have been determined by many workers^(28,32,33). Some workers have used 90% reduction as an arbitrary degree of reduction for reducibility measurements: others have used values as low as 50% reduction for reducibility measurements whichever is most suitable for the particular process. With improved reducibility, fuel consumption and productivity are favoured^(21,28).

It has been reported in previous work that reducibility is strongly dependent on the physical and chemical nature of iron oxide pellets as well as on the operating variables. Before studying the effect of these factors on reducibility, it is necessary to study the mechanisms of reduction by which iron oxides are converted to the metallic state. For reduction of iron oxide, these mechanisms are very complex because the oxide must go through a series of changes step by step before the conversion is complete. The slowest step in the process is referred to as the "rate-controlling step".

2.4.1 Mechanism of Iron Oxide Reduction

Reduction of iron oxides may be accomplished by hydrogen and carbon monoxide either individually or as a mixture. Reaction takes place when reducing gases come in contact with iron oxide surfaces. In

previous work^(13, 19, 34, 35) it has been reported that iron oxide particles are reduced either non-topochemically (homogeneously) or topochemically (layer wise), the mode of reduction being mainly dependent on the porosity and size of particles.

Homogeneous reduction occurs when iron oxide pellets are very porous and permit the reducing gases to diffuse freely throughout the whole structure and reduce each iron oxide grain individually. In such cases, microstructural observation does not show any distinct interface between groups of reduced and unreduced oxides. Wen⁽³⁵⁾ reported that iron oxide particles having moderate porosity values (20 - 40%) are initially reduced in a homogeneous manner. However, as the outer surface of iron oxide particles continues to be exposed to the reducing gases which have sufficient potential to reduce iron oxide to metallic iron, the outer zone becomes reduced to a higher degree although the reduction occurs throughout the whole particle. After a certain time a significant outer layer of reduced iron forms and reduction thereafter proceeds by another mode similar to that found by Turkdogan and Vinter⁽³⁴⁾ reported as mixed mode and described below.

Turkdogan and Vinter⁽³⁴⁾ reduced hematite particles of varying size in hydrogen and found three different modes of reduction, (1) Homogeneous, (2) Mixed mode and (3) Topochemical. Homogeneous mode prevails in small particles and reduction takes place throughout the whole structure. Mixed mode is in fact a special case of the topochemical mode of reduction, where partial internal reduction ahead of the nominal iron/wustite interface takes place. The topochemical mode of reduction they found confined to larger particles, where iron is nucleated only at the iron/wustite interface. In this mode, reduction

follows ~~three~~ advancing surfaces which proceed towards the centre of the particle during reduction. Fig. 2.8 illustrates a typical example of such type of reduction, where the hematite core is surrounded by a layer of magnetite which, in turn, is surrounded by a layer of wustite and finally by a layer of wustite and finally by a layer of completely reduced iron.

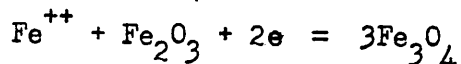
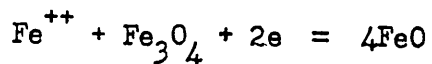
Frazer et al⁽¹⁹⁾ reported two modes of reduction, under the names topochemical and non-topochemical. He classified the reduction of pellets exhibiting successive layers from the surface of iron, wustite and magnetite as "topochemical". On the other hand, reduction of iron oxide pellets which are initially reduced throughout the whole structure to magnetite, followed by reduction to iron only after substantial reduction to magnetite and wustite, is classed as "non-topochemical".

The above modes of reduction arise from different mechanisms of oxygen removal. Oxygen is removed from iron oxides through the following basic steps:

- (a) Diffusion of the reducing gas from the bulk gas phase through the boundary layer, which builds up around the surface of the iron oxide particle.
- (b) Diffusion of reducing gases through the reduced layer surrounding the unreacted core.
- (c) Chemical reaction at the interface of reduced and unreduced layer.
- (d) Diffusion of product gases H_2O , CO_2 or $H_2O + CO_2$ through the reduced layer.
- (e) Diffusion of product gases through the boundary layer.

These steps are valid for the above reduction modes except steps (b) and (d), which are not significant in homogeneous reduction, because, when iron oxide particles contain enough voidage to allow the reducing gases to diffuse into the interior of the particles, reduction of each grain takes place separately throughout the particle and there is no distinction between the product layer and the unreacted core.

In other modes of reduction, the reducing gas is unable to contact the magnetite layer and hematite core directly. Edstrom⁽³⁶⁾ proposed a reduction mechanism based on solid state diffusion of ferrous ions. The solid state diffusion of ferrous ions through the wüstite crystal lattice is facilitated by the presence of lattice vacancies. Ferrous ions and electrons diffuse across the wüstite and magnetite layers, where they react with magnetite and hematite to produce wüstite and magnetite respectively according to the reactions:



According to the McKewan⁽³⁷⁾ solid-state reduction of magnetite and of hematite are faster than gas-solid reaction at the Fe/FeO interface, the latter being regarded in his early work as the rate-controlling step.

In topochemical reduction oxygen removal is the result of:

- (i) Mass transfer through boundary layer.
- (ii) Mass transfer through reduced layer(s).
- (iii) Chemical reaction at the interface.

In spite of extensive work carried out in this area, there is still some disagreement about which is or are the rate-controlling step(s). This is basically due to the complexity of the reduction of iron oxides, the similarity of the rate relationships and the involvement of many variables.

Mass Transfer Through Boundary Layers

The gas boundary layer is one of the factors which influence heat and mass transfer at the outer surface of a solid phase. The reduction rate is partially controlled by the rate of diffusion of gas and heat through the gas boundary layer that builds up around each particle in the flowing process gas. The rate of diffusion of gas through this layer is proportional to the concentration difference of reactant or product gas across the layer. Similarly, heat flow is proportional to the temperature difference across this layer. These rates are a function of the surface geometry, the location along the surface, the fluid velocity, the properties of the fluid and its concentration. Mass transfer has been characterized by the dimensionless Sherwood Number (Sh) which is a function of the Reynolds Number (Re) and the Schmidt Number (Sc).

For a single particle of iron oxide suspended in a laboratory reactor, most workers have stated that the boundary layer resistance is minimized by maintaining the gas velocity above the "critical velocity". It is contended that further increase in the gas velocity above this value does result in an increase in the rate of reduction. Such views have been held by Edström⁽³⁶⁾, McKewan⁽³⁷⁾, Wright⁽³⁸⁾ and Seth and Ross⁽³⁹⁾.

However, Warner⁽⁴⁰⁾, Hills⁽⁴¹⁾ and Harrington⁽⁴²⁾ have shown that the establishment of a critical flow rate does not preclude the existence of significant partial pressure differences across the boundary layer. Establishment of critical flow merely indicates that sufficient reactant gas is provided to the vicinity of the sample for the reaction rate to be independent to the rate of gas supply. At lower rates, the reaction uses up such a large fraction of the gas supplied that the composition of the gas in the reaction zone departs significantly from the inlet gas composition.

Warner⁽⁴⁰⁾ estimated the mass transfer coefficient at high reduction temperature from a dimensionless correlation based on a room temperature mass transfer analogue. Warner⁽⁴⁰⁾ studied the vaporization of cast naphthalene cylinders of the same dimensions as hematite specimens being examined. The rate of vaporization was determined by using a quartz-spring balance. He plotted the dimensionless term (Sherwood Number) (Schmidt Number) ^{$\frac{1}{3}$} against the Reynolds Number in order to obtain the mean mass transfer characteristics through the boundary layer. From his experimental work, Warner⁽⁴⁰⁾ deduced the following form of the Ranz and Marshall⁽⁴³⁾ equation:-

$$Sh = 2.0 + 0.6 (Re)^{0.5} (Sc)^{0.33}$$

Within the range of Reynolds number employed to establish the "critical gas flow", the gas film mass transfer coefficient is not affected and the employment of a critical gas flow rate only ensures that the system is not suffering from gas starvation. The increase of Reynolds Number from 1 to 2, by doubling gas velocity, increases the mass transfer coefficient by only 15%. Harrington⁽⁴²⁾ has pointed out a similar effect together with the influence of tube geometry. He found that the reduction rate is more highly controlled by the gas

boundary layer in a reaction chamber of larger diameter than in one of smaller diameter even though in both sets of apparatus, the flow rate used was above the critical flow rate. Rao and Moirpour⁽⁴⁴⁾ have mentioned very recently that mass transfer through the boundary layer has a significant influence on the rate of reduction, even though reduction was carried out in excess of starvation level. They reduced hematite foils of 2.5 cm long x 1.25 cm wide and approximately 35 μ m in thickness and found the actual rate of reduction to be much less than one which is not affected by boundary layer resistance.

Mass Transfer Through the Reduced Iron Layer

Many workers have reported that the rate of reduction is controlled by the diffusion of reducing and product gases through the reduced iron layer. Bogdandy and Janke⁽³³⁾ have reported that reduction is controlled by diffusion through pores of reduced iron. Warner⁽³⁸⁾ came to a similar conclusion viz. that the rate of reduction depends on the gas film resistance and particularly the diffusion of reactant and product gases through the product layer. Seth⁽³⁹⁾ presented a model based on the general rate equation for gaseous diffusion control in spherical particles and showed that during the intermediate stages of reduction, i.e. with a degree of reduction between 0.4 and 0.85, the reduction rate is controlled predominantly by gaseous diffusion. The deviations found in early and final stages could be due to the other rate-controlling factors such as chemical control in the initial stages and the influence of sintering of the reduced iron on diffusion in the later stages. Turkdogan and Vinter⁽³⁴⁾, Towhidi and Szekely⁽⁴⁵⁾ and Olsen and McKewan⁽⁴⁶⁾ have also reported that gaseous diffusion through the reduced iron layer plays an important role.

Early studies, including those of McKewan⁽³⁷⁾, have examined the role of the chemical reaction at the FeO-Fe interface. An early model based on chemisorption of hydrogen at this interface as the rate-controlling step up to about 70% reduction was subsequently replaced by the same author in collaborative work with Olsen⁽⁴⁶⁾ by a largely controlled diffusion-controlled model.

2.4.2 Influence of Chemical Constituents of Iron Oxide Pellets on Reducibility

The iron oxides usually found in pellets are Fe_2O_3 and Fe_3O_4 , either individually or in combined form with other oxides. These two oxides have different reducibilities, as determined by Edström⁽³⁶⁾. Hematite has a superior reducibility compared with raw magnetite because when hematite is reduced it expands and the resulting product (magnetite) is more porous, which favours its reducibility. On the other hand, the reduction of magnetite results in a product (wustite) which is dense and hence has a lower reducibility. Edström⁽³⁶⁾ showed that a small degree of oxidation can significantly affect the rate of reduction. Oxidized magnetite was shown to give very similar reduction rates to natural hematite.

Impurities have a profound effect on the reduction kinetics of iron oxide pellets. Some improve the reducibility while others have a deleterious effect. Some impurities in ores are in solid solution whilst others are in the form of compounds with the iron oxides: thereby lowering the activity of the latter. In other cases, the impurities form a binding phase that cements the iron oxide particles together. In these cases the binding phase or matrix affects the

accessibility of the reductant. The commonest impurities are calcium oxide, silica and alumina. These have different influences on reducibility by forming different matrices depending on whether they are present together or individually.

The effect of lime on the reducibilities of iron oxides has been investigated extensively with considerable variation in the experimental observations made and the accompanying explanations. Some authors state that lime has an accelerating effect, while others the reverse effect. Since many of the explanations include reference to ferrite formation between lime and hematite, details of ferrite formation are shown in Fig. 2.2 (b).

Ross et al⁽⁴⁷⁾ and Seth⁽⁴⁸⁾ have investigated the effect of lime on the reducibility in hydrogen of iron oxides. The effects of the addition of up to 6.0 mass % lime were investigated by Ross et al⁽⁴⁷⁾ who found an improvement in reducibility at 0.6 mass % CaO. However, higher additions did not have much influence. The beneficial effect of lime up to 0.6 mass % was attributed to the increased porosity of the pellets and also to the role of lime in promoting dissociation of wustite. Seth⁽⁴⁸⁾, however, reported that reducibility increased with the increase of lime because of the latter effect only, and neither were due to change of porosity nor to the formation of calcium ferrite. He suggested that wustite is unstable in the presence of lime and breaks down according to the reaction

$$2 \text{CaO} + 3 \text{FeO} \longrightarrow \text{Fe} + 2 \text{CaO} \cdot \text{Fe}_2\text{O}_3$$

into metallic iron and dicalcium ferrite.

According to McKewan⁽³⁷⁾ formation of dicalcium ferrite allows reduction to iron without passing through the wustite stage, which is otherwise a rate-controlling step.

Turkdogan and Vinter⁽¹⁵⁾ have reported that the addition of lime in sintered synthetic 100% hematite pellets reduced at 900°C by hydrogen has little effect on reducibility. However, lime lowers the reducibility when added to sintered commercial grade hematite or magnetite pellets. Similarly, the addition of silica and lime up to 10% by mass does not have much effect on reducibility when added to pure hematite pellets. On the other hand, when added to commercial grade hematite pellets it lowers the reducibility to half of the initial value. The same effect was observed with magnetite and this was attributed to the formation of glassy ferrites and a structure containing closed pores. The addition of lime to hematite and magnetite also changes the mode of reduction. Whereas with lime addition pellets are reduced topochemically, without lime addition they are reduced homogeneously. Kaneko and Narita⁽²¹⁾ reported that the formation of calcium ferrites and iron calcium silicates in the basic pellets giving low reducibilities in comparison to pure iron oxide, because iron oxides fixed in this slag are very difficult to reduce at the low temperatures at which DR processes operate.

Moon and Walker⁽¹⁴⁾ reduced iron oxide pellets in carbon monoxide and found that the addition of lime improves the reducibility because the reaction of lime and hematite to form $\text{CaO} \cdot 2\text{Fe}_2\text{O}_3$ results in extensive pore formation. These pores may be expected to facilitate gaseous diffusion, thereby accelerating the reduction rate. Shehata et al⁽¹⁹⁾ reduced iron oxide pellets containing 0 - 5.0% lime in a hydrogen/carbon monoxide gas mixture and they reported that lime improves the reducibility of iron oxide pellets and suggested that this effect is partly due to the intrusion of calcium atoms in the Fe_2O_3 lattice which decrease its stability and

and partly due to the formation of ferrites. They also reported that with high lime content the reduction rate is less marked because of $\text{CaO} \cdot \text{Fe}_2\text{O}_3$ formation but despite this, it always remains at a value higher than that of pure Fe_2O_3 .

Mazanek⁽⁴⁹⁾ and Asada⁽⁵⁰⁾ reported the relative values of reducibilities of various compounds. Mazanek⁽⁴⁹⁾ reported reducibilities in the following order:

$\text{Fe}_2\text{O}_3 > \text{CaOFe}_2\text{O}_3 \gg 2\text{CaOFe}_2\text{O}_3 > \text{magnetite} > \text{olivine}$, i.e. slightly different from the Asada⁽⁵⁰⁾ who quoted $\text{Fe}_2\text{O}_3 > \text{CaO} \cdot 2\text{Fe}_2\text{O}_3 > \text{CaOFe}_2\text{O}_3 \gg 2\text{CaOFe}_2\text{O}_3$

The combined effect of CaO , SiO_2 and Al_2O_3 on reducibility is related to the particular matrix formation and to its basicity, defined as the ratio of $\text{CaO}/\text{SiO}_2 + \text{Al}_2\text{O}_3$. The matrices generally comprise crystalline silicates, silicate glass, calcium ferrites and silico-calcium alumino-ferrite (SCAF). Shehata et al⁽¹⁷⁾ found that the reducibility decreases at a basicity in the range 0.58 - 0.77 because the iron oxide particles in this basicity range are present in a glassy matrix of silicates and also due to the presence of fayalite. At higher basicities the reducibility increases because of improved porosity.

However, Frazer et al⁽¹⁹⁾ reported that the basic pellets reduce more slowly than acid and less basic pellets because the former pellets possess a coarse grain and close pores structure, while the latter pellets possess an open-pore structure and provide a large surface area for reduction.

The influence of Al_2O_3 on the reducibility of iron oxides has been studied by Bowling and Carter⁽⁵¹⁾, Mazanek and Jasienka⁽²⁶⁾ and Suzuki et al⁽⁵²⁾. Bowling and Carter⁽⁵¹⁾ reported that an increase of alumina from 2 to 4% has no influence on reducibility. Mazanek and Jasienka⁽²⁶⁾ reported that the reducibility of sinter containing 7% Al_2O_3 is lower than that of alumina-free sinter, but the reducibility is higher at 12% Al_2O_3 . They attributed this effect to the varying reducibility of the minerals present, e.g. the high reducibility at 12% Al_2O_3 arises from the presence of $\text{CaO} \cdot \text{Al}_2\text{O}_3 \cdot \text{Fe}_2\text{O}_3$. Suzuki et al⁽⁵²⁾ have reported that the addition of 5% coarse alumina to hematite increases the reducibility and also produces cracks during reduction.

2.4.3 Influence of Physical Characteristics of Iron Oxide Pellets on Reducibility

Maximum porosity in a polycrystalline material would occur when each individual grain is separated from its neighbour and has a reducing atmosphere around it.

The result would be that each grain is reduced individually in a topochemical manner. With increased porosity the surface area for reduction increases in comparison with dense pellets and hence reducibility is improved^(53, 54).

In general it may be said that an increase in initial porosity reduces impedance to gaseous diffusion and increases reduction rates. Where there is little or no porosity, then gas diffusion may become rate-controlling. Joseph⁽⁵⁵⁾ has shown that the time for 90% reduction is proportional to the reciprocal of % porosity. Seth⁽⁴⁸⁾, however, reported that at higher reduction temperatures

of 900 - 1000°C, the initial porosity does not favour the reducibility.

In addition to the effect of initial pellet porosity, it has been shown that any induced porosity caused by the reduction process improves the reducibility. Wustite formed from hematite is more porous than from magnetite as a result of crystal structure changes^(36,56). This porosity during reduction is a function of the process and the size, shape and nature of the pores which, in turn, are functions of the initial form of the oxide and temperature of reduction. If during reduction pores do not form, a retardation in reducibility occurs^(56,57).

A finer particle size is beneficial by virtue of the higher surface area per unit mass provided. It has been confirmed experimentally that when a pellet is reduced by a CO-H₂ mixture or by H₂ alone, the rate of removal of oxygen per unit mass of oxide decreases with the increase of particle size, because large particles provide a lower surface area per unit mass. On the other hand, with packed beds of particles of variable size, fine particles tend to choke the beds during reduction. In practice, it has been found that particles of size from 10 to 20mm appear to be ideal for DR processes^(28,45).

2.4.4 Influence of Operating Variables on Reducibility

It is generally known that increasing the reduction temperature frequently causes a marked increase in the reduction rate⁽⁴¹⁾.

For a simple reaction the rate may be considered according to the "Arrhenius activation energy" concept, which states that the

reaction rate varies exponentially with temperature. Thus, the reaction rate at temperature θ is given by:

$$[\dot{n}] = \nu_0 \exp \left(\frac{-E}{R \theta} \right)$$

where

$[\dot{n}]$ = reaction rate at temperature θ (K)

ν_0 = frequency factor

E = activation energy

R = gas constant

θ = temperature in K

As reported by Sandoval⁽⁵⁾ the higher the reduction temperature the faster is the rate of reduction. In direct reduction shaft furnaces, it has been estimated that production can be increased by as much as 20% for every 55°C increase in the reduction temperature without any increased consumption of reducing gas.

It has been reported by Wright^(38, 57), Henery⁽⁵⁸⁾, Kaneko and Narita⁽²¹⁾ and Hills⁽⁴¹⁾ that reaction rate increases with increase of temperature, no minima or maxima in the reduction rate for hematite being observed by such workers^(21, 38, 57, 58).

Contributory reasons proposed for such increase in reduction rate have been increased porosity by Wright^(38, 57) and Kaneko and Narita⁽²¹⁾ and cracking and gaseous diffusion by Henery⁽⁵⁸⁾. On the other hand, Shehata et al⁽⁵⁹⁾ and Geasy et al⁽⁶⁰⁾ observed minima and maxima with temperature variation in the reduction rate. This is purported to arise from such effects as sintering to produce a dense iron layer, recrystallization and formation of slag.

As already indicated in Section 2.3 hydrogen, carbon monoxide or gas mixtures of hydrogen and carbon monoxide can be used as

reducing agents. Wiberg⁽⁵⁷⁾ reported that at 1000°C hydrogen reduces faster than carbon monoxide up to 75% reduction, beyond which the reduction rate in hydrogen decreases more than in carbon monoxide, resulting in a longer overall time for complete reduction in hydrogen. The reason proposed for the faster reduction in the later stages of reduction by carbon monoxide is that it carburizes the reduced iron forming thin shells surrounding the wüstite. Reaction between the carbon in austenite and the oxygen in wustite results in a high pressure which breaks up the iron shell, facilitating gas exchange at the oxide/metal reaction interface, thereby favouring reducibility.

However, there is a general agreement among many workers - Nixon⁽⁶²⁾, Geasy et al⁽⁶⁰⁾, Towhidi and Szekely⁽⁴⁵⁾, Szekely and Tawil⁽⁹²⁾, Turkdogan and Vinter⁽¹³⁾, Gare et al⁽²⁷⁾, Shehata et al⁽⁵⁹⁾ and Mazanek et al⁽⁶³⁾ that the higher the hydrogen content of reducing gas the faster is the overall rate of reduction as shown in Fig. 2.9⁽⁶⁰⁾. As reported by Nixon⁽⁶²⁾ and Geasy et al⁽⁶⁰⁾, the reduction rate is high in hydrogen because of high diffusivity, and the formation of a thin wustite layer, which has no marked effect on diffusivity. In contrast to Wiberg's⁽⁶¹⁾ finding, incomplete reduction in carbon monoxide at 700 - 800°C is ascribed to the greater amount of carbon deposition and sealing of the porosity, thereby preventing diffusion of reducing gas.

It has been reported by previous workers - Wright⁽³⁸⁾, Nixon⁽⁶²⁾ and Seth et al⁽³⁹⁾, that at low flow rates of reducing gas, the reaction rate is strongly dependent on the velocity of reducing gas. Increasing the flow rate has a decreasing effect on the reaction rate until a plateau is established where the reaction

rate is virtually independent of gas velocity. Some workers use the term "critical velocity" for that beyond which reaction rate is independent of flow rate. As explained in Section 2.4.1, use of a flow rate above this value ensures that the system does not suffer from "gas starvation".

With single pellet studies in the laboratory, it is very easy to work above critical flow rate, but in a commercial packed bed it is quite difficult since segregation of coarse and fine particles will alter the packing density, with the result that gas flow will increase in the more open sections with concomitant decrease in flow in the more close-packed sections. It is clearly possible to control gas flow above the critical flow rate by using properly sized particles in the bed⁽²⁸⁾.

Increased pressure of reducing gas has a favourable effect on reducibility of iron oxide pellets because it gives a greater mass of gas per unit volume. McKewan⁽³⁷⁾ investigated the effect of hydrogen pressure and found the rate of reduction increases with increase of pressure.

2.5 DIMENSIONAL CHANGES OF IRON OXIDE PELLETS DURING REDUCTION

The dimensional changes of iron oxide pellets during gaseous reduction is not a recent discovery, although more attention has been paid to this effect in recent years. This is because of the increased use of pellets in place of sinter and lump ore in the blast furnace (BF) and more recently as a major burden material for direct reduction (DR) processes, e.g. Midrex and HyL.

The dimensional changes of iron oxides during reduction using carbon monoxide (CO) as the reducing gas have been reported as early as 1936 by Joseph⁽⁵⁵⁾. A more fundamental study was carried out by Edström⁽³⁶⁾ and later on by other workers^(13, 21, 64, 65, 67, 69, 70, 71, 73, 74, 75). Edström⁽³⁶⁾ determined the specific volumes at room temperature of hematite, magnetite, wustite and iron as 0.272, 0.270, 0.231 and 0.128 cm³/g respectively. By simple calculation the real solid volume would be decreased by 0.7, 14.3 and 37.9% as hematite is reduced successively through Fe₃O₄ and Fe_xO (x ≈ 0.95) to iron. On the other hand, Turkdogan et al⁽¹³⁾ reported that at room temperature, the specific volumes of hematite, magnetite, wustite and iron are 0.146, 0.193, 0.175 and 0.127 cm³/g respectively and from these values deduced that expansion in the early stages of reduction followed by some shrinkage in the final stages was likely to occur.

Although there is some disagreement in the values for specific volume used by the above authors, it has been generally accepted by these authors among others^(64, 65, 66, 67, 68, 69, 70, 71, 73, 74) that iron oxide pellets show expansion and shrinkage during reduction. The expansion of iron oxide pellets is classified as normal and acceptable when it has values of up to 20% by volume. Normal swelling is caused by structural and volumetric changes occurring during the anisotropic transformation from hexagonal structure of hematite to cubic structure of magnetite, followed by the contraction which occurs during further reduction to metallic iron due to the lower volume and sintering of reduced iron^(64, 65). Bleifuss⁽⁶⁴⁾ and Walker et al⁽⁶⁵⁾ reported that magnetite forms from hematite in such a way that the (111) planes of the magnetite are parallel to the (0001) planes in the hematite. The average

spacings between oxygen atoms in the two structures are not, however, equal so that considerable stress is developed in the lattice when hematite is converted into magnetite, which causes swelling. However, under certain conditions some pellets show abnormal swelling with values considerably in excess of 20%. This is because swelling rather than contraction occurs during the final reduction stage from wustite to iron. Bleifuss⁽⁶⁶⁾ reported that swelling results due to the growth of iron whiskers from the surfaces of wustite grains. Such whiskers are thought to exert pressure against adjacent grains in the pellet causing extensive swelling. On the other hand, Fuwa et al⁽⁶⁷⁾ suggested that excessive swelling results from fibrous iron formation during reduction. Walker et al⁽⁶⁵⁾ reported that excessive swelling may occur without whisker formation and in this case iron grows as squat protuberances from wustite. These protuberances cause swelling in the same way as whisker growth.

Abnormal swelling and shrinkage both have adverse effects on the productivity of reduction furnaces. Abnormal swelling lowers the permeability of the bed and gas flow through the bed⁽²⁸⁾, shrinkage increases the tendency to clustering, thereby preventing the smooth descent of the charge in a shaft furnace and making discharge more difficult in a fixed-bed furnace^(21,28). The magnitude of the dimensional changes during reduction has been found to be strongly dependent on :

- (i) the chemical constituents of iron oxide pellets,
- (ii) the physical characteristics of iron oxide pellets,
- (iii) the operating variables.

Generally the gangue minerals present in iron ores are oxides of calcium, silicon and aluminium, forming different types of phases as discussed in Section 2.2. The effect of these constituents individually or together on dimensional changes has been studied by many workers.

It has been reported by Bleifuss⁽⁶⁰⁾ that the addition of calcium oxide to magnetite or hematite could lead to the growth of iron whiskers⁽⁶⁶⁾. This worker argues that during reduction the limited mutual solubility of CaO and FeO results in the production of calciferrous wustite from calciferrous magnetite or calciferrous hematite. He concluded that the presence of a thin lime-rich wustite would prevent the general nucleation and growth of metallic iron on the main surface. Instead, the iron migrates to a few nucleation points only causing the development of an iron whisker. It has been shown that the presence of calcium oxide in the pellets gives abnormal swelling because of an uneven distribution of lime in wustite, which favours whisker formation. The use of high firing temperature has been recommended in order to homogenize the lime in the iron oxide lattice, so avoiding the formation of calciferrous hematite, magnetite or wustite.

Ponghis et al⁽⁶⁸⁾ have reported that the addition of limestone improves the swelling properties by the formation of a better slag bond. Turkdogan et al⁽¹³⁾ showed that pellets with an addition up to 4% of lime gave less swelling than lime-free pellets on reduction in carbon monoxide. A detailed study was carried out by Kortman⁽⁶⁹⁾,

who has determined that the dimensional changes resulting from the addition of lime depends on the amount added and on the presence of other impurities. He found maximum swelling to occur at 0.25% lime. The effect of lime in the range 0.05 - 5^m/_o has been studied by Moon and Walker⁽¹⁴⁾ who found that the presence of lime prevents "abnormal swelling" provided that the firing temperature is high enough to produce $\text{CaO} \cdot 2\text{Fe}_2\text{O}_3$ and eliminate free lime. Who found that the extent of swelling decreases with increase of lime because of the bonding action of calcium ferrite: maximum swelling was observed to occur at a degree of reduction of 30 - 40%. This work strongly supports the work of Akitoshi⁽⁷⁰⁾ who considers that the presence of free lime should be avoided by selecting a proper firing cycle. Chang⁽⁷¹⁾ investigated a sample containing free lime using a pellet containing 1% CaO fired at 900°C for 3 hours. In this sample, the maximum swelling was recorded as 170%. Another similar sample fired for an increased time of 6 hours gave homogenization of the lime and less swelling was observed.

Only limited work has been carried out by Wright^(56, 57, 72) and Kaneko and Narita⁽²¹⁾ on the influence of constitution with respect to pellets to be reduced by Direct Reduction. The effect of lime was studied by Kaneko and Narita⁽²¹⁾ using a reduction-under-load test apparatus, who found that pellets shrink after a slight initial swelling. Such shrinkage was less than observed with pure hematite.

It has been reported^(70, 71, 73, 74, 75) that the presence of silica and alumina hinders excessive swelling and prevents cracking of pellets during reduction. This is attributed to the nature of acidic oxides which give slag bonds having enough strength to resist the stresses developed during reduction. In such cases ~~after normal~~

swelling slight shrinkage occurs. Suzuki⁽⁵²⁾ reduced green and preheated iron oxide pellets containing separate additions of silica and alumina in hydrogen. He found that preheated pellets containing alumina expand more and contract less than pure hematite, whereas those containing silica expand slightly more but contract to the same extent as pure hematite. No conclusive reasons have been suggested for these effects, but it is probable that the pellets containing silica have a lower apparent density and therefore show larger contraction. At the same time, Suzuki⁽⁵²⁾ reported that green pellets contract more than preheated because of the lower initial apparent density of green pellets.

The effect of the $\text{CaO/SiO}_2 + \text{Al}_2\text{O}_3$ basicity ratio on the dimensional changes of pellets when reduced by carbon monoxide and hydrogen has been studied by many workers^(14, 19, 57, 69), who have observed maximum swelling to occur at basicity ratios of 0.2 - 0.8, low to 0.7, 0.7 and 0.49 respectively. According to Kortman⁽⁶⁹⁾, high swelling at such basicities is caused by the formation of olivines which bring about a solution of iron oxide grains at their peripheries, thus leading to the destruction of iron oxide bridges, and allowing volume increase..

Frazer et al⁽¹⁹⁾ explained high swelling in the basicity range 0.2 to 0.8 to be caused by the "mobile" or "plastic" nature of the gangue which provides a medium for absorption of the reduction stresses by increased distances between the particles. This theory is supported by the observation that pellets containing low melting point olivines show high swelling on reduction.

Moon and Walker⁽¹⁴⁾ have shown that the maximum swelling value occurs at a basicity value of 0.7 because, at this basicity, the slag bond is very weak. Wright⁽⁵⁷⁾ in his work found the maximum swelling to occur at a basicity of 0.49, but he did not give any reason for this.

The influence of the mode of reduction on swelling has been studied by Frazer et al⁽¹⁹⁾ and Granse⁽⁷⁶⁾. Frazer et al⁽¹⁹⁾ found that high basicity pellets swell less because the microstructure of such pellets possesses a "closed pore" structure and coarse hematite grains. During reduction this structure does not permit rapid diffusion of the reducing gas to the interior of the pellet. The resulting concentric layer of iron produces sufficient resistance to the swelling. On the other hand, acid pellets possess an "open pore" structure and fine hematite grains swell to a greater extent. This is because this structure permits the rapid diffusion of gas throughout the pellet, and reduction of the individual grains takes place. Hence cumulative reduction stresses cause extensive swelling which the iron layer is not sufficient to resist. Granse⁽⁷⁶⁾ has also reported that swelling of iron oxide pellets is lowered due to topochemical reduction.

The influence of the speed of hematite to magnetite reduction has been studied by Akitoshi⁽⁷⁰⁾, Brill-Edwards⁽⁷⁵⁾, Edström⁽³⁶⁾ and Surtees et al⁽⁷⁷⁾ who have reported that the swelling is increased when magnetite is produced at higher rate, because of the high stresses produced. Brill-Edwards⁽⁷⁵⁾ reported that these stresses are relieved by the plastic flow of calcium monoferrites. Swann and Tighe⁽⁷⁸⁾ have also shown in their work that the relief of transformation stresses (hematite to magnetite) can only be brought about by plastic flow in the magnetite or hematite.

2.5.2 Effect of Physical Characteristics of Iron Oxide Pellets on Dimensional Changes

To date, little attention has been paid to the effect of physical characteristics on dimensional stability, a possible reason being that other parameters have been considered to be more important. However, the work of Linder⁽⁷⁹⁾ and Thaning⁽⁸⁰⁾ shows that large pellets swell proportionately less than smaller pellets when reduced under similar conditions. No valid reason was given.

Frazer et al⁽¹⁹⁾ found that pellets formed from mixtures containing higher percentages of fines gave lower volume changes than those formed from coarse mixtures but offered no explanation.

The influence of porosity of pure iron oxide pellets on swelling has been studied by Taniguchi⁽⁸¹⁾ who showed the maximum swelling to occur with initial porosity values of 25%. The view has been proposed that, as the initial porosity increases, bonding becomes weaker and the reduction rate increases leading to a large degree of swelling. However, when the porosity exceeds a certain value, the swelling tends to decrease, possibly because the larger pore space can relieve the stresses responsible for swelling.

2.5.3 Effect of Operating Variables on Dimensional Changes

The effect of the various operating variables on dimensional changes has been studied, but with more attention being paid to the major variables, i.e. temperature and gas composition.

The influence of reduction temperature on dimensional changes has been reported by various authors with differing findings as follows.

The effect of reduction temperature on dimensional changes was investigated by Wright⁽⁵⁷⁾ who found that, at 700°C, pellets undergo shrinkage throughout the whole reduction period, whereas a linear relationship between temperature and expansion was experienced between 800 and 1050°C. The reason for this is explained in terms of mechanism of reduction, reported by the same author. For the temperatures from 700 - 950°C, Taniguchi^(82, 83) reported that volume increases with temperature, because with increase of temperature, the developed stresses become higher so pushing the grains apart. However, elsewhere, he reports without explanation that pure hematite shows a minimum volume change at a reduction temperature of 800°C. Lu⁽⁸⁴⁾ and Henery⁽⁵⁸⁾ reported a maximum swelling to occur at reduction temperatures in the range of 800 - 1100°C. Brill et al⁽⁷⁵⁾ and Walker et al⁽⁶⁵⁾ studied swelling in carbon monoxide and show that swelling increases with the increase of reduction temperature in the range of 800 - 1100°C. The reason for such expansion is possibly due to the increase of carbon deposition.

There are also differing opinions about the effect of gas composition on volume changes. Edström⁽³⁶⁾, Fuwa⁽⁶⁷⁾, Turkdogan et al⁽¹³⁾ and Mazanek et al⁽⁵²⁾ have reported that pellets reduced by hydrogen swell less than those reduced by carbon monoxide. Lu et al⁽⁸⁴⁾ found that swelling did not occur at all with hydrogen as reducing gas because a dense reduced layer is formed. Wright⁽⁵⁷⁾, on the other hand, reported that severe swelling does occur with hydrogen, although the swelling is usually less than with carbon monoxide and only occurs when appreciable quantities of water vapour are present in the system. Akitoshi⁽⁷⁰⁾ reported that only slight swelling occurs in hydrogen. He assumed that the reduction power of hydrogen was so high that the formation of metallic iron occurred very rapidly,

with the metal phase product resisting swelling.

The effect of stresses on volume changes have not been studied to any great extent. Limited work has been carried out by Kaneko and Narita⁽²¹⁾ who found that, with the increase of stress, expansion of pellets is decreased whilst shrinkage of the pellets is increased.

2.6 STRENGTH OF IRON OXIDE PELLETS DURING REDUCTION

It is important that the strength of iron oxide pellets during reduction is high because any fines produced result in a drastic decrease in the permeability of the shaft, giving poor fuel economy and variability in the degree of reduction⁽²⁸⁾.

When iron oxide pellets are charged into a DR furnace, they are subjected to drying, preheating, reduction and cobling. In the initial step at low temperature (400 - 600°C) iron oxide pellets decrepitate because of rapid evolution of free or combined moisture or relief of stresses. As the reducing temperature increases to about 1000°C, swelling and softening may occur, which further diminish the strength of iron oxide pellets. However, it has been reported by Heinrich et al⁽⁸⁰⁾ that low temperature (400 - 600°C) disintegration of pellets is not relevant to direct reduction processes, and therefore emphasis should be paid to their behaviour at the high temperature range used in commercial DR furnaces.

Reduction strength tests are often performed by determining the compressive strength of individual pellets although usually this

is done at room temperature. However, it has been shown that both the binding phase and iron oxide phase display different strength properties at ambient temperature than they do at the temperature at which reduction actually takes place^(73, 74). Stalhed⁽⁸⁶⁾ and Linder⁽⁷⁹⁾ developed the well-known technique by which the resistance of the burden to degradation can be evaluated. Burghardt⁽⁸⁷⁾ designed a test, which appears to be more realistic, in order to measure strength at high temperature under constant load and controlled reducing atmosphere throughout the reduction.

It can be seen from reduction phenomena that oxygen is being progressively removed from the iron oxide pellets, and that the bonds formed by oxide bonding or crystal growth during the induration of pellets are disappearing. As a result of this, the strength of the pellets during reduction is changing with the strength in the reduced state depending on the degree of reduction, the chemical composition and the physical changes which take place, e.g. changes in porosity^(56, 81) and volume^(75, 81). Therefore, a detailed study of the above influencing factors on strength is important.

2.6.1 Influence of Chemical Composition and Mineralogy on Strength

It has been reported by Russ and Fine⁽⁸⁸⁾ that magnetite possesses high strength during reduction in comparison to hematite. The reason suggested for the high strength of magnetite pellets is that exothermic oxidation of magnetite to hematite increases the internal temperature of the pellets and fosters diffusion, grain growth and better bonding of individual grains. However, when hematite is heated in air, the chemical structure remains stable and there is

no such exothermic reaction to assist the agglomeration phenomena.

These views were supported by heating magnetite in a neutral atmosphere when the conversion to hematite is blocked and hence there is no exothermic reaction with the result that the pellet never acquires any significant hot strength. Removal of oxygen produces wustite with a lower bulk density, thereby increasing the interstices between the particles, and disrupting the pellet coherency.

Similar findings were later reported by Thaning⁽⁸⁹⁾, who suggested a different explanation. He contended that during reduction of hematite to magnetite, transformation of the crystal structure from hexagonal to cubic occurs creating defects in the lattice, thereby initiating fissure of the magnetite grains and formation of pores.

It can be concluded from a study of previous work that the reduction strength varies inversely as the degree of oxidation of pellet with magnetite having a higher reduction strength than hematite.

The effect of mineral constituents on the strength of iron oxide pellets during reduction at high temperature has been described in previous work^(18, 70, 74, 84, 85) and is closely related to the amount of gangue minerals present, e.g. lime, silica and alumina. Whalter⁽⁹⁰⁾ and Pepper⁽⁹¹⁾ reported that pure iron oxide or high grade iron oxide ($\text{Fe} > 65\%$) undergoes a large decrease in strength during reduction at a degree of reduction of about 20%, because of the structural changes and weak bonding of the grains. This means strength can be improved with proper bonding, in the presence of

gangue, such effects being related to the chemical composition and amount of gangue present.

It has been reported by Thaning⁽⁸⁹⁾, Brill-Edwards⁽⁷⁵⁾ and Pepper⁽⁹¹⁾ from hot compressive strength testing (HCS) and by Shehata et al⁽¹⁷⁾ from cold compressive strength testing (CCS) that the iron oxide pellets with acid gangue have sufficient strength because, at basicity values of less than 1, silicates are formed and act as binding phases. These phases are not affected by reduction but remain intact and have a sufficient mechanical strength to hold together the structure of porous reduced phase.

With basic gangue however minerals such as calcium ferrite and calcium silicate are formed. Brill-Edwards⁽¹⁷⁾ and Shehata et al⁽¹⁷⁾ reported that strength increases if there is sufficient calcium ferrite present to hold the structure together. Thaning⁽⁸⁹⁾ reported that the addition of calcium oxide improved the strength by the interlocking of dislocations in the wustite lattice formed as a reduction product, and through the formation of a gel-like binding matrix consisting mainly of calcium silicate produced by hydrothermal treatment.

2.6.2 Effect of Operating Variables on Strength During Reduction

Since reduction temperature is a main operating variable, the influence of this parameter on strength has been studied by Shehata et al⁽¹⁷⁾, Taniguchi et al⁽⁸¹⁾, Wright⁽⁵⁶⁾ and Thaning⁽⁸⁰⁾. The first three authors have reported that the strength of reduced pellets decreases with increase of reduction temperature. Shehata et al⁽¹⁷⁾ reported that the lower strength at high temperature is due to the formation of micropores in magnetite, subsequently in

iron. On the other hand, Thaning⁽⁸⁰⁾ reported that the strength is higher at high temperature. This effect he attributed to the dense magnetite formation. The difference in the findings of these workers could arise from the use of different reducing gas and testing conditions.

Taniguchi et al⁽⁸¹⁾ and Wright⁽⁵⁶⁾ have related strength to volume changes and shown that strength varies inversely with swelling as shown in Fig. 2.10⁽⁸¹⁾. The reason for the decrease in strength is due to increase of porosity and destruction of bonds.

3.1 INTRODUCTION

The major aim of the present study, is to investigate the effect of doping agents on the reduction properties of hematite iron oxide pellets, with particular emphasis on the various microstructures developed during sintering. The main attention was paid to the properties required by Direct Reduction (DR) processes viz. high reducibility with high strength and low volume changes during reduction.

In accordance with this aim, doped and undoped hematite pellets were prepared. Optical and scanning electron microscopic techniques were used to study the microstructure of these iron oxide pellets and their reduction properties determined.

The reduction properties studied are grouped into two parts according to the two different types of apparatus involved. The reducibility of iron oxide pellets was determined by an existing thermogravimetric spring balance technique. However, with regard to dimensional changes and strength during reduction under load it was considered that a suitable apparatus did not exist for the study of such phenomena in a single pellet under constant load. Hence a new apparatus was developed to determine the change in length and strength of a single iron oxide pellet during reduction under a range of initially constant stresses.

3.2 PREPARATION OF IRON OXIDE PELLETS

A high grade hematite iron ore concentrate supplied by British Steel Corporation (Teesside Division) was used as base

material for this work. Its grading and chemical composition are given in Table 3.1. In order to determine the effect of doping agents, laboratory grades of lime, silica and alumina supplied by Hopkin and Williams were used in the production of doped pellets. Table 3.2 lists the impurity levels of these agents.

The green iron oxide pellets were made in cylindrical form with the addition of 8 mass % of distilled water as a binder. The doping agents were added in varying amounts as given below:

lime:	0.88 to 4.88 mass %
silica:	0.78 to 2.78 mass %
alumina:	0.76 mass %

The cylindrical undoped iron oxide pellets were made by mixing the iron oxide concentrate with water. Where additions were used, the required mass of these compounds were individually mixed carefully by hand followed by treatment in a rotating tumbler mixer to which the required amount of water was then added. The green mixture was weighed in a paper boat, an amount of 3.1 ± 0.01 gram being adopted in order to get consistency in mass of the final pellet. This material was pressed in a hardened steel die (Fig.3.1) using an Avery compressive testing machine. A load of 300 ± 20 kg per pellet was found to give consistency of dimensions in the green state, the pellets having dimensions 1.1 cm in height and 1.0 cm in diameter. Preference was given to a cylindrical pellet shape because its dimensions could be reproduced more consistently and because it allowed greater simplicity in the apparatus design.

The green compacted pellets were fired in a muffle-type furnace in air which provides a sufficiently oxidising atmosphere for the reoxidation of any small proportion of magnetite present in the initial iron ore. The green pellets were placed on platinum foil in order to avoid reaction between the chrome-magnesite refractory furnace base and the iron oxide pellets which would result in contamination of the pellets. The sintering of iron oxide pellets was carried out in such a way as to avoid cracking and thermal shocks. These pellets were dried at $200 \pm 20^{\circ}\text{C}$ for two hours, including the time taken to heat the furnace from room temperature to 200°C . Preheating was carried out at $400 \pm 20^{\circ}\text{C}$ for two hours also including the time taken to heat the furnace from 200 to 400°C . Finally, sintering was carried out at 1250°C and 1325°C for various times in order to develop different phases and microstructures. The time taken to heat the furnace from 400 to either 1250°C or 1325°C , $1\frac{1}{2}$ hours or 2 hours respectively, was not included in sintering time. The final sizes of the fired pellets were found to be about 9.96-10.0 mm in diameter and about 10.0 mm in height, depending upon the sintering time and temperature and the level of doping agents. The initial calculated composition of the iron oxide pellets is given in Table 3.3 and their physical properties (density and porosity) after sintering are given in Table 4.1 and described in section 4.2.

3.3 DEVELOPMENT OF THE REDUCTION-UNDER-LOAD APPARATUS

An apparatus was designed and built to allow assessment of the dimensional stability and strength of a single iron oxide pellet during reduction under specified initial stress.

An outline diagram of the apparatus developed is shown in Fig.3.2 and photographs in plates 3.1 and 3.2. This apparatus was designed to determine the above properties under various stresses and at different temperatures up to 900°C. 900°C was the temperature limit because heat resistant 25% chromium, 20% nickel stainless steel platens used in this apparatus would soften above this temperature.

The iron oxide pellet was placed between two platens, the upper platen being attached to a screw-jack system above the furnace and the lower platen supported on a cantilever beam. Friction between the platen and beam was minimized by the incorporation of a roller bearing. As the pellet expands or shrinks during reduction the stress in the beam is changed, these stresses being determined using strain gauges attached to the beam and connected to a resistance bridge with the out of balance voltage read by a digit voltmeter (see below). In order to maintain a constant load on the specimen the digit voltmeter reading was returned to the specified original reading for each experiment by the rotation of the top screw assembly. Since a constant load on the beam implies a constant deflection, the dimensional changes experienced by the pellet during its reduction could be read by a micrometer scale attached to the rotating head of the screw-jack assembly.

The furnace was heated electrically by silicon carbide rods and its temperature controlled automatically using a Eurotherm controller with an accuracy of 0.5%. A vertical alumina tube of 60 mm inside diameter and 630 mm long was used, the ends being

closed by a water-cooled aluminium base and a similar top. Reducing gas was introduced at the bottom end and was taken off from the top of the assembly, the Rotameters being used to monitor the flow of gases into the reaction chamber.

Leakage of gases was prevented by use of a silicone-greased 'O' ring at the top and an oil seal at the bottom of the reduction tube as shown in Fig.3.2. A detailed diagram of the oil seal which consists of a tank filled with oil up to 15 mm and an inverted cup attached to the lower platen is given in Fig.3.3. This cup is adjustable to any position of the lower platen, using zero and 3 kg load, in such a way that it can be ensured that it is immersed in oil up to approximately 10 mm. This adjustment of the cup in the oil seal compensates for expansion of the platens up to 6 mm and of the pellets up to 4 mm without leakage of gases.

A frictionless roller ball bearing, shown in Fig.3.4 supplied by R.H.P. Components, was used to align the lower platen with its axis vertical.

Strain Gauges

The strain gauges used in this work were type PL10 as supplied by Tokyo Sokki Kenkyozo Co., Ltd. These are fixed on cantilever beam as shown in Fig.3.5 to detect any strain produced by bending the beam. The ratio between the percentage change in resistance and the percentage change in length is called the gauge factor G , and this had a value of $2.02 \pm 1.0\%$ for the gauges used in this work.

Strain Gauge Bridge

The usual way of measuring the change in the resistance of strain gauges is by incorporating them into a Wheatstone Bridge as shown in Fig.3.6. The voltage output from this bridge is read through a digit voltmeter and given by:-

$$V \text{ output} = \frac{e \times V \times G \times \text{no. of active gauges in strain gauge bridge}}{4}$$

where: V output is in microvolts
e is strain in microstrain
V is bridge voltage input 5.95 ± 0.01
G is gauge factor

Active gauges are those which are actually strained and mounted on strained material. The full bridge comprises four active gauges since this arrangement gives better temperature compensation, all the gauges being subjected to similar temperature effects and therefore not affecting the bridge output, and also gives higher voltage output.

Cantilever Beam

The beam designed for this apparatus is shown in Fig.3.5 having dimensions: length ($l = 1.10 \text{ m}$), width ($h = 6.55 \text{ mm}$) and breadth ($b = 37 \text{ mm}$). The last 200 mm of the beam were firmly held in an horizontal clamp.

Any static or dynamic load applied at the free end, or at any part along the beam, gives maximum stresses at the fixed end.

When a load is applied to the free end of beam the maximum slope and deflection are given by $\frac{WL^2}{EI}$ and $\frac{WL^3}{3EI}$ respectively.

Where I is the cross-section area of beam = $b \times h$
 b is the breadth (cm) of beam
 h is the thickness (cm) of beam
 L is the length between the clamp support and the
point of application of the load
 E is the modulus of elasticity of beam
 W is the applied load kg ($209 \times 10^9 \text{ N m}^{-2}$)

Scaled screw-jack system

The scaled screw-jack supporting the upper platen is used in this apparatus to impose the desired stress on the pellet between the upper and lower platen and to measure, using a micrometer scale, the deflection of the beam and the expansion or shrinkage of the pellet.

The stresses were developed between two platens by rotation of the screw-jack assembly. The load developed, as transmitted via the lower platen to the beam, is detected by the strain gauges. A 360° scale was mounted at the top of the Jack: one full revolution of the screw corresponds to a movement of the upper platen of 6 mm.

The sensitivity of the system is such that a vertical deflection of the beam or iron oxide pellet of $\frac{1}{60}$ mm can be detected. This corresponds to a sensitivity of 0.15% of the original cylindrical pellet length.

3.3.1 Calibration of the strain-gauged cantilever beam

Calibration of the strain-gauged cantilever beam was carried out at two different distances from the fixed end in order to avoid overstraining the strain gauges at high load. It was decided to

calibrate for lower loads with the lower platen supported at a point 90 cm from the fixed end of the beam and for high loads at a reduced distance of 60 cm from the fixed end of the beam. The different loads were applied to determine the output of the strain gauges at known voltage inputs using specially designed weights applied to the lower platen. Calibrations were carried out both loading and reloading the cantilever beam in this way. A constant voltage of 5.95 ± 0.01 volts was supplied to the bridge and the output read through the digit voltmeter which was sensitive to $\pm 10 \mu V$. The different loads were applied for at least ten times and mean values of the corresponding output voltages are given in Tables 3.4 and 3.5 respectively. The resultant calibration curves for output voltage versus load are linear with correlation coefficients of virtually 1.0. These curves are shown in Figs. 3.7 and 3.8.

3.3.2 Temperature Control in the Reduction Furnace

A carbolite sillite-rod furnace of total resistance 60Ω and with a maximum operating temperature of $1300^\circ C$ was used. The temperature of the furnace was controlled by using a twin-bore ceramic-sheathed platinum/rhodium thermocouple connected to a Eurotherm thyristor controller. The furnace thermocouple was positioned at the mid-height of the furnace between the heating elements and the alumina tube.

The temperature profile along the axis of the alumina tube was determined with the two platens positioned inside the tube as shown in Fig. 3.2 and in the presence of the water cooling coils on the aluminium base and top. This was done in order to allow

for any heat losses due to the presence of the platens and the water cooling. The inside temperature was measured by inserting a chromel-alumel thermocouple of 1.5 mm diameter in a stainless steel sheath as shown in Fig.3.2. The e.m.f. output was fed into a Cropico P₃ Potentiometer. This system allowed accurate determination of the actual temperature inside the tube. Temperature variation in the reduction furnace at two different controller settings is given in Fig.3.9.

It was observed that the hot zone at working temperatures ($\pm 2^{\circ}\text{C}$ or better) extends over a distance of 3 cm from the 16.0 cm to 19.0 cm positions measured from the top. The effect of gas flow on the hot zone temperature profile was measured by blowing Argon at a rate of 3.5 litres per minute through the reduction tube after stabilization of the temperature. The hot zone temperature remained stable to within the maximum variation of $\pm 2.0^{\circ}\text{C}$. However, the temperature variation over the length of the sample held centrally in the hot zone is $\pm 1^{\circ}\text{C}$.

3.3.3 Gas Purification

High purity (99.9%) Argon and Hydrogen were used in the heating and reduction tests, removal of any moisture present being accomplished by a two-stage drying system consisting of anhydrous magnesium perchlorate with an intermediate stage to remove any oxygen present using a 3.175 mm molecular sieve type 54 (Aluminium calcium silicate).

The gas flow was regulated by rotameter-type flow meters and introduced to the furnace tube from the bottom. The gas purification train is shown in Fig.3.10.

3.3.4 Critical Flow Rate

In order to determine the critical flow rate, high grade hematite (99.2%) pellets were reduced in hydrogen for 10 minutes at 850°C, using flow rates varying between 1.87 l/min and 7.5 l/min. The relationship between the percentage reduction occurring in the given time and volumetric flow rate of hydrogen is shown in Fig.3.11. On the basis of these results, it was decided to use a hydrogen flow rate of 5.6 l/min in the subsequent reduction runs in order to avoid any problem of gas starvation.

3.3.5 'Blank' testing and reproducibility of reduction-under-load apparatus

'Blank' testing of apparatus was carried out at 830°C and 850°C. Pellets of fused silica of a size identical to the initial size of the iron ore pellets were used to determine the response of the strain gauges caused by the behaviour of the platen at these temperatures. Argon at a flow rate of 3.5 litres per minute was introduced for 15 minutes before the stabilization of the hot zone at both temperatures. By the end of the period of Argon flow the platens have achieved an almost constant degree of expansion. However, when the Argon flow was replaced by Hydrogen at a flow rate of 5.6 litres per minute, the platens begin to contract. The blank test in Hydrogen were carried out for 30 minutes, which is the normal maximum time for reduction used in this investigation. The values of the contraction of these platens with time at both reduction temperatures used are given in Table 3.6. During the subsequent reduction of iron oxide pellets these blank values were used to correct the observed changes in pellet dimensions.

Platens show this behaviour when Argon is replaced by Hydrogen because of the different thermal conductivities of these gases as can be seen from Fig.3.12.⁽⁹⁴⁾ It can be deduced from this figure that Argon and Hydrogen have thermal conductivity values at 800°C of 0.05 W.m⁻¹ °C⁻¹ and 0.46 W.m⁻¹ °C⁻¹ respectively, i.e. the value for hydrogen is approximately nine times that of Argon. During Argon flow less heat is conducted from the hot zone and platen towards the cooler sides of reaction tube with the result that more heat is conducted through the platens giving a profile of higher temperatures in the platens. On the other hand, during Hydrogen flow, heat is conducted at high rate from the hot zone and platens resulting in a profile of low temperatures which gives rise to contraction.

The reproducibility of the apparatus was determined by reducing iron oxide pellets containing 0.5 mass % lime at 850°C in Hydrogen under an initial stress of 0.75 kg.cm⁻². Five samples were reduced under nominally identical conditions, for a period of ten minutes each. The values of the percent change in length against reduction time are given in Table 3.7 and Fig.3.13. Test results show mean expansion values with corresponding standard deviation and percent error at different times. The standard deviation varies from 0.03 to 0.4% and the % error from (0.96 to 9.86) .

3.4 THE THERMOGRAVIMETRIC SPRING BALANCE

The reducibility of the pellets was determined by their loss in weight during reduction. A gravimetric technique was used involving a sensitive quartz spring. The spring balance apparatus

used is shown diagrammatically in Fig.3.14 and a photograph of the whole system is given in Plate 3.3.

The description of the apparatus which follows is given in three sections viz: the spring balance, the reduction chamber and furnace and the gas flow system.

The spring balance

A quartz spring was used as the balance; the sensitivity of the spring depends on the number of loops, the glass diameter and the loop diameter. The length of the spring was chosen so that it could support the weight of the sample and sample holder, that it gave a high sensitivity with the weight changes and that, even with the contraction of the spring, the sample remained in the hot zone.

The glass outer tube (see Fig.3.14) with a hook was used in which to suspend the spring. A silica rod of 1 mm diameter suspended from the lower end of the spring supported the sample holder and sample in the hot zone of the furnace. The sample holder and its hook were made of 0.2 mm diameter nichrome wire. The glass outer tube was attached at the top of the reduction chamber by a water-cooled aluminium head.

Reduction chamber and furnace

The reduction chamber consists of an alumina tube with inside diameter 2.3 cm and 100 cm in length, sealed by means of O-rings and clamping plates secured by Allen screws to aluminium head and base pieces. A Wilson seal was incorporated at the bottom

of the base piece to provide a gas tight seal for the working thermocouple. The gases used were introduced via the base and taken off at the top after passing through the reduction chamber.

A vertical tube furnace of the electric resistance type as outlined in Fig.3.14 was used. The furnace had a resistance, of 35 ohm, an internal tube diameter of 3.7 cm and a height of 37 cm. A porous plug was fitted just below the hot zone in order to ensure adequate heating of the gases and a more even flow prior to entering the reduction zone. The porous plug was of M23 siliceous alumina brick and of the necessary diameter just to fit inside the reduction chamber. The plug was 2 cm thick bored with a 1.5 mm diameter hole through its centre to accommodate the thermocouple.

Gas flow system

The gases used were introduced from the bottom of the reduction chamber and taken off at the top. The seals used to prevent gas leakage from the reduction chamber and accessories have already been described. The gases used were supplied from individual gas cylinders and were of high purity. Removal of any moisture present was accomplished in the same manner as described in Section 3.3.3. The system used for gas drying and mixing is shown in Plate 3.3. These gases were introduced at the required flow rates which were controlled by separate rotameters for each gas. The gases were mixed in a transparent plastic chamber filled with spherical glass balls before entering the reduction chamber.

3.4.1 Temperature control

A tube type furnace of resistance $35\ \Omega$ and with maximum working temperature 1000°C was used. The temperature of the furnace was controlled using a twin-bore ceramic-sheathed chromel/alumel thermocouple positioned at about mid-height between the reduction tube and the furnace inside wall (see Fig.3.14). This control thermocouple was connected to a carbolite commercial galvanometer cut-off controller.

The temperature profile along the reduction tube was determined within the actual operating system (see Fig.3.14). To this end a stainless steel sheathed chromel/alumel thermocouple of 1.5 mm diameter was incorporated inside the reduction chamber. The e.m.f. output from this thermocouple was fed to Cropico P_3 potentiometer allowing accurate determination of the actual working temperature. The constant temperature zone was found to be 6 cm long with temperature variation of $\pm 4^{\circ}\text{C}$ as shown in Fig.3.15. The temperature variation in zone within which the sample moved during reduction was no more than $\pm 1.5^{\circ}\text{C}$.

3.4.2 Calibration of the glass spring

The glass outer tube was removed from the reduction apparatus and clamped in a draught-free laboratory. The glass spring, silica rod and specimen holder were suspended vertically from the hook. Grade A master weights to a total of 3 grams were added to the specimen holder, successive weights were then removed to cover the weight loss expected during reduction and the contraction of the spring was measured using a cathetometer to sight onto the tip of the silica rod and measuring its change of position. The results are given in Table 3.8.

Figure 3.16 shows the relationship between the spring displacement and the suspended weight. It can be seen that a linear relationship has been obtained, with a regression coefficient of 3.722 and a spring constant of 26.86 mg.mm^{-1} . As the minimum displacement detectable by the cathetometer is 0.05 mm, the minimum detectable weight change is $0.05 \times 26.86 = 1.34 \text{ mg}$ i.e. of sufficient sensitivity to detect a fractional loss of 0.15% the available oxygen in the 2.9 gram hematite pellet used in this work.

To confirm that the spring calibration when assembled in the reduction apparatus for actual reduction tests at high temperature gives the same calibration as determined in the prior calibration, the total weight loss during several reduction tests calculated from the calibration constant of the spring was compared with the actual total weight loss determined by an accurate analytical balance. The two figures always agreed to within 0.5%.

2.4.3 Reduction procedure

Single iron oxide pellets of known weight were suspended via the spring balance in the reduction chamber (see Fig.3.14). The furnace was then heated to the required temperature: this involved a heating period of 50 minutes to attain 830°C and 60 minutes to attain 850°C , as monitored by the working thermocouple and recorder. After the above mentioned times, nitrogen was introduced at a flow rate of 1.0 l/min. for about 10 minutes, in order to flush out the air present in the reduction chamber. The nitrogen flow was then replaced over a period of 30 sec. by reducing gases, either hydrogen or a mixture of hydrogen and carbon monoxide.

The reducing gases were supplied at a total flow rate of 1.0 ± 0.05 l/min.* either totally hydrogen or a mixture of H_2 and CO each supplied at 0.5 ± 0.05 l/min. At the point of cessation of nitrogen flow, a cathetometer reading was taken with the telescope cursor focussed on the tip of the balance sighting marker. Reduction time was monitored by a stop watch and cathetometer readings were taken at minute intervals except during the later stage of some samples when readings were taken at two minute intervals. The reduction was regarded as complete when no significant change in cathetometer readings was observed for a period of 5 minutes. The furnace was then switched off and the reducing gases replaced by nitrogen and the reduced iron oxide pellets allowed to cool down to room temperature. The reduced sample was reweighed by laboratory balance in order to allow comparison between the spring balance and direct weighing methods.

Replication of the reduction testing of lime and silica doped pellets was carried out in order to check the extent to which variations in reducibility were due to variations in pellet homogeneity or testing procedure. It was found from replicate tests that duplicate samples doped with 1% lime (Fig.3.17) and 1% lime plus 1% silic (Fig.3.18) showed a maximum scatter of $\pm 12\%$ in the early stages of reduction decreasing to about $\pm 2.5\%$ in the later stages. At higher additions, however, the scatter

* Foot Note: The reducing gases were used at a flow rate of 1.0 l/min. since this flow rate was known from previous work⁽⁴²⁾ to avoid any problem due to gas starvation in the reduction chamber.

was significantly lower: duplicate samples containing 5% lime (Fig.3.19), 5% lime plus 1% silica (Fig.3.20) exhibited a maximum scatter of less than $\pm 5\%$ throughout reduction even lower in the later stages.

3.5 POROSITY AND TRUE DENSITY DETERMINATIONS

The porosity of unreduced and reduced samples was measured by comparing the apparent density of samples with the true density of their components.

True density was measured using the specific gravity bottle technique. The procedure is described in Appendix I. The true density of the iron ore used was found to be 5.12 g.cm^{-3} and the true density of powders containing additions were calculated by taking the true densities of lime, silica and alumina to be 3.3, 1.8 and 3.97 g.cm^{-3} respectively. In calculating the porosity of reduced pellets, the true density of iron was taken to be 7.86 g.cm^{-3} .

The apparent density of unreduced pellets was determined by weighing and by estimation of their external volume using a micrometer. The apparent density of pellets was measured by the liquid displacement method. Mercury was adopted as the liquid and mercury balance, as shown in Fig.3.21, was used as laid down in British Standard BS1302 Part 1A 1966. In the absence of a pellet the piano-wire frame was loaded until the marker just touched the surface of mercury. Then with the sample in position, weights were loaded onto the pan until the increased upthrust was balanced and the pointer again touched the mercury surface.

For both unreduced and reduced pellets the percentage porosity was then calculated from the relationship:-

$$\frac{\text{True density} - \text{Apparent density}}{\text{True density}} \times 100$$

For unreduced pellets this gave a value of $\left(1 - \frac{W_1}{\rho V}\right) \times 100$

and for reduced pellets a value of $1 - \frac{W_1 D}{(W_1 + W_2)} \times 100$

where: W_1 is the weight of sample (pellet)
 W_2 is the weight to overcome the increased upthrust
 D is the density of mercury
 ρ is the true density of the pellet material
 V is the volume of the pellet

3.6 METALLOGRAPHY

The microstructure of unreduced and reduced pellets were examined by optical microscopy and by scanning electron microscopy including micro-analysis.

3.6.1 Optical Microscopy

A Zeiss ultraphot III microscope was used to examine the microstructure and to produce photomicrographs. The latter were taken on 35 mm F.P.4 film using automatic exposures.

The samples to be examined were mounted in a cold-setting epoxy-resin using a catalyst as hardener. The samples were vacuum impregnated by means of a vacuum dessicator connected to a single stage rotary pump, as shown in Plate 3.4, vacuum being applied for 30 minutes. These samples were then allowed to harden slowly for at least 24 hours.

These samples were sectioned across the height using a diamond wheel with paraffin as coolant. The sample surface was polished on a rotary wheel using silicon carbide paper with paraffin as lubricant and then re-impregnated as before using cold setting resin.

After hardening the samples were hand polished on silicon carbide paper using paraffin and polishing was continued until scratch-free at 600 mesh.

Prolonged polishing was then carried out using an automatic polisher in conjunction with a diamond wheel using $6\mu\text{m}$, $1\mu\text{m}$ and $1/4\mu\text{m}$ diamond paste with white spirit as lubricant. The unreduced samples were found to be more difficult to polish because of the tearing of grains on the silicon carbide paper. The most successful sequence used to produce a satisfactory polish on both types of sample was as follows:-

{	240 mesh	Hand polishing using a rotating wheel and carbide paper, with paraffin as lubricant.
	400 mesh	
	600 mesh	

{	$6\mu\text{m}$ for 8 hours	Automatic polisher with diamond paste and white spirit as lubricant
	$1\mu\text{m}$ for 4 hours	
	$1/4\mu\text{m}$ for 4 hours	

3.6.2 Scanning electron microscopy (S.E.M)

A Cambridge scanning electron microscope with Edax (Energy dispersive analysis of X-ray) facilities was used to analyse the microstructure quantitatively and qualitatively. The samples used in optical microscopy were also used for analysis by the scanning microscope except that they were attached to aluminium specimen stubs by colloidal silver, a vacuum dessicator being used to speed the drying of the colloidal silver. In order to produce a conducting surface the samples were then surface treated with carbon. Throughout the work a filament voltage of 30 kV was generally used.

The Edax system was employed to investigate the distribution of particular elements, by selecting the energy level of the element concerned and producing an 'X-ray map'. In this work, the distributions of lime, silica and alumina were studied by producing maps of the distributions of calcium, silicon and aluminium. The combination of the S.E.M. and Edax system allowed quantitative analysis to $\pm 5\%$ of the element content present.

3.7 GAS BOUNDARY MASS TRANSFER DETERMINATION EXPERIMENTS

In order to determine the mass transfer across the gas boundary layer at the surface of iron oxide pellets, it was necessary to simulate the reduction system using a non-reduction system at room temperature i.e. where effects due to the chemical reaction and to product layer diffusion are non-existent. Naphthalene was used for this work because it sublimates at such a rate that its weight loss can be measured in reasonable time and because its sublimation is known to be mass transfer controlled.

3.7.1 Naphthalene sample preparation

Cylindrical samples of naphthalene identical in shape and dimensions to the iron oxide pellets used in reduction tests were cast. Naphthalene was heated in a pyrex glass beaker until just molten, i.e. to $82-85^{\circ}\text{C}$, then cast into the die shown in Fig.3.22. Any overflowing naphthalene was removed by scalpel. Several samples were cast at the same time to ensure consistency of casting temperature thereby avoiding variations in pellet grain structure. Careful handling was necessary when the pellets were introduced into or removed from the furnace tube due to their friable nature.

3.7.2 Temperature determination

Determination of the temperature during Naphthalene sublimation is very important, because a very small change in temperature alters the vapour pressure of naphthalene significantly. The vapour pressure, p in torr, of naphthalene is calculated from the relationship⁽⁴²⁾ :-

$$\log p = \frac{-3765}{^{\circ}\text{K}} + 11.55$$

From this relationship it can be seen that a change of temperature of only 2°C will alter the vapour pressure of naphthalene (C_{10}H_8) by about 0.018 torr.

A copper-constantan thermocouple calibrated in hot water against an accurate thermometer was used to determine the temperature in the non-reducing system. This temperature was recorded hourly on a data logger.

3.7.3 Sublimation of Naphthalene pellets

The naphthalene pellets, identical in dimensions to hematite pellets, were placed between the plattens in a similar manner to hematite pellets during reduction experiments. Because of the fragility of the naphthalene pellets, vaporization runs were carried out only at zero stress. Sublimation was carried out in air at different flow rates, the temperature being continuously measured by a copper constantan thermocouple and automatically recorded by a data logger.

The naphthalene pellets were weighed before and after each sublimation experiment and from the total mass of the

naphthalene evaporated, the vapour pressure of the naphthalene for the mean air temperature recorded, and the duration of the evaporation, the mean convective mass transfer coefficient was calculated as later described in section 4.3.

4.1 INTRODUCTION

This chapter presents the results of the experimental work described in chapter 3 which was carried out to determine the influence of doping agents on the reduction properties of iron oxide pellets.

Section 4.2 and 4.3 present the results of the investigations into the physical characteristics (density and porosity) and the microstructural characteristics of the iron oxide pellets produced by sintering at different times and temperatures. The results of the study of mass transfer through the boundary layer in the reduction apparatus are presented in section 4.4. These sections are followed in the next two sections by the reduction properties of the range of iron oxide pellets produced. Section 4.5 presents the reduction rate data determined at different temperatures and gas compositions and section 4.6 presents the results relating to dimensional stability and strength during reduction in hydrogen at various temperatures.

The results of density and porosity determination for reduced iron oxide pellets are given in section 4.7. The final section, section 4.8 contains observations on the macrostructure and strength of reduced samples.

4.2 DENSITY AND POROSITY OF IRON OXIDE PELLETS

The results of the density and porosity determinations on iron oxide pellets containing varying amounts of lime, silica and alumina, and sintered for various times and temperatures, are given below. The apparent density was determined as described in section 3.5.

4.2.1. Density of base material and doped hematite pellets

The results of the apparent density measurements on iron oxide pellets at different levels of doping agents are shown in Table 4.1. and in Fig.4.1.

The results for iron oxide pellets fired at 1250°C for 3 hours are given in Table 4.1a and Fig.4.1, from which it will be seen that at low silica and alumina levels (0.22 and 0.24 mass percent respectively), the apparent density of hematite pellets increases from an initial value of 3.7 g.cm⁻³ with increase of lime content up to 2.0 mass percent, and then decreases with further increase of lime up to 5.0 mass percent. The fractional changes involved are 0.103 (mass percent CaO)⁻¹ and -0.038 (mass percent CaO)⁻¹ respectively.

At high silica and low alumina content (1.0 and 0.24 mass percent) respectively, lime has a similar effect on apparent density with fractional changes 0.007 (mass percent CaO)⁻¹ and -0.028 (mass percent CaO)⁻¹ respectively. Simple mixing of lime (density 3.3 g.cm⁻³) would have given a factor of approximately -0.004 (mass percent CaO)⁻¹.

It is also shown in Fig.4.1 that an increase of lime content in the range 1 to 4 mass % causes the density of pellets containing 1 mass % alumina to decrease. The fractional change for such pellets with a silica content of 0.22 mass % is -0.018 (mass percent CaO)⁻¹ whilst at the higher silica level of 1.0 mass % the fractional change is -0.038 (mass % CaO)⁻¹.

Fig.4.1 also shows variations of the density of iron oxide pellets fired at 1325°C for 30 minutes, the data being given in Table 4.1b.

It can be seen that the density is increased with increase of lime up to 2.0% and then decreases slowly.

Densities of an iron oxide pellet containing 1.0% lime, 3.0% silica and alumina 0.24 mass %, sintered at 1250°C for 12 hours are given in Table 4.1c

4.2.2. Porosity of base material and doped hematite pellets

The porosity values of iron oxide pellets doped at different levels of lime, silica and alumina are given in Table 4.1 and Fig.4.2.

Fig. 4.2 shows the results for iron oxide pellets fired at 1250°C for 3 hours. From this figure it will be seen that at both silica levels (0.22 and 1.0 mass %) and with the lower alumina content 0.24%, the porosity is decreased with increase of lime up to 2.0% and then increases, though not as far as the original value, with increase of lime up to 5.0%. It will also be seen, for the range of composition considered in this work, that increasing the silica content from 0.22 to 1.0 mass % increases the porosity of iron oxide pellets at any given lime content.

For pellets containing a higher alumina content (1.0%) and at the lower silica content (0.22%), the porosity rises with increase of lime content. The porosity increases resulting from an increase in alumina content from 0.24 to 1.0 mass % is greater than that resulting from a similar increase in silica. The higher values for porosity are obtained with alumina and silica both at the 1.0% level. In these pellets an increase of lime content from 1.0 to 2.0 mass % has the same effect on porosity as it has at the alumina

1.0% and silica 0.22%. However further increase of lime to 4.0% causes a more rapid increase in porosity.

It will be seen also from Fig.4.2 that pellets containing the lower content of silica and alumina (0.22 and 0.24 mass %) when produced by sintering at the 1325°C for 30 minutes, compared with 1250°C for 3 hours, behave in a similar manner with respect to increases in lime content but generally have lower porosities for any given composition.

Porosities of iron oxide pellets containing 1.0 mass % lime, 3.0 mass % silica and alumina 0.24 mass %, sintered at 1250°C for 12 hours are given in Table 4.1c.

4.3 THE MICROSTRUCTURE AND CONSTITUENT OF SINTERED IRON OXIDE PELLETS

This section describes the metallographic study of iron oxide pellets carried out by optical microscopy and scanning electron microscopy, in order to examine the effect of doping agents on the microstructure and phases formed during the sintering process. Separate and joint additions of lime, silica and alumina in the range 0.12-5.0, 0.22-1.0 and 0.24-1.0 mass percent respectively were made.

4.3.1. Variation in microstructure with the addition of different amounts of doping agent

The main content of this section comprises a description of the microstructure of pellets of varying composition sintered at 1250°C for a period of 3 hours. Subsidiary sub-sections describe the microstructure of pellets produced under different conditions of time and temperature.

4.3.1.1. The microstructure of iron oxide pellets sintered at 1250°C for 3 hours

Iron oxide pellets were studied in the unetched condition using the Zeiss Optical Microscope. The pellets examined were divided into four series with respect to content in mass percent of doping agents as follows:

	mass % CaO	mass % SiO ₂	mass % Al ₂ O ₃
Series 1	0.12-5.0	0.22	0.24
Series 2	0.12-5.0	1.00	0.24
Series 3	1.0-4.0	0.22	1.0
Series 4	1.0-4.0	1.00	1.0

Series 1: In this series the silica and alumina content were kept constant at their initial levels (0.22 and 0.24 mass % respectively) and the lime content was varied in the range 0.12-5.0 mass percent.

The microstructure of iron oxide pellets made from the base material and at the original low lime level is shown in Plate 4.1 and comprises angular hematite grains. The photomicrograph reveals the presence of considerable porosity but bonding across grains is also evident. With an increase of lime content to 1.0%, the pellets formed are more dense and less porous than those containing 0.12 mass % lime. The microstructural features of these pellets are shown in Plate 4.2 from which it will be observed that the lime has formed some calcium ferrite which is non-uniformly distributed and that a high amount of fine inter-connected pores is also present. The hematite grains have lost their angular shape and more grain growth and cross-grain bonding are observed compared with the structure at the original lime content.

The microstructure of the iron oxide pellets with an addition of 2.0 mass % lime (Plate 4.3) shows a denser and less porous structure than pellets at other levels of lime content. Larger grains of hematite encircle calcium ferrites and pores. Plate 4.4 shows the microstructure of the same pellet at a high magnification, which reveals the presence of calcium ferrites on the grain boundaries. The well-banded microstructure of this pellet has resulted from grain growth and also from considerable replacement of porosity by the calcium ferrite phase.

Plates 4.5-4.7 show the microstructures of pellets containing 3, 4 and 5.0 mass % lime respectively. The microstructures of these pellets are similar to the 2.0 mass % lime pellets (Plate 4.3), except for the presence of an increasing fraction of calcium ferrite and large globular pores.

Series 2: in this series, the silica and alumina contents were kept constant at 1.0 and 0.24 mass % respectively and the lime content varied as for series 1. At this level of silica (1.0 mass %) there was little evidence of phases other than hematite in the pellets containing 0.12 and 1.0 mass % lime. Plates 4.8 and 4.9 show the microstructures of both these pellets to consist of very fine grains together with microporosity. However, a difference between these structures is that the pellet of low lime content (0.12 mass %) has angular hematite grains (Plate 4.8), whilst at 1.0 mass % of lime the hematite grains become less angular (Plate 4.9). A very small proportion of a very fine grey phase is also present at this composition.

Plate 4.10 shows the microstructure of pellets containing 2.0 mass % lime. This material has a random distribution of calcium ferrite phase in smaller proportion than the corresponding sample with a low level of silica (0.22 mass %). The microstructure shows fine pores.

The microstructure of pellets containing 3.0 mass % lime is shown in Plate 4.11, which shows fine hematite grains, fine porosity and a fine calcium ferrite phase which exists partially in the form of needles. Plate 4.12 shows the microstructure developed in the pellet containing 4.0 mass % lime. This microstructure reveals that the phases formed in this pellet are coarser and consist mostly of needles and laths, with long channelled pores. Plate 4.13 shows the same microstructure at high magnification and clearly reveals the calcium ferrite laths interlocking with the hematite grains.

Plate 4.14-4.16 show the microstructural features of pellets containing 5.0 mass % lime. Plate 4.14 shows porous grains of calcium ferrite with internal and surface needle and lath formation. The structure also contains pores in the form of elongated channels. Plate 4.15 shows the lath formation at a higher magnification. Plate 4.16 shows needle formation at high magnification and reveals the porous nature of the calcium ferrite. The pores are mostly angular in shape.

Series 3: In this series the silica and alumina content were kept constant at 0.22 and 1.0 mass % respectively, the lime content being used in the range 1.0 to 4.0 mass %. Plate 4.17 shows the microstructure of a pellet containing 1.0 mass % lime, to obtain globular phases, adjacent to and bonded to the hematite grains. Plate 4.18

shows at high magnification one of the globular phases present in Plate 4.17. In this photomicrograph alumina in dendritic form is surrounded by calcium ferrite.

Plate 4.19 shows the microstructure of pellets containing 2.0 mass % lime. The micrograph shows rounded particles containing pores, and needles and hematite grains separated by elongated pores.

Plate 4.20 shows the microstructure of pellet containing 4.0 mass % lime. This shows that calcium ferrite has formed in the solid state on the grain boundaries as well as in the pores. The hematite grains are relatively coarse.

Series 4: In this series the silica and alumina were kept constant each at their high levels of 1.0 mass % and the lime content varied in the same range as in series 3.

Plate 4.21 shows the microstructure at 1.0 mass % lime which shows two different types of grain (i) grey in colour . formed by additions and surrounded by white hematite grains. Plate 4.22 shows the microstructure of pellets containing 2.0 mass % lime. A particular feature is the presence of globular particles with large central cavities. Most of the hematite grains which show slight grain growth are relatively disconnected by pores.

The microstructure of pellets containing 4.0 mass % lime is given in Plate 4.23 which shows globular type calcium ferrite phases with considerable needle and pores formation. Plate 4.24 shows calcium ferrite in needles form in the same pellet examined at higher magnification.

4.3.1.2. The microstructure of iron oxide pellets sintered at 1325°C for 30 minutes

This section describes the microstructures of iron oxide pellets containing 0.22 mass % silica, 0.24 mass % alumina and lime in the range of 0.12 to 3.0 mass %. A section of an iron oxide pellet containing 0.12 mass % lime is shown in Plate 4.25. This microstructure reveals that the hematite grains have sintered together and slight grain growth has occurred although the structure retains a high degree of porosity.

The microstructure of the pellet containing 1.0 mass % lime is shown in Plate 4.26. In this pellet the calcium ferrite is evenly distributed along the grain boundaries as a continuous network and the pores are isolated from one another.

The microstructure of pellets containing 2.0 mass % lime is shown in Plate 4.27. In this pellet, lime has reacted with some of the iron oxide to form small grains of calcium ferrite uniformly distributed along the hematite grain boundaries. The matrix is strongly bonded by calcium ferrite and the structure is less porous and stronger. Plate 4.28 shows a section of the pellet containing 3.0 mass % lime. The microstructure of this pellet is similar to that displayed in Plate 4.27 except for a slightly higher amount of calcium ferrite and porosity.

4.3.1.3. The microstructure of an iron oxide pellet sintered at 1250°C for 12 hours

The microstructure of a pellet containing 1.0 mass % lime, 3.0 mass % silica and 0.24 mass % alumina is shown in Plate 4.29. This microstructure shows a fine grained hematite matrix with high porosity.

The phases found were hematite and iron-calcium silicate. The latter phase is present as very fine particles and at the hematite grain boundaries.

4.3.2. Analysis of microstructural constituents of iron oxide pellets

A scanning electron microscope (SEM) with energy dispersive micro-analyser (EDAX) was used to analyse the microstructural constituents of most of the oxide pellets considered in section 4.3.1. The phases present in the sintered pellets were studied both quantitatively and qualitatively. With point analysis being carried out on various phases at a number of locations.

Table 4.2 shows the content of various oxides present, and the mean point analysis of each phase detected in the different iron oxide pellets.

4.3.2.1. Analysis of microstructural constituents of iron oxide pellets sintered at 1250°C for 3 hours

Microstructural analysis of these pellets was carried out on four series of composition as described in section 4.3.1.

Series 1: The microstructure of iron oxide pellets containing silica, alumina and lime (0.22, 0.24 and 1.0 mass % respectively) is shown in Plate 4.30 with Plate 4.31 and 4.32 showing X-ray maps of the corresponding calcium and silica distribution. These photomicrographs show that some grains are particularly rich in lime, but that silica is more uniformly distributed. Analysis at various positions confirms that the structure consists primarily of hematite a small proportion of calcium ferrite.

Plate 4.33 shows a section of the microstructure of an iron oxide pellet containing 0.22 mass % silica, 0.24 mass % alumina and 2.0 mass % lime at high magnification, with Plate 4.34 showing an X-ray map of the corresponding calcium distribution. From these plates it can be seen that phases rich in lime have developed at grain boundaries. Analysis of these phases shows that a wide range of calcium ferrites have formed (see Table 4.2). The microstructure consists mainly of hematite and calcium ferrites. These ferrites are classified as $\text{CaO} \cdot \text{Fe}_2\text{O}_3$ and $\text{CaO} \cdot 2\text{Fe}_2\text{O}_3$.

Plate 4.35 shows the microstructure of a pellet containing 0.22 mass % silica, 0.24 mass % alumina and 5.0 mass % lime, followed by the corresponding X-ray map of calcium distribution in Plate 4.36. The analysis of this pellet and also the pellets containing 3.0 and 4.0 mass % lime at the same silica and alumina level confirms that the phases are mainly hematite and calcium ferrites but a very small proportion of silicate can also be detected.

Series 2: Plate 4.37 shows the microstructure of an iron oxide pellet containing 1.0 mass % silica, 0.24 mass % alumina and 1.0 mass % lime whilst Plates 4.38 and 4.39 show the corresponding X-ray maps of calcium and silicon distribution. The phases formed and detected by microanalysis are very fine and difficult to see on the unetched samples by optical microscopy. The phases found are mainly hematite and silicates of varying composition as given in Table 4.2.

Plate 4.40 shows the microstructure of a pellet containing 1.0 mass % silica, 0.24 mass % alumina and 2.0 mass % lime, followed by the

corresponding X-ray maps of silicon and calcium distribution in Plates 4.41. and 4.42. The microanalysis of this pellet and also of a pellet containing 3.0 mass % lime at the same silica and alumina levels confirms that the microstructure consists mainly of hematite-calcium ferrites and complex iron-calcium silicates.

Plate 4.43 shows the microstructure of a pellet containing 1.0 mass % silica, 0.24 mass % alumina and 5.0 mass % lime with plates 4.44 and 4.45 showing X-ray maps of the corresponding calcium and silicon distributions. The analysis of this pellet and also of a pellet containing 4.0 mass % lime at the same silica and alumina levels confirms that the phases are mainly hematite and a wide range of calcium ferrite (see Table 4.2).

Series 3: Plate 4.46 shows the microstructure of a pellet containing 0.22 mass % silica, 1.0 mass % alumina and 1.0 mass % lime, whilst Plate 4.47 and 4.48 shows corresponding X-ray maps of aluminium and calcium. From these Plates it is clear that the dendritic structure previously observed is rich in alumina and the encircling phase is rich in lime. Though few other grains have a high content of lime and alumina, analysis confirms that the phases present are mainly hematite, free alumina and calcium diferrites with a small proportion of silica and alumina (see Table 4.2).

Plate 4.49 shows the microstructure of a pellet containing 0.22 mass % silica, 1.0 mass % alumina and 4.0 mass % lime, with corresponding X-ray maps of aluminium and calcium distribution shown in Plates 4.50 and 4.51 respectively. These Plates show that the phases other than hematite are rich in lime only. Analysis confirms that mainly

hematite and calcium ferrites are formed (see Table 4.2). Some calcium ferrites also contain a smaller proportion of silica and alumina.

Series 4: In this series analyses of pellets containing lime (1 and 4.0 mass %) at 1.0 mass % of silica and 1.0 mass % alumina were carried out. Plate 4.52 shows the microstructure of an iron oxide pellet containing 1.0 mass % silica, 1.0 mass % alumina and 1.0 mass % lime, with Plates 4.53 and 4.55 showing corresponding X-ray maps for the distribution of aluminium, silicon and calcium respectively. Point analyses at four locations in the large grain were taken with the following results.

Composition /mass %	Location				Mean
	1	2	3	4	
Fe ₂ O ₃	23.45	33.90	41.83	50.69	37.49 ± 10
CaO	31.18	32.2	25.22	27.35	28.99 ± 2.82
SiO ₂	22.99	20.54	9.67	13.60	16.7 ± 5.32
Al ₂ O ₃	22.47	13.27	23.27	8.37	16.8 ± 6.27

From these figures it can be seen that this phase varies in chemical composition even within a single grain. The main phases found in this pellet are hematite and calcium ferrites. Most of the calcium ferrites contain a significant amount of silica and alumina (see Table 4.2).

The microstructure of a pellet containing 1.0 mass % silica, 1.0 mass % alumina and 4.0 mass % lime is shown in Plate 4.56 with Plate 4.57 and 4.58 showing X-ray maps of aluminium and calcium distribution. Again it will be seen that alumina is almost uniformly distributed, but that a high proportion of lime is present in significant grains. The phases found in this pellet are mainly hematite and calcium ferrites.

3.4.2.2. Analysis of the microstructural constituents of iron oxide pellets sintered at 1325°C for 30 minutes

The microstructure of a pellet containing 0.22 mass % silica, 0.24 mass % alumina and 1.0 mass % lime is shown in Plate 4.59 with Plates 4.60 and 4.61 showing X-ray maps of calcium and silicon distribution respectively. These plates confirm that some grains show enrichment in calcium, forming different types of calcium ferrites (see Table 4.2).

Plate 4.62 shows the section of a pellet containing 0.22 mass % silica, 0.24 mass % alumina and 3.0 mass % lime with Plates 4.63 and 4.64 showing corresponding X-ray maps of the distribution of silicon and calcium respectively. From these Plates it will be seen that silicon is uniformly distributed but again with enrichment of calcium in the network. The phases developed during sintering are mainly hematite and calcium ferrites as detailed in Table 4.2.

4.3.2.3. Analysis of the microstructural constituent of iron oxide pellet sintered at 1250°C for 12 hours

Plate 4.65 shows a section of iron oxide pellet containing 3.0 mass % silica, 0.24 mass % alumina and 1.0 mass % lime with Plates 4.66 and 4.67 showing X-ray maps of the distribution of

calcium and silicon respectively. These plates show that the phases developed during sintering are rich in both lime and silica. Analysis of this pellet confirms that the phases found are calcium silicates and complex-iron calcium silicates.

4.4 RESULTS OF MASS TRANSFER EXPERIMENTATION

Values of the mass transfer coefficient were determined using naphthalene as described in section 3.7. The mass transfer coefficient for evaporating naphthalene was evaluated from the relationship⁽⁶⁵⁾ :-

$$\Delta_{C_{10}H_8} = \frac{\dot{n} R T}{S V_p} = \frac{W}{t M_{C_{10}H_8}} \frac{RT}{S V_p} \quad \text{--- (1)}$$

where: \dot{n} = the rate of mass loss of naphthalene

W = mass loss in time t

$M_{C_{10}H_8}$ = molar mass of naphthalene (= 128 g.mol⁻¹)

S = surface are of the cylindrical sample

T = temperature (K)

R = gas constant (= 82.06 cm³ atm.K⁻¹ mol⁻¹)

V_p = the equilibrium vapour pressure of naphthalene

The above relationship regards the equilibrium vapour pressure of naphthalene as the driving force for evaporation by assuming the partial pressure of naphthalene in the bulk gas to be zero. The equilibrium vapour pressure of naphthalene was calculated from the following equation⁽⁶⁵⁾ :-

$$\text{Log } p = 8.67 - \frac{3765}{T} \quad \text{--- (2)}$$

where: p is in atmospheres and T is in K.

The results for the mass transfer coefficient of naphthalene for varying air flow rates through the system are presented in Table 4.3. Figure 4.3(a) shows that there is a linear relationship between these two variables. This is consistent with a dimensionless correlation of the form:-

$$Sh = A + B Re^n Sc^{1/3} \quad \text{----- (3)}$$

$$\text{and } Sh = \frac{\lambda_i d}{D_{A-B}} \quad (\text{the Sherwood number})$$

λ_i = mass transfer coefficient

$D_{C_{10}H_8\text{-Air}}$ = diffusivity of naphthalene in air

d = is a characteristic length of sample (1 cm)

$$R = \frac{u d}{\nu} \quad (\text{the Reynold's number})$$

U = the flow rate per unit cross-sectional area

ν = kinematic viscosity of flowing medium (air)

$$\text{and } S_c = \nu / D_{A-B} \quad (\text{Schmidt number})$$

The values of A , B and n in equation (3) are specific to the tube-particle geometry involved in this experimental work. The value of A , can be determined from Fig.4.3(a), where the intercept on the ordinate axis is $A D_{C_{10}H_8\text{-Air}}/d$. At room temperature, the binary diffusion coefficient, $D_{C_{10}H_8\text{-Air}}$, is $0.0611 \text{ cm}^2 \text{ sec}^{-1(96)}$ giving A , the value of 1.68.

The value of B and n can then be determined from the intercept and slope respectively of: $\text{Log} \left[\frac{(Sh-1.68)}{Sc^{1/3}} \right]$ against $\text{log } Re$ as shown in Fig.4.3(b), drawn from the data given in Table 4.4. Substituting the values thus obtained for B and n into equation (3) gives:-

$$Sh = 1.68 + 0.126 Re^{1.22} Sc^{1/3} \text{ - - - - - (4)}$$

In equations (3) and (4) the Schmidt number exponent has been assumed to be $1/3$ in view of the almost universal acceptance of this value for turbulent flow conditions. (The definition of the Chilton Colbur J-factor for mass transfer, for example, is based on this exponent value).

Using this mass transfer correlation and substituting values for the kinematic viscosity, molecular diffusivity of H_2/H_2O gas system (see Appendix 2 and 3) and Re calculated for a hydrogen flow rate of 5.6 l.min^{-1} , the mass transfer coefficient $k_{H_2-H_2O}$ during reduction at 1123 K would have value of $16.80 \text{ cm.sec}^{-1}$. The relationship between this estimated value for mass transfer characteristics based on the gas flow model and the actual rate of reduction experience in the reduction-under-load apparatus are discussed in section 5.2.

4.5 THE REDUCIBILITY OF IRON OXIDE PELLETS

The reducibility of iron oxide pellets with varying contents of lime, silica and alumina has been determined in hydrogen at 830°C and 850°C using a thermogravimetric spring balance. Reduction tests at 830°C using a gas mixture of hydrogen and carbon monoxide were also carried out. The results obtained in these reducibility tests are given in the sections which follow.

4.5.1 Reducibility in hydrogen gas at 830°C of different iron oxide pellets sintered at 1250°C for 3 hours

Reducibility curves for iron oxide pellets containing 0.22 mass \% silica and 0.24 mass \% alumina with different amounts of lime in the

range 0.12 to 5.0 mass % are shown in Fig.4.4. It can be seen from this figure that the reducibility is decreased with increasing content of lime. At higher silica and low alumina contents (1.0 mass % and 0.24 mass % respectively), the variation in reducibility of the pellets with change of lime content shows a different behaviour as shown in Fig.4.5. The reducibility is slightly increased when the lime content is changed from 0.12 to 1.0 and from 2.10 to 4.0 mass %. However changes from 1.0 to 2.0 mass % and from 4.0 to 5.0 mass % both result in a decrease in reducibility. An addition of silica from 0.22 to 1.0 mass % at the low alumina level (0.24 mass %) increases the reducibility at all the levels of lime considered in this work except at the lowest lime level (0.12 mass %) where reducibility is slightly decreased.

Figure 4.6 shows the reducibility curves of pellets containing 1.0 mass % alumina and 0.22 mass % silica at different lime contents. The reducibility of these pellets is decreased with increase of lime, but the curves show that increasing the alumina content from 0.24 to 1.0 mass % increases the reducibility of the pellets, at all lime levels, much more than a similar increase in silica content.

At high contents of alumina and silica (each equal to 1.0 mass %), the reducibility is marginally decreased with increase of lime content as shown in Fig.4.7.

These pellets have very similar rates of reduction at the 2.0 mass % lime level to high alumina low silica pellets, but, at all other lime contents, the latter pellets have a greater reducibility, indeed they were the most reducible pellets studied in this investigation.

Using the reducibility curves in Figs.4.4 to 4.7 the times required for a degree of reduction of 95% for different pellets have been abstracted and are shown in Fig.4.8.

4.5.2 Reducibility of doped iron oxide pellets produced by sintering 1250°C for 3 hours and reduced in a gas mixture of hydrogen and carbon monoxide at 830°C

Pellets of compositions given in series 1 and series 2 (section 4.3.11.) were reduced in an equi-molar mixture of hydrogen and carbon monoxide at 830°C. Graphs of the apparent degree of reduction versus time are given in Figs.4.9 and 4.10. The most significant differences between such reduction and that in pure hydrogen were the lower rate of reduction experienced and the occurrence of carbon deposition with the mixed reductant. Carbon deposition was suspected because the reduction appeared to stop at a degree of about 0.88 rather than at 0.95 often experienced in hydrogen. Also, after taking the samples out of the thermogravimetric spring balance, it was observed that the reduced samples possessed a deposit of soot which was particularly heavy on those pellets which contained a low proportion of doping agents. The presence of carbon in one of the undoped samples was confirmed by chemical analysis when a content of 0.3% carbon was found in the reduced sample.

The reducibility of pellets with two silica levels, 0.22 and 1.0 mass % and with varying amounts of lime in the gas mixture of hydrogen and carbon monoxide is shown in Figs4.9 and 4.10 respectively. It can be seen from these figures, that the reducibility is increased when the lime content is increased up to 1.0 mass %, beyond which a decrease is experienced. It will be

seen that an increase of silica from 0.22 to 1.0 mass % increases the reducibility at all the lime levels.

This confirmed in Fig.4.11 which plots the lime required for the end of reduction against lime content for both silica levels. The detrimental effect of increasing lime content on the reducibility of pellets in this composition range is also evident.

4.5.3 The reducibility in hydrogen at 850°C of iron oxide pellets sintered at 1325°C for 30 minutes

Figure 4.12 shows the reducibility curves of pellets containing 0.22 mass % silica, 0.24 mass % alumina and lime in the range of 0.12 to 3.0 mass %. It can be observed that the reducibility is decreased with increasing lime content. Figure 4.13 shows the time taken for the 95% reduction of these pellets.

4.5.4 The reducibility in hydrogen at 850°C of iron oxide pellets sintered at 1250°C for 12 hours

The reducibility of pellets containing 1.0 mass % lime, 0.24 mass % alumina and 3.0 mass % silica were found to behave similalry to the reducibility of pellets containing 0.12 mass % lime as described in section 4.5.3. The percent reductions at different times are shown in Table 4.5.

4.6 DIMENSIONAL STABILITY AND STRENGTH OF IRON OXIDE PELLETS DURING REDUCTION IN HYDROGEN

The dimensional changes of iron oxide pellets during reduction were determined in the specially designed apparatus described in section 3.3. The tests were carried out at three nominal levels of loading viz: 0, 1.18 and 2.36 kg for a nominal pellet diameter of

10 mm and corresponding to initial compressive stresses of 0, 1.5 and 3.0 kg cm⁻². To allow for slight variation in pellet diameter, yet to maintain the same initial stress, the loads used were in the ranges, 0, 1.11-1.18 and 2.22-2.36 kg. The results based on graphs of percentage change in length against reduction time for different pellets are given in this section.

4.6.1 Dimensional changes

The dimensional changes occurring during reduction of pellets containing controlled contents of silica, alumina and lime are given in Fig.4.14 to 4.25 as graphs of linear expansion against time. Details of the composition, reduction temperature and initial stress applying to the respective figures are as follows:

Composition of doping agent. Mass %			Reduction Temperature	Stress	Figure No.
SiO ₂	Al ₂ O ₃	CaO			
0.22	0.24	0.12	830°C	0	4.14
		1.00		1.5 kg cm ⁻²	4.15
		2.00		3.0 kg cm ⁻²	4.16
		3.00			
		4.00			
		5.00			
1.00	0.24	0.12		0	4.17
		1.00		1.5 kg cm ⁻²	4.18
		2.00		3.0 kg cm ⁻²	4.19
		3.00			
		4.00			
0.22	1.00	1.00		0	4.20
		2.00		3.0 kg cm ⁻²	4.21
		3.00			
1.00	1.00	1.00		0	4.22
		2.00		3.0 kg cm ⁻²	4.23
		3.00			

Table continued overleaf

Composition of doping agent. Mass %			Reduction Temperature	Stress	Figure No.
SiO ₂	Al ₂ O ₃	CaO			
3.00	0.24	1.00	850°C	0 1.5 kg cm ⁻²	4.24 4.25
0.22	0.24	0.120			
		1.000			
		2.00			
		3.00			

The results given in Figs.4.14 to 4.25 together with those of the reducibility tests described in Section 4.5 have been used to relate the dimensional changes of the pellets to the degree of reduction, assuming that identical rates of reduction apply in both apparatus. The resulting curves are shown in Figs.4.26-4.33.

4.6.2 Relationships between composition and reduction properties (reducibility and linear change) of iron oxide pellets containing varying amounts of doping agents at different stresses

Percentage changes in length are shown in Figs.4.26-4.33 plotted against percentage degrees of reduction for iron oxide pellets reduced at 830°C with Fig.4.34 showing the results for pellets reduced at 850°C.

Figures 4.26 and 4.27 present results for pellets containing 0.12 to 5.0 mass % lime, 0.22 mass % silica and 0.24 mass % alumina of two different stress levels, zero and 3 kg cm⁻² respectively.

Figure 4.26 shows that low lime pellets (0.12 mass % lime) expand significantly up to a degree of reduction of about 35% and then shrink with further reduction. Pellets containing 1.0 mass % lime expand progressively and significantly up to 80% reduction and then

shrink in the later stage of reduction. In contrast, iron oxide pellets containing 2 to 5.0 mass % lime expand slowly, some only showing expansion maxima at degrees of reduction in excess of 80%. Figure 4.27 shows corresponding relationships at the high stresses level of 3.0 kg cm^{-2} . At this stress, iron oxide pellets containing 0.12 and 1.0 mass % lime expand significantly up to about 30% and 60% reduction respectively, followed by high shrinkage. Pellets containing 2-5 mass % lime show similar expansion behaviour to their behaviour at zero stresses.

Figure 4.28 and 4.29 show the results obtained at two different stresses (zero and 3.0 kg cm^{-2}) for a range of iron oxide pellets containing 0.12 to 5.0 mass % lime, 1.0 mass % silica and 0.24 mass % alumina. Figure 4.28 demonstrates that these high silica low alumina iron oxide pellets show an initial rapid expansion during the early stages of reduction at zero stress followed by a period of dimensional stability and then varying degrees of contraction in the final stages of reduction. In general terms, the degree of expansion exhibited decreases with increasing lime content up to 5.0%.

Figure 4.29 shows results at the stress of 3.0 kg cm^{-2} for the same series of pellet compositions. In general the expansion characteristics are similar to those shown at zero stress although the degrees of expansion are lower. Indeed, for two of the pellets, viz: those containing 0.12 and 2.0 mass % lime, the final lengths show an overall contraction.

Figures 4.30 and 4.31 give plots of expansion against degree of reduction at stresses of zero and 3 kg cm^{-2} respectively for a range

of iron oxide pellets containing 1.0-4.0 mass % lime, 0.22 mass % silica and 1.0 mass % alumina. Both sets of curves are of similar form: initial expansion, a plateau of relative dimensional stability followed by shrinkage in the final stages of reduction. Figure 4.32 and 4.33 show plots of the degree of expansion versus percentage reduction of stresses of zero and 3.0 kg cm⁻² respectively for a range of iron oxide pellets containing 1.00 to 4.00 mass % lime, 1.0 mass % silica and 1.0 mass % alumina. These figures have the same general form as that shown by the previous set with the degree of expansion decreasing with increasing lime content and increasing stresses.

Figure 4.34 shows results of a range of iron oxide pellets containing 0.12 to 3.0 mass % lime, 0.22 mass % silica and 0.24 mass % alumina and a single sample containing 1.0 mass % lime, 3.0 mass % silica and 0.24 mass % alumina at 850°C and zero stresses. Again the format of the curves is expansion during the early stages of reduction, relative stability or slight expansion in the intermediate stages and varying degrees of contraction in the final stages. It is interesting to note that the sample containing 1.0 mass % lime, 3.0 mass % silica and 0.24 mass % alumina exhibits the highest degree of expansion of all samples examined.

4.6.3 Relationship between peak expansion and pellet composition at different stresses

Values obtained for the peak expansion of the iron oxide pellets reduced at 830°C in hydrogen, expressed as a percentage of the initial pellet length are plotted against lime content in Fig. 4.35-4.38, different curves being presented for the different levels of initial stress. Table 4.6 shows similar data for a reduction temperature of

850°C. For the low silica (0.22 mass %) and low alumina (0.24 mass%) pellets, Fig.4.35 reveals that the maximum peak expansion is shown by iron oxide pellets containing some 1.0 mass % of lime and that the value of the peak expansion decreases with the increasing lime content up to 5.0 mass %. It can also be seen that the peak expansion at all compositions in this series decreases with increase of load, this decrease being particularly significant for pellets containing 1.0 mass % of lime.

Figure 4.36 shows peak expansion values for the high silica (1.0 mass %) low alumina (0.24 mass %) pellets containing 0.12 to 5.0 mass % lime. These results again show that maximum peak expansion occurs in pellets containing some 1.0 mass % lime and then decreases with further increase in lime content. Again, increasing the applied stresses reduces the peak expansion, particularly in those pellets for which the values of peak expansion are high.

Comparison of Fig.4.35 and 4.36 shows that the increase in silica content from 0.22 to 1.0 mass % has raised the values of the peak expansion for all lime contents. Figure 4.37 and 4.38 show how the peak expansion varies with lime content between 1.0 and 4.0 mass % for low silica (0.22 mass %) high alumina (1.0 mass %) pellets and for high silica (1.0 mass %) and high alumina (1.0 mass %) respectively. It is clear from these figures that the peak expansion values in both series decreased with an increase of lime content and with an increase of stress.

It is clear that low silica pellets containing 1.0 mass % alumina have lower maximum peak expansion values at 1.0 mass % lime than

those containing only 0.24 mass % alumina. However, increasing the lime content beyond 1.0 mass % has a smaller effect in the high alumina pellets than in the low alumina pellets, with the result that, at 4.0 mass % lime, the peak expansion value for the high alumina pellets is the higher.

Table 4.6 shows values of peak expansion at 850°C at various lime content for low silica (0.22 mass %) low alumina (0.24 mass %) content at zero and 1.5 kg cm⁻² stresses. From this Table it will be observed that the peak expansion value decreases with increasing lime content and increasing initial stress. The highest fractional peak expansions 8.4% and 6.1% at the stress levels of zero and 1.5 kg cm⁻² respectively were determined for pellets containing 1.0 mass % lime, 3.0 mass % silica and 0.24 mass % alumina. Plots of peak expansion values during reduction at 830°C, against lime content given in Fig.4.35 and 4.38 are summarised in Fig.4.39a and 4.39b. The general effects are that the peak expansion value decreases with increase of stresses, with increase of lime content above 1.0 mass %, and with decrease of silica content whatever the total level doping agents present.

Increase of alumina increases the peak expansion value at all levels of doping agent except of 1.0 mass % lime. However, its influence in this direction is less than for corresponding additions of silica.

4.6.4 Relationship at different stresses between the terminal expansion and composition of iron oxide pellets containing varying amounts of doping agents

Values for the fractional terminal expansion of iron oxide pellets reduced at 830°C and 850°C are shown in Figs.4.40-4.43 and in Table 4.6 respectively. For the purpose of this section terminal expansion is defined as that occurring at a degree of reduction equal to 95%, or at the finally achieved degree of reduction, whichever is the lower. Values for terminal expansion against lime contents varying between 0.12 and 5.0 mass % are plotted in Fig.4.40 for pellets containing 0.22 mass % silica and 0.24 mass % alumina for two different initial stresses viz: 0, 3.0 kg cm⁻². This figure shows that, for these low silica low alumina pellets at stress of zero, there is a sharp increase in the fractional terminal expansion as the lime content increases from 0.12 and 1.0 mass %, followed by a gradual decrease as the lime content rises to 5.0 mass %. Similar changes occur at 3.0 kg cm⁻² with the maximum terminal expansion occurring at 2.0 mass % lime. At all the lime levels used, the terminal expansion is lowered by applied stress. All pellets, except the two low lime compositions at maximum stress have positive values for their terminal expansions.

Figure 4.41 shows similar plots for pellets containing a higher silica content (1.0 mass %) but the same alumina content (0.24 mass %) at different loads. The results shown in this figure are similar to those for the lower silica levels except that:

- (i) the terminal expansion values are higher for corresponding calcium oxide and stress levels at zero kg cm⁻²,
- (ii) the maximum terminal expansion was obtained in all cases at 1.0 mass % lime

- (iii) sharper decreases occur beyond the peak values as the lime content increases,
- (iv) the curve for 3.0 kg cm^{-2} has a minimum at 2.0 mass % followed by a gradual increase up to 5.0 mass % lime,
- (v) there is a slight increase in terminal expansion between 4.0 and 5.0 mass % lime.

Figure 4.42 shows the results of terminal expansion against lime content between 1.0 and 4.0 mass % for pellets at low silica (0.22 mass %) and high alumina (1.0 mass %) for initial stress levels of zero and 3 kg cm^{-2} . It can be seen from this figure that the behaviour is similar at both stress levels, the expansion value in each case being decreased by increasing the stress level and with the lowest value at 2.0 mass % lime. Figure 4.43 shows graphs of terminal expansion values obtained at two loads plotted against lime for iron oxide pellets containing high silica (1.0 mass %) and high alumina (1.0 mass %). At both stress levels, the terminal expansion decreases almost linearly with lime content between 1.0 and 4.0 mass %, the values obtained at 3 kg cm^{-2} being lower than those obtained at zero stress. This figure also demonstrates that pellets containing 4 mass % lime show a slight terminal contraction under an initial stress of 3.0 kg cm^{-2} .

Terminal expansions measured for pellets of the four compositions reduced at 830°C are plotted against lime content in Figs. 4.44a and 4.44b for the two initial stress levels used.

From Fig. 4.44a it can be seen that, at zero stress, the terminal expansion of pellets containing silica in the range 0.22-1.0 mass %

and alumina in the range 0.24-1.0 mass % are high up to a lime content of 1.0 mass % and then decrease as the lime content is further increased with the exception of pellets containing 0.22 mass % silica and 1.0 mass % alumina. Pellets with a silica content of 1.0 mass % at the 0.24 mass % alumina level gave the highest terminal expansion of all the pellets studied. However, when the alumina content was also increased to 1.0 mass %, the terminal expansion observed was found to be less than that observed for pellets with 0.22 mass % silica and 0.24 mass % alumina except at 4.0% lime.

Figure 4.44b shows that under the stress of 3.0 kg cm^{-2} iron oxide pellets containing silica in the range 0.22-1.0 mass % and 0.24 mass % alumina contract considerably at 0.12 mass % lime. At 1.0 mass % CaO on the other hand, pellets containing 0.22 mass % silica expand and pellets containing 1.0 mass % silica contract. At 2.0 mass % lime and 0.22 mass % silica, pellets show a small significant expansion but the remainder of the compositions produce no significant behaviour, showing almost insignificant expansions or contractions without clear patterns emerging. The terminal expansion at 850°C of pellets containing 0.12 mass % lime, 0.22 mass % silica and 0.24 mass % alumina are plotted against lime content in Table 4.6. From this Table it can be seen that the results are similar to those obtained at 830°C but at a lower level of expansion throughout. In one further solitary result, a single pellet containing 3.0 mass % silica, 1.0 mass % lime and 0.24 mass % alumina showed the high terminal expansion value of 7.0%.

4.7 DENSITY AND POROSITY OF IRON OXIDE PELLETS REDUCED IN HYDROGEN AT 830°C

The results for density and porosity of unreduced and reduced iron oxide pellets are shown in Figs. 4.45 and 4.46 respectively. The density values for unreduced pellets, previously quoted in Fig. 4.1 are combined with those for pellets with degrees of reduction 0.92-0.95 and shown in Fig. 4.45. It is clear from these figures that the density of reduced pellets is much lower than the unreduced pellets for all pellets examined.

The porosity values for unreduced pellets, previously quoted in Fig. 4.2, are combined with those for pellets with degrees of reduction 0.92-0.95 and shown in Fig. 4.46. It is clear from this figure that the porosity of reduced pellets is much higher than the unreduced pellets at all doping agent concentrations examined.

4.8 MACROSCOPIC OBSERVATION OF PARTIALLY REDUCED PELLETS

Partially reduced iron oxide pellets of a wide range of doped compositions were examined by optical microscopy. Typical macro- and micrographs obtained are shown in Plate 4.68 and 4.69.

Three distinct modes of reduction behaviour were identified and these, after Turkdogan⁽¹³⁾, have been termed homogeneous, mixed mode and topochemical.

Plate 4.68 presents several macrographs ($\times 3.5$) of the vertical mid-section of the upper half of pellets at different degrees of reduction and illustrates most clearly the distinction that has been recognised between the different reduction modes. These

distinctions are further clarified in Plate 4.69 which shows a series of micrographs (X320) for each mode of reduction, the micrographs being taken from particular pellets for which macrographs are presented in Plate 4.68. The micrographs were taken at the mid-plane of these pellets at the radial positions indicated by the arrows in Plate 4.68.

In the homogeneous mode of reduction, the reduction step from hematite to magnetite occurs very rapidly at an early stage in the reduction process - certainly well before reduction is 30% complete. The next reduction step, from magnetite to wustite, then occurs generally throughout the entire pellet so that both phases exist together within the inner regions of the pellet during much of the reduction process. Iron, moreover, is also nucleated generally throughout the pellet although the growth of this nucleated iron occurs more rapidly in layers closest to the surface. Thus, an outer layer of almost pure iron can be recognised even in the pellets that show the homogeneous reduction mode.

In the topochemical mode of reduction, on the other hand, the reduction steps from hematite to magnetite and from magnetite to wustite occur slowly. Thus unreduced hematite exists in the centre of the pellet until a late stage in the reduction process and the magnetite and wustite phases are concentrated in a narrow region separating the hematite from the outer layer of pure iron. Magnetite and wustite are indistinguishable under the optical microscope so that it has not been possible to ascertain whether they are distributed uniformly within the two phase region or whether a

layer of wustite exists outside a layer of magnetite. It is possible to ascertain, however, that iron nucleates almost exclusively within a narrow band on the outside of the magnetite/wustite region.

In the mixed mode of reduction, the hematite reduction step occurs sufficiently fast for it to be almost complete by the time 50% of the reduction process is complete. Much of the pellet is thus occupied by the two phase magnetite/wustite region. Moreover, the nucleation and growth of iron is restricted to the outer regions of the pellet, although these regions are more extensive and diffuse than they are in the topochemical mode.

The main features of the different modes are set out in the table below and Table 4.7 shows which of the pellets investigated exhibited which mode of reduction. This latter table also indicates the extent to which the pellets became cracked during reduction and suggests that pellet cracking is strongly associated with the homogeneous mode of reduction.

Mode Constituents	Homogeneous Mode	Mixed mode	Topochemical Mode
Fe	White outer layer plus particles nucleated throughout	White outer layer	White outer layer
FeO/Fe ₃ O ₄ mixture	Throughout the core	Wide intermediate zone	Narrow intermediate zone
Fe ₂ O ₃	None present following extremely rapid reduction throughout the pellet	Small central region	Large central region

5.1 COMMERCIAL IMPORTANCE OF REDUCTION PROPERTIES OF IRON OXIDE PELLETS

It is generally accepted that the most important properties of iron oxide pellets influencing uniformity of operation and productivity of Direction Reduction furnaces are reducibility, strength and dimensional stability.

High reducibility, according to Kaneko and Narita⁽²¹⁾ and Stephenson et al⁽²⁸⁾ is associated with improved productivity and low fuel consumption. High strength lowers the proportion of fines produced, thereby preventing an increase in the pressure difference through the furnaces and decreasing dust losses. Significant volume changes, positive or negative, are undesirable in that expansion results in loss of pellet strength and contraction leads to clustering at high temperature. The latter effect causes hanging problems interfering with smooth descent of the charge and ease of discharge from the furnace.

The present work recognises (a) the dependence of reduction properties of pellets on the presence of oxides present with iron oxide, (b) the method of preparation of pellets, (c) the general desirability of having minimum gangue present as far as the pellet consumer is concerned e.g. to ensure maximum iron units and minimum energy for melting, (d) the general view that lime is a desirable impurity oxide and (e) the general view that silica and alumina are undesirable impurity oxides.

With this background, pellets containing up to 5.0% lime and up to only 1.0% each of silica and alumina were prepared and used to develop the wide range of microstructures obtained and examined. The microscopic examination detailed in Chapter 3 has revealed variations in morphology as well as in uniformity of the individual constituents.

The rates of reduction of pellets of varying composition in a thermogravimetric apparatus have been compared at temperatures consistent with industrial reduction temperatures (830-850°C) in hydrogen and a hydrogen/carbon monoxide mixture (830°C) of industrial significance. In the latter gas mixtures, the significance of carbon deposition will be discussed. In another apparatus, of known gas flow characteristics, the dimensional stabilities of pellets of varying composition reduced in hydrogen and at varying stresses of (0 to 3.0 kg.cm⁻²), related to the stresses experienced in industrial furnaces, will be discussed.

Density and porosity determinations of unreduced and reduced pellets will be used to supplement the discussion of the results of the metallographic studies. These properties of reduced pellets are of particular concern to the steelmaker using them. The densities and porosities of uncracked reduced pellets measured in the present investigation are of the same order as the denser end of the range (density 3.3 g.cm⁻³ and porosity 50-60%)⁽²⁸⁾ of currently used industrial pellets i.e. in a range for which transport costs and ease of charging are tolerable without compaction of the finished pellets prior to melting.

5.2 DISCUSSION OF EXPERIMENTAL ACCURACY AND MASS TRANSFER THROUGH GAS BOUNDARY LAYER

5.2.1 Assessment of experimental errors

The experimental work was carried out to study reducibility and dimensional stability during reduction of doped hematite pellets. A wide range of doped hematite pellets in cylindrical form was prepared. Green masses of 3.10 ± 0.001 gram were compressed on an Avery machine at load of 300 ± 20 kg/pellet and sintered in a muffle furnace in air generally at $1250 \pm 15^\circ\text{C}$, but with a few samples at $1325 \pm 15^\circ\text{C}$.

Porosity and density

The porosities of most of the pellets in each batch were found to vary in absolute terms by $\pm 1.0\%$ and density by $\pm 0.05 \text{ g.cm}^{-3}$. Any pellets lying outside these limits were discarded. The pellets showed a great consistency in dimensions, having a maximum relative error of $\pm 0.1\%$ in both height and diameter.

Composition

The quantitative analysis of the microstructural constituents present in the vertical central cross-section ± 0.1 mm of the pellets, as determined by the combination of scanning and energy dispersive X-ray analysis, is considered to be correct to $\pm 5\%^{(10)}$. The greater variation in analysis that was found in some of the pellets examined in this work was therefore taken to suggest non-uniformity of phase composition. This will be discussed in detail later in section 5.5.

Reduction time and temperature

The reproducibility data can be assessed from the curves shown in Fig.3.17-3.20. These show a maximum scatter of $\pm 6.7\%$ at the lower doping levels and less scatter with increasing additions of doping agents. The higher scatter in the former pellets is possibly due to an uneven distribution of phases, while in the latter the micro-structure possesses a more even distribution. The time for a degree of reduction of 0.95 shows a maximum variation of ± 30 seconds e.g. pellets containing 5% lime, 0.22% silica, see Fig.3.19.

In the reduction apparatus, the hot zone temperature varies by $\pm 4^{\circ}\text{C}$ whereas within the zone of pellet movement during reduction the temperature variation is $\pm 1.5^{\circ}\text{C}$ as shown in Fig.3.15. With such a low temperature variation, it can be assumed that the differences determined between the reducibilities of pellets of varying compositions are due to the variations in composition and not to any significant extent to minor variation in temperature.

The gas flow rate in the thermogravimetric spring balance varies by ± 0.05 l/minute when hydrogen is used alone, but with the gas mixture of hydrogen + carbon monoxide, the flow rate varies by ± 0.1 l/minute. The calibration data for the glass spring gave a regression correlation coefficient of 1.0 as shown in Fig. 3.16. The cathetometer used is able to detect a displacement of 0.05 mm which allows the detection of a weight change of 1.34 mg. This weight is about 0.16% of the mass lost during the reduction of a typical undoped pellet of 2.86 ± 0.01 g. Hence the system used to determine weight changes during reduction is of adequate sensitivity.

Dimensional changes

Apparatus designed in this work is able to determine dimensional changes in the length of the pellet (expansion/shrinkage) as explained in detail in section 3.2.4. Curves showing the results of a series of runs to study the reproducibility of the measurement of length changes are given in Fig.3.13 and Table 3.7. The values of standard deviation varies from 0.03 to 0.4% and the percentage error from (0.96 to 9.86) . In fact, this reduction under load apparatus works at a flow rate of 5.60 ± 0.1 l/minute with hot zone temperature variation of $\pm 1.9^{\circ}\text{C}$. The strain gauges used having a gauge factor $2.1 \pm 1.0\%$, and power supply of 5.96 ± 0.01 volts. Calibration curves for the cantilever beam clamped at two fixed distances from the free end showing load against the millivolt output from the strain gauges are shown in Fig.3.7 and 3.8. These figures give correlation factors of 1.0 and 0.99 respectively. The actual millivolt output is readable to ± 0.005 mv on the digit-voltmeter, this accuracy being equivalent to an applied load ± 3.42 or ± 4.24 grams depending on the position of the clamp, these weights being equivalent to $1.5 \text{ kg} \pm 0.29\%$ and $3.0 \text{ kg} \pm 0.15\%$ respectively. As far as pellet length is concerned, this error of digitvoltmeter is equal to $\pm 0.0125 \text{ mm}$ and $\pm 0.015 \text{ mm}$, depending on clamp position, equivalent to $\pm 0.125\%$ and $\pm 0.15\%$ of a pellet having 10.0 mm length.

5.2.2 Comparison of mass transfer across the gas boundary layer in the reduction under load (RUL) apparatus and in the thermogravimetric spring balance

In section 4.6.2 an assumption has been made that the rate of reduction is of ^{the} same magnitude in both sets of apparatus used in this work. However it is known from the work carried out by e.g Warner⁽⁴⁰⁾, Hills⁽⁴¹⁾, Harrington⁽⁴²⁾ and Rao and Moinpour⁽⁴⁴⁾ that mass transfer across the boundary layer plays some role in controlling the rate of reduction. Hence, work was carried out to determine mass transfer coefficient between bulk gas phase and surface of pellet in (RUL) apparatus by use of a mass transfer model using naphthalene pellets. Mass transfer coefficients in the spring balance apparatus were calculated from the well known correlation developed by Ranz and Marshal⁽⁴³⁾.

The results of mass transfer across the boundary layer in the reduction under load apparatus have been presented in section 4.4. The mass transfer coefficients determined in this system have a correlation:-

$$Sh = 1.68 + 0.126 Re^{1.22} Sc^{1/3}$$

and mass transfer coefficient is given as:-

$$K_{H_2-H_2} = (1.68 + 0.126 Re^{1.22} Sc^{1/3}) \frac{D_{H_2-H_2}}{d} \quad (1)$$

Values at 1123 K of the kinematic viscosity, the molecular diffusivity of H_2/H_2O (from Appendix 2 and 3) and the values of Re at a hydrogen flow rate $5.6 \text{ l/minute}^{-1}$ were substituted and a mass transfer coefficient was determined.

$$d = \text{characteristic length of sample (1 cm)}$$

$$Re = \frac{u \cdot d}{H_2} = 1.31$$

$$u = \frac{\dot{V}}{A} = 12.65 \text{ cm. sec}^{-1}$$

$$\dot{V} = 364 \text{ cm}^3 \cdot \text{sec}^{-1}$$

$$A = 28.27 \text{ cm}^2$$

$$V_{H_2} \text{ at } 1123K = 9.955 \text{ cm}^2 \cdot \text{sec}^{-1}$$

$$D_{H_2 - H_2O} \text{ at } 1123K = 8.9833 \text{ cm}^2 \cdot \text{sec}^{-1}$$

$$Sc^{1/3} = \left(\frac{H_2}{D_{H_2 - H_2O}} \right)^{1/3} = 1.108$$

$$L_{H_2 - H_2O} = 16.80 \text{ cm. sec}^{-1}$$

The mass transfer coefficient through the boundary layer in the spring balance has been calculated from the available mass transfer correlation, reported by Ranz and Marshal⁽⁴³⁾.

$$Sh = 2 + 0.6 Re^{0.5} Sc^{1/3}$$

which gives the mass transfer coefficient as:-

$$L_{H_2 - H_2O} = (2 + 0.6 Re^{0.5} Sc^{1/3}) \frac{D_{H_2 - H_2O}}{d} \text{ ----- (2)}$$

Values at 1123K of the kinematic viscosity, the molecular diffusivity of H_2/H_2 (from Appendix 2 and 3) and the values of Re at a flow rate of 1.0 l/minute⁻¹ can be substituted in equation (2):-

$$Re = \frac{u \cdot d}{H_2} = 1.33$$

$$u = \frac{\dot{V}}{A} = 13.26 \text{ cm. sec}^{-1}$$

$$\dot{V} = 64.99 \text{ cm}^3.\text{sec}^{-1}$$

$$A = 4.9 \text{ cm}^2$$

$$\alpha_{\text{H}_2\text{-H}_2\text{O}} = 24.86 \text{ cm}.\text{sec}^{-1}$$

Thus the values of the mass transfer coefficient in the two apparatuses used in this work do not differ very greatly. The slight difference is due to the different flow patterns set up around the suspended sphere in the reduction apparatus and around the two plattens in the reduction under load apparatus.

In order to assess the effect of this difference on the validity of the assumption that the rates of reduction do not vary very greatly between the two apparatuses, it is necessary to assess the role that mass transfer plays in determining the kinetics of the reduction reaction. This can be done by calculating the reduction rate in the reduction under load apparatus on the assumption that it is entirely mass transfer controlled and comparing this with the experimentally measured rate. The ratio between the two rates will indicate approximately the fraction of the overall resistance to the reaction that is contributed by the mass transfer process.

If the rate of reduction were controlled by mass transfer of hydrogen through a gas boundary layer it would be given by:-

$$\dot{n}_{\text{H}_2\text{O}} = A \frac{\alpha_1}{R\theta} \left\{ (P_{\text{H}_2\text{O}})_s - (P_{\text{H}_2\text{O}})_b \right\} \quad \text{----- (1)}$$

where \dot{n} = rate of molar transfer of H_2O from the surface of the pellet

α_1 = mass transfer coefficient

θ = Temperature K

A = the surface area of pellet

$(P_{H_2O})_s$ = partial pressure of H_2O at the surface of pellet

$(P_{H_2O})_b$ = partial pressure of H_2O in the bulk gas flow

The partial pressure of H_2O in the bulk gas phase is normally low and can be taken as zero. Hence equation (1) becomes:

$$\dot{n}_{H_2O} = A \frac{D_1}{R\theta} \left\{ (P_{H_2O})_{\text{equilibrium}} \right\} \text{-----} (2)$$

assuming the H_2O content of the gas at the pellet surface to have reached equilibrium with H_2 , FeO and Fe .

The rate of film mass transfer of H_2O at $1123^\circ K$ was calculated by substituting the values of the mass transfer coefficient K ($16.80 \text{ cm. sec}^{-1}$) and the values of $(P_{H_2O})_{\text{equilibrium}}$ in equation (2). The values of $(P_{H_2O})_{\text{equilibrium}}$ were calculated considering the equilibrium $FeO + H_2 \rightleftharpoons Fe + H_2O$ and assuming the total pressure $P = \left\{ (P_{H_2})_s + (P_{H_2O})_{\text{equil}} \right\}$ to remain constant at 1 atm. The thermodynamic data were drawn for this calculation from Kabaschewski and Alcock⁽⁹⁷⁾. The rate of reduction \dot{n}_{H_2O} was found to be $1.13 \times 10^{-4} \text{ g.mol. sec}^{-1}$. This calculated rate is some three times higher than the experimentally determined rate $3.28 \times 10^{-5} \text{ g.mol. sec}^{-1}$ for an undoped pellet during the first five minutes of reduction, suggesting that the resistance to mass transfer constitutes some third of the overall resistance to the reaction. This appreciable proportion of the overall resistance that is due to mass transfer occurs even though experiments carried out in the reduction under load apparatus were carried above the so-called "critical flow rate".

However, even during the first five minutes of reaction time, the bulk of the resistance to the reaction stems from processes that occur within the pellet. As the reaction proceeds further, the relative importance of these processes will increase so that gas phase mass transfer will play a less important role. Thus, overall, we would expect mass transfer in the gas phase outside the pellet to contribute no more than 10% to the total reduction resistance. Since the mass transfer coefficients in the two apparatuses are fairly close, we would not expect the difference that does exist to lead to significantly different total reduction times in the two apparatuses.

5.3 PRESENTATION OF THE RESULTS IN TERNARY DIAGRAM FORM

In this work, reduction properties of doped hematite pellets have been studied, the doping agents being lime, silica and alumina. The results have been presented in Section 4.5 in the form of graphs showing the variation of each measured property with changes in the content of one doping agent.

This form of presentation tends to obscure the effect of different combinations of doping agent content and it was therefore decided to present the data on ternary diagrams. Figures 5.1(a) and (b) show the two base diagrams that were used and show the compositions of the individual pellets or series of pellets that were studied.

Figure 5.1(a) shows the compositions of those pellets in which the basic hematite ore was doped with varying amounts of lime and silica. The iron-rich corner of the diagram contains the compositions

that were studied up to 5% CaO and up to 1% SiO₂. The 'iron oxide corner' of the diagram represents the composition of the original hematite ore less its lime and silica contents. Thus 100% 'Fe₂O₃' on the diagram represents 100% of the mixture: 99.46% Fe₂O₃, 0.24% Al₂O₃, the remaining 0.3% comprising MnO, P₂O₅, Cr₂O₃, V₂O₅, TiO₂, MgO.

Figure 5.1(b) shows the compositions of those pellets in which the original alumina content was increased to 1%. The 'iron oxide corner' of this diagram represents 98.7% Fe₂O₃, 1% Al₂O₃, the remaining 0.3% being as for Fig.5.1(a).

The reduction properties of the pellets are shown in Figs.5.2 and 5.4 in which the measured values of each parameter are entered on the diagram as spot values at the points representing the compositions of the pellets on which the measurements were made. The diagrams also show the estimated paths of isometric lines for each parameter each line linking compositions on the diagram where the parameter would have the same measured value. The paths of these isometrics have been drawn to be as consistent as possible with the spot values measured on the individual pellets.

The reducibility results are presented as the time in minutes for 95% reduction for pellets reduced in hydrogen and for the 'end' of reduction for pellets reduced in the hydrogen/carbon monoxide gas mixture.

Figures 5.2(a) and 5.3(b) show, respectively, the variation of reduction times for doped pellets at the two alumina levels, 0.24% and 1.0%. The isometrics in these figures show that an increase of lime content as the doping agent decreases the reducibility, but increases in silica and alumina contents increase the reducibility. There is also, however, a dip in reducibility curves at about 3 to 4% lime at the higher silica level.

The microstructures of partially reduced pellets at each composition were studied and it was observed that their reduction follows three different modes as given in Table 4.7 and Fig. 5.2(b). The isometrics in this figure show that the mode of reduction varies from homogenous to mixed mode and topochemical mode, with the increase of lime content as the doping agent, at low alumina content 0.24%. With the increase of lime as doping agent at 0.22% silica, the mode of reduction changes from homogenous to topochemical, but at a content of 1.0% silica the mode changes in sequence from homogenous to mixed mode and topochemical mode. On the other hand, at 1.0% alumina content, lime does not have any influence on the mode of reduction and all the pellet compositions studied are reduced by the homogenous mode.

The results of dimensional changes during reduction of doped hematite pellets are shown in Figs. 4.14-4.25 and the results of the important parameters based on these figures, i.e. peak expansion and terminal expansion values at various stresses are presented in the ternary diagrams shown in Figs. 5.2(c, d, e, f) and 5.3(b, c) for two alumina levels, 0.24% and 1.0% respectively. For the low

alumina pellets the values of peak expansion at the two stress levels, zero and 3.0 kg.cm^{-2} , are given in Figs.5.2(c), 5.3(b) and 5.2(d), 5.3(c) respectively. The isometrics in these figures shows that peak expansion increases with increase of silica and alumina contents in the doping agent and decreases with increase in lime content and stress. It was particularly noted that the decrease in peak expansion with increase of stress was more significant at those pellet compositions which exhibited high peak expansion.

The results for terminal expansion at zero and 3 kg.cm^{-2} are shown in Figs.5.2(e) and 5.2(f) respectively for low alumina pellets. The isometrics in Fig.5.2(e) show that an increase of lime content as the doping agent to pellets reduced at zero stress decreases the terminal expansion, whereas an increase in silica content increased the terminal expansion value. On the other hand, the isometrics in Fig.5.2(f) for a stress of 3 kg.cm^{-2} , show that an increase of silica content or a decrease of the lime content results in a decrease of the dimensional stability of iron oxide pellets and the high shrinkage encountered in some cases giving negative values for the terminal expansion. Corresponding ternary diagrams for the terminal expansion of the high alumina pellets could not be drawn because the results that had been obtained were inconsistent.

The isometrics in Fig.5.4 for the hydrogen/carbon monoxide gas mixture show that doping agents have a similar effect on reducibility as they have in pure hydrogen. Comparing the isometrics of Fig.5.2(a) and 5.4, it is observed that the times for 'end' of reduction in the hydrogen/carbon monoxide mixture are

higher than in the pure hydrogen. The extension of reduction time has been increased by a factor of 22-66%.

The isometrics in Fig.5.5(a) and (b) show the porosity variation for iron oxide pellets of varying composition. Fig.5.5(a) for low alumina pellets shows that porosity decreases with increase of lime up to 2% and then decreases with further increases of lime content. On the other hand, silica increases porosity at all lime levels studied. Figure 5.5(b) for higher (1%) alumina pellets shows that porosity continuously increases with increase of lime content with consistently higher porosity values than for the corresponding low alumina pellets.

5.4 THE DESIGNATION OF THE DIFFERENT REDUCTION MODES AND THEIR INFLUENCE ON DIMENSIONAL STABILITY

Section 4.8 in the results section showed that the reduction process in the pellets investigated occurred in one of three different modes - designated as topochemical, mixed mode and homogenous. As the description of the different modes suggests, their incidence is controlled by the different relative speeds of the reduction steps from hematite to magnetite and from wustite to iron. These relationships can be set out as:-

<u>Mode</u>	<u>Relative Rates</u>
Homogenous	$\dot{n}_{\text{Fe}_2\text{O}_3 \rightarrow \text{Fe}_3\text{O}_4} \gg \dot{n}_{\text{FeO} \rightarrow \text{Fe}}$
Mixed	$\dot{n}_{\text{Fe}_2\text{O}_3 \rightarrow \text{Fe}_3\text{O}_4} > \dot{n}_{\text{FeO} \rightarrow \text{Fe}}$
Topochemical	$\dot{n}_{\text{Fe}_2\text{O}_3 \rightarrow \text{Fe}_3\text{O}_4} \approx \dot{n}_{\text{FeO} \rightarrow \text{Fe}}$

The different reduction modes described by Wen⁽³⁵⁾, Turkdogan and Vinter⁽³⁴⁾ and Frazer et al⁽¹⁹⁾ resemble those identified in this work.

Wen⁽³⁵⁾ examined iron oxide pellets having a porosity 20-40%. These were observed to be reduced homogenously in the early stages but as the degree of reduction increased, the outer surface of pellets with a greater potential for reduction formed an iron layer, i.e. the reduction mode changed from homogenous to shrinking mode with reduction claimed to be controlled by gaseous diffusion through the iron layer. This mode seems quite similar to the homogenous mode as presently designated.

Turkdogan and Vinter⁽³⁷⁾ reduced hematite particles of different sizes in hydrogen and found three different modes of reduction. These were homogenous reduction and two different types of reduction which he called (a) topochemical and (b) mixed mode of reduction. Homogenous reduction he defined as that which takes place throughout the whole structure i.e. like the initial part of the presently found homogenous. They attributed the other two modes to the formation of layers of different products and distinguished 'topochemical' from 'mixed mode' on the basis of the location and extent of the nucleation of metallic iron. In 'mixed mode' iron is nucleated to a greater extent ahead the iron-wustite interface whilst in his 'topochemical mode' iron is nucleated only at the iron/wustite interface. These modes have points of similarity to the mixed mode and topochemical mode of reduction respectively of the present work.

Frazer et al⁽¹⁹⁾ identified only two modes of reduction, naming them non-topochemical and topochemical. He classified the reduction of pellets initially reduced throughout the whole volume of the pellet to magnetite, followed by reduction to iron only after substantial

reduction to magnetite and wustite as non-topochemical. On the other hand pellets exhibiting successive layers from the surface of iron, wustite and magnetite they classed as 'topochemical'. Such modes resemble homogenous and topochemical mode of the present work.

The relationship between the different reduction modes and the doping composition of the low alumina pellets is represented in the ternary diagram in Figure 5.2(b). A similar diagram is not shown for high alumina pellets because all such pellets reduced by the homogenous mode.

The ternary diagrams showing isometrics for 95% reduction time and for peak pellet expansions at initial loads of zero and 3 kg.cm⁻² are shown in Figs.5.2(a)(c) and 5.2(d). Comparison between these figures and Fig.5.2(b) shows that the reducibility of pellets decreases as the mode of reduction changes from the homogenous to the topochemical mode but the dimensional stability increases.

The dimensional stability of the pellets can be assessed in three ways. In the first place and obviously, the lower the expansion of the pellet during reduction, the higher will be its dimensional stability. It is thus the isometric curves in Figs.5.2(c) to (f) that should be considered in assessing the dimensional stability of the low alumina pellets. Similarly, Figs.5.3(b) and (c) should be considered for the high alumina pellets. In the main these figures show the dimensional stability of pellets to increase as the lime content increases and as the silica content decreases.

The influence of the higher alumina content is small. It increases dimensional stability at low lime contents, but decreases it marginally at high lime contents.

The isometrics for the terminal expansion of low alumina pellets at an initial load of 3 kg.cm^{-2} behave unusually. This is in part due to the negative expansion shown under these conditions at low lime contents followed by a slight prominence where the terminal expansion can rise as high as 2.0%. At low contents higher than some 2%, however, a large 'plateau' region is shown in which the terminal expansion is virtually zero.

The second indicator of dimensional stability is provided by comparison between the behaviour of the pellets at the two stress levels considered. The behaviour of the pellets showing high dimensional stability will be more or less independent of the initial stress level at which reduction took place. The use of this criteria as a method of assessing dimensional stability is restricted to the low alumina pellets, thus to comparisons between Figs.5.2(c) and (d) and Figs.5.2(e) and (f). Once again, we see that high dimensional stability is linked with high lime contents - when the lime content is about 4% the peak expansion of the pellets, for example, is almost independent of load. We also see that the large plateau region of almost zero terminal expansion that existed for pellets reduced under the initial load of 3 kg.cm^{-2} can also be discerned at zero stress, although it is of somewhat smaller extent. Moreover, terminal expansions at low lime contents behave in significantly different fashions at the low stress levels showing

that dimensional stability of these pellets is very poor indeed.

Considerable similarity exists between the shapes of the isometrics concerned with dimensional stability and the boundaries drawn in Fig.5.2(b) showing the compositional ranges in which the different modes of reduction have been observed. The similarity is certainly sufficient to support the conclusion that the topochemical reduction mode is linked to high dimensional stability during reduction.

The third criterion that can be used to assess dimensional stability is the tendency of the pellets to crack during reduction. This criterion, although not shown in ternary diagram form, also shows the link between the topochemical mode and dimensional stability. Table 4.7 presents the entire list of pellets that have been investigated in this work showing their mode of reduction and the degree of cracking. Without exception, the pellets that did not crack were those that showed the topochemical mode of reduction.

The conclusion that the topochemical mode is associated with high dimensional stability is in keeping with the conclusions of Frazer et al⁽¹⁹⁾ and of Granse⁽⁷⁶⁾. Frazer⁽¹⁹⁾ concluded that "the formation of a suitably thick outer layer of metallic iron during reduction is likely to produce resistance to further deformation" and Granse came to the same conclusion.

The full nature of the link between dimensional stability and the topochemical mode of reduction will be considered subsequently. For the moment, however, it is pertinent to note that the envelope

of porous iron that forms during the topochemical mode appears to allow the pellet as a whole to resist the effect of applied stress. The regions of the ternary diagrams in which the dimensional changes are independent of the level of the applied stress are those which the topochemical mode exists. In regions where reduction follows the homogenous mode, on the other hand, the dimensional changes at the two stress levels are significantly different. For the lowest lime contents, for example, pellets which react homogeneously show a terminal expansion of 3% at zero load but a terminal contraction of 4% at a load of 3 kg .cm⁻². It would appear that the iron envelope present in the topochemical mode is able to bear the applied stress without deformation.

Unfortunately, it would appear that the topochemical mode is also linked to low reducibility. Figure 5.2(a) shows the time taken for low alumina pellets to be reduced to 95%. As with the isometrics relating to dimensional stability, the isometrics on this diagram exhibit the same shape as the boundary showing the extent of the topochemical mode of reduction. The region of the diagram in which the topochemical mode exists, however, is the region in which long reduction times occur - in some cases as much as twice the reduction time for the undoped hematite.

The microstructural and composition factors that influence the mode of reduction will be considered further in the next two sections.

5.5 INFLUENCE OF DOPING AGENTS ON THE MICROSTRUCTURE OF THE SINTERED PELLETS

5.5.1 Identification of phases

The pellet microstructures examined in this work have been presented in Section 4.3. The pellets were examined by optical microscopy and the compositions of the phases involved determined by quantitative X-Ray energy dispersive analysis. Apart from hematite, the most prevalent phases were a range of calcium ferrites containing varying amounts of silica up to 13% and an iron calcium silicate phase. In addition, pure alumina and calcium aluminates were occasionally found in the high alumina pellets and some of the calcium ferrites found in these pellets contained dissolved alumina as well as silica.

Table 4.2 in the results section shows all the phase analyses that were obtained and Table 5.1 below groups those analyses in terms of the calcium ferrite which is closest to the determined phase composition. The first phase listed in the table, however, is one which has a composition that can be represented by $\text{CaO}(\text{Fe}_2\text{O}_3)_{3.5}$ so does not resemble a known calcium ferrite. It is a phase that has been recognised before, however, being reported by Ahsan et al⁽¹⁰⁾ as a calcium ferrite.

The second phase listed in the table is calcium di-ferrite $(\text{CaO}.2\text{Fe}_2\text{O}_3)$. Depending on the silica content of the pellet, this phase was found either with negligible silica content, or with appreciable silica contents up to 13% dissolved silica. An asterisk has been used in the table to denote these high silica phases. Moreover, the calcium di-ferrite phase was additionally

found to contain dissolved alumina in the high alumina pellets. Two asterisks have been used in the table to denote such phase compositions.

The presence of calcium di-ferrite in sintered iron ore pellets has been reported by a number of different authors^(12, 13, 14, 15, 16, 17). However, the binary lime-hematite phase diagram⁽⁹⁾ indicates that the di-ferrite should decompose at 1155°C to form hematite and the mono-ferrite. Moon and Walker⁽¹⁴⁾ and Lu et al⁽¹²⁾ suggested that the presence of the di-ferrite in pellets at room temperature is due to high pellet cooling rates that suppress its decomposition. As we will see later on, however, the results obtained in this work suggests a somewhat more complicated situation.

Calcium mono-ferrite ($\text{CaO} \cdot \text{Fe}_2\text{O}_3$) is the third of the phases listed in the table. It was only found in the low alumina pellets and so either contained negligible amounts of dissolved silica or dissolved concentrations of up to 13% (one asterisk). The presence of the mono-ferrite in sintered iron ore pellets has also been reported by many previous workers including Shehata et al⁽¹⁷⁾, Ahsan et al⁽¹⁰⁾ and Matsuno⁽¹¹⁾.

The fourth phase listed in the table is di-calcium ferrite ($2\text{CaO} \cdot \text{Fe}_2\text{O}_3$) although this phase was found only rarely and then principally in the high alumina pellets. The presence of this phase has also been reported by a number of previous workers, Shehata et al⁽¹⁷⁾, Ahsan et al⁽¹⁰⁾, Matsuno⁽¹¹⁾ and Mukherjee and Whiteman⁽²⁵⁾. The presence of CF_2^* has also been reported by Friel et al⁽¹⁵⁾ though

not designated separately from CF_2 . The presence of CF_2^{**} has also been reported by a number of workers including Ahsan et al⁽¹⁰⁾, Hamilton⁽²²⁾, Hancart⁽²⁴⁾, Coheur⁽²³⁾ and Mukherjee and Whiteman⁽²⁵⁾ who have all symbolised this phase as SFCA (silica ferrite of calcium aluminium). On the other hand Mamoru⁽²⁰⁾ has classified this phase simply as calcium ferrite.

The final phase in the diagram is a complex iron calcium silicate which has also been reported by previous authors Brill-Edward et al⁽⁷⁵⁾ and Kaneko and Narita⁽²¹⁾ and Turkdogan and Vinter⁽¹³⁾.

5.5.2 Incidence of phases

Not all the phases listed in the table were present in all the samples. Indeed, each phase was found to exist only within a definite range of pellet doping compositions although the ranges for the different phases overlap.

The ternary diagram shown in Fig.5.6(a) shows the composition ranges over which the different phases existed in the low alumina pellets. The only phase present at the lowest lime levels was hematite but calcium di-ferrite was to be found at the low silica levels at all lime concentration exceeding 1%. At the 1% silica level, however, the lime content that coincided with the appearance of the di-ferrite phase was some 2%. At this silica level, the first phase to appear within the hematite was the iron calcium silicate that existed at lime contents between 1 and 3%. At lime contents greater than 3% at this higher silica level, the calcium di-ferrite phase was found

to be the only phase present - at least until the lime content had risen to something approaching 5%.

Although calcium di-ferrite was found at the low silica levels as soon as the lime content exceeded 1%, it was found together with the complex calcium ferrite of composition $\text{CaO} \cdot (\text{Fe}_2\text{O}_3)_{3.5}$ and this complex phase persisted until the lime content had risen to something between 3 and 4%. In addition calcium mono-ferrite was found at these low silica levels once the lime content had exceeded about 2%. Indeed, the presence of the mono-ferrite in the high silica content pellets containing 5% lime, suggested that the range of silica levels over which the mono-ferrite can exist increases as the lime content increases.

In addition to these phases, and apparently unusually, di-calcium ferrite was found in one pellet containing 3% lime and 1% silica.

In the high alumina pellets, calcium di-ferrite was found to exist at all the doping compositions investigated and the only other ferrite observed was the di-calcium ferrite, once again a relatively rare occurrence and principally at low lime levels. At low lime and silica levels, pure alumina and calcium aluminate phases could be observed. The occurrence of these phases is shown in the ternary diagram shown in Fig.5.7(a).

Typical optical micrographs and scanning electron micrographs of the pellets are shown in Plates 4.1 to 4.6 and have been described in the results section of the thesis. The morphologies of the different

phases shown by these plates have also been found to be dependent of composition. Figure 5.6(b) shows how the presence of the different morphologies varies. At low lime levels, the phases other than hematite are rare and the hematite has an open porous structure. Plates 4.1 (pure hematite), 4.2 (low silica and 1% lime) and 4.11 (3% lime and 1% silica) show typical structures. Hematite is present alone in Plate 4.1 but Plate 4.2 shows a structure in which iron calcium silicate is also present and Plate 4.11 is taken in the region where these two phases are joined by calcium di-ferrite.

At higher lime levels and low silica levels, the porosity of the structure is still high but the pores are closed and the calcium ferrite phase are dense and tightly bound to the hematite grains - Plate 4.7 at 5% lime is an example showing the presence of both calcium di-ferrite and calcium mono-ferrite. At the higher silica level and high lime levels, the porosity is more open and linked, the ferrite phases having a needle-like structure. Plates 4.12 (at 4% lime) and 4.14 (at 5% lime) illustrate typical structures, calcium di-ferrite being present alone in Plate 4.12 but joined by the mono-ferrite in Plate 4.14.

Figure 5.7(b) shows how the morphologies of the high alumina pellets vary with composition. At low lime levels, the structure is an open porous structure and the phases, other than hematite, are globular in form, suggesting that they have been formed in the solid state. Certainly there is no phase present that has flowed in the molten state between separate grains under the action of surface tension. Plate 4-17 shows a typical structure and Plates 4.47 and 4.48 show X-Ray maps of the typical distributions of

aluminium and calcium. These maps show that the centre of the globular phases is alumina with calcium ferrite forming the outer layers. It is the abrupt and smooth outer demarcation of these outer layers that indicates that liquid calcium ferrites were not formed at the sintering temperature.

Plate 4.21 shows a pellet composition in the composition range where calcium di-ferrite and di-calcium ferrite are the phases other than hematite present in the high alumina pellets. At low silica levels and most lime levels, where the principal phase other than hematite is purely the calcium di-ferrite, the microstructure is extremely porous. At high silica levels and low lime levels it is the di-calcium ferrite that is formed. When this phase contains dissolved silica it has a porous structure (see Plate 4.19) but it has a dense structure in the absence of dissolved silica (see Plate 4.20). Only very rarely is there evidence in the microstructure of the high alumina pellets that a molten phase has been present in firing. This is probably the explanation for the high porosities of the high alumina pellets at all doping levels. Figure 5.5(b) for the high alumina pellets demonstrates that the porosities of the fired pellets increase with the level of doping agents. Comparison with Fig.5.5(a) for the low alumina pellets shows that the porosities of the high alumina pellets are very much greater than those of the low alumina pellets.

5.5.3 Comparison with previous work

A number of other workers have reported structures similar to those found in this work for the low alumina pellets.

Turkdogan and Vinter⁽¹³⁾ reported that lime added to iron ore reacted with the hematite to form calcium di-ferrite. This phase is fluid at the sintering temperature and the action of this fluid results in growth of the hematite crystals and the formation of faceted surfaces - a structure similar to that shown in Plate 4.6 in this work. He also reported that the calcium di-ferrite did not decompose to the mono-ferrite on cooling as the phase diagram would suggest. Indeed, Turkdogan and Vinter⁽¹³⁾ did not report the presence of the mono-ferrite at all, determining the presence of calcium di-ferrite by X-Ray crystal analysis. A similar result has been reported by Moon and Walker⁽¹⁴⁾ who used microprobe analysis to show that the di-ferrite formed at high temperature did not decompose to the mono-ferrite on cooling.

In high silica pellets Turkdogan and Vinter⁽¹³⁾ were unable to detect crystals of the di-ferrite and concluded that the silica reacted with the ferrite to form a glassy phase. Frazer et al⁽¹⁹⁾ reported very similar observations, X-Ray analysis of his high basicity pellets indicating the presence of crystalline di-ferrite but crystalline products of lime and silica being undetectable in the high silica pellets. Frazer et al⁽¹⁹⁾ also concluded that a glass was formed in the presence of silica.

The presence of mono-ferrite has been reported by Matsuno⁽¹¹⁾ whose investigation involved very much higher levels of lime and silica. Indeed his least doped pellets contained 10% of lime and silica and the first pellets to show the presence of the mono-ferrite had a composition of 20% lime and 10% silica. He reported, however, that

the mono-ferrite formed by solid state diffusion in pellets heated to temperatures below 1200°C but when the pellets were heated to higher temperatures, a liquid phase was formed which lead to calcium di-ferrite. The presence of the mono-ferrite was also reported by Shehate et al⁽¹⁷⁾ using X-Ray analysis of doped hematite pellets. They investigated pellets containing about 2.5% silica and from 1.0 to 5.0% lime and detected dicalcium ferrite and calcium diferrite as well. In the pellets that were acid, they reported the presence of calcium silicate glasses.

The occurrence of calcium mono-ferrite in the pellets investigated in this work appears, however, to be unusual. The fact that pellet ranges were also found in which the di-ferrite existed alone, together with the weight of previous evidence suggesting that the di-ferrite does not decompose on cooling, would suggest that the mono-ferrite found in this work had been present at the firing temperature. Indeed the binary/lime hematite phase diagram shows that liquid containing the mono-ferrite can exist on the lime rich side of the eutectic just as liquid containing the di-ferrite exists on the hematite side. The region of contact between a hematite grain and a lime grain at the firing temperature would thus contain both the mono-ferrite and the di-ferrite. The change that the di-ferrite would have to remain throughout the firing cycle would depend on the amount of lime present. In line with this, Fig.5.6(a) shows that the region in which the mono-ferrite has been found increases in size as the lime level is increased.

5.6 INFLUENCE OF THE MICROSTRUCTURE ON THE SPEED OF THE HEMATITE TO MAGNETITE REDUCTION AND HENCE ON THE REDUCTION MODE

Figures 5.2(a) and (b) show that the high rates of reduction in the low alumina pellets occurred in the regions where the reduction process took place by the homogenous mode. Movement across these ternary diagrams in the direction of longer reduction times is also a movement towards the composition ranges in which the reduction occurs in the topochemical mode.

Section 5.4 showed that the nature of the reduction mode appears to be determined by the relative speeds of the reduction steps from hematite to magnetite and from wustite to iron. In the homogenous mode, the first of these steps occurs very much more rapidly than the second. In the topochemical mode, on the other hand, the two reduction steps occur at very much the same speed. Since the change from homogenous to topochemical mode corresponds to reduction in overall reaction speed, it can be seen that the reduction in the speed of the hematite to magnetite reduction step must be even more marked. Indeed, it appears likely that it is the speed of this particular reduction step that is the factor that most principally controls the mode of reduction. A substantial reduction in the first reduction step appears to be required to change from the homogenous mode to the topochemical mode.

The speed of a gas/solid reaction is determined by the speed at which reactant and product gases can diffuse into the porous solid and by the intrinsic reactivity of the solid itself. Which of these two phenomena has the greater influence over the reduction

of hematite has been a matter of continuous debate over several years e.g. (33,34,37,39,40,41,45,46,). The current investigation suggests that the two phenomena can interact so that a clear distinction cannot, perhaps, be made between them.

The situation is complicated by the substantial volume change that occurs when hematite is reduced to iron - theoretically a reduction of 53% - and by the intermediate volume changes that occur as the intermediate oxides form. Using theoretical values of the specific volumes of the different materials⁽⁹³⁾ shows that 1 mole of hematite occupies 30.4 cm³ and that the magnetite, wustite and iron that this yields on reduction would occupy 29.8 cm³, 25.2 cm³ and 14.2 cm³ respectively at their theoretical densities. That the reduction of pellets is normally accompanied by some degree of expansion, or at least by minimal shrinkage, shows that the porosity of the pellets increases considerably during the reduction process. Moreover, the initial hematite pellets are themselves porous and the initial diffusion of gases into the pellets, at least to reduce hematite to magnetite, may be strongly influenced by this initial pellet porosity.

A clear connection cannot necessarily be drawn, however, between the porosity of pellets and the rates of gaseous diffusion into and out of the pellets. If, for example, a substantial proportion of the porosity is in closed pores, this porosity will not be available to the reactant gases from the outset. In addition, gaseous diffusion in iron ore pellets involves Knudsen diffusion⁽¹⁶⁾ and this diffusion process is influenced by the sizes of pores as well as by the overall porosity. If it is the reduced diffusion into the hematite pellets that explains the decrease in the hematite reduction rate with

increased lime contents in the low alumina pellets, it must be due to a considerable increase in the proportion of closed pores.

Figure 5.5(a) shows a ternary diagram showing the isometrics of low alumina pellets for overall fired pellet porosity plotted from the data shown in Fig.4.2. It can be seen that the shape of these isometrics shows no similarity with the shape of the isometrics for reduction time, reduction mode or percentage expansion. Moreover, after a rapid reduction in porosity in the 2% lime region, the porosity of the pellets consistently increases with subsequent increases in lime content. This increase in porosity occurs in the region where the overall reduction rate decrease and where, as inferred from the increased prevalence of the topochemical mode, the rate of the hematite to magnetite reduction step shows an even greater decrease. Thus the rate of this reduction step is decreasing as the initial pellet porosity increases.

It is possible, however, that the increased volumes of molten phases present at the firing temperature with increased lime content in the low alumina pellets result both in reduced pore sizes and in increased proportions of the porosity that is initially closed. Either of these processes would reduce the rate at which the hematite structure is reduced to magnetite and could therefore explain the increased prevalence of the topochemical mode. Plate 4.1 (the original hematite) and Plate 4.3 (2% lime low silica) show micrographs that indicate that such a change could take place in the nature of the porosity. However, as we will see below, increased prevalence of the topochemical mode tends to be associated with lower slag volumes rather than with higher slag volumes.

An important coincidence shown by the ternary diagrams throws further light on the influences that control the speed of the hematite to magnetite reduction and hence the reduction mode. Comparison of Figs. 5.2(b) and 5.6(a) shows that the topochemical mode of reduction only occurs in the low alumina pellets when calcium mono-ferrite is present in the structure. That a link exists between the topochemical mode and the presence of the calcium mono-ferrite is further supported by consideration of the high alumina pellets. None of the pellets was found to contain the mono-ferrite and they all reduce in the homogenous mode.

This link between the topochemical mode and the presence of calcium mono-ferrite shows that the topochemical mode is not associated with the larger slag volume. A given mass of lime will form a larger mass, and therefore volume of calcium ferrite if it forms the di-ferrite than if it forms the mono-ferrite. Thus regions on the phase diagrams in which mono-ferrite is formed are regions of low slag volume rather than regions of higher slag volume. That these are also regions in which the topochemical mode of reduction occurs tends to suggest that the topochemical mode is not associated with higher slag volumes.

That this is so is also supported by the effect of silica. The X-Ray energy dispersion maps, e.g. Plates 4.40 to 4.42, show that the silica in the high silica pellets is incorporated into the molten calcium ferrite phase at the firing temperature, thus increasing the volume of this molten phase. Figure 5.2(b), showing the incidence of the different reduction modes, shows that the

presence of increasing amounts of silica decreases the likelihood of the reduction process following the topochemical mode. Once again the topochemical mode is associated with the lower slag volumes.

This association of the topochemical mode with the presence of calcium mono-ferrite rather than with the presence of higher slag volumes suggests that it is not a reduction in gaseous diffusion rates as lime is added to the low alumina pellets that slow down the speed of the hematite to magnetite reduction step. It appears that the calcium mono-ferrite behaves in a way that calcium di-ferrite does not and the binary $\text{Fe}_2\text{O}_3/\text{CaO}$ phase diagram shown in Fig.2.2(b) suggests what this difference in behaviour may be. The diagram shows that the mono-ferrite is stable down to room temperature whereas the di-ferrite is unstable at temperatures below 1172°C . Under the oxidising conditions that exist in the normal firing of pellets the di-ferrite formed during sintering does not decompose on cooling which, of course, is the reason why it has been observed in fired pellets by so many different workers. Under reducing conditions, however, it is likely that the instability of the di-ferrite will have a significant effect on its reducibility. Thus it would be expected that the di-ferrite would be reduced more rapidly than the mono-ferrite and independent evidence exists to suggest that this is so. Asada, Omori and Sanbongi⁽⁵⁰⁾ studied the reducibility of different calcium ferrites determining reduction times for calcium mono-ferrite that were 35% greater than those for the di-ferrite. They also, incidentally, obtained reduction times for hematite that were 14% shorter than the corresponding reduction times for calcium di-ferrite.

The microstructure of the low alumina pellets containing lime and

silica (e.g. Plates 4.3, 4.5 to 4.7) show that the calcium ferrite phases surround hematite grains. These phases must therefore be reduced substantially before the reducing gases can contact the surface of hematite grains. The lower reducibility of the mono-ferrite suggests that this reduction would occur much more slowly for the mono-ferrite than for the di-ferrite and that the presence of the mono-ferrite would therefore lead to low rates of hematite reduction. As we have inferred previously, it is low rates of the initial hematite reduction step that cause the reduction process to adopt the topochemical mode.

At first sight it might appear contradictory that low, intrinsic rates of hematite reduction lead to the topochemical mode of reduction. It is normally inferred that low solid reactivity is associated with homogeneous reaction since unspent reactant gas can penetrate into the interior of the porous pellet allowing reaction to occur generally throughout the entire pellet. Topochemical behaviour, on the other hand, is normally considered to occur when the solid's intrinsic reactivity is high since the reactant gas is then used up before it can penetrate into the interior of the pellet. The reaction must therefore be concentrated into a narrow band or reaction front which separates reacted from unreacted material. However, the above arguments ignore the effect that the reaction rate can have on the structure of the porous solid.

Magnetite has a cubic crystal structure whereas hematite is hexagonal. It has been generally established^(e.g. 64, 65) that magnetite forms from hematite in such a way that the (111) planes of the magnetite are parallel to the (0001) planes in the hematite. The average spacings between oxygen atoms in the two structures are not, however,

equal so that considerable stress is developed in the lattice when hematite is converted into magnetite. This stress can either be relieved by solid state diffusion in the lattice or by the formation of massive cracks in the product magnetite grains. The faster magnetite is formed from the hematite, the less time will be available for stresses to be relieved by solid state diffusion and the more porous will be the magnetite that forms. Diffusion rates in through this highly porous magnetite will thus be very high and the subsequent reduction will tend to occur homogeneously.

It might be argued, however, that the porosity of the magnetite is not important since the subsequent diffusion processes are through wustite reduced from the magnetite or through iron reduced from that wustite. However, it is the reduction from hematite to magnetite that involves the major crystallographic change since both wustite and iron are cubic structures. Thus the formation of neither phase produces so much lattice stress as the formation of magnetite from hematite. This reaction therefore is all but entirely responsible for the structure that the pellets have throughout the remaining reaction time. High rates of magnetite formation would thus be associated with the creation of an open structure and therefore with high degrees of swelling. High gaseous diffusion rates will exist in the open structure thus leading to the homogeneous reduction mode.

When the magnetite is formed slowly, on the other hand, the stress in the magnetite lattice can be relieved by solid state diffusion, micro-cracks do not form, the gaseous diffusion rates are low and reduction occurs in the topochemical mode. Low rates of magnetite formation are associated with the presence of calcium mono-ferrite because its lower reducibility means that it exists in the pellet microstructure for a considerable time during reduction, impeding

the access that the reducing gases have to the hematite.

A similar effect of mono-ferrite has on hematite reduction has been reported by Brill-Edwards et al⁽⁷⁵⁾ who made pellets from hematite with mono-ferrite or iron calcium silicate added as a specific constituent before firing. These pellets were then subjected to compressive strength tests after through reduction to the different oxides. Pure hematite pellets and those containing iron calcium silicate showed brittle fracture behaviour. At temperatures above about 800°C, however, the pellets containing the mono-ferrite did not fracture but deformed plastically up to the 5% limit that was chosen by the authors as a limit to their experiments. These pellets also showed greater strength after reduction and swelled to a much lesser extent. Both these characteristics were explained by the authors in terms of the relief of transformation stresses by plastic flow in the mono-ferrite. This explanation is obviously very similar to that advanced here except that it is not obvious how plastic flow in the calcium ferrite slag phase can relieve transformation stresses at the hematite/magnetite interface due to lattice mismatch. The relief of such stresses can only be brought about by plastic flow in the magnetite or hematite phases as has been shown by the work of Swann and Tighe⁽⁷⁸⁾.

It is much more likely that the effect of the mono-ferrite is to slow down the rate of the hematite to magnetite reaction by impeding the access of gas to the boundary where that reaction is taking place. Once the rate of reaction has been reduced in this way, plastic flow and lattice diffusion in the magnetite phase will

have greater time to relieve the transformation stresses.

The effect of the plasticity of the mono-ferrite phase itself is more probably related to its own reduction. The more plastic is the mono-ferrite, the less will it be fractured during its own reduction and hence the longer will it be able to impede gas flow to the hematite grains.

Thus it is suggested that the mode of the entire pellet reduction process and thus the pellet's swelling characteristics are controlled by the speed of the hematite to magnetite reduction step. The effect on these characteristics that different constituents in the as-fired pellet microstructure have is related to their effect on gaseous access to the hematite/magnetite reaction zone. Mono-ferrite has a particularly marked effect because its thermodynamic stability and its plasticity give it greater permanence as a microstructural component during the reduction process.

This explanation is in keeping with the reduction characteristics of the high alumina pellets as determined in this work. The reduction process in these pellets always followed the homogeneous mode and was slowed relatively little by the addition of lime. Examination of typical microstructures of these pellets prior to reduction - Plates 4-17 to 4-24 - shows little evidence of the formation of a molten slag phase during firing. Only in plate 4-20 for the low silica pellet containing 4% lime is there any evidence of a molten phase and even then its volume fraction in the microstructure is extremely small. It appears that the incorporation of alumina raised the melting point of the slag

phases that form above the firing temperature thus prohibiting their flow through the structure. As a consequence, the calcium di-ferrite phases that do form containing silica and alumina take on a globular or acicular shape. The globular shape is shown in the calcium and aluminium maps obtained by X-Ray energy dispersive analysis shown in Plates 4-46 to 4-58 and the acicular form is shown typically in the optical micrograph in Plate 4-24. In all these cases, it can be seen that outer surfaces of the hematite grains are relatively little obscured by the non-hematite phase which contain the lime, alumina and silica. These latter phases thus have a small effect on the rate at which hematite is reduced to magnetite. The wustite that forms thus tends to be porous whatever the lime level so that the reduction process occurs homogeneously and rapidly.

This tendency is shown in detail by the 95% reduction time isometrics in Fig. 5.3(a) which demonstrate that the speed of reduction is relatively little affected by the level of doping. Only for the low silica pellet containing 4% lime has there been any effect. The lesser reduction rate that this pellet shows is in keeping with the small volume of molten slag formation that has taken place in the microstructure as shown in Plate 4-20.

Although the alumina/silica/calcium di-ferrite phase that forms in the high alumina pellets does not slow the hematite to magnetite reduction reaction sufficiently for the topochemical mode to occur, its presence in the microstructure obviously adds some strength. The peak expansion isometrics shown in Figs. 5.3(b) and (c) show the dimensional stability of the high alumina pellets to increase on doping, an initial change at low doping levels being followed by

relatively little subsequent alteration. It is apparent that the doping agents produce phases in the structure that strengthen the pellet whereas their low fluidity on firing allows the reduction process to occur rapidly. The reduction process is homogeneous, the pellets remaining highly porous and cracking during reduction.

Thus, this work has shown that it is the presence of a fluid slag at the firing temperature that slows the reduction rate sufficiently for non-cracking dimensionally stable pellets to be produced.

Although very few previous workers have isolated the effect of the mono-ferrite, a number have come to very similar general conclusions about the effect of slag constituents in the microstructure.

Turkdogan and co-workers⁽¹³⁾ showed that the addition of lime to hematite with and without silica lessened its reducibility and changes the reduction mode from homogeneous to topochemical. They attributed these changes to the blockage of pores in the hematite by molten calcium ferrites at the firing temperature. Similarly, Frazer et al⁽¹⁹⁾ attributed the topochemical mode of reduction in basic pellets to the presence of closed pores which he stated did not form in acid pellets.

A number of other authors have reported that the addition of lime, while lessening swelling, increase reducibility. The conditions in their experiments, however, cannot be easily compared with those in this work. Moon and Walker⁽¹⁴⁾, for example, varied the lime and silica contents of their pellets so that their total remained constant at 1.5% in one set and at 4% in a second set. The former set of compositions lie in the extreme right hand corner of the ternary diagram in Fig. 7.2 (a), where the result obtained in this work does not provide information on a fine scale, and the latter

set lie beyond the range of silica values studied. Furthermore, reduction was carried out under step wise composition changes either athermally or isothermally at 950°C - conditions that are significantly different from the isothermal reduction in pure hydrogen at 830°C used in this work. Shehata et alia⁽¹⁷⁾ also found that the addition of lime improved reducibility but in pellets that initially contained 2.5% silica as well as a range of other gangue impurities. Seth and Ross⁽⁴⁸⁾ also found that lime increased the reducibility of hematite pellets and showed that this improvement was paralleled by an increase in the porosity of the as-fired pellets. The compaction pressures that they used in their work were very much higher than those used in almost all other investigations and the pellet porosity was all uncharacteristically low - typical values in their experiments were some 7%.

Although no previous workers have discussed the effect of alumina content in the range cover here (0.24 - 1.0%), other workers including Bowling et al⁽⁵¹⁾ have reported that an increase of alumina from 2 to 4% has no influence on reducibility. Mazanek and Jasienka⁽²⁶⁾ reported that the reducibility of sinter containing 7.0% Al_2O_3 is lower than that of alumina-free sinter, but that the reducibility is higher at 12% Al_2O_3 . They attributed this effect to the varying reducibility of the minerals present, e.g. the high reducibility at 12% Al_2O_3 arises from the presence of $\text{CaO} \cdot \text{Al}_2\text{O}_3 \cdot \text{Fe}_2\text{O}_3$. Suzuki et al⁽⁵²⁾ have reported that addition of 5% coarse aluminium to hematite increases the reducibility but produces cracking during reduction.

From this work, and by inference from that of a number of other workers, it appears that microstructural components in hematite

pellets are effective solely through their effect on the speed of the hematite to magnetite reduction. If this is so, it would be expected that similar effects would result from alternate methods of controlling the speed of this reaction. Thus it would be expected that pellets reduced to magnetite at reduction potentials lowered to produce magnetite at slow controlled rates would show much less expansion and cracking and would also reduce in the topochemical mode. No systematic study of such an effect has been undertaken but a number of workers, principally Akitoshi⁽⁷⁰⁾, Brill-Edwards⁽⁷⁵⁾, Edström⁽³⁶⁾ and Surtees⁽⁷⁷⁾ have reported that pellet swelling is reduced when magnetite is produced slowly at reduction potentials lowered sufficiently to produce it as the only reduction product.

5.7 INFLUENCE OF DOPING AGENTS AND A HYDROGEN/CARBON MONOXIDE GAS MIXTURE ON REDUCIBILITY

The isometrics of Fig. 5.2(a) and Fig. 5.4 show that doping agents have a similar effect on reducibility in hydrogen/carbon monoxide gas mixture as they have on reducibility in pure hydrogen, i.e. reducibility decreases with increase of lime and increases with increase of silica.

Fig. 4-10 and 4-11 represents the reduction curves of doped hematite pellets in an H_2/CO gas mixture. These figures show that the reduction of some pellets appears to stop before 95% reduction, e.g. reduction of an initial hematite pellet (without any addition) appears to stop at 88% reduction. This apparent arrest of the reduction process results from carbon deposition, such deposition to be expected because freshly formed iron was a great potential

as a catalyst for carbon deposition. Carbon deposition is more pronounced with highly porous and less doped pellets, possibly because of their large surface area that is available for carbon deposition and because these pellets are heavily cracked during reduction providing more surface area available for carbon deposition.

Carbon deposition has already been reported by previous workers, e.g. Towhidi et al⁽⁴⁵⁾ and Geasy et al⁽⁶⁰⁾, who found respectively that the reduction of commercial pellets stopped slightly above 85% reduction in an equimolar hydrogen/carbon monoxide gas mixture at 780°C and at 800°C.

Due to carbon deposition it is difficult to estimate the influence that the reducing gas mixture has on the rate of reduction compared to pure hydrogen. This is because reducibility curves such as those shown in Fig. 4-10 and 4-11 have been determined from direct measurement on thermogravimetric spring balance, and do not indicate the balance between the weight reducing process of iron ore reduction and the weight increasing process of carbon deposition. However, if carbon deposition is ignored, and a comparison made between the time for the end of reduction in the gas mixture (see Fig. 5-4) and the time for 95% reduction in hydrogen (see Fig. 5.2 (a)), it can be deduced that reduction is slower in the gas mixture than in pure hydrogen. The comparison is influenced by the level of doping agent, i.e. the time for 88% reduction of commercial pellets in the CO/H₂ gas mixture is 66% higher than for 95% reduction in hydrogen, although for pellets with the maximum lime content, this difference is less than 22%.

This shows that the rate of reduction of the pellets in CO/H₂ gas mixtures was decreased by the addition of lime to a lesser extent

than the rate of reduction in pure H_2 . A full investigation of this phenomenon was not carried out because reduction under load experiments could not be carried out in CO/H_2 gas mixtures and because metallographic investigations were not carried out on the samples used in these experiments. However, the explanation advanced previously in this discussion that the reduction mode changes from homogeneous to topochemical as the rate of the initial hematite reduction reaction is decreased, is in keeping with these findings. The slower hematite reduction reaction that would occur would mean that the reaction in the undoped pellets was closer to the topochemical mode in the CO/H_2 mixture than in pure hydrogen. Thus the change in reduction mode and rate that would occur on doping would be less in the CO/H_2 mixture than in pure hydrogen.

Whether the experimental evidence gives strong support for this trend or not was obscured by the carbon deposition process that occurred more vigorously in the undoped pellets than in the doped pellets. For example, the undoped pellets cracked in the CO/H_2 mixture whereas the doped pellets did not. This observation in itself is in keeping with the trends discussed earlier for reduction in pure hydrogen since it would be expected that the undoped pellets would present a greater surface area for carbon reduction, the rapid hematite to magnetite reaction producing an open porous structure which, once reduced to iron, would provide a large surface area for carbon deposition.

The slower rate of reduction in CO/H_2 gas mixtures is due to the bigger CO molecules which cannot easily penetrate through the micropores. On the other hand, small hydrogen atoms can easily

penetrate into micropores and also hydrogen has a better absorption ability on oxides surfaces. The influence of CO/H₂ gas mixtures on reducibility has been mentioned by e.g. Towhidi et al⁽⁴⁵⁾, Al Geasy et al⁽⁶⁰⁾ and Mazanek et al⁽⁶³⁾ who have reported that the rate of reduction in CO/H₂ gas mixtures is less than in pure hydrogen, the decrease in rate depending on the proportion of the two gases.

5.8 INFLUENCE OF DOPING AGENTS ON THE REDUCTION PROPERTIES OF HEMATITE PELLETS REDUCED AT 850°C IN HYDROGEN

Some initial experiments have been carried out in which the reduction characteristics of hematite pellets were studied at 850°C. These experiments were carried out as part of the initial investigation aimed at determining the consistent conditions to be used for the bulk of the work. Thus the pellets used were fired at more than one temperature and at different times. No detailed discussion of the reduction characteristics determined at 850°C can thus be undertaken, it is merely pertinent to show that they are similar to those determined at 830°C.

The reducibility results, presented in Fig. 4-13 and Table 4.5, again confirm that reducibility decreases with increase of lime content and improves with increase in silica content.

The results of dimensional changes during reduction at 850°C of doped hematite pellets are shown in Fig. 4-24 and 4-25 and the parameter defining these changes, viz. peak expansion and terminal expansion values, are shown in Table 4-

It will be seen that the peak expansion value increases with

increase of silica content of the doping agents, decreases with increase in lime content, and decreases at higher stress. The results for terminal expansion at zero stress show that higher levels of doping with lime decreases the terminal expansion, whereas increased doping with silica raised the terminal expansion values.

As experienced with reduction at 830°C the influence of doping agents on the reduction properties can be related to the microstructure of original sintered pellets, and to the mode of reduction. Pellets undergoing reduction at 850°C follow two modes of reduction, viz. homogeneous and topochemical as described in Table 4-7. The influence of these modes on reduction characteristics is similar to that experienced at 830°C , i.e. pellets undergoing the homogeneous mode exhibit high reducibility and low dimensional stability, whilst those reduced in the topochemical mode show greater dimensional stability but less reducibility. The reasons for these relationships are believed to be similar to those given in Section 5.3 and 5.6 for reduction at 830°C .

5.9 RELEVANCE OF PRESENT FINDINGS TO INDUSTRIAL DR PROCESSES

In this work the influence of doping agents on the reducibility and dimensional stability of hematite pellets has been determined. These properties are most important for DR furnace operation. Reducibility is important because reduction takes place in the solid state at relatively low reduction temperatures to minimise cluster formation. However, this tends to result in inefficient use of reducing gases and lower productivity of the DR process. The tendency to cluster and the strength during reduction are also related to the dimensional changes which occur during reduction. It has been shown by

Wright⁽⁷²⁾ and Taniguchi et al⁽⁸²⁾ that pellets exhibiting high expansion characteristics are weaker both during and after reduction. On the other hand, as reported by Kaneko and Narita⁽²¹⁾, pellets with a high degree of contraction have a greater susceptibility to produce stable clustering which can cause a hanging problem, making it difficult to discharge the furnace.

Although experiments carried out on single pellets in a laboratory reactor cannot be directly related to behaviour in an actual DR furnace, considerable understanding can be developed. In DR furnaces iron oxide pellets undergo drying, preheating and reduction with temperature, gas composition and stress all varying from the top of the furnace to the reduction zone. The main part of the present work was carried out at constant temperature of 830°C in hydrogen at stresses varying between zero and 3 Kg.cm⁻² together with a limited number of reduction tests in a mixture of carbon monoxide and hydrogen. Such conditions resemble those under which iron oxide pellets are reduced in different locations in the Midrex and HyL reduction units.

The reduction properties of doped hematite pellets as determined in the present work are summarised in Fig. 5.2 and 5.3 at two alumina levels, 0.24 and 1.0% respectively. Values for dimensional changes and degrees of reduction for pellets reduced by hydrogen at 830°C are shown in these figures, from which it will be seen that expansion values increase with increasing reducibility. Most of the published work has stipulated that adequate pellet strength in the DR process is obtained where pellet expansion is less than 20% by volume (28, 57, 72, 82). Assuming expansion to be uniform in all directions this would correspond to linear

expansion values of about one third of this value, i.e. less than about 6.7%. Except for one with a value of 8.4%, all the pellets tested satisfy this criterion for the conditions stated.

Accordingly, all those pellets which did not crack heavily during reduction are acceptable, preferably those with high reducibility.

On an industrial scale, one of the most important properties of DRI required is high strength to resist handling stresses during transportation and the loading stresses to which the pellets are subjected during charging and melting in the EAF process. It has been shown by Wright⁽⁷²⁾ and Taniguchi et al⁽⁸²⁾ that metallized pellet strengths are closely related to the volume change undergone by the pellet during reduction: the lower the volume expansion or greater the contraction, the higher is the final metallized pellet strength.

It has been reported⁽²⁹⁾ that DR plants, e.g. Midrex and HyL accept iron oxide pellets with a maximum gangue content ($\text{Al}_2\text{O}_3 + \text{SiO}_2$) of 3%. Such limitation on gangue content is due to the associated increased energy consumption in DR processes and electric arc furnaces (EAF) resulting from the presence of gangue. In the EAF energy consumption depends upon the amount of DRI used as a charge material and also on the content and type of gangue present. The more acid the gangue is, the more lime is needed to give a slag basicity in the range 1.5-2.0, thereby increasing the amount of slag and energy required. Figs. 2.4 and 2.5 show the increase of slag weight and energy consumption respectively with variation in gangue content and composition of metallized pellets.

The work presented in this thesis suggests that the greater dimensional stability of iron oxide pellets is associated with the topochemical mode of reduction. Unfortunately, this mode of reduction has an adverse effect on reducibility. On the other hand, greater reducibility is associated with the homogeneous mode of reduction but with less dimensional stability.

Bearing in mind the requirements of DR processes and suitable specifications for the DRI product, it has been possible to deduce the likely acceptability of a range of pellets tested. The following table has been drawn up, classifying the acceptability or otherwise of a range of pellets based on the following specification for expansion characteristics and reducibility :

Maximum peak expansion : 3% at 3.0 Kg.cm⁻²
 Terminal expansion : -0.7 to 0.7% at 3.0 Kg.cm⁻²
 Average rate of reduction : > 5% min.⁻¹
 (thermal balance test)

Sample Designation	% Composition			Reducibility	Peak Expansion*	Terminal Expansion*
	CaO	SiO ₂	Al ₂ O ₃			
Al ₃	2.0	0.22	1.00	✓	✓	✓
Al ₄	4.0	0.22	1.00	x	✓	✓
Al ₈	4.0	1.00	1.00	✓	✓	✓
C ₃	1.0	0.22	0.24	✓	✓	✓
E ₃	2.0	0.22	0.24	✓	✓	✓
F ₃	3.0	0.22	0.24	x	✓	✓
G ₃	4.0	0.22	0.24	x	✓	✓
H ₃	5.0	0.22	0.24	x	✓	✓
F ⁺	3.0	1.00	0.24	x	✓	✓
G ⁺	4.0	1.00	0.24	x	✓	✓
H ⁺	5.0	1.00	0.24	x	✓	✓

✓ = within specification
 x = outside specification

* at 3.0 Kg.cm⁻²

This table suggests that only four pellets (Al_3 , Al_8 , C_3 and E_3) fulfil all these requirements. However, due to their cracking during reduction and their porous nature, all except E_3 are not suitable to transport over long distances because of disintegration and reoxidation. These are only acceptable if used at the same place since such use would minimise the handling they received. Furthermore, the gangue content of pellet Al_8 is high so that its use in electric arc steelmaking would result in inefficient power utilisation.

CHAPTER 6 - CONCLUSIONS AND SUGGESTIONS
FOR FURTHER WORK

CONCLUSION

In the present investigation, the influence of doping agents on the microstructure of iron oxide (hematite) pellets and on their reduction properties (reducibility in H_2 and a $CO + H_2$ gas mixture, and dimensional stability in hydrogen) has been examined. The main conclusion of this work stems from the different modes of reduction that have been recognised.

- (i) Three different modes of reduction in hydrogen have been identified, viz. (i) Homogeneous Mode, (ii) Mixed Mode and (iii) Topochemical Mode. These modes have been related to the doping composition of the pellets and their resulting microstructure.
- (ii) The dimensional stability of iron oxide pellets is related to the mode of reduction. The topochemical mode of reduction offers the greatest dimensional stability. Dimensional stability in general decreases from the topochemical mode of reduction through the mixed mode to the homogeneous mode of reduction. On the other hand, reducibility is increased from the topochemical mode through the mixed mode to the homogeneous mode.
- (iii) The addition of lime as a doping agent decreases the reducibility and increases dimensional stability. On the other hand, increase of silica and alumina increases the reducibility and decreases the dimensional stability.

- (iv) Carbon deposition as a soot was observed when a carbon monoxide-hydrogen gas mixture was used. The reduction rate was found to be slower using this gas mixture than pure hydrogen.

SUGGESTIONS FOR FURTHER WORK

- (1) It would be useful to dope hematite pellets with 0.5% silica and 0.5% alumina at similar lime levels in order to investigate whether the mode of reduction is affected and what effect this has on the reduction properties and also to confirm the consistency of isometrics for each measured parameter.
- (2) In this work, the main reduction experiments were carried out at 830°C; it would be valuable to work over a range of slightly higher temperatures so that an even closer relationship to industrial DR processes could be investigated.
- (3) It would be interesting to modify the platens in the reduction under load apparatus in order to reduce two cylindrical pellets in contact under load with a view to investigating their sticking properties.
- (4) It would be useful to investigate more fully the effects of various sintering times and temperatures for a similar doping range in order to examine

whether different phases and morphologies could be produced and then to investigate their influence on reduction properties.

- (5) It would be interesting to measure the effect of different doping agents on gaseous diffusion rates in reduced and unreduced pellets, in order to investigate the extent to which gaseous diffusion characteristics control pellet reducibility.

REFERENCES

- 1 - Darken L. S., Gurry R. W., J. Am. Chem. Soc. 68, 1946, P.798
- 2 - Abouzeid A. Z. M. and Seddik A. A. "Effect of Iron Ore Properties on its Balling Behaviour" Powder Tech. 29 (1981) P.233-241.
- 3 -- Filton J. T. and Goldering D. C. "Constitution of Iron Ore Pellets in Relation to Time and Temperature of Firing" JISI May 1966 P.452.
- 4 - Traice F. B. and Lappin R. L. "Survey of Modern Pelletizing Techniques" Special Report BSC General Steel Division.
- 5 - Sandoval J. A. et al "Method of Reducing Iron Ore Background of the Invention" U.S.A. Patent No. 3957486 18th May 1976.
- 6 - Urich D. M. and Tsu-Ming Han. Agglomeration P.669-714, Interscience, New York, 1962.
- 7 - Ball D. F., Filton, J. T., Dawson P.R. and Goldring D. C. "Effect of Additives on the Strength of Fired Iron Ore Pellets". Inst. Mining and Met. March 1947. C.47.
- 8 - Strathmore R. B. Cooke and Thomas E. Ban "Microstructure in Iron Ore Pellets". Tran. AIME November 1952 Mining Engineer P.1052.
- 9 - Philips B. and Muan A. "Phase Equilibria in the System CaO- Iron Oxide-SiO₂ in Air". Journal American Ceramic Society, 42, 1959. P.413-423.
- 10 - Ahsan S. N., Mukherjee T. and Whiteman J. A. "Structure of Fluxed Sinter". Iron Making and Steel Making, 1983, Vol.10 No.2 P.54-64.
- 11 - Matsuno F. "Changes of Mineral Phases During the Sintering of Fe₂O₃-CaO-SiO₂ System". Transactions ISIJ, Vol.19, 1979. P.595-604.

- 12 - Lu W. K., Hegde V., Trofimov V. and Lu Yang "The Quality of Iron Ore Pellet". Ironmaking Proc. Vol.40. Canada 1981.
- 13 - Turkdogan E. T., Vinter J. V. "Reducibility of Iron Ore Pellets and Effect of Addition". Canadian Meta. Quar. Vol.12 No.1 (1973) P.9.
- 14 - Moon J. T. and Walker, R. D. "Swelling of Iron Oxide Compacts During Reduction". Iron Making and Steel Making (Quarterly) 1975 No.1 P.30.
- 15 - Friel J. J. et al "Chemistry and Reduction Characteristic of Dolomite Fluxed Magnetite Pellets". Met. Trans. B. Volume 11B June 1980 P.233.
- 16 - Staia M. H. Ph.D. Thesis 1983.
- 17 - Shehata K. A., El-Geasy A. A. and Nasr M. J. "Binding Phases in El-Gedida Iron Ore Pellets". Iron and Steel International February 1982 P.46.
- 18 - Kuni, K., Nishida R. and Koizumi. Cited by Ref. No.12.
- 19 - Frazer F. W., Westenberger H., Boss K. H. and Thumm W. "The Relationship Between Basicity and Swelling on Reduction of Iron Ore Pellets". International Journal of Mineral Processing 2 (1975) P.353-365.
- 20 - Mamoru Onoda, Osamu Tsuchiya "Quality Improvements on Lime-Fluxed Pellets".
- 21 - Kaneko D., Narita K. "Evaluation of Raw Materials for Gaseous Direct Reduction Processes" SEAIQI Quarterly January 1979.
- 22 - Hamilton J. D. G. "Constituents of Bond Development in Hematite Ore Pellets Fluxed with Lime Sand". Journal of Mining and Metallurgy. March 1976 C30.
- 23 - Coheur P. "Continuous Quality Control of Dwight-Lloyd Sinter". Journal of the Iron and Steel Institute. October 1969. P.1291-1297.
- 24 - Hancart et al cited by Ref.23.

- 25 - Mukherjee T. and Whiteman J. A. "Structure of Fluxed Sinter".
Centenary Conference - Department of Metallurgy, University
of Sheffield. 16th - 18th July, 1984.
- 26 - Mazanek E. and Jasienska S. "Effect of Al_2O_3 on the Mineral
Constituents of Self-Fluxing Sinters". Journal of the Iron
and Steel Institute. April 1964. P.319-324.
- 27 - Gare T. et al "A Review of the Fundamental Studies into the
Gaseous Direct Reduction of Iron Ores". Private report.
- 28 - Stephenson R. L. "Direct Reduced Iron Technology and Economics
of Production and Use". 1980
- 29 - Davis C. G., McFarlin J. F. and Pratt H. D. "Direct-Reduction
Technology and Economics". Iron making and Steel making 1982.
Vol.9 No.3.
- 30 - Rual Quintero "Operational Results of HyL 111 Process".
Iron Making Proceedings, Vol.40. Toronto, Ontario, Canada 1982.
- 31 - Rigaud M., Marquis A. H. and Dancy T. E. "Electric Arc Furnace
Steelmaking with Pre-reduced Pellets". Iron making and Steel
making 1976. No.5 P.366-372.
- 32 - Davison J. "Burden Testing and its Application to Blast Furnace
Operation". JISI February 1973. P.106-114.
- 33 - Bogdandy Von L., Engel H. J. "The Reduction of Iron Ores".
Revised and English translation edition. Springer-Verlag,
Berlin 1971.
- 34 - Turkdogan E. T and Vinter J. V. Metallurgical Trans:2, 3175 (1971)
- 35 - Wen C. Y. Ind. Eng. Chem. 60 ,34 (1968)
- 36 - Edström J. D. "The Mechanism of Reduction of Iron Oxides"
Journal of Iron and Steel Institute. November 1953. P.289.
- 37 - McKewan W. M. Trans MS-AIME (1060) Vol.218 P.2-6
- 38 - Wright J. K. "The Reduction of Iron Ore Pellet-bed with
Gaseous Reductants". The Aus. I.M.M. Newcastle and District
Branch, Pellets and Granules Symposium October 1979. P.121.

- 39 - Seth B. B. L. "Kinetics of Hydrogen Reduction of Ferric Oxide Briquettes". JISI August 1969. P.1104-1109.
- 40 - Warner N. A. "Reduction Kinetics of Hematite and the Influence of Gaseous Diffusion". Trans. of Metallurgical Society of AIME Volume 23, February 1964. P.163-176.
- 41 - Hills A. W. D. "Role of Heat and Mass Transfer in Gas-Solid Reactions Involving Two Solid Phases within Sintered Pellets". Proceedings of a symposium held by the John Percy Research Group in Process Metallurgy. Imperial College, London 19th and 20th April, 1966.
- 42 - Harrington M. J. PhD. Thesis 1972.
- 43 - Ranz W. E. and Marshall W. R. Chem. Eng. Prog. 48, 141 (1952).
- 44 - Rao Y. K. and Moynpour M. "Kinetics of Reduction of Hematite with Hydrogen Gas at Modest Temperature". Metallurgical Transactions B. Volume 14B December 1983 P.711-723.
- 45 - Towhidi N. and Szekely J. "Reduction Kinetics of Commercial Low-Silica Hematite Pellets with CO-H₂ Mixture Over Temperature Range 600 - 1234°C". Iron making and Steel making 1981. Nov. P.237.
- 46 - Olsen and McKewan Trans: Metl Society AIME, 236, 1966, P.1518.
- 47 - Ross et al -Blast Furnace Coke Ovens, Raw Material Proceedings. AIME 20. P.266-279, 1961.
- 48 - Seth B. B. L. and Ross H. U. "The Effect of Lime on the Reducibility of Iron-Oxide Agglomeration". Canadian Metallurgical Quarterly Vol.2, No.1 Jan-Mar 1963 P.15.
- 49 - Mazanek E. and Jasienka S. "The Mineralogy and Reducibility of Self-Fluxing Sinter". JISI, 1963, 201, P.60-67.
- 50 - Asada et al Trans ISIJ, 1968, 8. P.245-250.
- 51 - Bowling K. McG. and Carter N. B. "Chemical and Physical Variables Affecting Iron Ore Pellets Properties". Australia Japan Extractive Metallurgy Symposium. Sydney, Australia 1965. P.361.

- 52 - Suzuki S., Sayama S. and Nishisha K. "Expansion and Contraction During Hydrogen Reduction of Green and Pre-heated Hematite Compacts Containing Foreign Oxides". Transactions ISIJ Vol.21 1981 P.870-878.
- 53 - Basu S.N. and Ghosh A. "The Influence of Porosity on the Kinetics of Reduction of Hematite by Hydrogen". JISI August 1970 P.765.
- 54 - Brill-Edwards H. et al "Structural Changes Accompanying the Reduction of Polycrystalline Hematite". JISI April 1965. P.361
- 55 - Joseph T. L. Trans AIME (1936) Vo.120 P.72-98.
- 56 - Wright J. K. "Swelling of High Grade Iron Ore Pellets Reduced by Hydrogen in Fixed Bed". Proc: Australias Inst:Min. Metall. No.265, March 1978. P.1-7.
- 57 - Wright J. K., Morrison A. L. "Volume and Structural Changes Occurring during the Isothermal and Non-Isothermal Reduction of High Grade Hematite Pellets". Australia Japan Extractive Metallurgy Symposium, Sydney, Australia 1980. P.167.
- 58 - Henry U. Ross and Anatoly N. Pyricov. "The Agglomeration of Iron Ore Materials and their Behaviour during Reduction". Agglomeration 1977.
- 59 - Shehata K. A. et al "Study of the Final Stage of Reduction of Iron Oxides". Inst. Mining and Met. March 1973 (38).
- 60 - Geassy A. A. El et al "Mechanism of Iron Oxide Reduction with H_2/CO Mixture". Transaction JISI, Vol.17, 1977 P.629.
- 61 - Wiberg, M. Discussion of the Faraday Society No.4 (1948) P.231-233.
- 62 - Nixon I. G. "Relationship between Degree of Reduction of Iron Ore and Operating Variables". Iron making and Steel making 1980. No.1 P.2.
- 63 - Mazanek E., Jasienska S., Brachucy A., Bryk C. A. "The Influence of Hydrogen in Gas Mixture of H_2 and CO on the Dynamic of the Reduction Process". Metallurgia 1 Odlenictwo-Tom 8 - Zeszyt 1 - 1982.

- 64 - Bleifuss R. L. "Volumetric Changes in the Hematite Transition Related to the Swelling of Iron Ores and Pellets During Reduction". Proceedings ICSTIS 1971 P.52-56.
- 65 - Walker R. D., Ford N. S. and Carpenter D. L. "Structural Changes in Iron Oxide During Reduction by Carbon Monoxide". Proceedings ICSTIS Supl. Trans: ISIJ Vol. 11, 1971, P.473-477.
- 66 - Bleifuss R. L. "Calcium as a Cause of Catastrophic Swelling of Pellets During Reduction". Society of Mining Engineers AIME Transaction Vol.247 September 1970. P.225.
- 67 - Fuwa T. and Shiro-Ban-ya "Swelling of Iron Ore Pellets During Reduction". Transactions ISIJ, Vol.9, 1969, P.137.
- 68 - Ponghis N. et al "Degradation of Iron Rich Pellets During Reduction". Iron Making Proceedings 1967. P.146.
- 69 - Kortman H. A. et al "Effect of Lime Addition upon the Behaviour During the Reduction of Iron Ore Pellets". Society of Mining Engineers. AIME Trans Vol.254, June 1973, P.184.
- 70 - Akitoshi Ishimitsu "On the Swelling of Pellets During Reduction". Tetsu-to-Hagane Overseas, Vol.5, No.3, September 1983.
- 71 - Chang M. C., Vlnaty J. and Kestner D. W. "North American Pellet-Swelling Characteristics During Reduction". Iron making Proceedings 1967, P.140.
- 72 - Wright, J. K. "Swelling of High Grade Iron Ore Pellets Reduced in a Fixed Bed Under Isothermal and Non-Isothermal Conditions". Transaction ISIJ, Vol.17 1977, P.726.
- 73 - Borje Bjorkval and Gunnar Than "Test Methods for Agglomerated Products". Part III. Scandinavian Journal of Metallurgy. 1 (1973). P.157-158.
- 74 - Borje Bjorkval, Cyrill Schaub and Gunnar Thaning "Test Methods for Agglomerated Products". Part IV. Scandinavian Journal of Metallurgy. 1 (1972). P.293-294.

- 75 - Brill-Edwards H., Stone H. E. N. and Daniell B. L. "Effect of Structural Changes on the Reduction Strength of Compacted and Sintered Hematite". JISI, December 1969, P.1565.
- 76 - Granse L. "The Influence of Slag Forming Additions on the Swelling of Pellets from Very Rich Magnetite Concentrates". Proc. ICSTIS, Suppl. Trans Japan, 1971, 11, 45.
- 77 - Surtees N. et al "Effect of Reduction Rate on the Swelling and Cracking of Some Commercial Hematite Pellets". JISI July, 1970, P.609.
- 78 - Swann P. R. and Tighe N. J. "High Voltage Microscopy of the Reduction of Hematite to Magnetite". Metallurgical Trans B. Volume 8B, September 1977. P.479.
- 79 - Linder R. Journal of Iron and Steel Institute 1958. 189, 233-43.
- 80 - Thanning G. "Reduction Strength of Super Fluxed Pellets Made from Rich Magnetite Concentrate". Iron making and Steel making. 1976, No.2, P.57.
- 81 - Taniguchi et al "Influences of Reduction Temperature and Porosity on the Swelling Behaviour of Pure Hematite Pellets During Reduction". Presented at the One Hundredth ISIJ Meeting, October 1980. Lecture No.5610.
- 82 - Taniguchi et al "Influence of Structural Changes and Swelling During Reduction upon Crushing Strength of Metallized Pellets". Trans: ISIJ, Vol. 18, 1978. P.633.
- 83 - Taniguchi et al "Structural Changes of Hematite Grains Composing Self-Fluxing Pellets During Hydrogen Reduction". Trans. ISIJ Vol.20, 1980, P.753.
- 84 - Lu W. K. "On the Mechanism of Abnormal Swelling During Reduction of Iron Ore Pellets". Scandinavian Journal of Metallurgy 3 (1974) P.49-55.

- 85 - Heinrich, Kortman A. and Burghardt O. P. "Test Methods for Evaluating Iron Ores, Pellets and Sinters". Agglomeration 77.
- 86 - Stalhede Medd Jerkn. Tekn. 1955, 18, 415-458.
- 87 - O. P. Burghardt and Grebe K. "Study of the Mechanical Behaviour of Iron Ores and Pellets under Isothermal Reduction Conditions". Stahl und Eisen, 89, 561.73. 1969.
- 88 - Russ J. L. and Fine M. M. "Physical Strength of Iron Ore Pellets at Elevated Temperature". Private communication.
- 89 - Thaning G. "Testing of Reduction Strength of Iron Ore Pellets". Private communication from Royal Institute of Technology Division of Mineral Processing, Stockholm.
- 90 - Wahlster M. Krupp Technical Information 1961, 19, No.1.
- 91 - Pepper M. D. and Daniell B. L. "Changes in Compressive Strength and Volume Associated with the Reduction of Iron Ore Compacts". JISI, June 1970, P.553.
- 92 - Szekely J. and Tawil Y. El "The Reduction of Hematite Pellets with Carbon Monoxide-Hydrogen Mixture". Metallurgical Transaction Volume 7B, September 1976, P. 490.
- 93 - Handbook of Chemistry and Physics 1972-1973.
- 94 - Geiger G. H. and Poirer D. R. - Transport Phenomena in Metallurgy, Addison Wesley Publishing Co., 1973.
- 95 - Spiers H. M. Technical Data on Fuel, 1962, P.159.
- 96 - International Critical Tables V.3 P.208.
- 97 - Kubaschewski O. and Alcock C. B. Metallurgical Thermochemistry 5th Edition, Pergamon Press, New York, NY, 1979. P.378-84.
- 98 - Fuller E. N., Schettler P. D. and Gidding J. C. - Ind. Eng. Chem 58, (5), 1966.
- 99 - Hirschfelder J. O., Curtis C. F. and Bird R. B. - Molecular Theory of Gases and Liquids, Wiley, N.Y. (1956).

APPENDIX 1

DETERMINATION OF THE TRUE DENSITY OF THE IRON ORE CONCENTRATE

The true density of iron ore concentrate supplied by British Steel Corporation (Teesside Division) was determined by the specific gravity bottle method, using the following procedure and giving the stated results:

- (1) the density bottle was oven dried,
- (2) the bottle was weighed in air (A g),
- (3) the bottle was filled with distilled water and reweighed (B g)
hence the weight of the contained water (B-A)g,
- (4) the bottle was again oven dried, a known mass (xg) of concentrate added, and filled with water.

The total weight of bottle + ore + water = y g. Hence the weight of water in the (partially filled) bottle
= y - (A + x) g.

Therefore the weight of water displaced by the mass of concentrate
= (B - A) - [y - (A + x)]
= B - y + x g.

Therefore the true density of concentrate =

$$\frac{x}{\frac{B - y + x}{(P_w)_{20^\circ C}}} = \frac{x (P_w)_{20^\circ C}}{B - y + x} \quad \text{----- (1)}$$

The true density of iron ore concentrate was calculated by determining the values of A, B, x, y for use in equation (1). The values obtained were:

A = 23.3755 g, B = 72.8715 g, x = 4.0 g and y = 76.092 g.

The density of water at ambient temperature of 20°C is considered to
to be 0.9983 g.cm⁻³⁽⁹³⁾. Hence true density of iron ore concentrate is:

$$\frac{4 \times 0.9983}{72.8715 - 76.092 + 4.0} = 5.12 \text{ g.cm}^3$$

CALCULATION OF THE DIFFUSION COEFFICIENT IN BINARY GAS MIXTURE

It has been necessary to find a value for the diffusion coefficient

$D_{H_2 - H_2O}$ at 1123 K in order to determine the corresponding mass transfer coefficient ($k_{H_2 - H_2O}$).

The value in this work has not been determined experimentally but has been calculated from theoretical equation developed by Fuller et al⁽⁹⁸⁾, which is based on the kinetic theory of gases. They developed the following relationship for the binary diffusion coefficient D_{A-B} for the gas pair AB:

$$D_{A-B} = \frac{T^{1.75} \times 10^{-3}}{P (V_B^{1/3} + V_A^{1/3})^2} \sqrt{\frac{1}{M_A} + \frac{1}{M_B}} \quad (1)$$

where: T = temperature (K)

M_A and M_B = molecular masses of the two species A and B

P = Total pressure

V_A and V_B represents the diffusion volumes given for simple molecules.

Using this relationship they were able to predict the binary diffusion coefficients D_{AB} to within 10% of the measured values for most cases considered.

Equation (1) has been used in the present work to calculate the binary diffusion coefficient $D_{(H_2 - H_2O)}$ at different temperatures. These values, using values of V_{H_2} and V_{H_2O} equal to 7.07 and 12.70

respectively and values for M_{H_2} and M_{H_2O} of 2 and 18 g.mol⁻¹ are presented in Table .

Temperature K	* $D_{H_2 - H_2O}$ cm ² .sec ⁻¹
900	6.098
973	6.98
1000	7.34
1073	8.29
1100	8.66
1103	8.70
1123	8.9833
1173	9.6997
1200	10.088
1273	11.18

* The values of $D_{H_2 - H_2O}$ was calculated for 1 atm pressure

APPENDIX 3

CALCULATION OF THE KINEMATIC VISCOSITY OF GASES

The kinematic viscosity is a fundamental quantity which is a measure of momentum diffusivity. Kinematic viscosity is defined as the viscosity of a fluid divided by its density:

$$\nu = \frac{\eta}{\rho} \quad \text{-----} \quad (a)$$

where: ν = kinematic viscosity cm^2/s

η = viscosity $\text{g}/\text{cm} \cdot \text{s}$

ρ = density g/cm^3

The viscosity of a single, non-polar gas at low pressure is given by the equation developed by Chapman and Enskog⁽⁹⁹⁾ using the Lenard-Jones potential:

$$\eta = 2.67 \times 10^{-5} \frac{\sqrt{MT}}{\sigma^2 \Omega_n} \quad \text{-----} \quad (b)$$

where T = temperature, K

σ = characteristic diameter of a molecule \AA

Ω_n = collision integral which is a function of the

dimensionless temperature parameter $k_B T /$

K_B = Boltzmann constant

Σ = force constant in the Lenard-Jones potential function.

The viscosity of hydrogen was determined by using equation (b) appropriate values of $\Sigma / K_B \Omega_n$ and obtained from tabulated data.

The density of hydrogen was calculated from⁽⁹⁶⁾

$$\rho = \frac{273.16}{T} \times 0.0899 \times 10^{-3} \quad \text{g} \cdot \text{cm}^{-3} \quad \text{-----} \quad (c)$$

Using the three relationships (a), (b) and (c), values of density, viscosity and kinematic viscosity have been estimated at different temperatures and are presented in the following table:

Temperature T/K	Density (ρ) /g.cm ⁻³	Viscosity (η) /g.cm ⁻¹ sec ⁻¹	Kinematic Viscosity (ν) /cm ² .sec ⁻¹
900	0.0273x10 ⁻³	187.70	6.876
973	0.0252x10 ⁻³	197.31	7.83
1000	0.02456x10 ⁻³	201.46	8.203
1073	0.02288x10 ⁻³	210.72	9.21
1100	0.0223x10 ⁻³	214.37	9.613
1103	0.0222x10 ⁻³	214.70	9.657
1123	0.02186x10 ⁻³	217.67	9.955
1173	0.02093x10 ⁻³	223.90	10.70
1200	0.0205x10 ⁻³	227.65	11.105
1273	0.01929x11 ⁻³	235.34	12.20

TABLE 2.1 THERMOCHEMICAL DATA FOR REACTIONS OF INTEREST

(Mean values for the standard enthalpy and
entropy changes over the temperature range
600-1000°C)

Reaction	ΔH° (kJ/mol)	ΔS° (J/mol K)
$3 \text{ Fe}_2\text{O}_3 + \text{H}_2 \longrightarrow 2 \text{ Fe}_3\text{O}_4 + \text{H}_2\text{O}$	-10.0	74.0
$\text{Fe}_3\text{O}_4 + \text{H}_2 \longrightarrow 3 \text{ FeO} + \text{H}_2\text{O}$	+59.0	62.5
$\text{FeO} + \text{H}_2 \longrightarrow \text{Fe} + \text{H}_2\text{O}$	+15.0	10.0
$3 \text{ Fe}_2\text{O}_3 + \text{CO} \longrightarrow 2 \text{ Fe}_3\text{O}_4 + \text{CO}_2$	-44.5	43.5
$\text{Fe}_3\text{O}_4 + \text{CO} \longrightarrow 3 \text{ FeO} + \text{CO}_2$	+18.5	18.0
$\text{FeO} + \text{CO} \longrightarrow \text{Fe} + \text{CO}_2$	-18.5	19.5

TABLE 3.1 Grading and Chemical Composition of Hematite Ore Concentrate used as Base Material

Grading		Chemical Composition	
Sieve dimension/ μm	retained %	Oxide	Mass %
75	96.6	Fe ₂ O ₃	99.2
63	93.6	SiO ₂	0.22
45	79.0	MnO	<0.014
		P ₂ O ₅	0.06
		Cr ₂ O ₃	0.05
		V ₂ O ₅	0.05
		TiO ₂	0.06
		MgO	0.066
		CaO	0.120
		Al ₂ O ₃	0.24

TABLE 3.2 The Composition of Doping Agents

Lime (CaO)		Silica (SiO ₂)		Alumina (Al ₂ O ₃)	
Element	Mass %	Element	Mass %	Element	Mass %
Sulphur (S)	0.005	Sodium	0.01	Water soluble matter	0.2
Chloride (Cl)	0.005	Potassium	1.005	Chloride	0.005
		Iron	0.015	Sulphate	0.005
				Iron	0.005
				Loss on ignition	0.9

TABIE 3.3 Initial Constituents of iron oxide pellets

Sample No	Chemical Composition									
	% Fe	% SiO ₂	% MnO	% P ₂ O ₅	% Cr ₂ O ₃	% TiO ₂	% MgO	% CaO	% Al ₂ O ₅	% V ₂ O ₅
'A ₃	69.47	0.22	0.014	0.06	0.05	0.06	0.066	0.12	0.24	0.05
"A ₄	"	"	"	"	"	"	"	"	"	"
'C ₃	68.85	"	"	"	"	"	"	1.00	"	"
"C ₄	"	"	"	"	"	"	"	"	"	"
'E ₃	68.16	"	"	"	"	"	"	2.00	"	"
"E ₄	"	"	"	"	"	"	"	"	"	"
"F ₃	67.37	"	"	"	"	"	"	3.00	"	"
"F ₄	"	"	"	"	"	"	"	"	"	"
'G ₃	66.67	"	"	"	"	"	"	4.00	"	"
'H ₃	65.97	"	"	"	"	"	"	5.00	"	"
'A	68.84	1.00	"	"	"	"	"	0.12	"	"
'C	68.22	"	"	"	"	"	"	1.00	"	"
'E	67.52	"	"	"	"	"	"	2.00	"	"
'F	66.82	"	"	"	"	"	"	3.00	"	"
'G	66.12	"	"	"	"	"	"	4.00	"	"
'H	65.42	"	"	"	"	"	"	5.00	"	"
*β	66.93	3.00	"	"	"	"	"	1.00	"	"
'Al ₂	68.236	0.22	"	"	"	"	"	1.00	1.00	"
'Al ₃	67.54	"	"	"	"	"	"	2.00	1.00	"
'Al ₄	66.14	"	"	"	"	"	"	4.00	"	"
'Al ₆	67.70	1.00	"	"	"	"	"	1.00	"	"
'Al ₇	"	"	"	"	"	"	"	2.00	"	"
'Al ₈	65.60	"	"	"	"	"	"	4.00	"	"
"B ₄	69.10	0.22	"	"	"	"	"	6.50	"	"

' Firing temperature 1250°C for 3 hours

" Firing temperature 1325°C for 30 minutes

* Firing temperature 1250°C for 12 hours

TABLE 3.4 Calibration of strain-gauged cantilever beam at 90 cm
from fixed end

Load in kg	Voltage output in mv
0.20	0.29
0.30	0.44
0.50	0.72
0.7	1.00
1.00	1.45
1.2	1.76
1.5	2.20
1.6	2.30

TABLE 3.5 Calibration of strain-gauged cantilever beam
at 60 cm from fixed end

Load in kg	Voltage output in mv
1.2	1.40
2.0	2.30
2.40	2.80
2.45	2.87
2.75	3.20
2.95	3.40
3.00	3.50

TABLE 3.6 Blank test of reduction-under-load apparatus

At 850°C		At 830°C	
Time in minutes	Contraction of Platens in mm	Time in minutes	Contraction of Platens in mm
1	0.03	1	0.05
2	0.06	2	0.06
3	0.13	3	0.10
4	0.16	4	0.13
5	0.18	5	0.16
6	0.21	6	0.16
7	0.25	7	0.18
8	0.25	8	0.18
9	0.26	9	0.20
10	0.30	10	0.20
11	0.31	11	0.21
12	0.31	12	0.21
13	0.31	13	0.21
14	0.31	14	0.21
15	0.33	15	0.21
20	0.35	20	0.21
25	0.35	25	0.21
30	0.35	30	0.21

TABLE 3.7 Values of percentage change in length against time for five samples (B_1) reduced at 850°C at a constant stress of 0.75 kg.cm⁻²

Time Minutes	Sample No					Mean	σ_{n-1}	% σ
	1	2	3	4	5			
1	3.40	3.08	3.07	3.24	3.26	3.212	0.13	4.05
2	4.23	3.41	4.07	3.73	4.09	3.906	0.337	8.48
3	3.68	3.35	3.85	3.84	4.03	3.705	0.25	6.67
4	3.68	3.51	4.01	4.17	4.20	3.915	0.306	7.82
5	3.63	3.80	4.30	4.11	4.31	4.03	0.304	7.55
6	3.46	3.60	4.30	4.28	4.14	3.956	0.39	9.86
7	3.46	3.68	4.12	4.11	3.81	3.836	0.28	7.30
8	3.35	3.35	3.68	3.67	3.51	3.516	0.15	4.27
9	3.13	3.13	3.63	3.45	3.31	3.33	0.20	6.00
10	3.13	3.2	3.13	3.12	3.15	3.14	0.03	0.96

TABLE 3.8 Calibration of Glass Spring

Weight in basket/gram	Displacement of Spring/cm
3.0	11.065
0.1	0.350
0.2	0.720
0.3	1.075
0.4	1.460
0.5	1.830
0.6	2.23
0.8	2.95
1.0	3.695
2.0	7.795

TABLE 4.1(a) THE DENSITY AND POROSITY OF IRON OXIDE PELLETS AT DIFFERENT LEVELS OF DOPING AGENTS AND PRODUCED BY SINTERING AT 1250°C FOR 3 HOURS

Sample Designation	Hematite content /mass %	Content of doping agent /mass %			Density /g cm ⁻³	Porosity /Volume percent
		Lime	Silica	Alumina		
A ₃	99.12	0.12	0.22	0.24	3.7	28.4
C ₃	98.24	1.0	0.22	0.24	3.9	23.0
E ₃	97.24	2.0	0.22	0.24	4.4	15.0
F ₃	96.24	3.0	0.22	0.24	4.15	18.0
G ₃	95.24	4.0	0.29	0.24	4.10	19.0
H ₃	94.24	5.0	0.22	0.24	3.9	21.0
A	98.34	0.12	1.0	0.24	3.6	28.8
C	97.46	1.0	1.0	0.24	3.8	27.6
E	96.46	2.0	1.0	0.24	4.1	19.5
F	95.46	3.0	1.0	0.24	3.95	21.5
G	94.46	4.0	1.0	0.24	3.90	22.0
H	93.46	5.0	1.0	0.24	3.8	23.0
Al ₂	97.48	1.0	0.22	1.0	3.6	29.2
Al ₃	96.48	2.0	0.22	1.0	3.5	32.0
Al ₄	94.48	4.0	0.22	1.0	3.4	32.5
Al ₆	96.70	1.0	1.0	1.0	3.5	30.0
Al ₇	95.70	2.0	1.0	1.0	3.35	32.50
Al ₈	93.70	4.0	1.0	1.0	3.10	38.40

TABLE 4.1(b) THE DENSITY AND POROSITY OF IRON OXIDE PELLETS AT DIFFERENT LEVELS OF DOPING AGENTS AND PRODUCED BY SINTERING AT 1325°C FOR 30 MINUTES

Sample Designation	Hematite content /mass %	Content of Doping Agent /mass %			Density /g cm ⁻³	Porosity /Volume percent
		Lime	Silica	Alumina		
A ₄	99.12	0.12	0.22	0.24	3.70	28.5
C ₄	98.24	1.00	0.22	0.24	4.10	19.50
E ₄	97.24	2.00	0.22	0.24	4.47	13.0
F ₄	96.24	3.00	0.22	0.24	4.10	19.50

TABLE 4.1(c) THE DENSITY AND POROSITY OF AN IRON OXIDE PELLET PRODUCED BY SINTERING AT 1250°C for 12 HOURS

Sample No	Hematite /mass %	Main doping agent /mass %			Density /g cm ⁻³	Porosity /Volume percent
		Lime	Silica	Alumina		
	95.46	1.0	3.0	0.24	3.6	27.9

TABLE 4.2

POINT ANALYSIS OF DIFFERENT PHASES PRESENT IN VARIOUS
SAMPLES, CATEGORISED IN TERMS OF MOLAR Fe/Ca RATIO

Sample No.	Range of analysis wt %			Mean analysis			
	Fe ₂ O ₃	CaO	SiO ₂	Fe ₂ O ₃	CaO	SiO ₂	Phases
G ₃	96.9-99.5	0.1-0.8	1.2- 2.5	97.9	0.4	1.7	H
	86.1-89.5	6.0-9.5	1.2- 5.6	86.4	7.6	6.0	CF _x
	73.7-82.9	10.5-14.8	7.7-12.0	77.1	12.6	10.3	CF ₂ [⊗]
E ₃	94.3-99.4	0.1-4.4	0.7- 3.4	95.8	2.9	1.3	H
	88.3-90.6	9.3-11.1	0.4- 2.3	88.4	10.2	1.4	CF _x
	81.6-85.2	14.6-16.9	0.0-1.7	83.0	16.2	0.84	CF ₂
	-	-	-	79.7	20.4	-	CF
F ₃	94.4-99.8	0.1-3.4	0.2-2.4	97.2	1.6	1.2	H
	81.6-87.8	12.0-13.9	0.4-4.7	85.2	13.0	1.8	CF ₂
	57.8-79.6	19.9-38.2	0.0-3.94	68.9	29.10	1.9	CF
G ₃	93.6-99.7	0.1-3.4	0.0-3.9	97.6	1.2	1.3	H
	89.6-94.5	5.6-8.4	0.0-5.6	91.7	6.9	1.4	CF _x
	78.2-81.4	15.0-19.5	0.0-6.9	79.0	17.0	4.0	CF ₂
	57.8-80.0	11.0-30.3	0.0-3.9	68.9	29.1	1.9	CF
H ₃	93.7-99.9	0.2-3.6	0.9-2.7	96.6	1.5	1.9	H
	-	-	-	66.4	25.6	8.7	CF _x [⊗]
	79.6-84.9	13.6-18.5	0.0-3.8	82.6	16.3	1.2	CF ₂
G	96.7-97.0	0.1-0.6	1.5-4.0	97.8	2.8	1.9	H
	38.6-69.7	7.0-29.4	17.6-35.8	59.3	12.5	28.2	Complex iron-calcium silicate

Continued overleaf

Sample No.	Range of analysis wt %			Mean analysis			
	Fe ₂ O ₃	CaO	SiO ₂	Fe ₂ O ₃	CaO	SiO ₂	Phases
E	93.9-98.8	0.0- 2.5	1.4- 3.8	96.7	1.1	2.2	H
	71.4-82.9	9.3-14.3	9.9-15.2	77.6	10.9	11.5	CF ₂ ^x
	24.3-52.9	23.8-38.5	22.5-42.9	40.40	26.7	32.9	Complex iron-calcium silicate
F	98.0-99.5	0.1- 0.3	0.7- 1.5	98.5	0.2	1.3	H
	50.7-51.6	40.6-46.2	1.7- 7.8	51.0	44.2	4.8	C ₂ F
	67.8-77.8	11.2-17.5	11.0-15.0	71.2	15.4	13.5	CF ₂ ^x
	38.6-55.7	12.9-35.0	18.4-26.8	53.7	23.8	25.6	Complex iron-calcium silicate
G	97.8-99.9	1.1- 2.0	-	98.2	1.8	-	H
	82.1-87.1	10.5-13.5	1.9- 5.6	83.9	12.3	3.7	CF ₂
	68.0-72.9	15.3-16.1	11.6-16.0	70.4	15.7	13.9	CF ₂ ^x
H	95.3-98.6	0.3- 1.4	0.2- 2.1	97.3	0.6	2.1	H
	-	-	-	80.3	19.6	-	CF
	62.1-74.8	13.6-20.8	9.0-21.2	71.1	16.6	12.3	CF ₂ ^x
G ₄	-	-	-	95.9	4.1	-	H
	57.8-80.0	19.9-38.3	0.0- 3.9	68.9	29.1	1.9	CF
	-	-	-	85.0	14.0	-	CF ₂
F ₄	-	-	-	97.9	0.3	1.7	H
	85.7-87.7	12.4-14.3	-	86.9	13.1	-	CF ₂
	57.6-80.2	14.0-31.0	0.0- 4.0	70.7	28.9	1.4	CF

Continued overleaf

Sample No.	Range of analysis wt %			Mean analysis			
	Fe ₂ O ₃	CaO	SiO ₂	Fe ₂ O ₃	CaO	SiO ₂	Phases
36 β	-	-	-	99.4	0.3	0.3	H
	48.8-53.7	12.0-18.4	32.8-35.0	51.0	15.2	33.8	iron- calcium silicate
	23.7-38.9	25.7-37.0	33.0-39.4	33.3	30.2	36.4	iron- calcium silicate

Continued overleaf

Sample No	Range of analysis wt %				Mean analysis				
	Fe ₂ O ₃	CaO	SiO ₂	Al ₂ O ₃	Fe ₂ O ₃	CaO	SiO ₂	Al ₂ O ₃	Phases
Al ₂	-	-	-	-	96.3	0.1	0.9	2.6	H
	1.9-13.7	1.9-13.4	0.2-14.9	78.6-97.6	5.0	4.4	2.1	88.8	Al ₂ O ₃
	-	-	-	-	7.7	20.6	-	71.7	CaO 2Al ₂ O ₃
	-	-	-	-	9.0	14.7	-	76.2	CaO 3Al ₂ O ₃
	56.8-84.3	8.2-15.0	2.9-10.5	4.0-17.7	67.4	11.8	7.9	12.9	CF ₂ **
Al ₄	-	-	-	-	96.0	2.6	1.0	0.4	H
	84.0-88.6	12.5-16.2	-	-	86.6	13.4	-	-	CF ₂
	73.0-79.6	11.9-19.4	1.6-4.1	3.4-7.0	76.3	15.3	2.8	5.2	CF ₂ **
Al ₆	-	-	-	-	92.9	4.0	2.7	1.0	H
	-	-	-	-	77.6	17.4	5.0	-	CF ₂
	23.4-50.6	25.2-32.2	9.7-22.9	9.3-23.3	37.5	29.0	16.7	16.9	C ₂ F**
Al ₈	-	-	-	-	96.9	2.0	1.1	0.6	H
	86.7-87.6	12.3-12.9	-	-	87.4	12.6	-	-	CF ₂

Key: H = hematite: CF_x = Calcium ferrite: CF₂ = Calcium di-ferrite: CF = Calcium monoferrite

C₂F = Di-calcium ferrite: * = With high silica: ** = With high silica and alumina

CaO.Al₂O₃ = Calcium aluminate

TABLE 4.3 Measurement of the mass transfer coefficient in the naphthalene-air system

Naphthalene Sample	$\dot{V}/\text{cm}^3 \text{ sec}^{-1}$	Temp/ K	Time/ sec	Loss of Mass /mol.	P/ atmos	\dot{n} mol sec^{-1}	k cm sec
1	16.84	291.16	122400	0.0157	5.47×10^{-5}	9.378×10^{-9}	0.1500
2	25.43	293.16	32400	0.0075	6.7×10^{-5}	1.80×10^{-9}	0.2050
3	25.6	295.16	24400	0.0062	8.19×10^{-5}	3.36×10^{-9}	0.2154
4	25.43	293.16	12600	0.0027	6.7×10^{-5}	1.67×10^{-9}	0.19
5	34.5	293.16	36000	0.0091	6.7×10^{-5}	1.9739×10^{-9}	0.225
6	34.14	295.16	36000	0.0092	8.19×10^{-5}	1.9735×10^{-9}	0.2512
7	42.68	295.16	21600	0.0073	8.19×10^{-5}	2.639×10^{-9}	0.2477

TABLE 4.4 Measurement of the mass transfer coefficient of naphthalene-air system: results used for derivation of mass transfer equation

$\Delta / \text{cm sec}$	0.15	0.205	0.2154	0.19	0.225	0.2512	0.2477
$\dot{V} / \text{cm}^3 \text{sec}^{-1}$	16.84	25.43	25.6	25.43	34.5	34.14	42.68
$u = \frac{\dot{V}}{A} \text{ cm sec}$	0.60	0.90	0.90	0.90	1.22	1.20	1.51
Re	4.02	5.96	5.89	5.96	8.07	8.07	9.88
Log Re	0.61	0.775	0.770	0.775	0.907	0.896	0.996
$Sh = \frac{\Delta d}{D}$	2.45	3.36	3.53	3.10	3.69	4.11	4.06
$Sc^{1/3}$	1.34	1.35	1.36	1.35	1.35	1.36	1.36
$\text{Log } \frac{Sh-1.68}{Sc^{1/3}}$	-0.24	0.095	0.136	0.0219	0.169	0.255	0.24

A = Crosssectional area of tube 28.27 cm^2 .

d = Characteristic length of naphthalene 1 cm .

ν = Kinematic viscosity of Air $0.133 \text{ cm}^2 \cdot \text{sec}^{-1}$.

TABLE 4.5 REDUCTION TIME vs. PERCENT REDUCTION OF AN IRON OXIDE
PELLET CONTAINING 1.0 MASS % CaO, 3.0 MASS % SILICA
AND 0.24 MASS % ALUMINA, REDUCED IN HYDROGEN AT 850°C

Time in minutes	Percent oxygen removed
1-30	12.7
2-30	24.9
3-0	31.9
4-0	41.2
5-0	51.5
6-0	61.7
7-0	70.6
8-0	77.4
9-0	84.2
10.0	88.2
11.0	92.6
12.0	95.7
13.0	97.7
14.0	98.8
15.0	98.8

TABLE 4.6 REDUCTION PROPERTIES OF DOPED HEMATITE PELLETS REDUCED
IN HYDROGEN AT 850°C AND SINTERED AT 1325°C FOR 30 MINUTES

Composition of doping agents mass %			Reduction time in mins for 95%	Initial stresses			
				Zero		1.5 kg cm ⁻²	
CaO	SiO ₂	Al ₂ O ₃		Peak Expansion	Terminal Expansion	Peak Expansion	Terminal Expansion
0.12	0.22	0.24	13	6.2	1.2	4.2	-
1.00	0.22	0.24	17	2.65	2.4	2.0	-
2.00	0.22	0.24	25	1.2	0.6	1.2	-
3.00	0.22	0.24	25	1.1	0.15	0.35	-
1.00	3.00	0.24	12	9.4	7.0	6.0	-

* Sintered at 1250°C for 12 hours

TABLE 4.7 GENERAL OBSERVATION ON REDUCED PELLETS

Sample		Degree of Cracking	Mode of Reduction
Designation	Number		
A ₃ '	1	Cracked	Homogeneous
C ₃ '	2	Cracked	Homogeneous
C ₃ '	1	No cracking	Topochemical
f ₃ '	3	No cracking	Topochemical
G ₃ '	1	No cracking	Topochemical
H ₃ '	1	No cracking	Topochemical
A'	1	Cracked	Homogeneous
C'	2	Heavily cracked	Homogeneous
E'	**	Cracked	Homogeneous
F'	1	Slightly cracked	Homogeneous
G'	2	Slightly cracked	Mixed mode
H'	2	No cracking	Topochemical
Al ₂ '	2	Cracked	Homogeneous
Al ₃ '	1	Cracked	Homogeneous
Al ₄ '	2	Cracked	Homogeneous
Al ₆ '	2	Cracked	Homogeneous
Al ₇ '	1	Cracked	Homogeneous
Al ₈ '	2	Cracked	Homogeneous
A ₄ "	2	Cracked	Homogeneous
C ₄ "	3	Slightly cracked	Homogeneous
E ₄ "	***	No cracking	Topochemical
F ₄ "	3	No cracking	Topochemical
β*	1	Heavily cracked	Homogeneous

For sample composition see Table 3.3.

** 3.0 kg·cm⁻²

*** 1.5 kg·cm⁻²

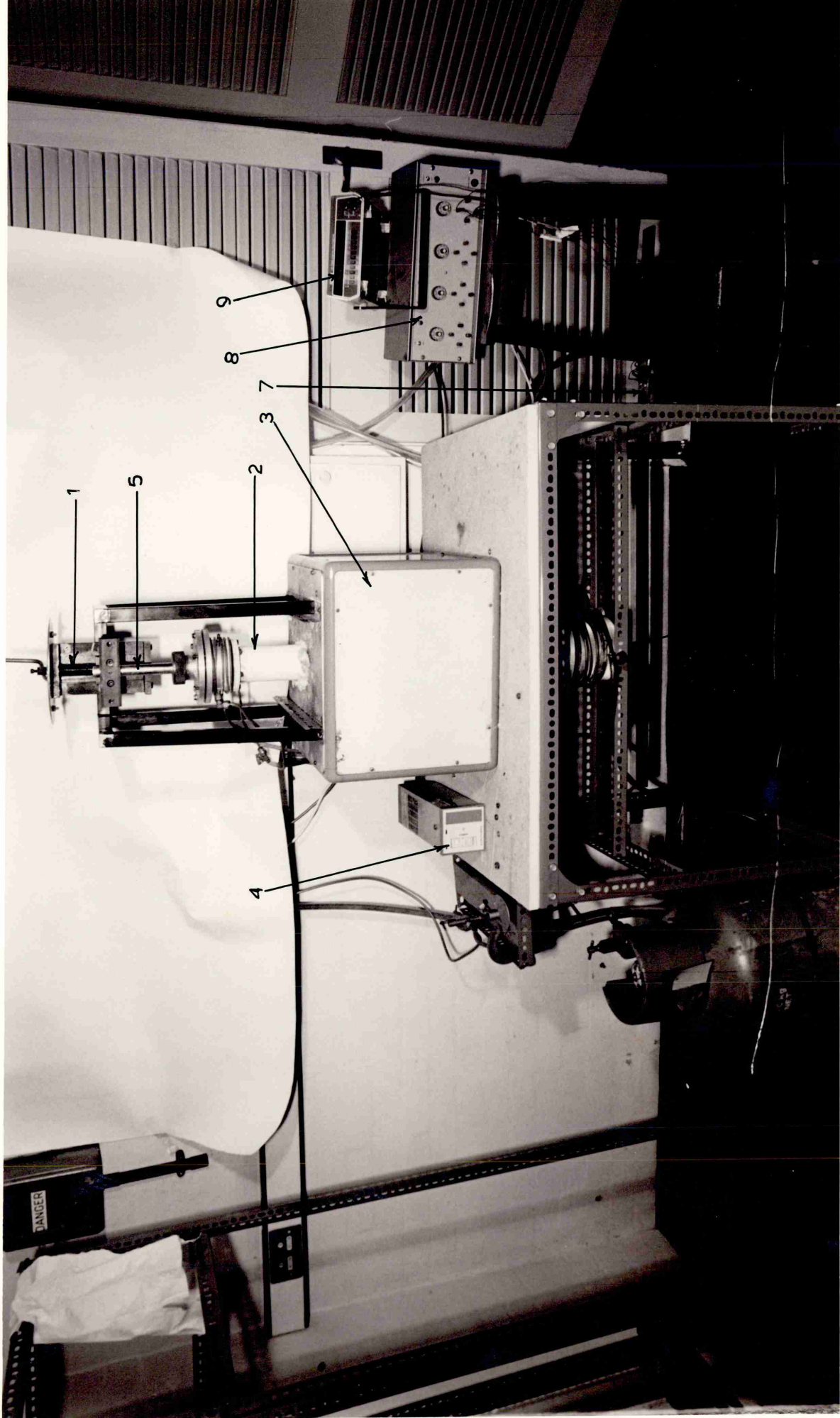
TABLE 5.1 MICRO-ANALYSIS OF PHASES PRESENT, CATEGORISED IN TERMS OF MOLAR Fe/Ca RATIO AND APPROXIMATE FORMULA

% Fe ₂ O ₃	% CaO	% SiO ₂	% Al ₂ O ₃	Molar Fe/Ca Ratio	Compounds
84.7-91.7	6.9-10.2	1.3- 7.6	-	7.93 [±] 1.15	CaO(Fe ₂ O ₃) _{3.5}
77.0-87.4	12.3-17.6	0.0- 5.0	-	4.22 [±] 0.65	CaO.2 Fe ₂ O ₃
70.4-77.5	11.9-16.8	10.2-13.9	-	3.85 [±] 0.60	CaO.2 Fe ₂ O ₃ [±]
67.0-76.0	11.8-15.7	2.8- 7.8	5.2-12.8	3.78 [±] 0.24	CaO.2 Fe ₂ O ₃ ^{±±}
69.0-80.0	19.7-29.1	0.0- 1.97	-	2.47 [±] 0.55	CaO·Fe ₂ O ₃
66.3	25.6	8.0	-	1.85	CaO·Fe ₂ O ₃ [±]
51.0	44.2	4.8	-	0.83	2 CaO·Fe ₂ O ₃
37.5	29.0	16.7	16.9	0.93	2 CaO·Fe ₂ O ₃ ^{±±}
33.4-59.3	12.5-30.6	22.0-36.4	-	1.84 [±] 1	Complex iron calcium silicates

PLATE 3.1 A Photograph of reduction under load apparatus

Key:

1. Screw-Jack
2. Refractory tube
3. Furnace
4. Eurotherm temperature controller
5. Upper plate "
6. Cantilever beam
7. Strain gauges
8. Strain gauges power → supply
9. Digit voltmeter



16

Plate 32 Photograph of gas train and alarm.

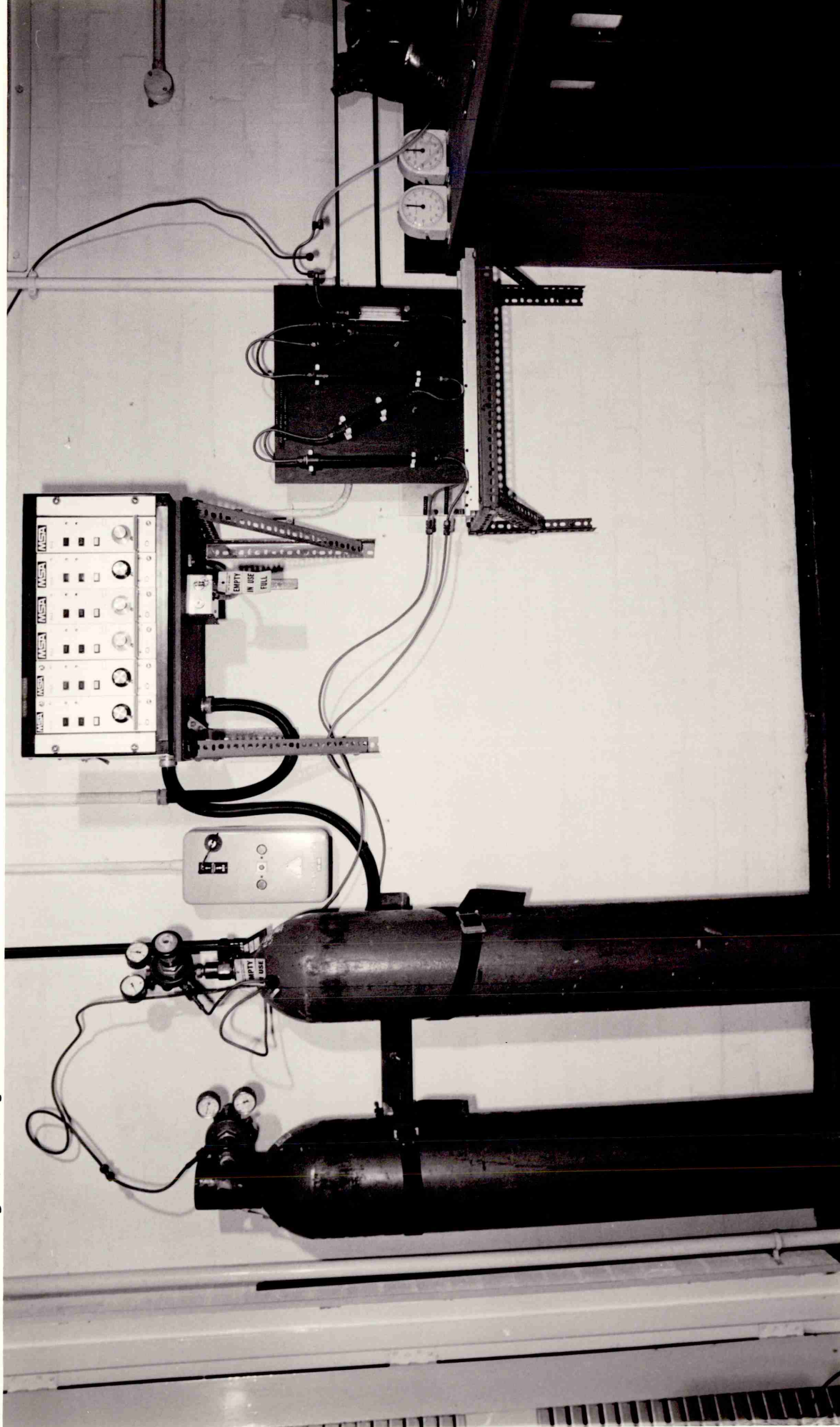
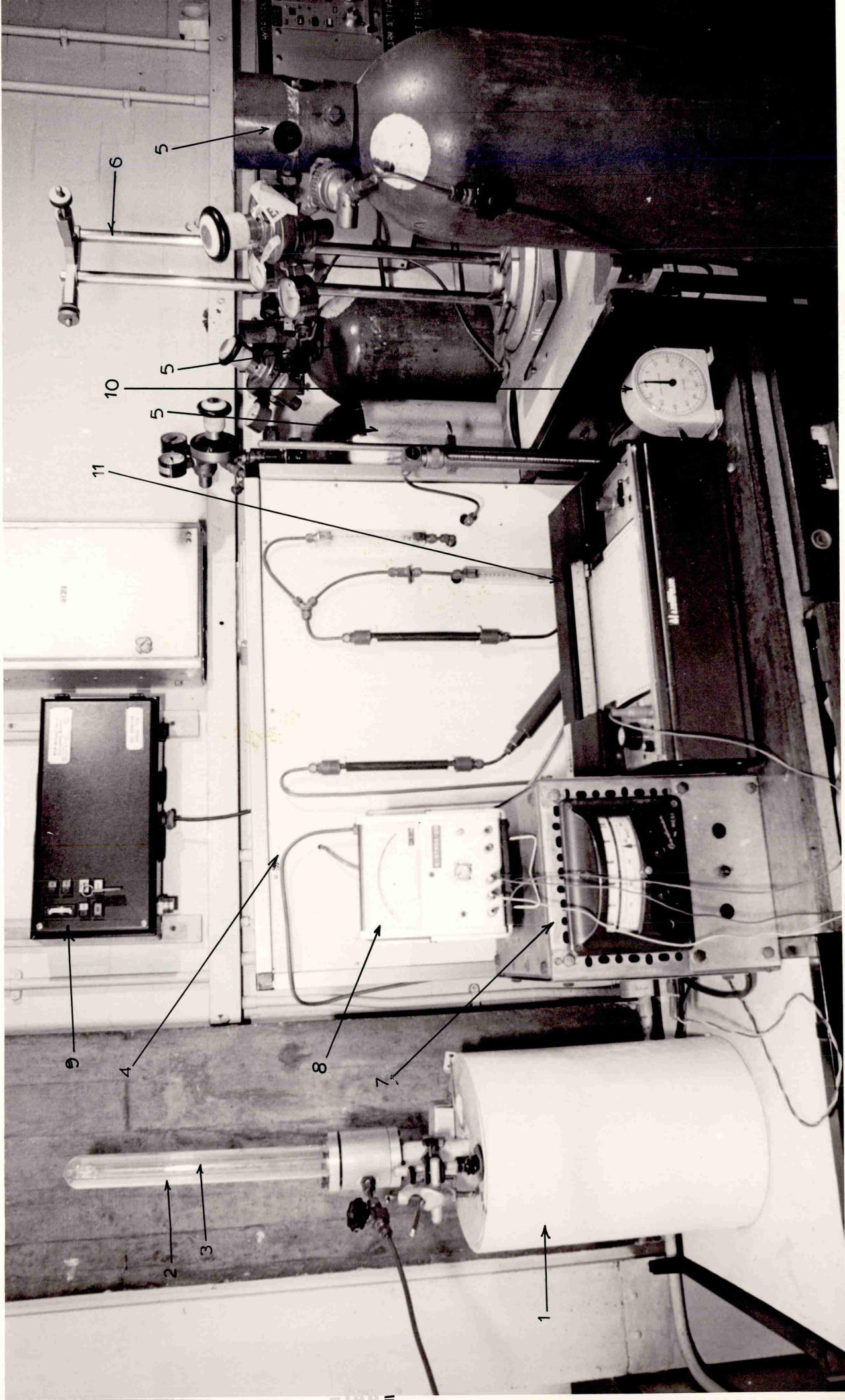


PLATE 3.2 A photograph of thermogravimetric spring balance

Key:

1. Furnace
2. Spring housing
3. Spring
4. Gas train with rotameters of CO, H₂ and nitrogen
5. Gas cylinders
6. Cathetometer
7. Temperature controller
8. Voltmeter
9. Gas alarm
10. Stop clock
11. Temperature recorder



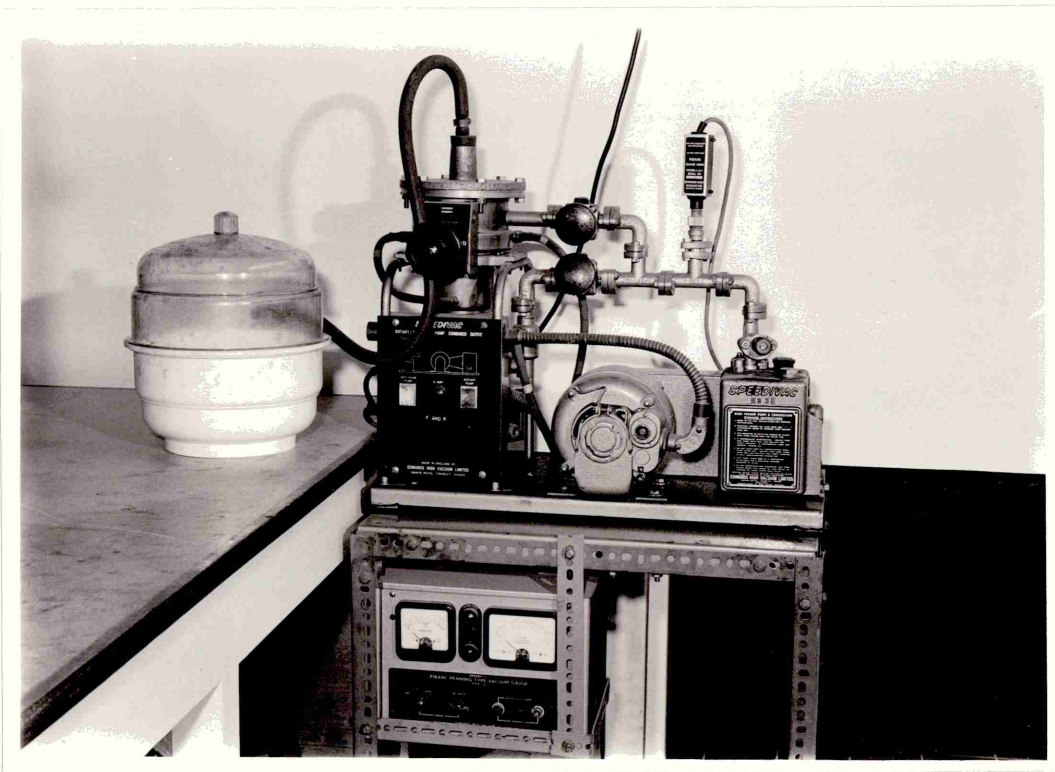


PLATE 3.4 VACUUM IMPREGNATION SYSTEM

Plate 4.1 A polished section of iron oxide pellet without addition, containing CaO 0.12%, SiO₂ 0.22%, Al₂O₃ 0.24% sintered at 1250°C for 3 hours. Black pores, white hematite grains. (190 x).

Plate 4.2 A polished section of iron oxide pellet containing CaO 1.0%, SiO₂ 0.22%, Al₂O₃ 0.24%, sintered at 1250°C for 3 hours. Shows pore distribution (Black) white hematite grains and grey calcium ferrite phase. (190 x).

Plate 4.3 A polished section of iron oxide pellet containing CaO 2.0%, SiO₂ 0.22%, alumina 0.24% sintered at 1250°C for 3 hours, showing black pores, white hematite and grey calcium ferrite. (190 x).

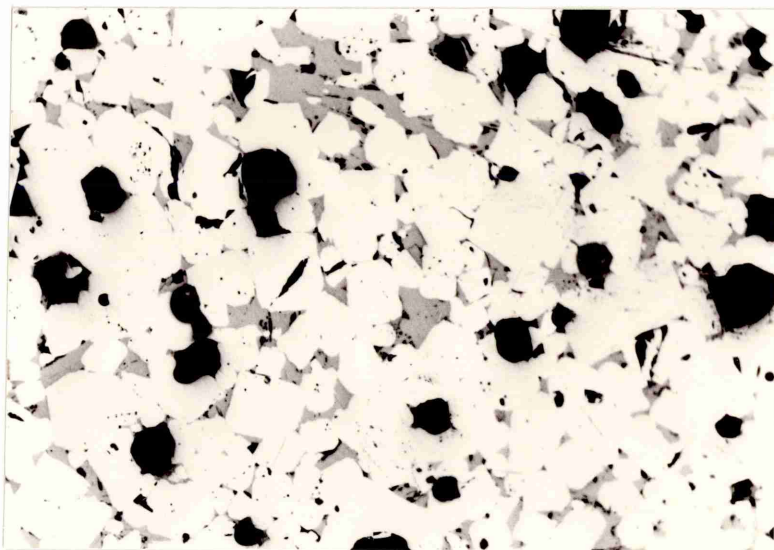
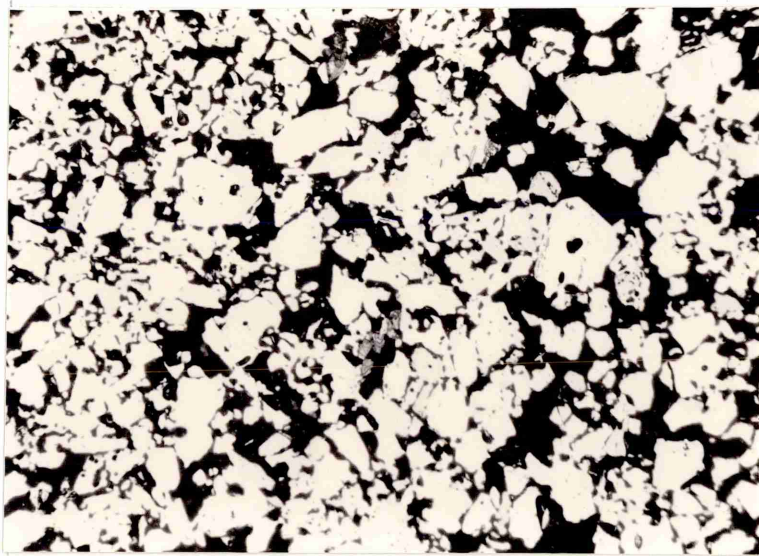


Plate 4.4 A polished section of iron oxide pellet, shown in Plate 4.3 at a high magnification (960 x) showing calcium ferrite grey in colour distributed on white hematite grain boundaries.

Plate 4.5 A polished section of iron oxide pellet containing CaO 3.0%, SiO₂ 0.22%, Al₂O₃ 0.24% sintered at 1250°C for 3 hours. Shows black pores, grey calcium ferrite and white hematite grains (480x).

Plate 4.6 A polished section of iron oxide pellet containing CaO 4.0%, SiO₂ 0.22%, Al₂O₃ 0.24%, sintered at 1250°C for 3 hours, showing hematite, calcium ferrites and pores. (480 x).

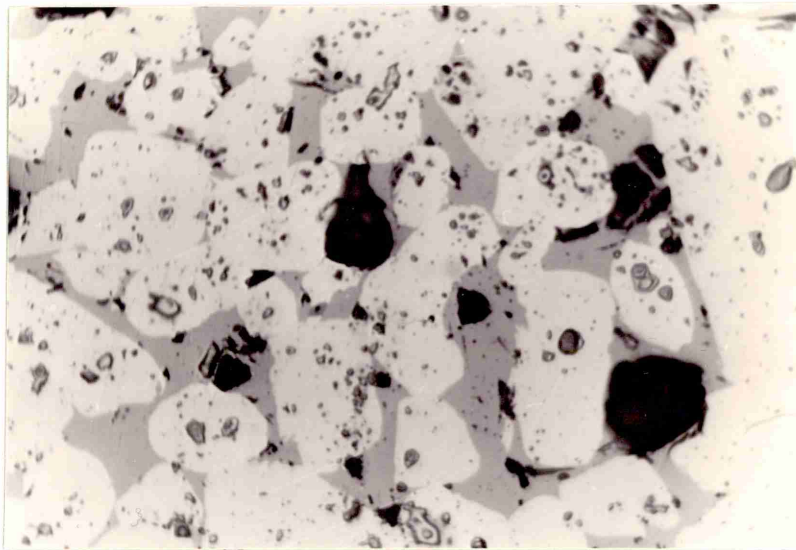


Plate 4.7 A polished section of iron oxide pellet containing CaO 5.0%, SiO₂ 0.22%, Al₂O₃ 0.24% sintered at 1250°C for 3 hours showing dark pores, white hematite and grey calcium ferrite. (190 x).

Plate 4.8 A polished section of iron oxide pellet containing CaO 0.12%, SiO₂ 1.0%, Al₂O₃ 0.24% sintered at 1250°C for 3 hours, showing white hematite, black pores. (190 x).

Plate 4.9 A polished section of iron oxide pellet containing CaO 1.0%, SiO₂ 1.0%, Al₂O₃ 0.24% sintered at 1250°C for 3 hours showing white hematite, dark pores and very fine grey phase (slag). (190 x).

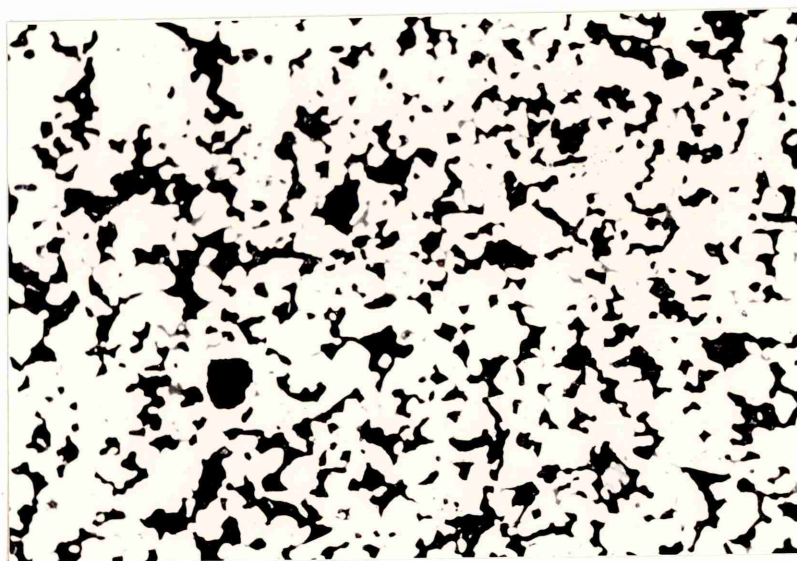
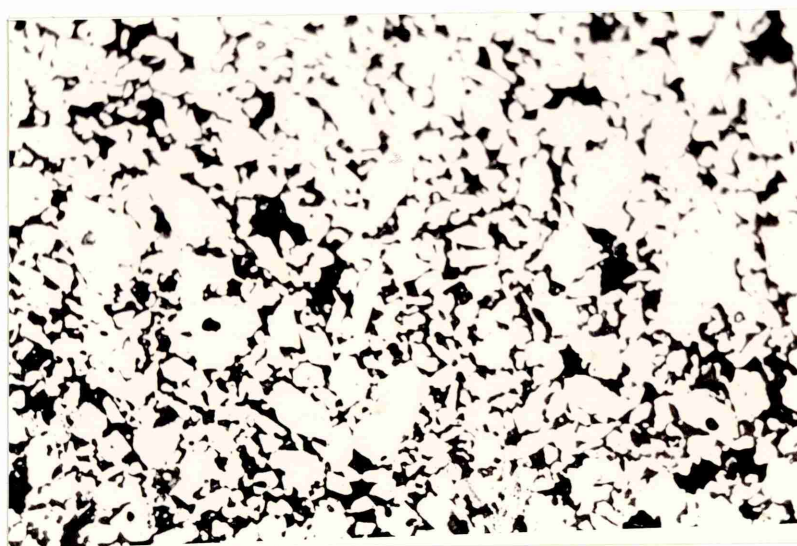
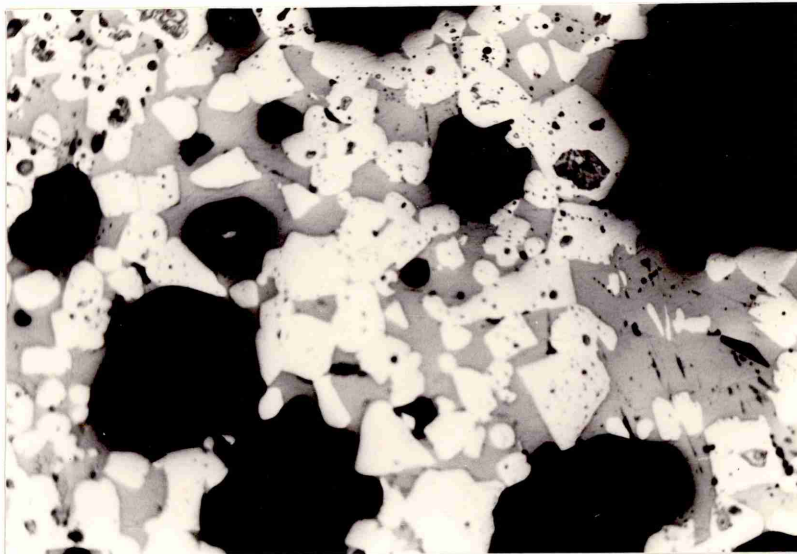


Plate 4.10 . A polished section of iron oxide pellet containing CaO 2.0%, SiO₂ 1.0%, Al₂O₃ 0.24% sintered at 1250°C for 3 hours showing grey calcium ferrite encircled by white hematite grains, dark pores. (190 x).

Plate 4.11 A polished section of iron oxide pellet containing CaO 3.0%, SiO₂ 1.0%, Al₂O₃ 0.24% sintered at 1250°C for 3 hours showing fine distribution of grey phase calcium ferrite white hematite, dark pores. (190 x).

Plate 4.12 A polished section of iron oxide pellet containing CaO 4.0%, SiO₂ 1.0%, Al₂O₃ 0.24% sintered at 1250°C for 3 hours showing grey needles of calcium ferrite, white hematite, dark pores. (190 x).

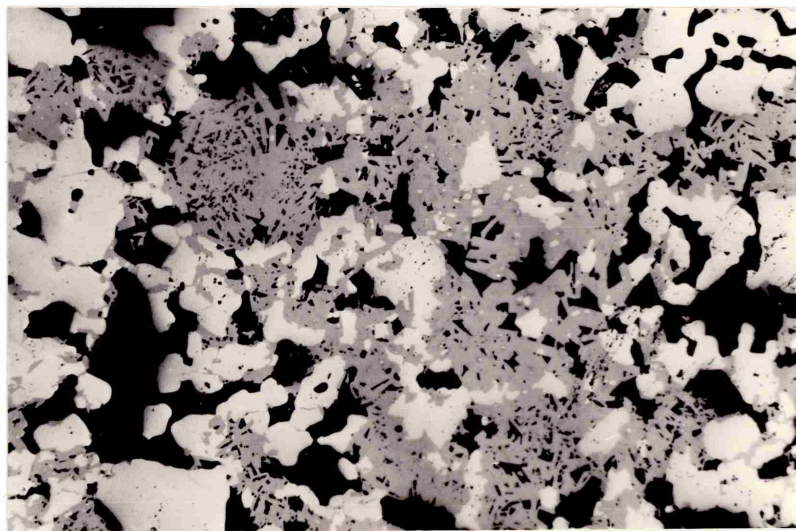
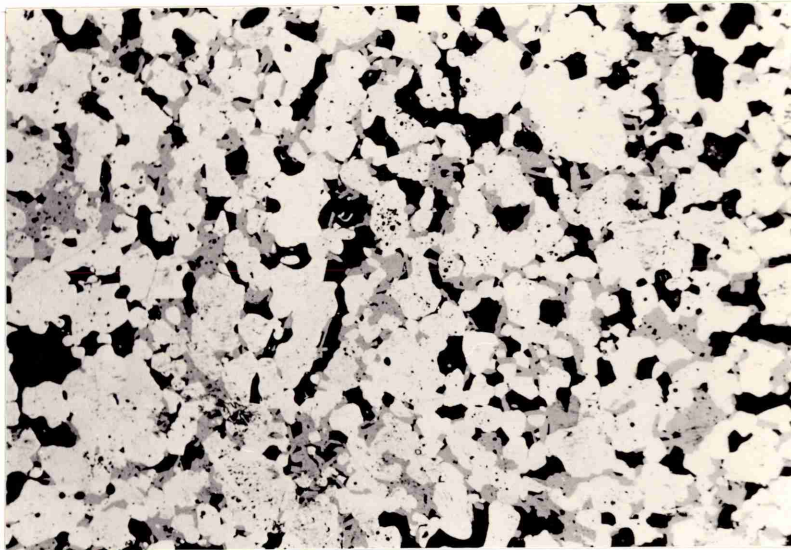
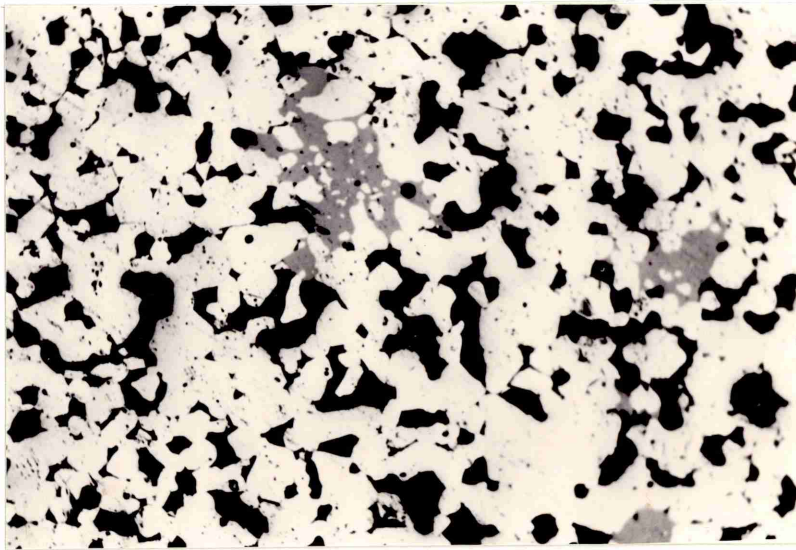


Plate 4.13 A polished section of iron oxide pellet containing CaO 4.0%, SiO₂ 1.0%, Al₂O₃ 0.24% sintered at 1250°C for 3 hours, showing calcium ferrite, grey in colour in laths and needle, white hematite, dark pores. (480 x).

Plate 4.14 A polished section of iron oxide pellet containing CaO 5.0%, SiO₂ 1.0%, Al₂O₃ 0.24% sintered at 1250°C for 3 hours showing dark pores, white hematite, grey calcium ferrite with pores and in solid state. (190x).

Plate 4.15 A polished section of iron oxide pellet shown in Plate 4.14 at high magnification (480 x) showing grey calcium ferrite phase with pores and laths, white hematite, dark pores.

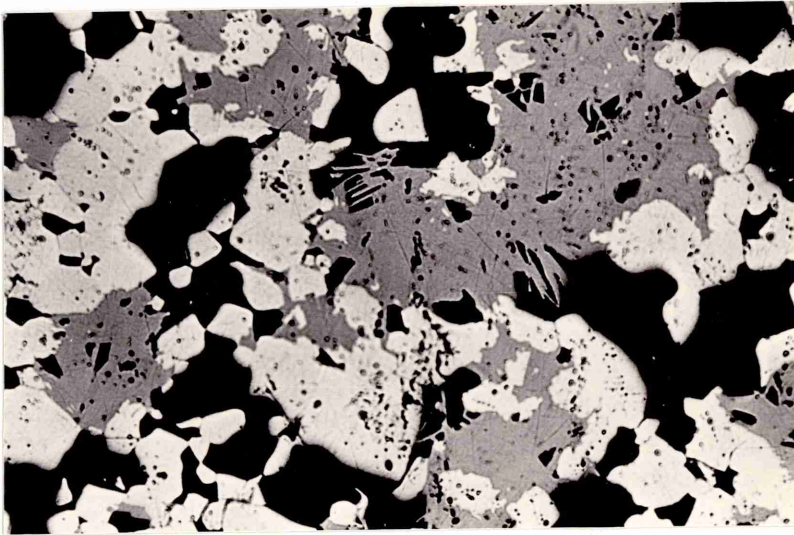
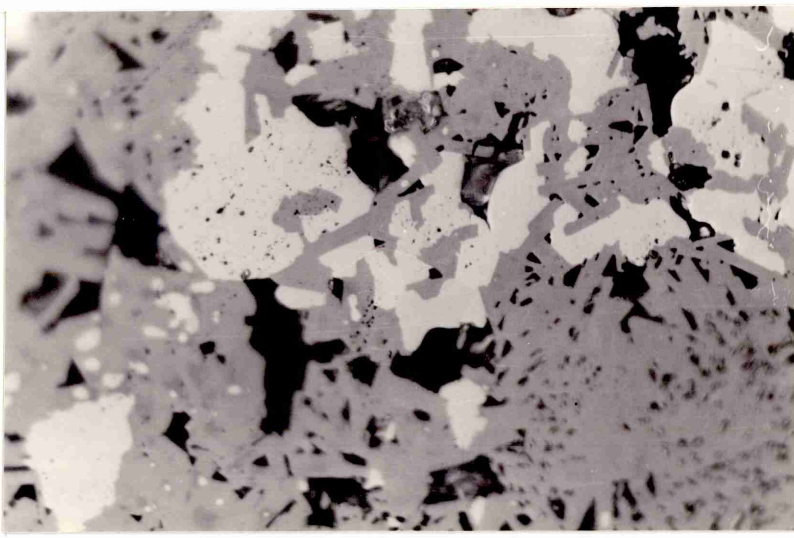


Plate 4.16 A polished section of iron oxide pellet shown in Plate 4.14 at high magnification (480 x) showing grey calcium ferrite with needles and pores, dark pores, white hematite.

Plate 4.17 A polished section of iron oxide pellet containing CaO 1.0%, SiO₂ 0.22%, Al₂O₃ 1.0% sintered at 1250°C for 3 hours. White hematite dark pore and dark phase with grey encircle. (190 x).

Plate 4.18 A polished section of iron oxide pellet shown in Plate 4.17 at high magnification (480 x). Dark pores, grey phase with encircle white, white hematite.

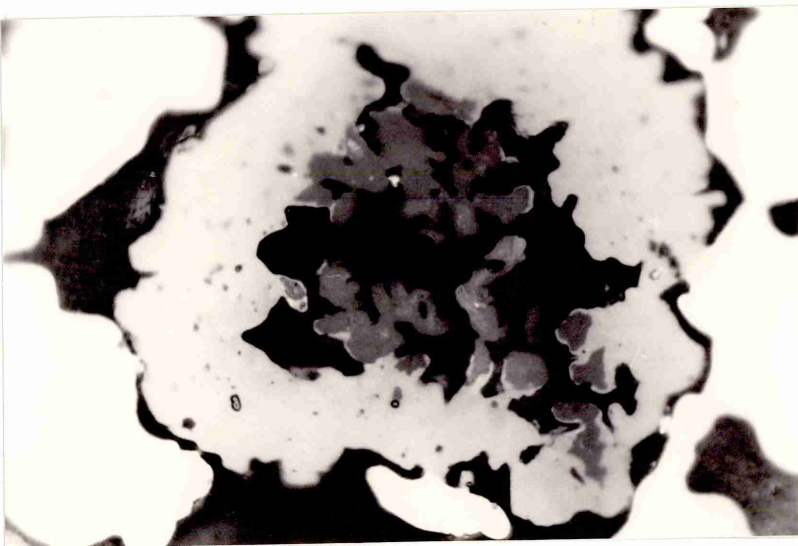
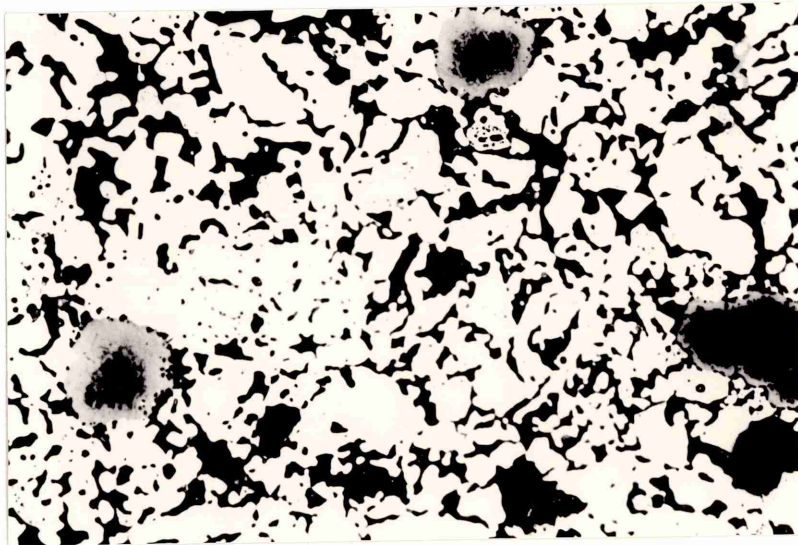
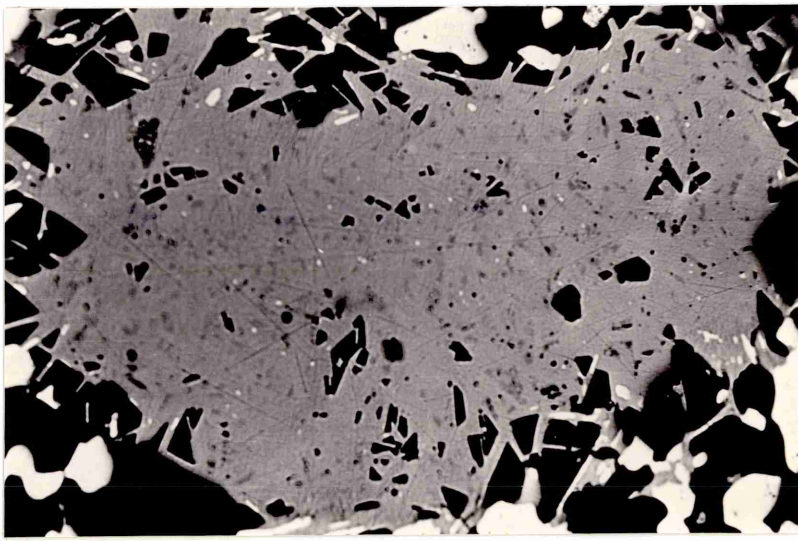


Plate 4.19 A polished section of iron oxide pellet containing CaO 2.0%, SiO₂ 0.22%, Al₂O₃ 1.0% sintered at 1250°C for 3 hours, showing dark pores, white hematite, grey calcium ferrite with pores and needles. (190 x).

Plate 4.20 A polished section of iron oxide pellet containing CaO 4.0%, SiO₂ 0.22%, Al₂O₃ 1.0%, sintered at 1250°C for 3 hours, showing dark pores, grey calcium ferrite and white hematite. (480 x).

Plate 4.21 A polished section of iron oxide pellet containing CaO 1.0%, SiO₂ 1.0%, Al₂O₃ 1.0% sintered at 1250°C for 3 hours, showing dark pores, white hematite, grey phase of doping agents with pores. (190 x).

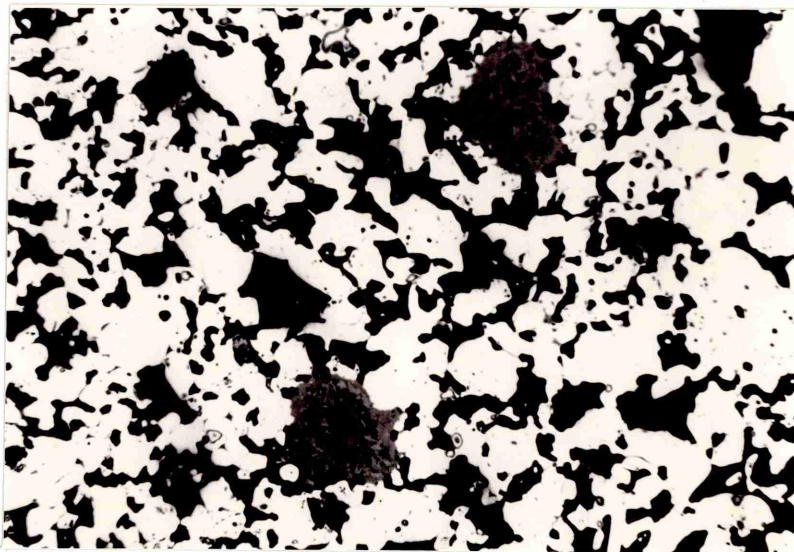
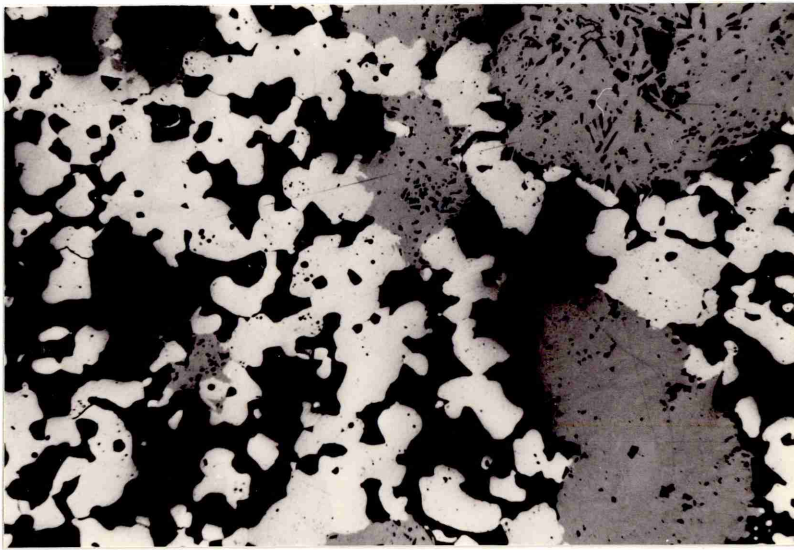


Plate 4.22 A polished section of iron oxide pellet containing CaO 2.0%, SiO₂ 1.0%, Al₂O₃ 1.0% sintered at 1250°C for 3 hours, showing dark pores, white hematite, grey phases. (190 x).

Plate 4.23 A polished section of iron oxide pellet containing CaO 4.0%, SiO₂ 1.0%, Al₂O₃ 1.0% sintered at 1250°C for 3 hours, showing dark pores, white hematite, grey calcium ferrite phases with pres. (190 x).

Plate 4.24 A polished section of iron oxide pellet shown in Plate 4.23 at high magnification (480 x) shows grey calcium ferrite in needle and grain form, dark pores with hematite.

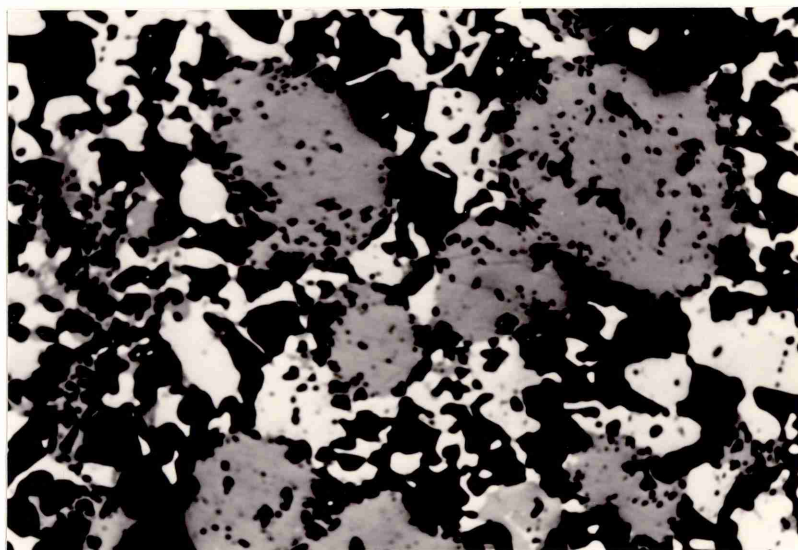
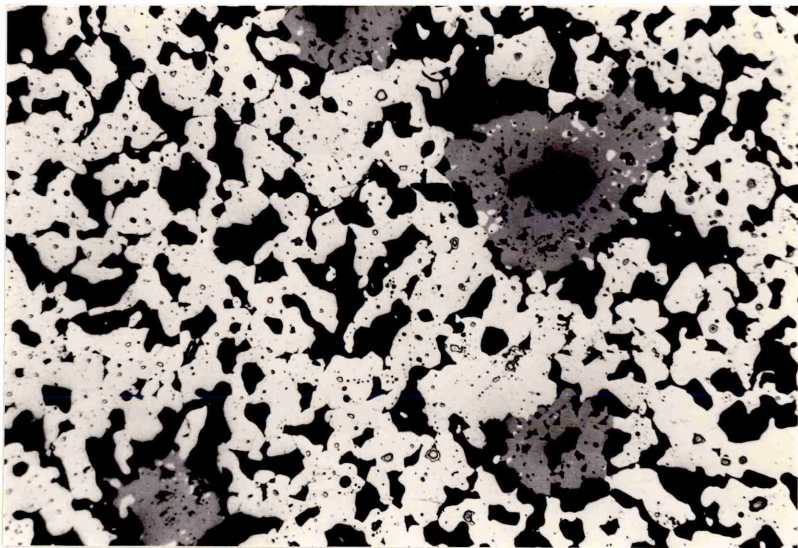


Plate 4.25 A polished section of iron oxide pellet containing CaO 0.12%, SiO_2 0.22%, Al_2O_3 0.24% sintered at 1325°C for 30 minutes showing dark pores, white hematite. (190 x).

Plate 4.26 A polished section of iron oxide pellet containing CaO 1.0%, SiO_2 0.22%, Al_2O_3 0.24% sintered at 1325°C for 30 minutes, showing dark pores, white hematite, grey calcium ferrite. (190 x).

Plate 4.27 A polished section of iron oxide pellet containing CaO 2.0%, SiO_2 0.22%, Al_2O_3 0.24% sintered at 1325°C for 30 minutes, showing dark pores, white hematite grey calcium ferrite. (190 x).

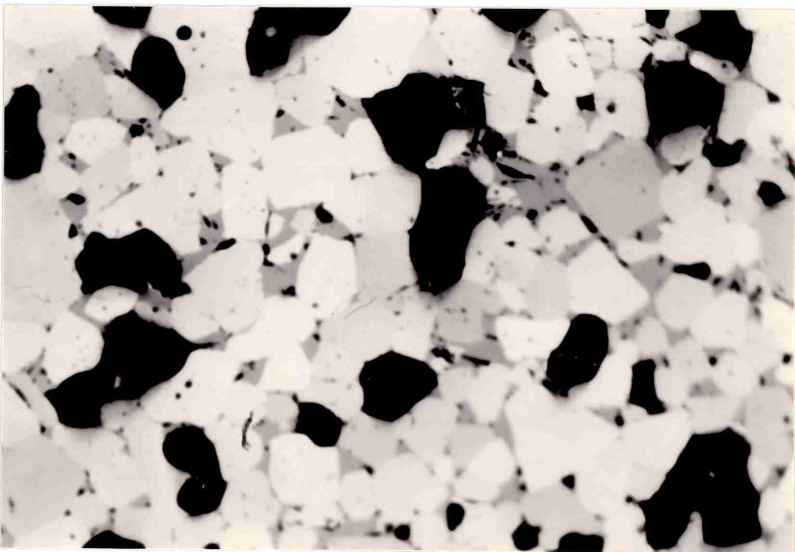
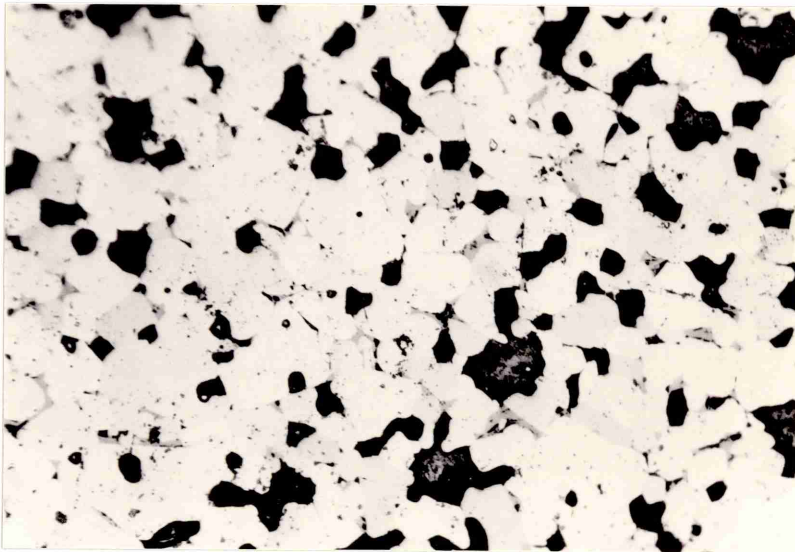
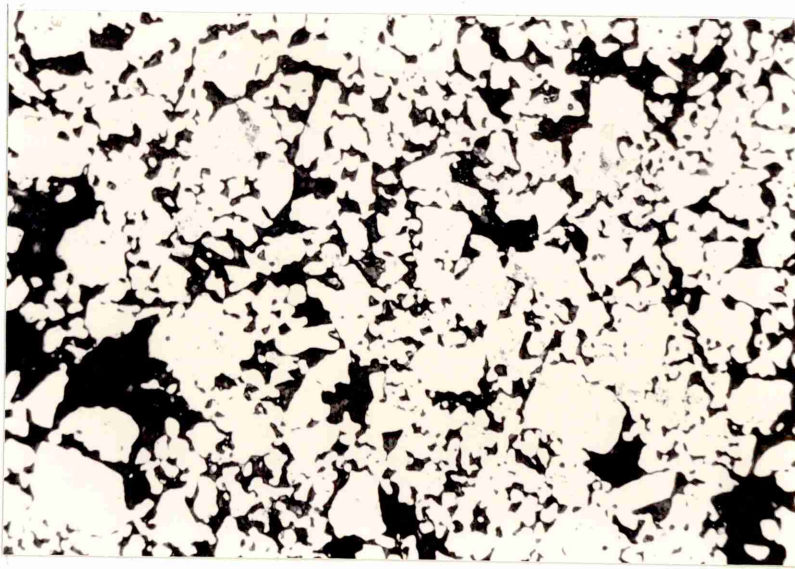


Plate 4.28 A polished section of iron oxide pellet containing CaO 3.0%, SiO₂ 0.22%, Al₂O₃ 0.24% sintered at 1325°C for 30 minutes showing dark pores, grey calcium ferrite and white hematite. (190 x).

Plate 4.29 A polished section of iron oxide pellet containing CaO 1.0%, SiO₂ 3.0%, Al₂O₃ 0.24% sintered at 1250°C for 12 hours showing dark pores, white hematite and very fine grey phases. (190 x).

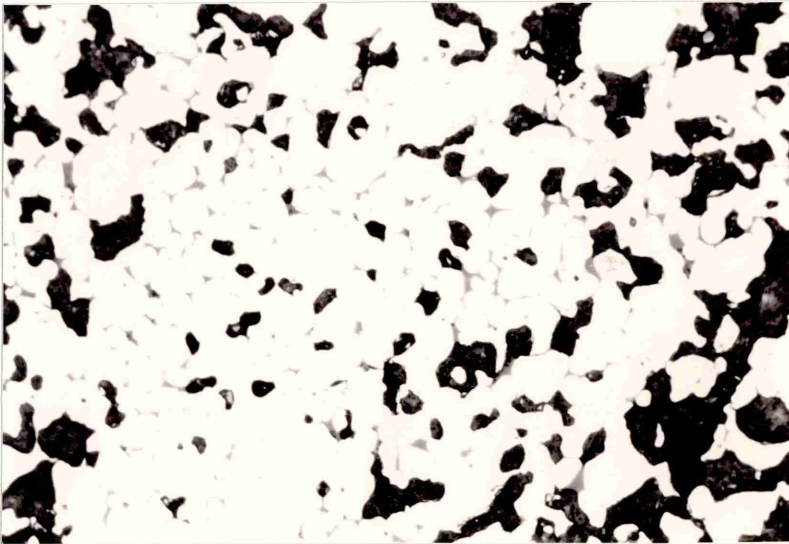
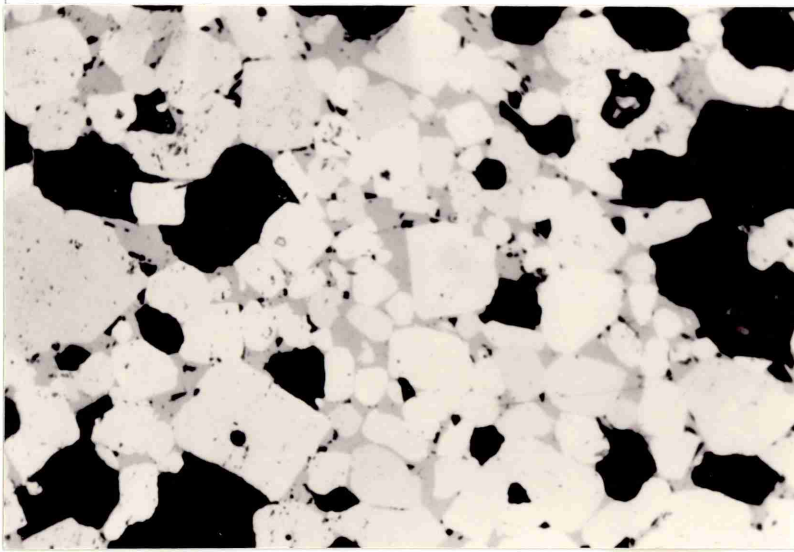


Plate 4.30 Scanning photomicrograph of iron oxide pellet containing CaO 1.0%, SiO₂ 0.22%, Al₂O₃ 0.24% sintered at 1250°C for 3 hours. (575 x).

Plate 4.31 X-Ray map of Calcium distribution in the area shown in Plate 4.30. (575 x).

Plate 4.32 X-Ray map of Silicon distribution in the area shown in Plate 4.30. (575 x).

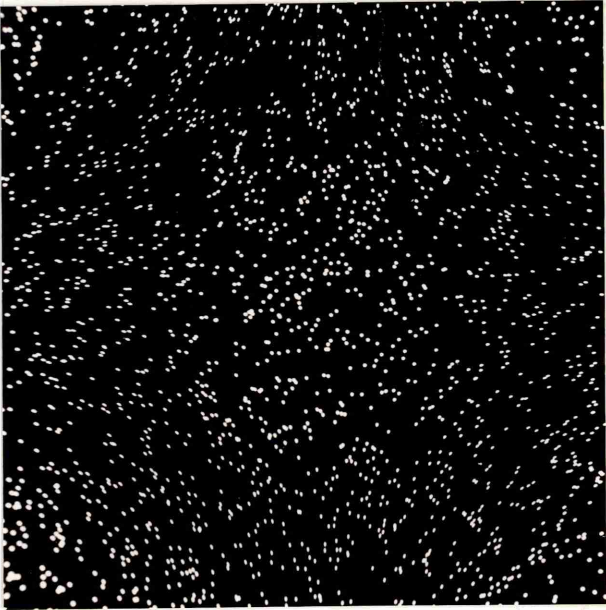
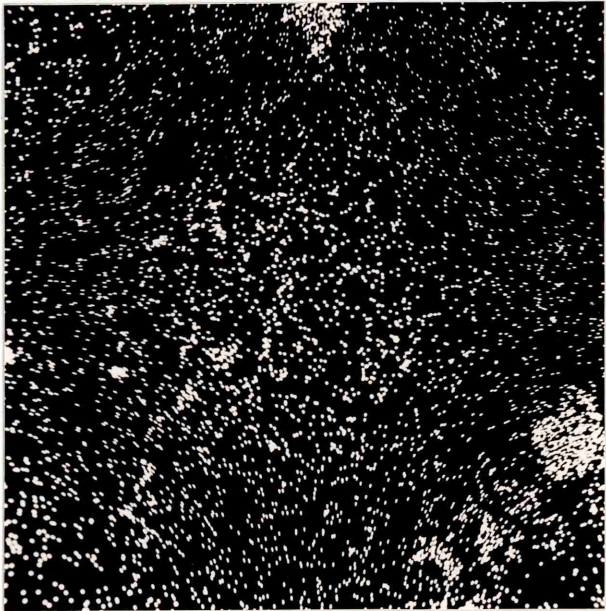
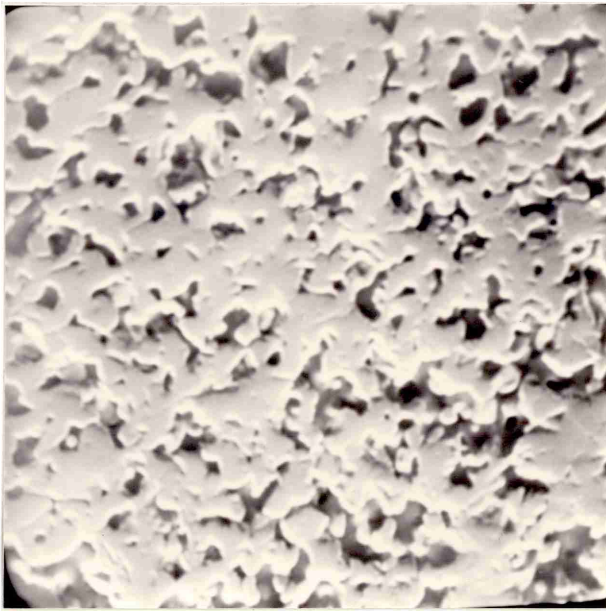


Plate 4.33 Scanning photomicrograph of iron oxide pellet containing CaO 2.0%, SiO₂ 0.22%, Al₂O₃ 0.24% sintered at 1250°C for 3 hours. (4560 x).

Plate 4.34 X-Ray map of Calcium distribution in the area shown in Plate 4.33. (4560 x).

Plate 4.35 Scanning photomicrograph of iron oxide pellet containing CaO 5.0%, SiO₂ 0.22%, Al₂O₃ 0.24% sintered at 1250°C for 3 hours. (600 x).

Plate 4.36 X-Ray map of Calcium distribution in area shown in Plate 4.35. (600 x).

Plate 433



Plate 434

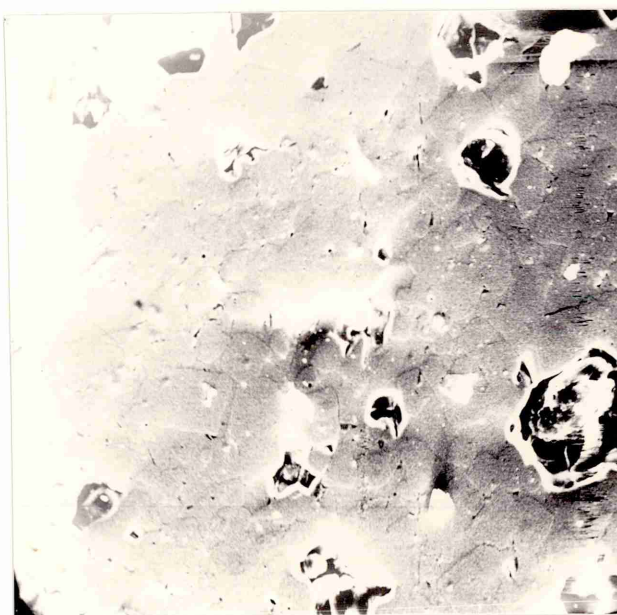


Plate 435

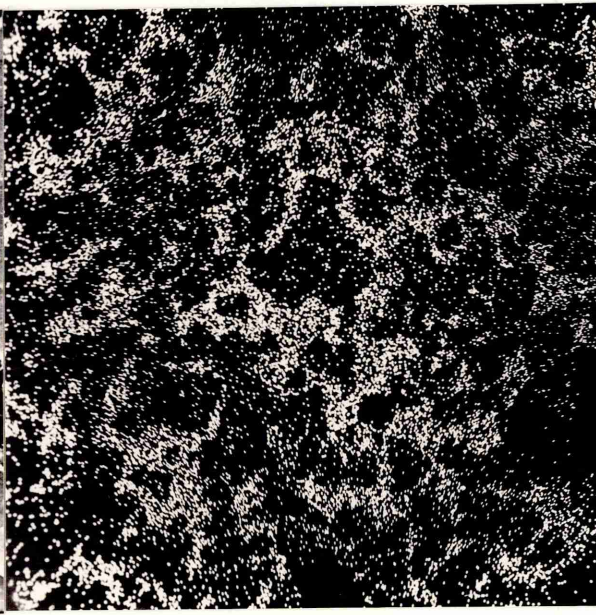


Plate 436

Plate 4.37 Scanning photomicrograph of iron oxide pellet containing CaO 1.0%, SiO₂ 1.0%, Al₂O₃ 0.24% sintered at 1250°C for 3 hours. (1500 x).

Plate 4.38 X-Ray map of Calcium distribution in the area shown in Plate 4.37. (1500 x).

Plate 4.39 X-Ray map of Silicon distribution in area shown in Plate 4.37. (1500 x).

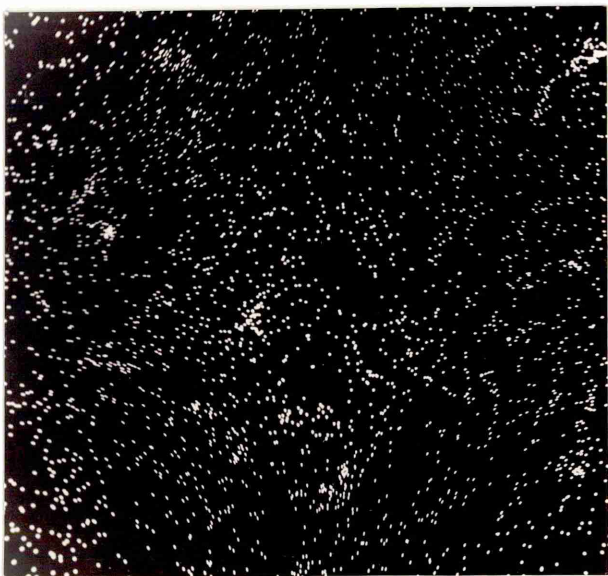
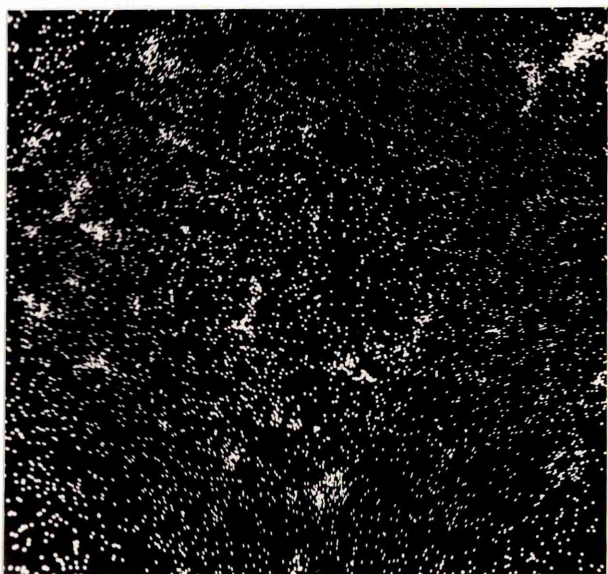
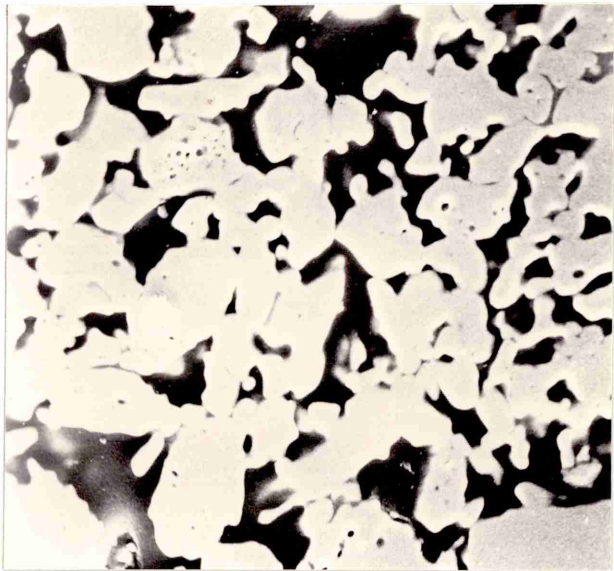


Plate 4.40 Scanning photomicrograph of iron oxide pellet containing CaO 2.0%, SiO_2 1.0%, Al_2O_3 0.24% sintered at 1250°C for 3 hours. (1500 x).

Plate 4.41 X-Ray map of Calcium distribution in the area shown in Plate 4.40. (1500 x).

Plate 4.42 X-Ray map of silicon distribution in the area shown in Plate 4.40. (1500 x).

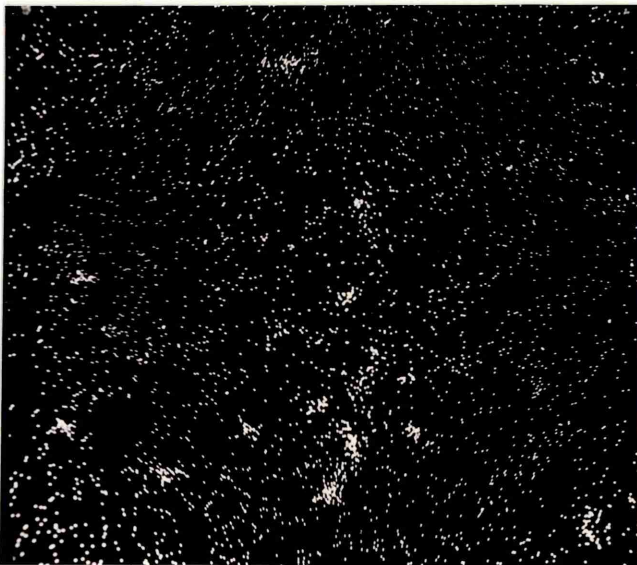
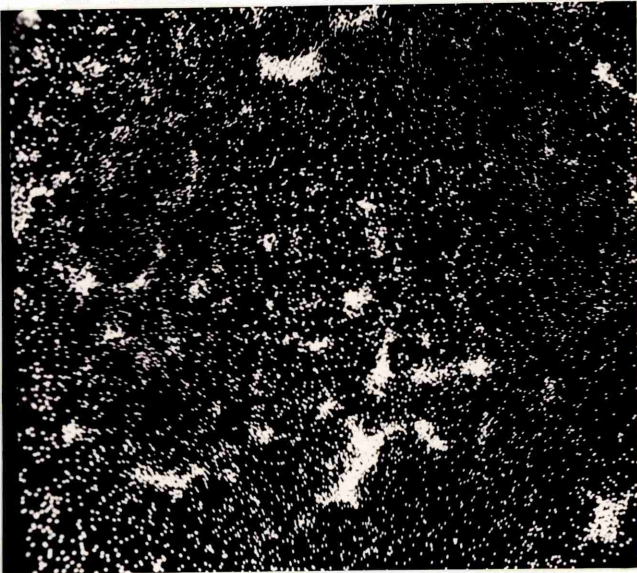
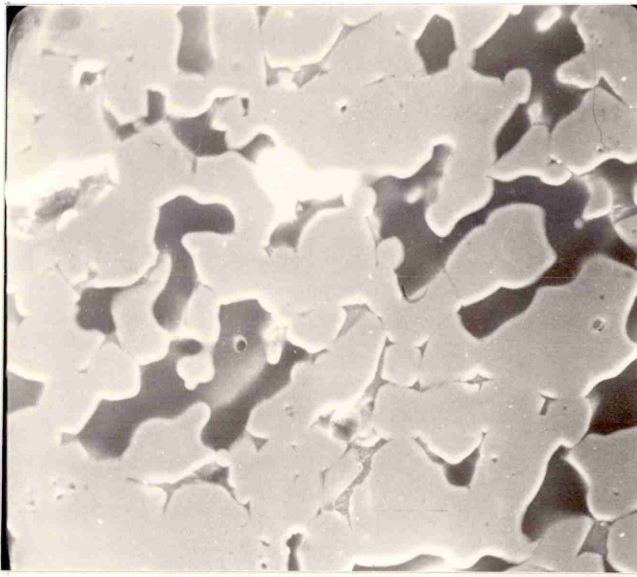


Plate 4.43 Scanning photomicrograph of iron oxide pellet containing CaO 5.0%, SiO₂ 1.0%, Al₂O₃ 0.24% sintered at 1250°C for 3 hours. (960 x).

Plate 4.44 X-Ray map of Calcium distribution in the area shown in Plate 4.43. (960 x).

Plate 4.45 X-Ray map of Silicon distribution in the area shown in Plate 4.43. (960 x).

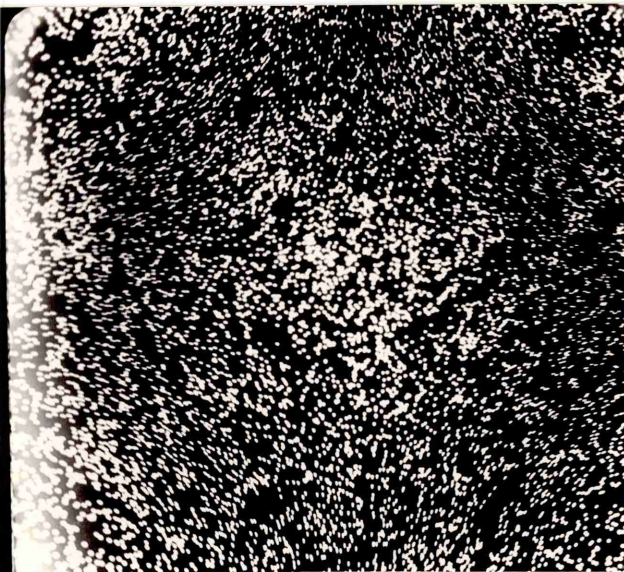
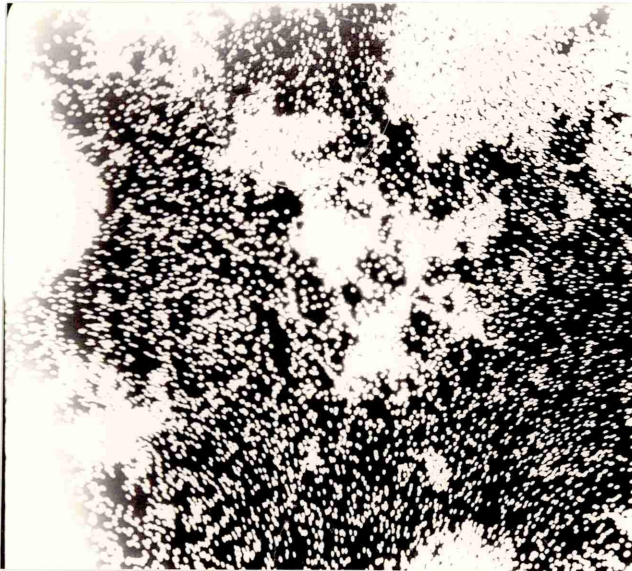
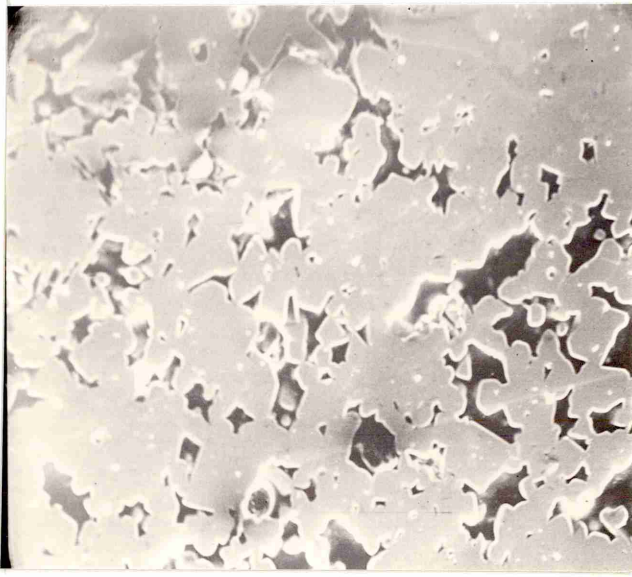


Plate 4.46 Scanning photomicrograph of iron oxide pellet containing CaO 1.0%, SiO₂ 0.22%, Al₂O₃ 1.0% sintered at 1250°C for 3 hours. (600 x).

Plate 4.47 X-Ray map of Aluminium distribution in the area shown in Plate 4.46. (600 x).

Plate 4.48 X-Ray map of Calcium distribution in the area shown in Plate 4.46. (600 x).

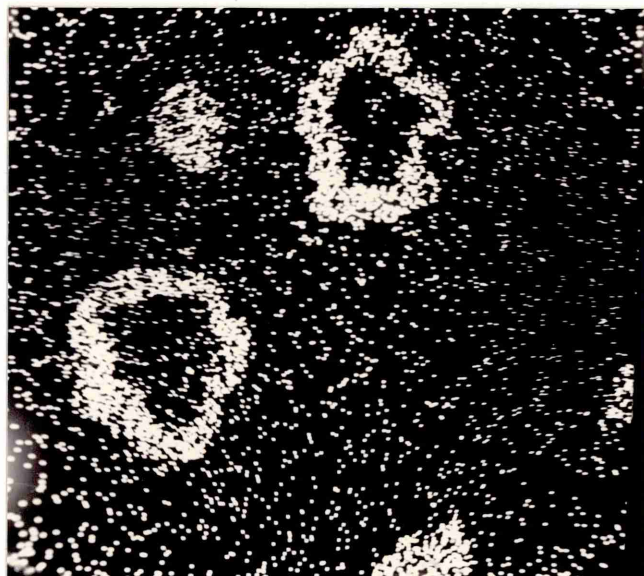
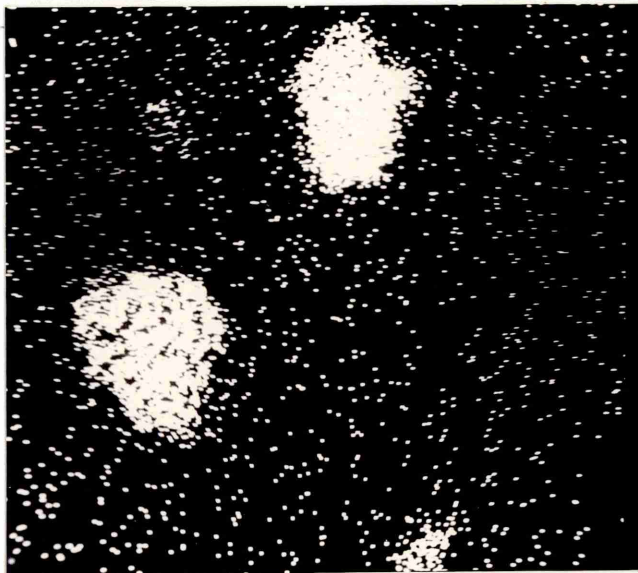
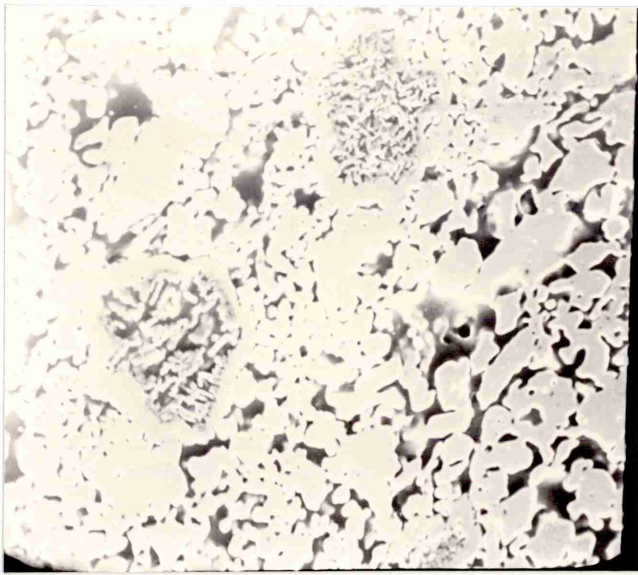


Plate 4.49 Scanning photomicrograph of iron oxide pellet containing CaO 4.0%, SiO_2 0.22%, Al_2O_3 1.0% sintered at 1250°C for 3 hours. (600 x).

Plate 4.50 X-Ray map of aluminium distribution in the area shown in Plate 4.49. (600 x).

Plate 4.51 X-Ray map of Calcium distribution in the area shown in Plate 4.49. (600 x).

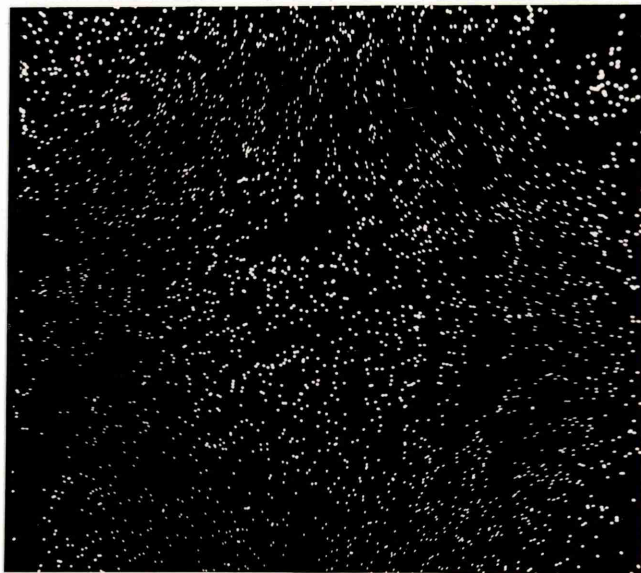


Plate 4.52 Scanning photomicrograph of iron oxide pellet containing CaO 1.0%, SiO₂ 1.0%, Al₂O₃ 1.0% sintered at 1250°C for 3 hours. (3000 x).

Plate 4.53 X-Ray map of aluminium distribution in area shown in Plate 4.52. (3000 x).

Plate 4.54 X-Ray map of Silicon distribution in area shown in Plate 4.52. (3000 x).

Plate 4.55 X-Ray map of Calcium distribution in area shown in Plate 4.52. (3000 x).

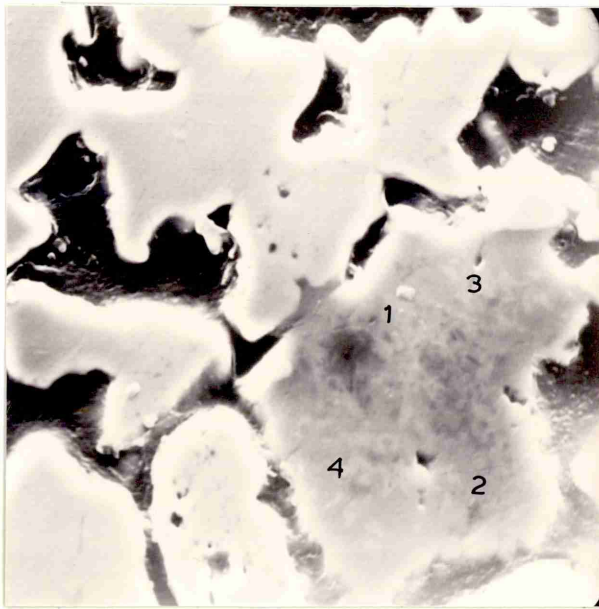


Plate 4.52



Plate 4.53



Plate 4.54



Plate 4.55

Plate 4.56 Scanning photomicrograph of iron oxide pellet containing CaO 4.0%, SiO₂ 1.0%, Al₂O₃ 1.0% sintered at 1250°C for 3 hours. (780 x).

Plate 4.57 X-Ray map of aluminium distribution in area shown in Plate 4.56. (780 x).

Plate 4.58 X-Ray map of Calcium distribution in area shown in Plate 4.56. (780 x).

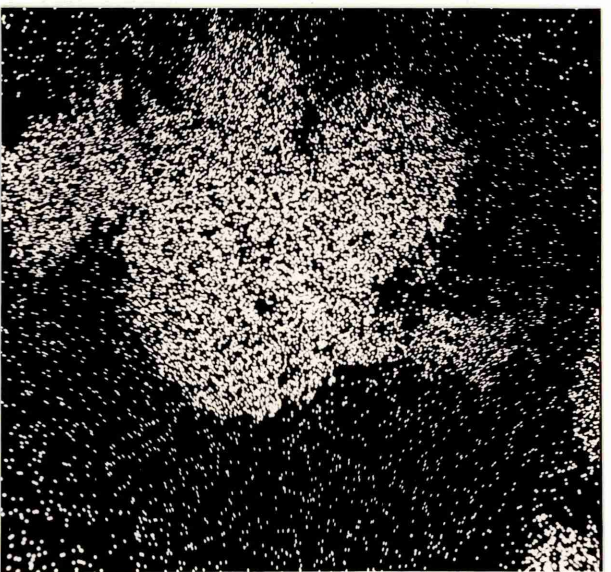
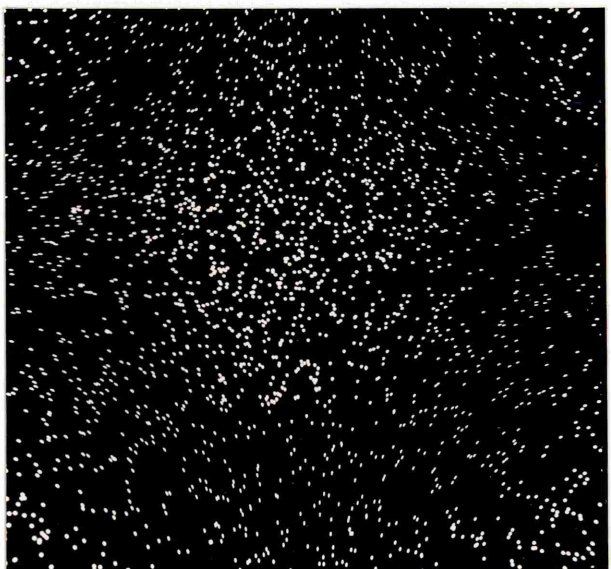
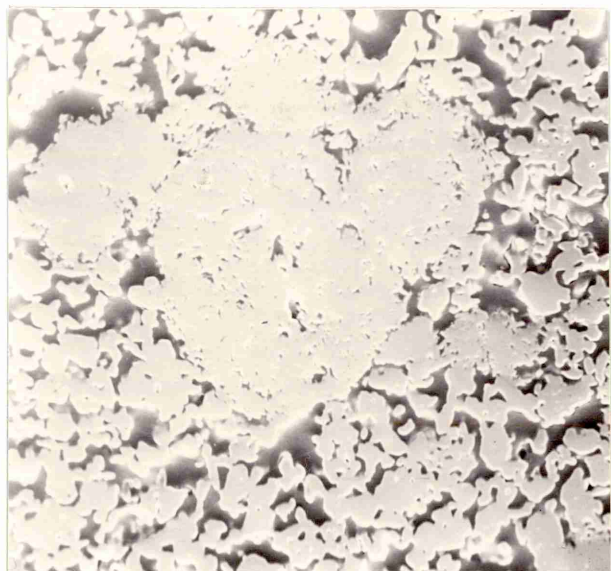


Plate 4.59 Scanning photomicrograph of iron oxide pellet containing CaO 1.0%, SiO₂ 0.22%, Al₂O₃ 0.24% sintered at 1325°C for 30 minutes. (1800 x).

Plate 4.60 X-Ray map of Calcium distribution in area shown in Plate 4.59. (1800 x).

Plate 4.61 X-Ray map of silicon distribution in area shown in Plate 4.59. (1800 x).

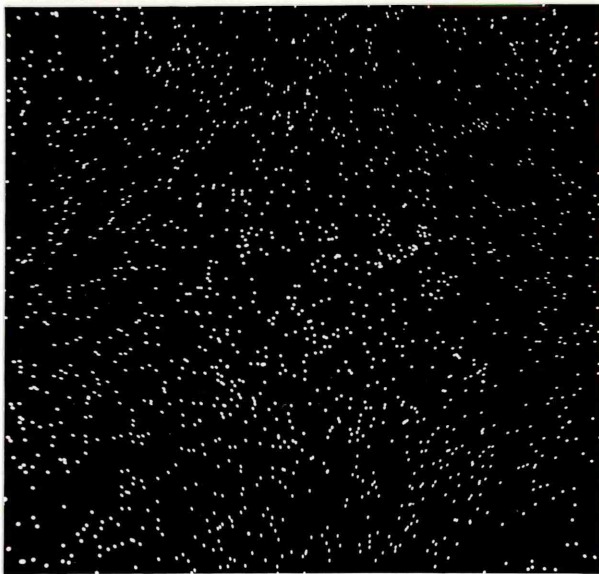
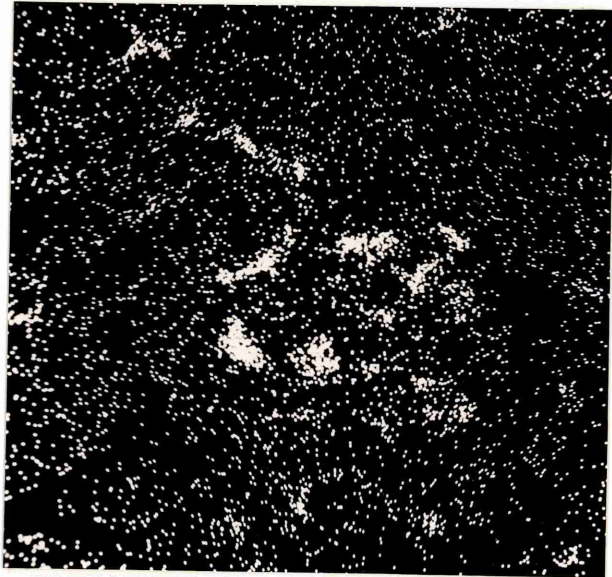
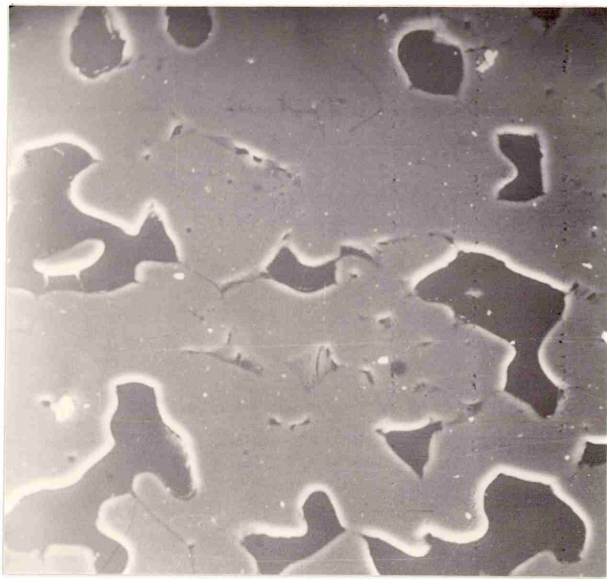


Plate 4.62 Scanning photomicrograph of iron oxide pellet containing CaO 3.0%, SiO₂ 0.22%, Al₂O₃ 0.24% sintered at 1325°C for 30 minutes. (1800 x).

Plate 4.63 X-Ray map of Calcium distribution in area shown in Plate 4.62. (1800 x).

Plate 4.64 X-Ray map of Silicon distribution in area shown in Plate 4.62. (1800 x).

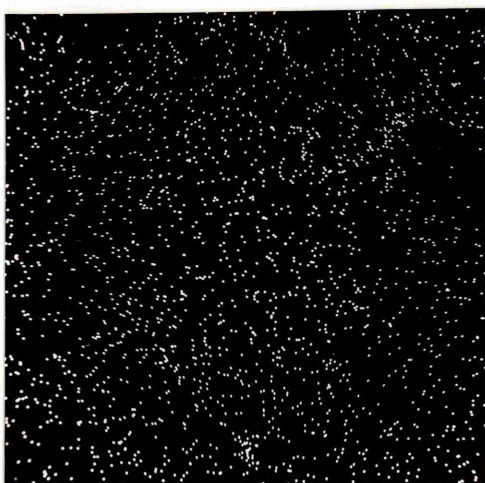
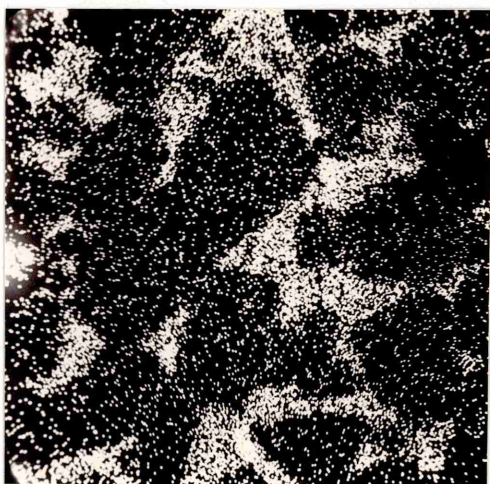
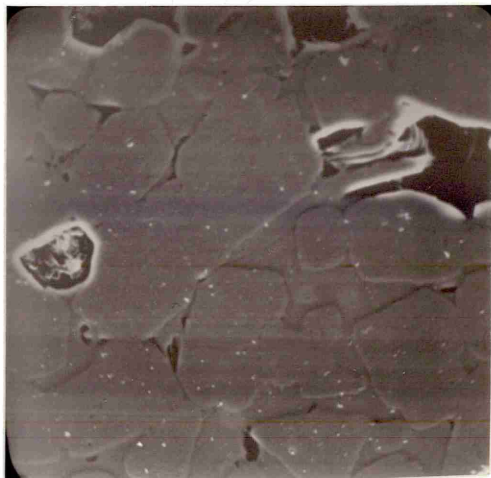


Plate 4.65 Scanning Photomicrograph of iron oxide pellet
containing CaO 1.0%, SiO₂ 3.0%, Al₂O₃ 0.24%
sintered at 1250°C for 12 hours. (1800 x).

Plate 4.66 X-Ray map of Calcium distribution in area
shown in Plate 4.65. (1800 x).

Plate 4.67 X-Ray map of Silicon distribution in area
shown in Plate 4.65. (1800 x).

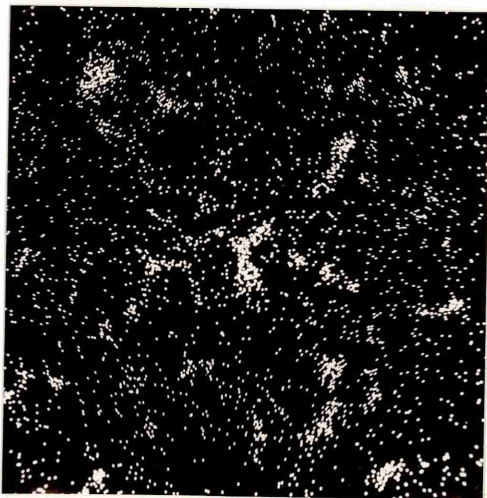
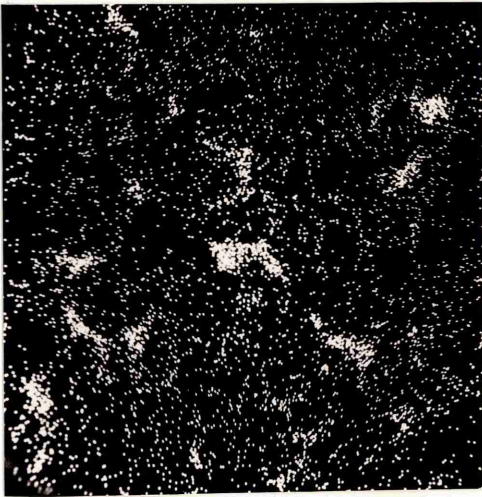
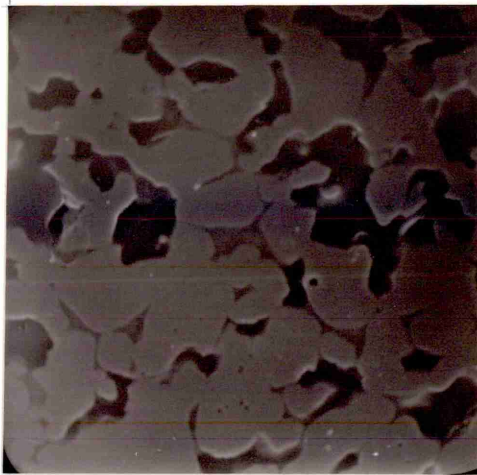


Plate 4.68:- Reduced iron oxide pellets showing different modes of reduction (35x)


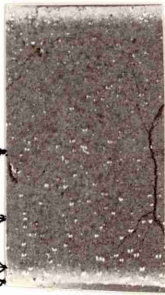






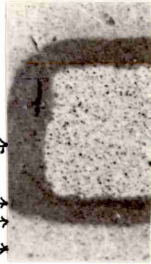

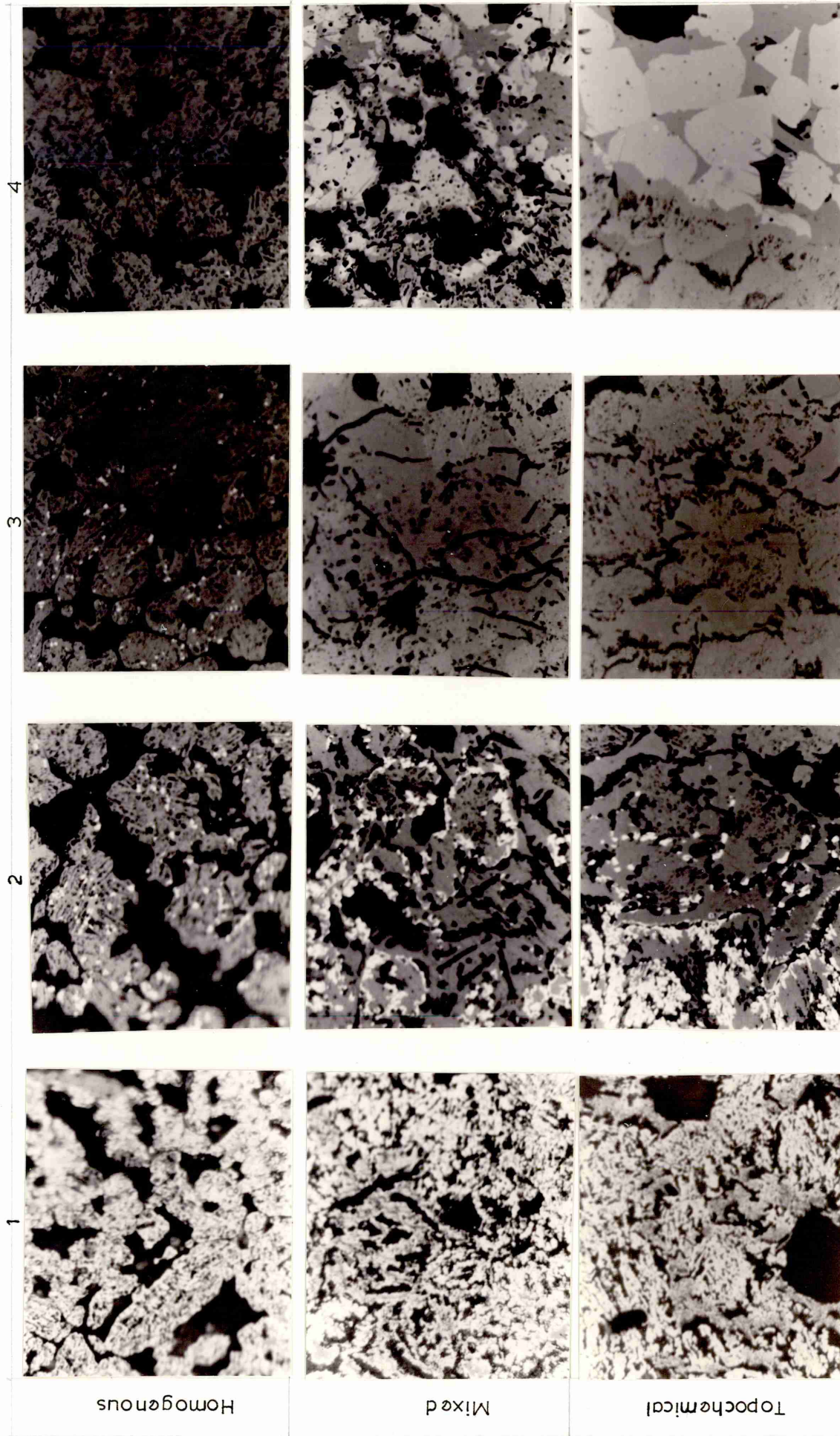
% Reduction Mode of Reduction	33%	38%	50%	58%	68%
Homogeneous					
Mixed					
Topochemical					

Plate 469 Micrograph(320X) relating to the different modes of reduction and positions indicated in plate 4.68 .



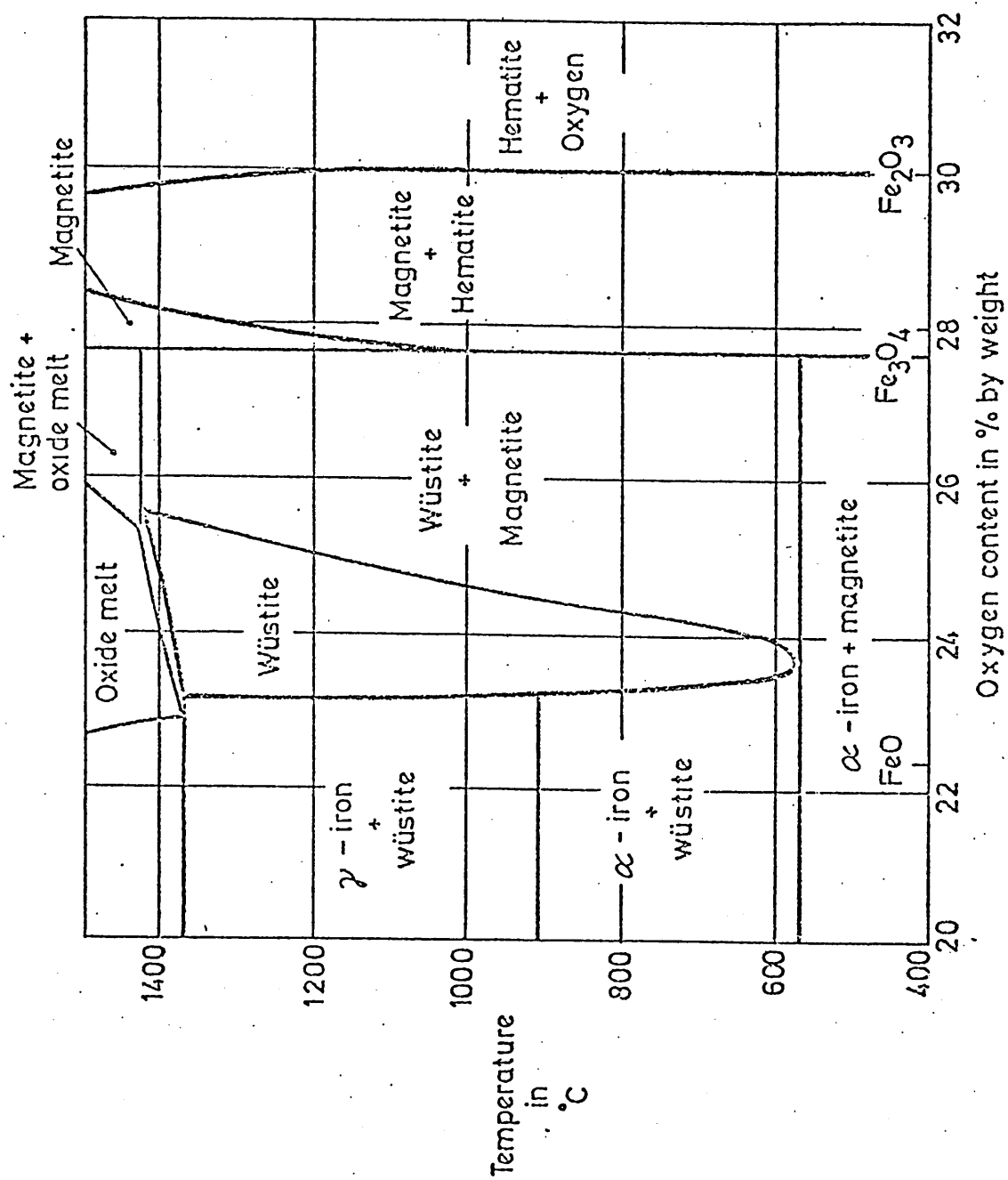


FIG. 2.1 A SECTION OF THE IRON-OXYGEN PHASE DIAGRAM. ⁽¹⁾

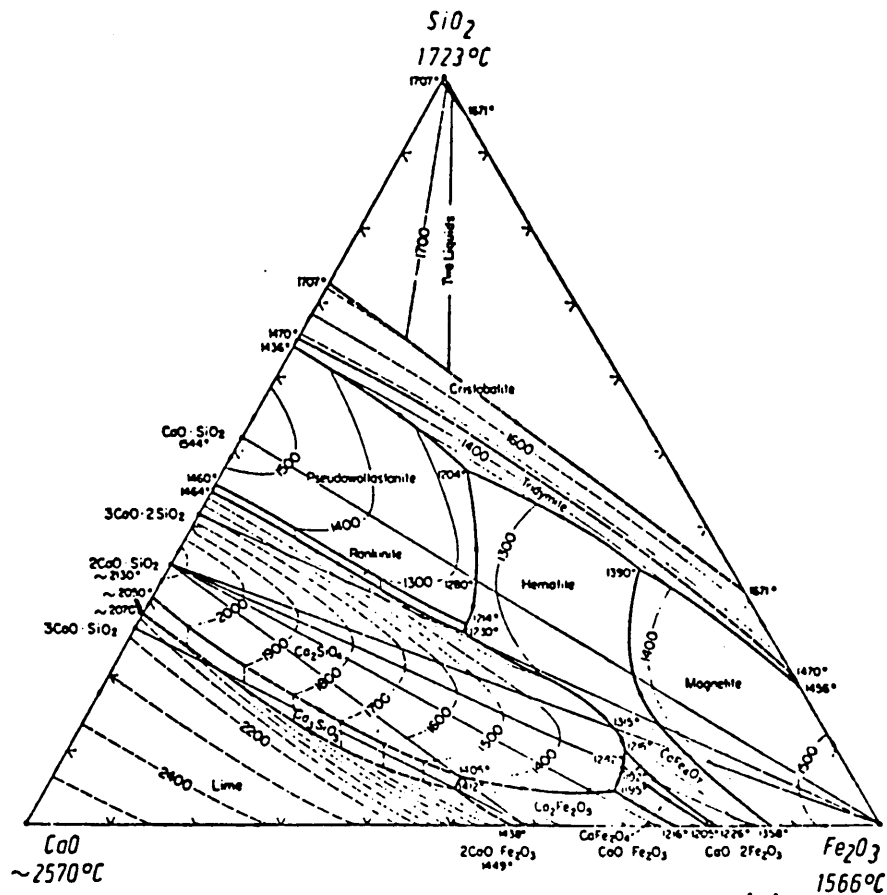


FIG:2.2(a) A Phase diagram of CaO-Fe₂O₃-SiO₂ system⁽⁹⁾

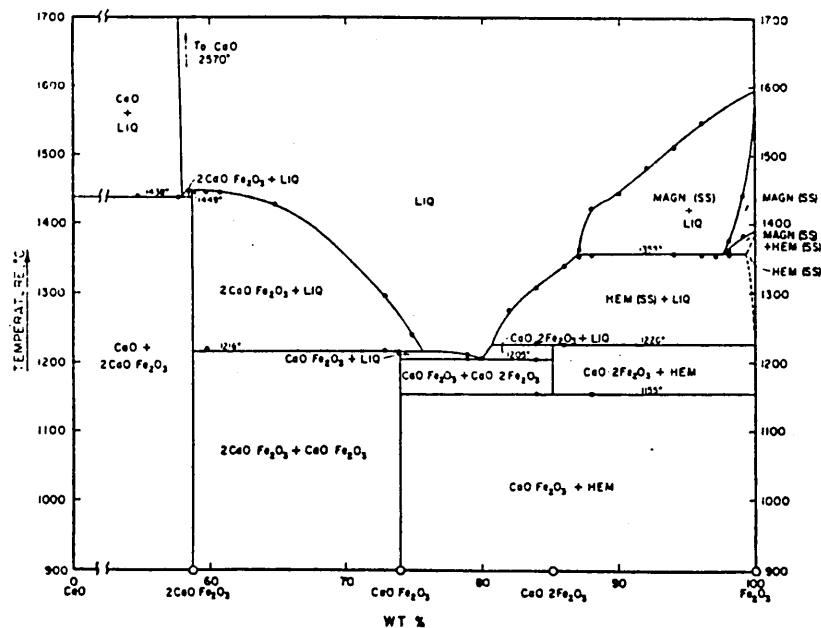


FIG:2.2(b) Phase equilibrium diagram for the CaO-Fe₂O₃ system at one atmosphere pressure of oxygen, as a function of temperature and composition. (Reproduced from Philips and Muan⁽⁹⁾).

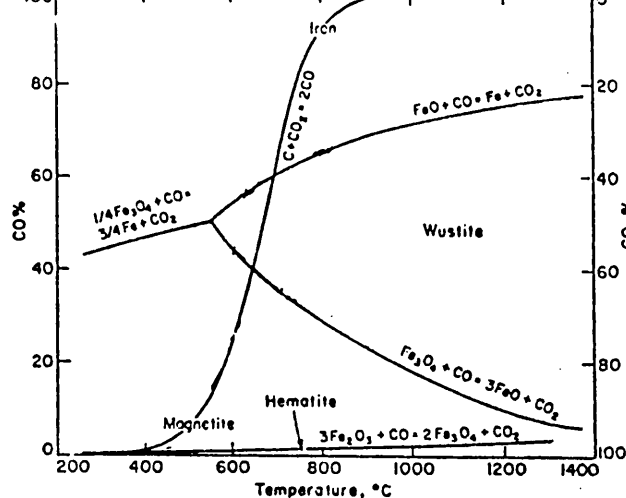


Fig.2.3 Influence of temperature on the CO/CO₂ gas compositions in equilibrium with Fe₂O₃/Fe₃O₄, Fe₃O₄/FeO, FeO/Fe and with carbon(28).

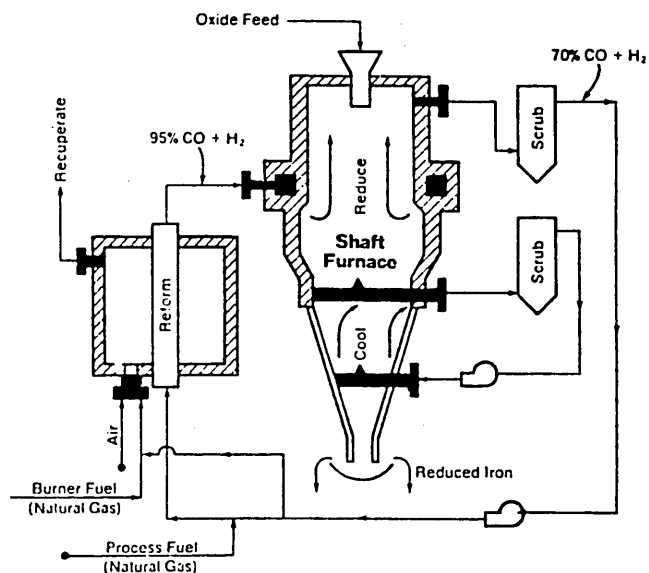


Fig.2.4 Midrex Direct Reduction Process Standard flow Sheet(28).

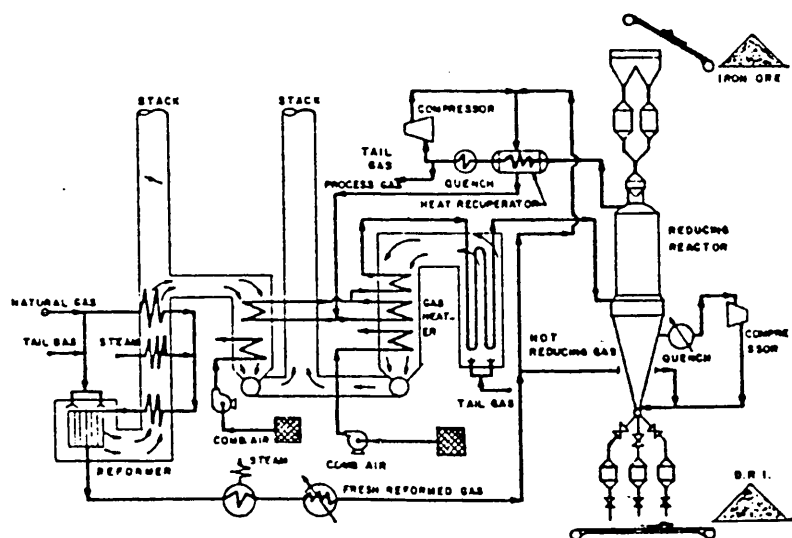


Fig.2.5 HYL 111 Direct Reduction Process diagram(30).

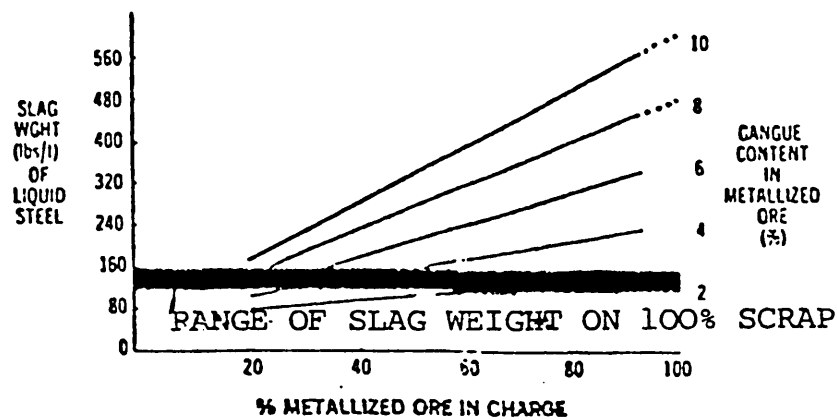


Fig. 2.6 — Effect of gangue on slag weight.

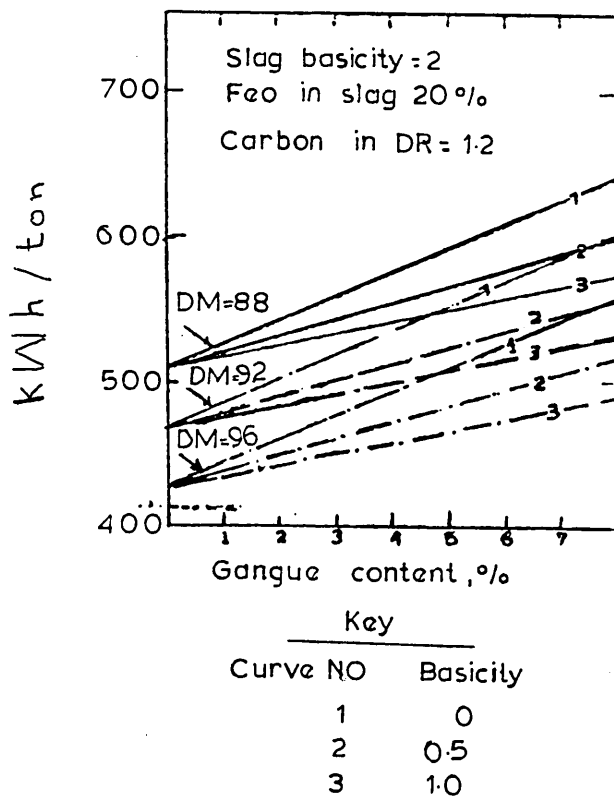


Fig:2.7 Effect of the gangue content on the energy required to produce 1 ton of liquid steel (31).

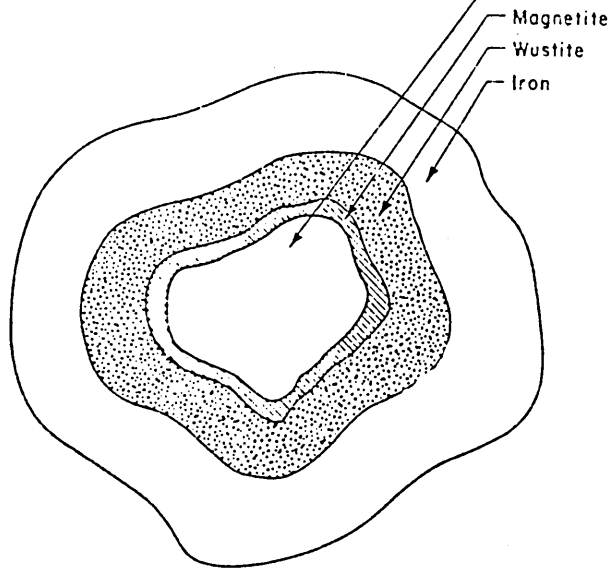


FIG.2.8 Cross-section of a partially reduced dense iron ore particle showing topochemical type of reduction(28) .

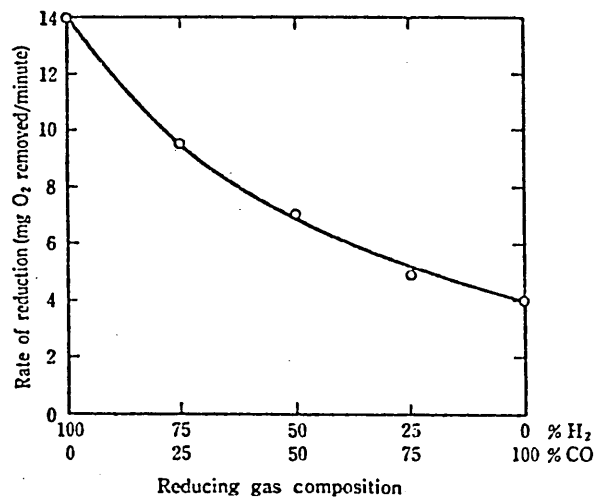


Fig.2.9 Effect of gas composition on the rate of reduction of dense briquettes at 1 000°C(60) .

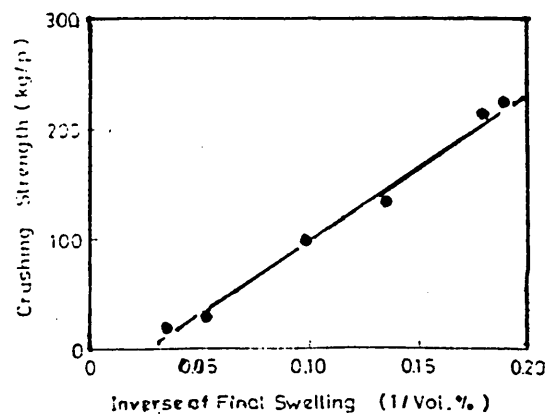


Fig.2.10 Relationship between crushing strength of the metallized peller and the inverse of degree of final swelling(81)

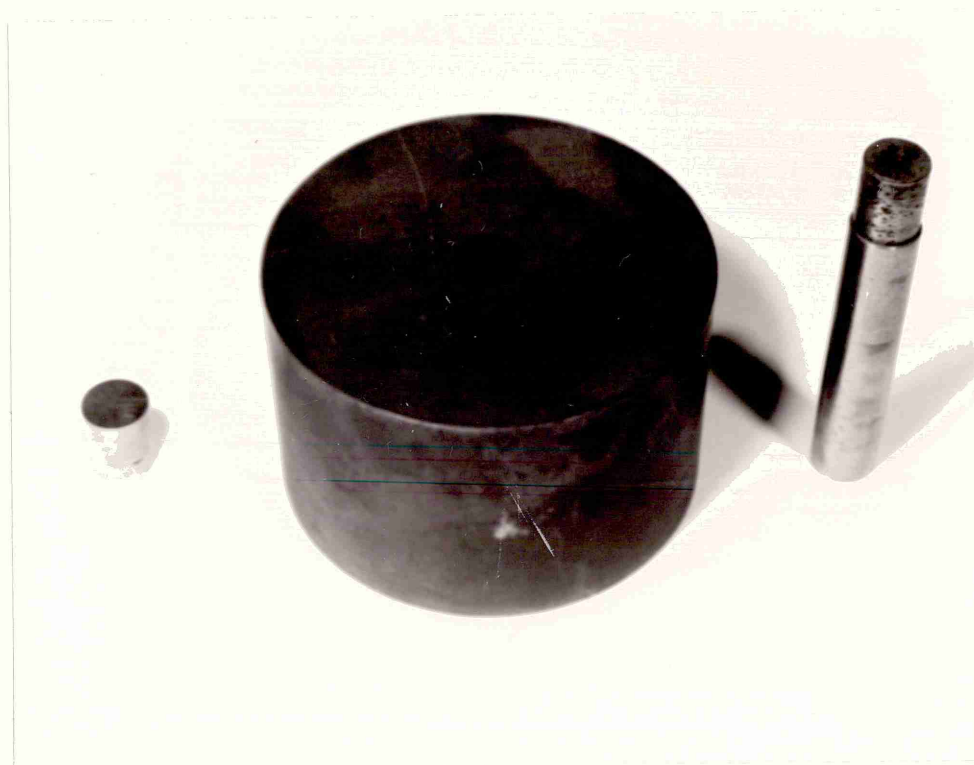
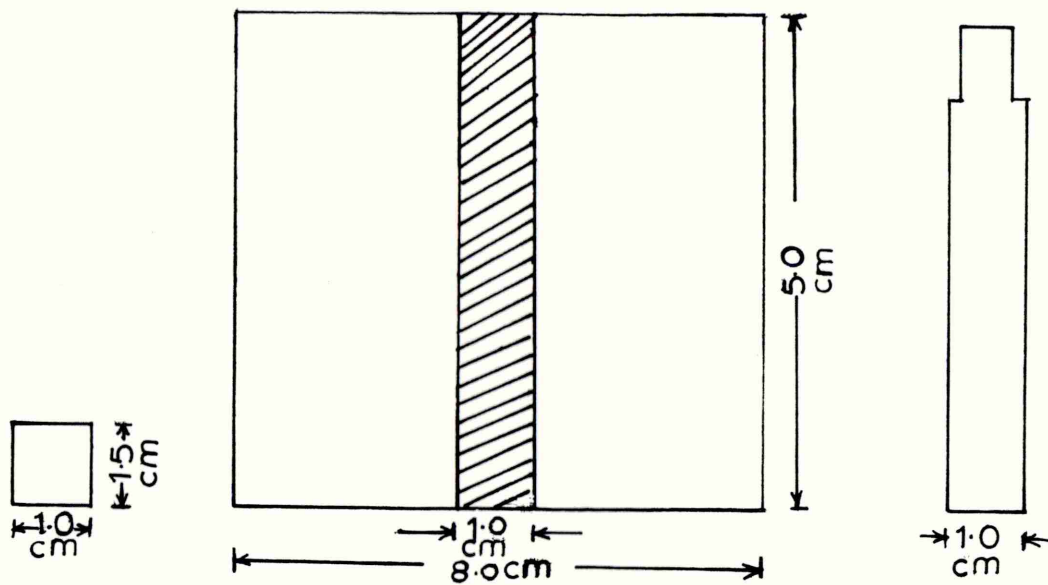


FIG 3-1 DIE FOR PELLET FORMING

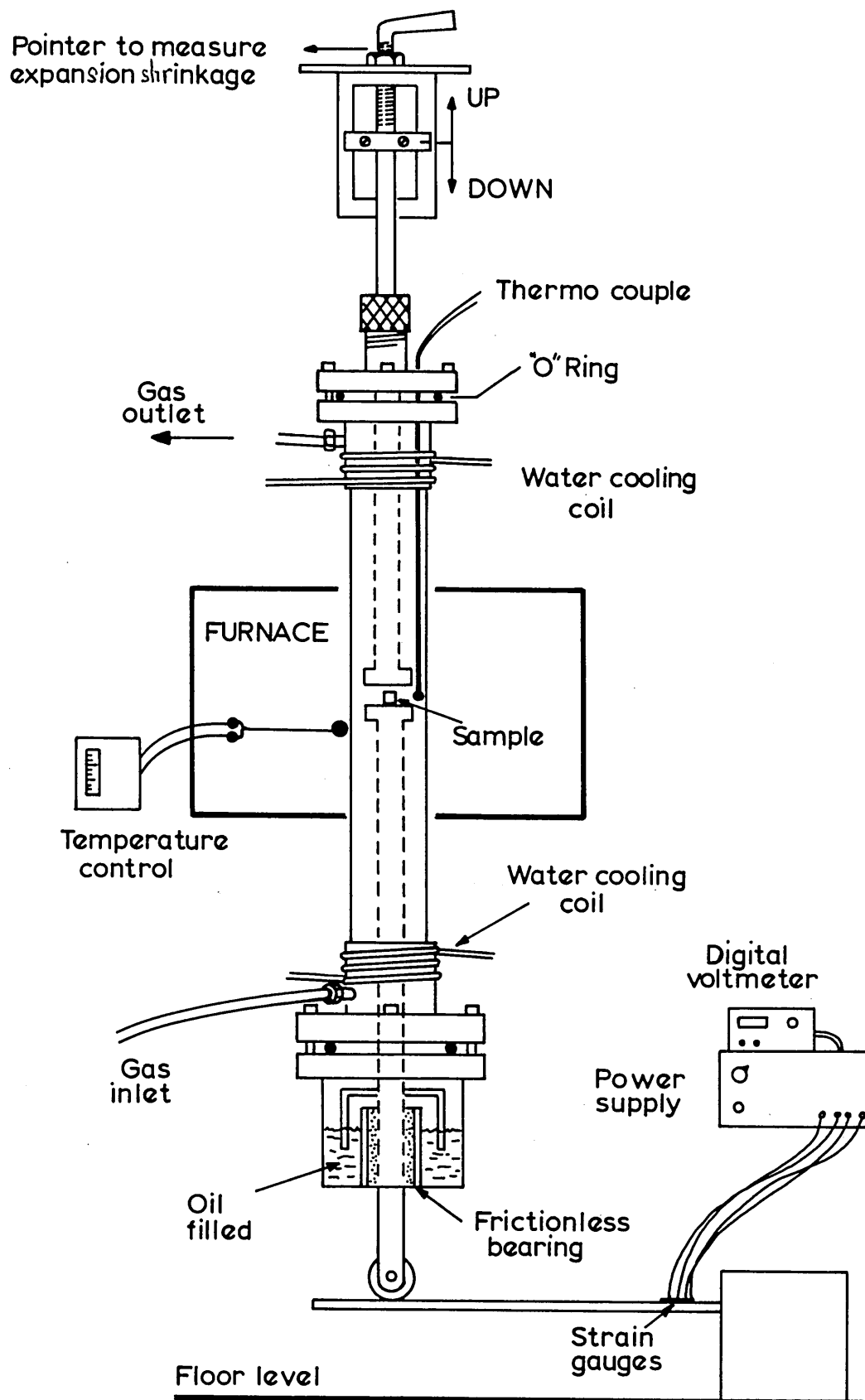


FIG.3-2 REDUCTION UNDER LOAD APPARATUS.

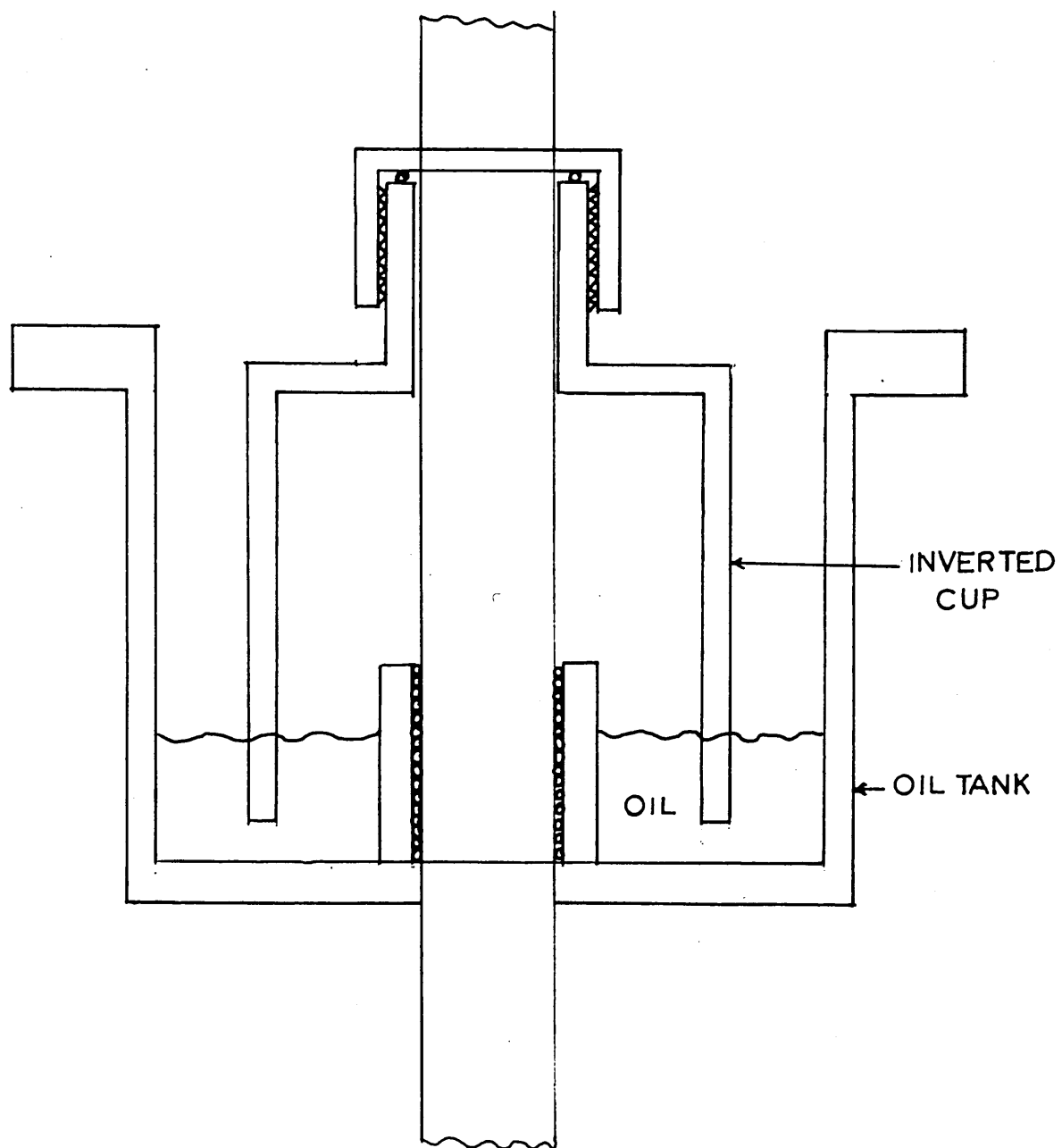


FIG 3-3 OIL SEAL

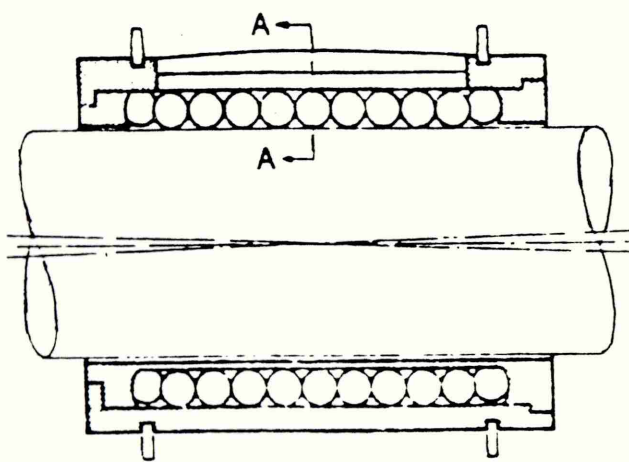


Fig3.4 Bearing.

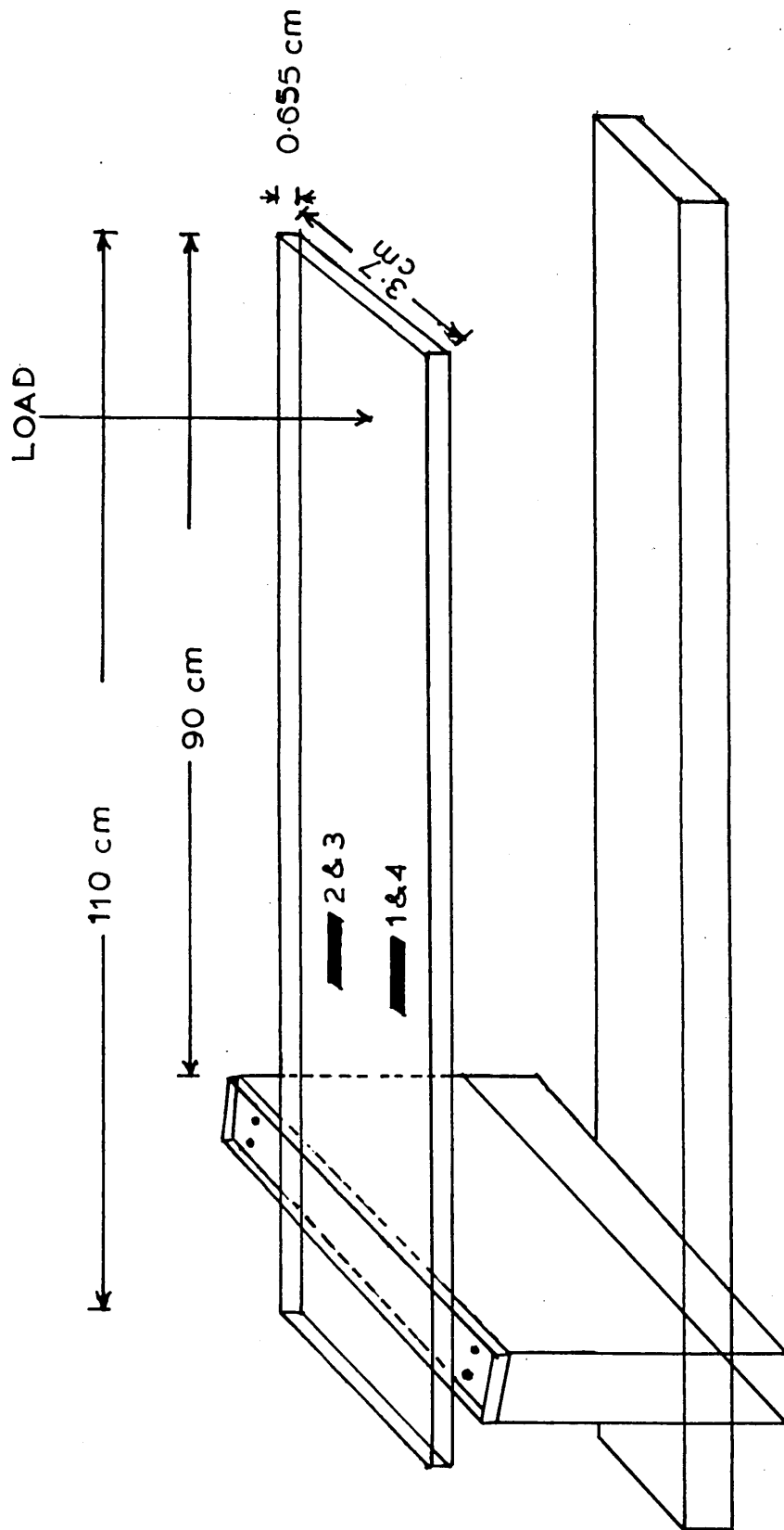
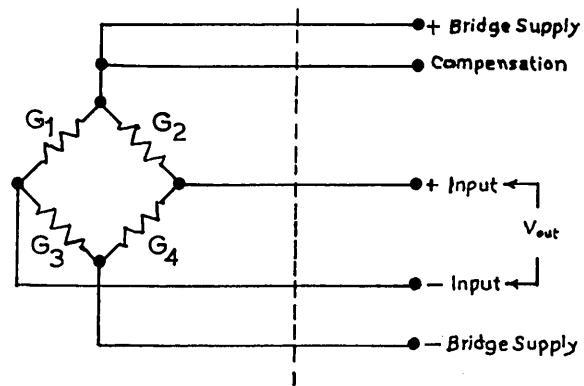


FIG 3.5 CANTILEVER BEAM WITH 1 TO 4 STRAIN GAUGES.



$$V_{out} = e \times V \times G$$

Where

V_{out} is in μV .

e is strain in microstrain.

V is bridge voltage.

G is gauge factor.

$G_1 G_2 G_3 G_4$ all active gauges.

FIG 3.6 STRAIN GAUGES BRIDGE.

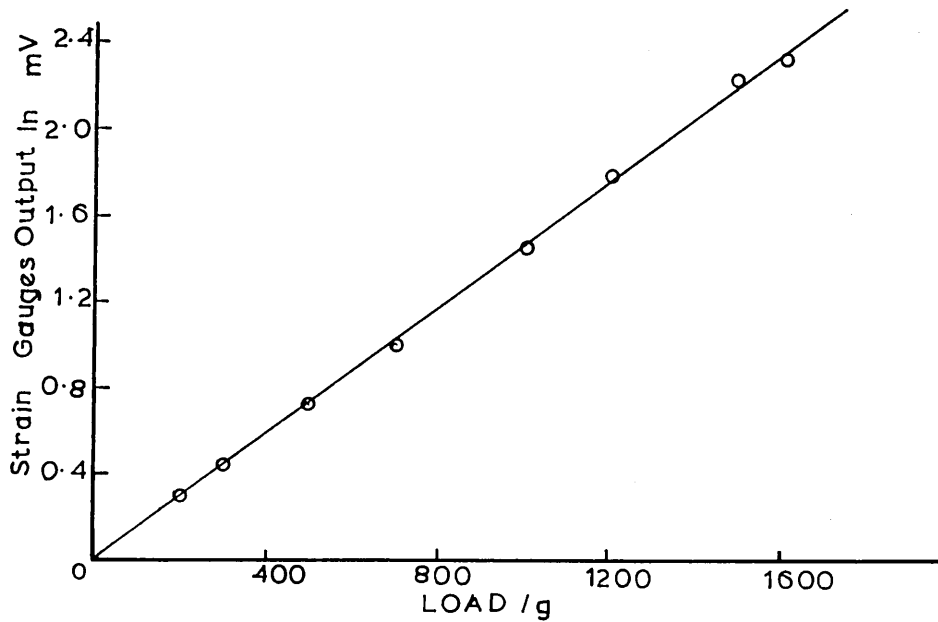


FIG 3.7 Calibration Of Strain-Gauged Cantilever Beam At 90 cm From Fixed End.

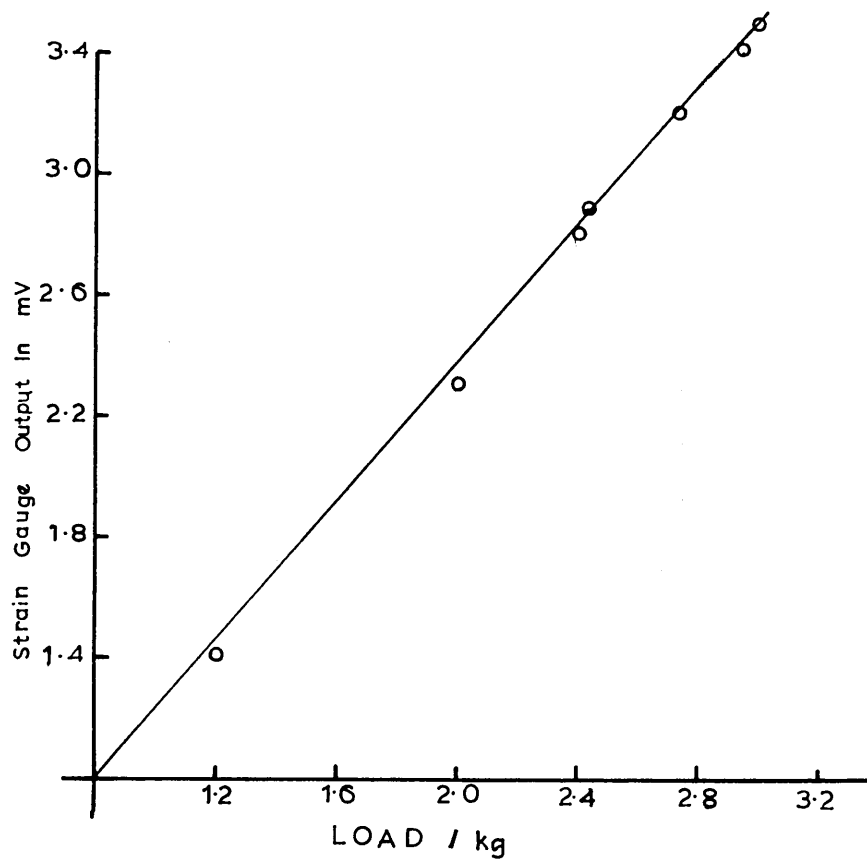


FIG 3-8 Calibration Of Strain Gauged Cantilever Beam
At 60 cm From Fixed End.

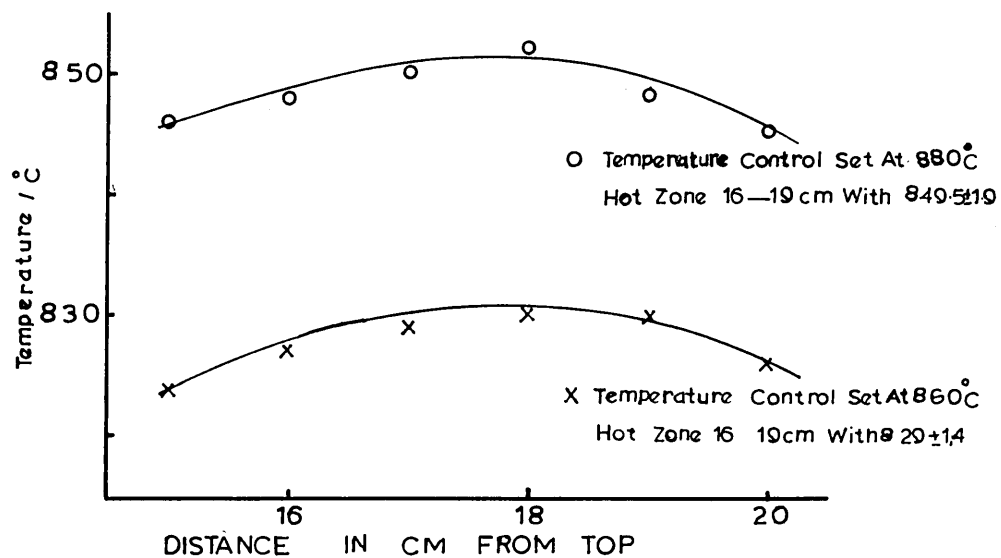


FIG 3-9 Temperature Profile In Reduction Under Load
Apparatus

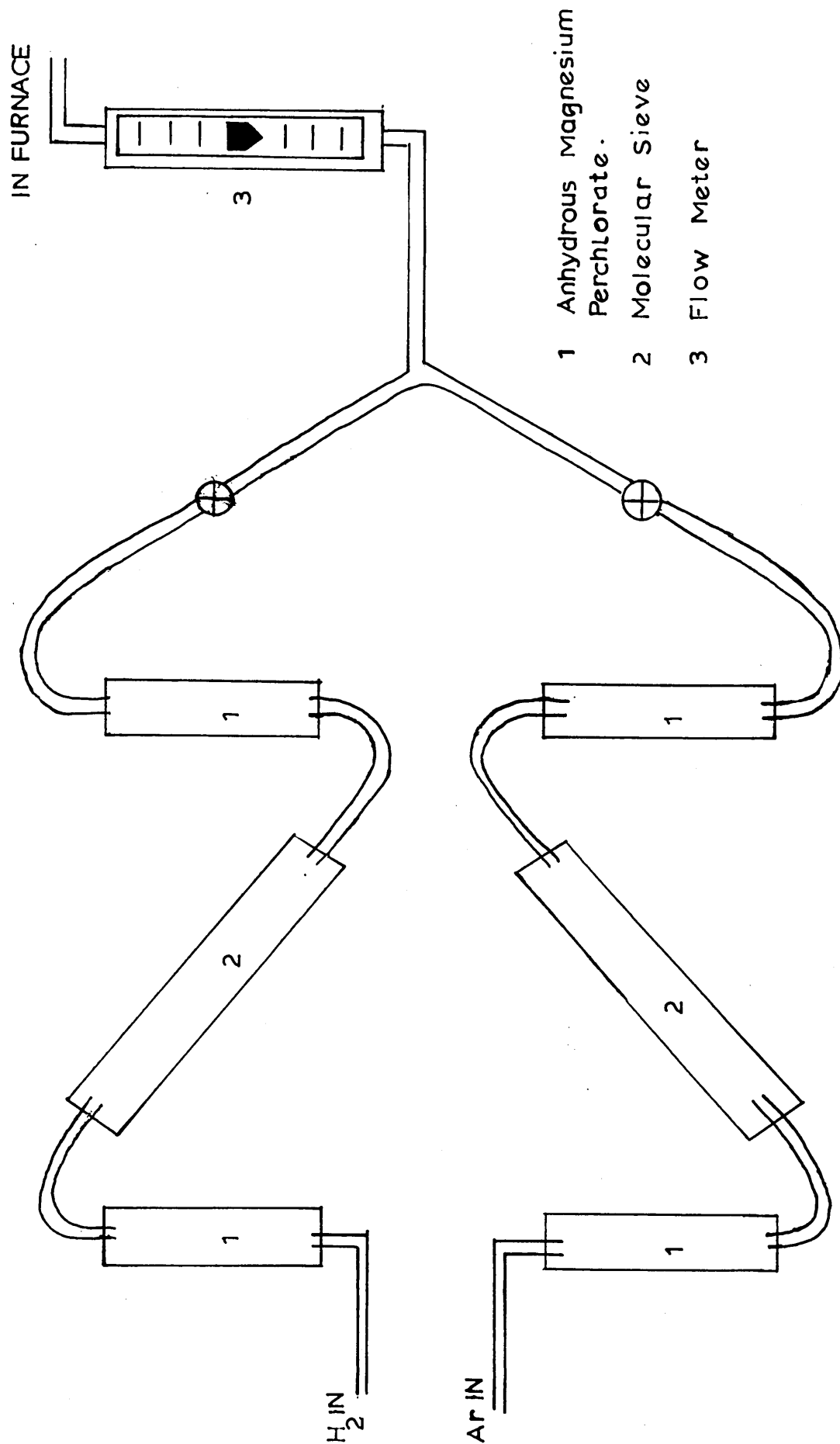


FIG 3-10 GAS PURIFICATION TRAIN.

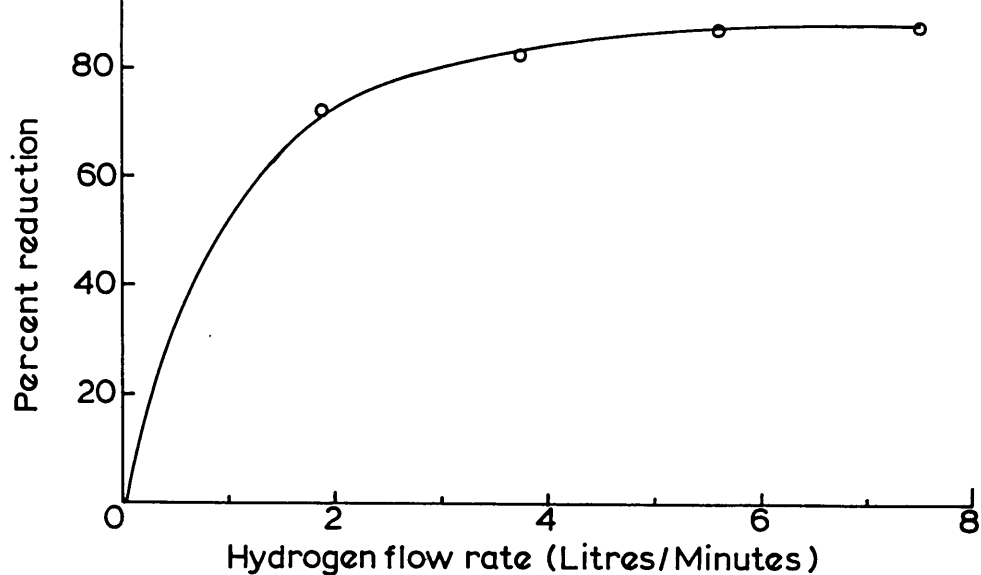


FIG. 3-11 THE REDUCTION OF COMMERCIAL HEMATITE PELLET, REDUCED IN HYDROGEN AT 850°C FOR 10 MINUTES.

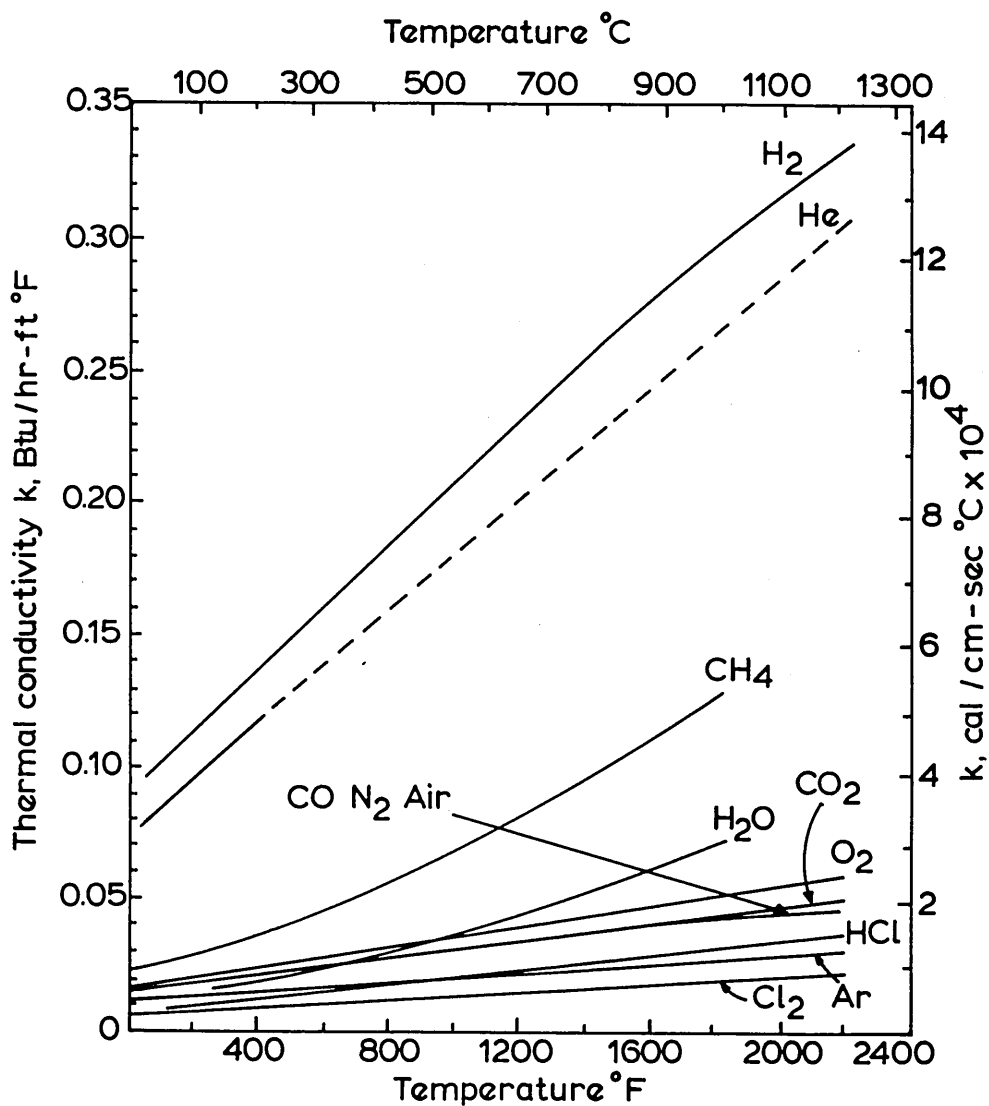


FIG. 3-12 THERMAL CONDUCTIVITY OF SEVERAL GASES. DATA VALID FOR UP TO 10 ATM.

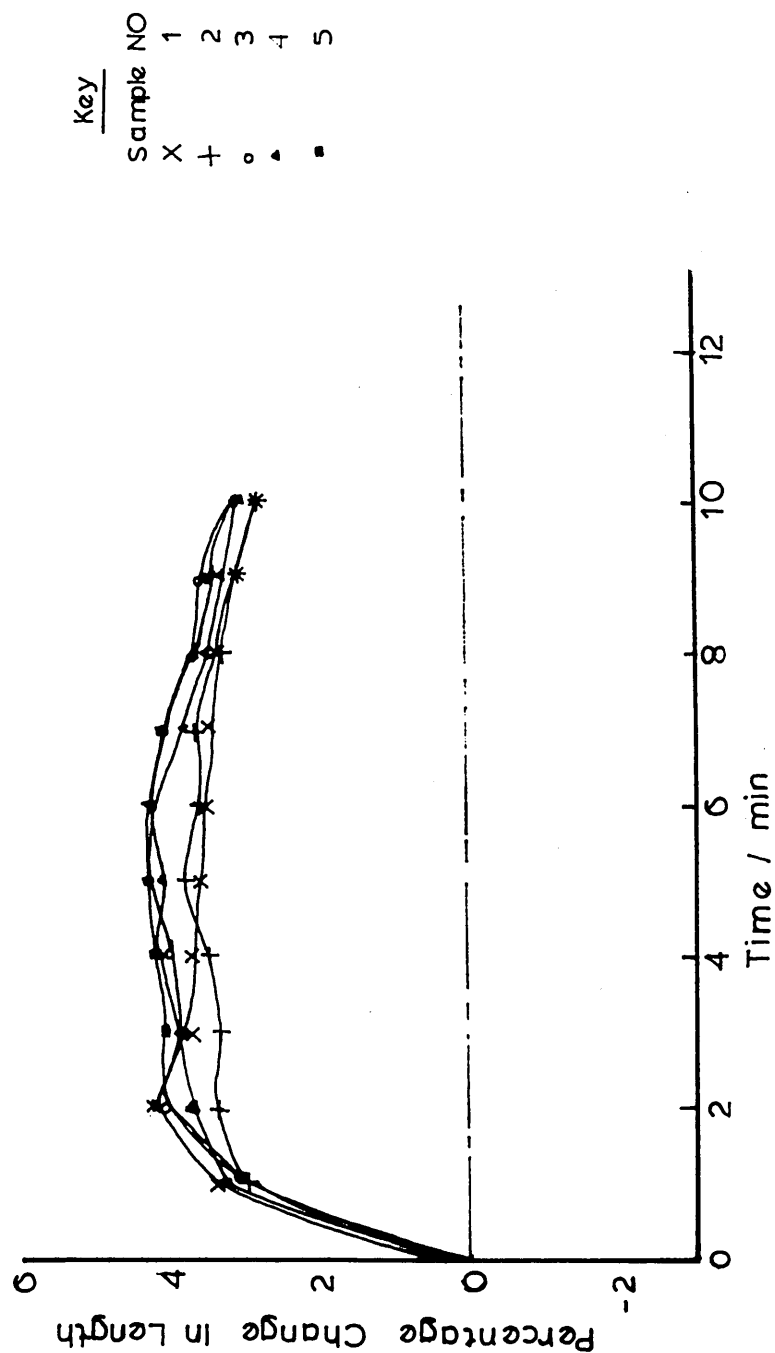


Fig.3.13 Values of percentage change in length against time for five samples (B_4) reduced at 850°C at a constant stress of 0.75 mg cm⁻². (sintered at 1325°C).

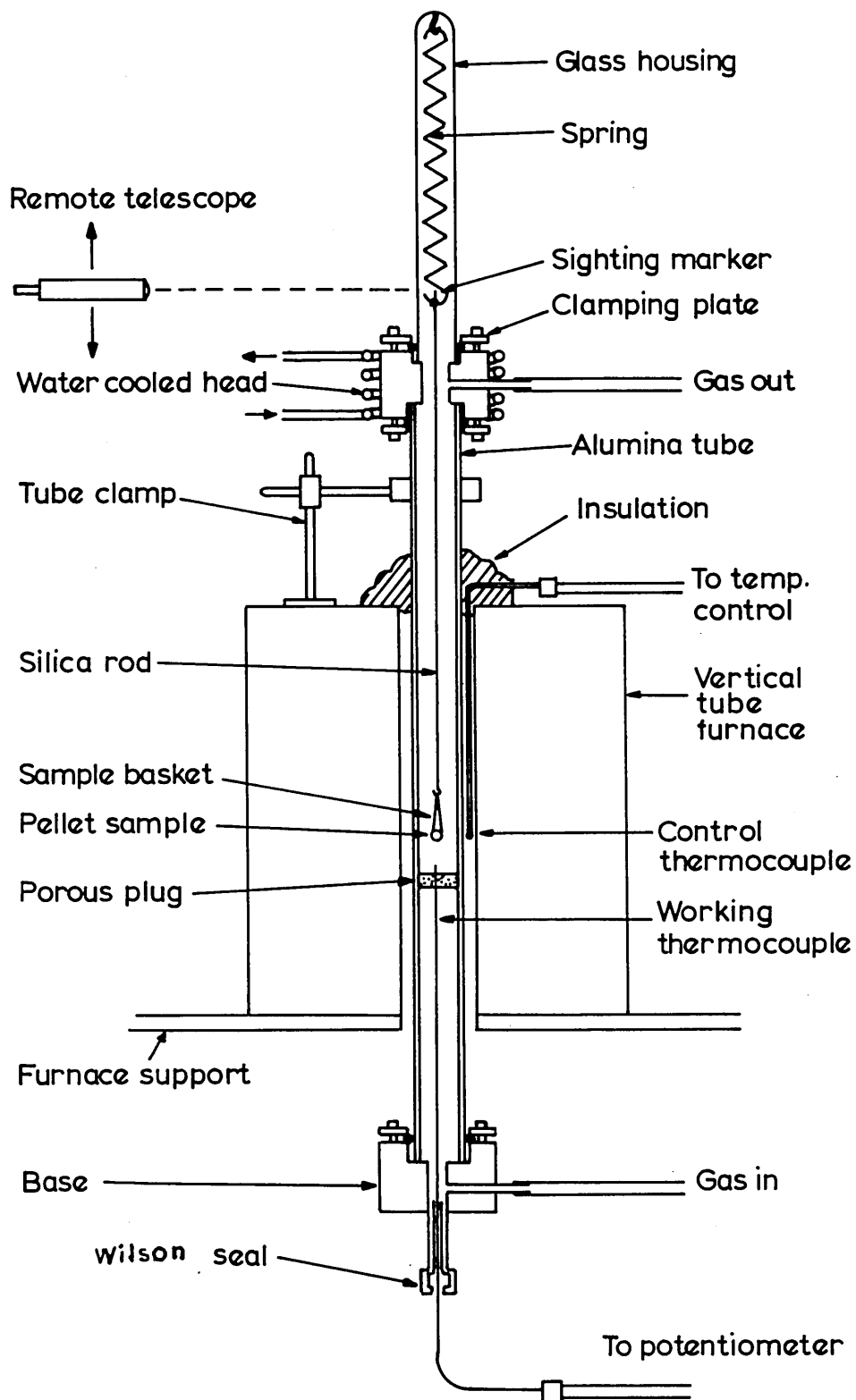


FIG. 3-14

THERMOGRAVIMETRIC TEST RIG.

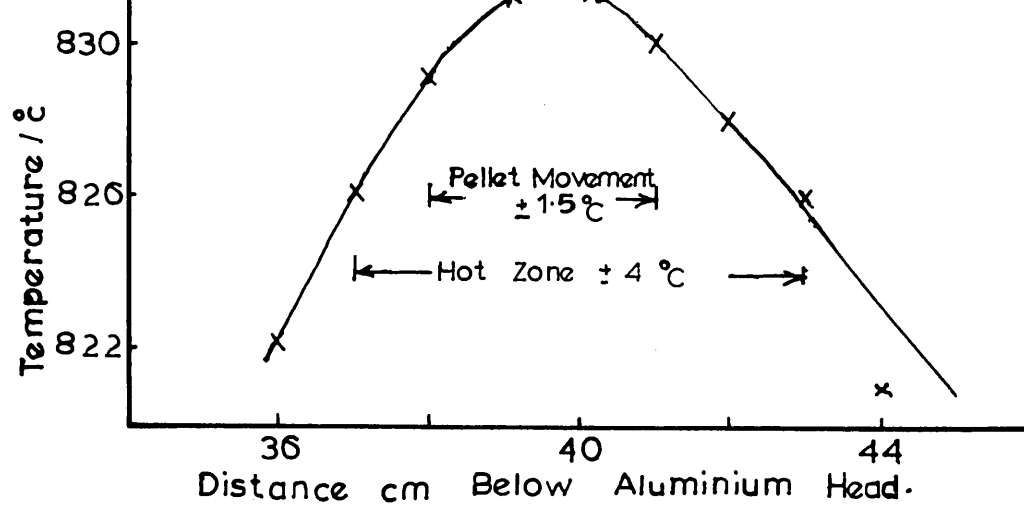


FIG 3.15 Temperature Profile In Specimen Chamber.

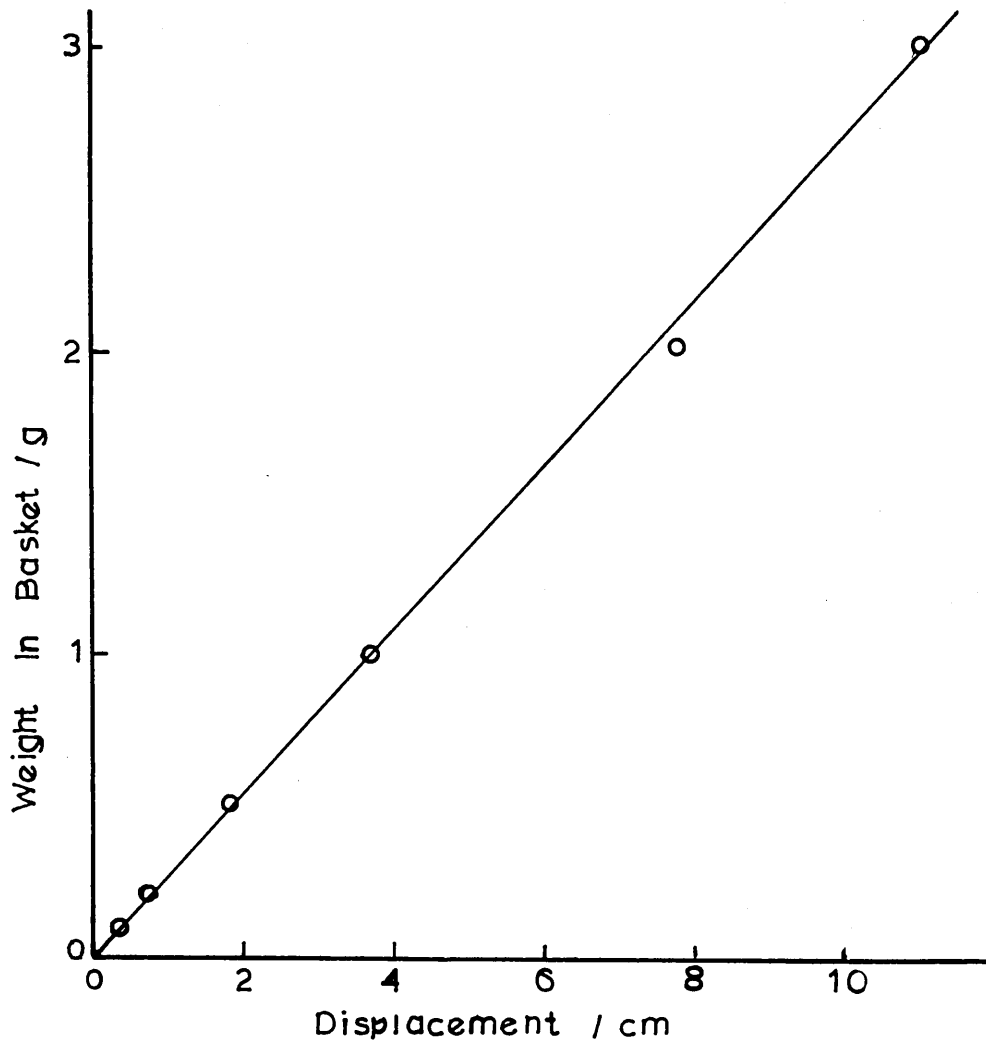


FIG 3.16 The Suspended Weight Plotted Against The Spring Displacement.

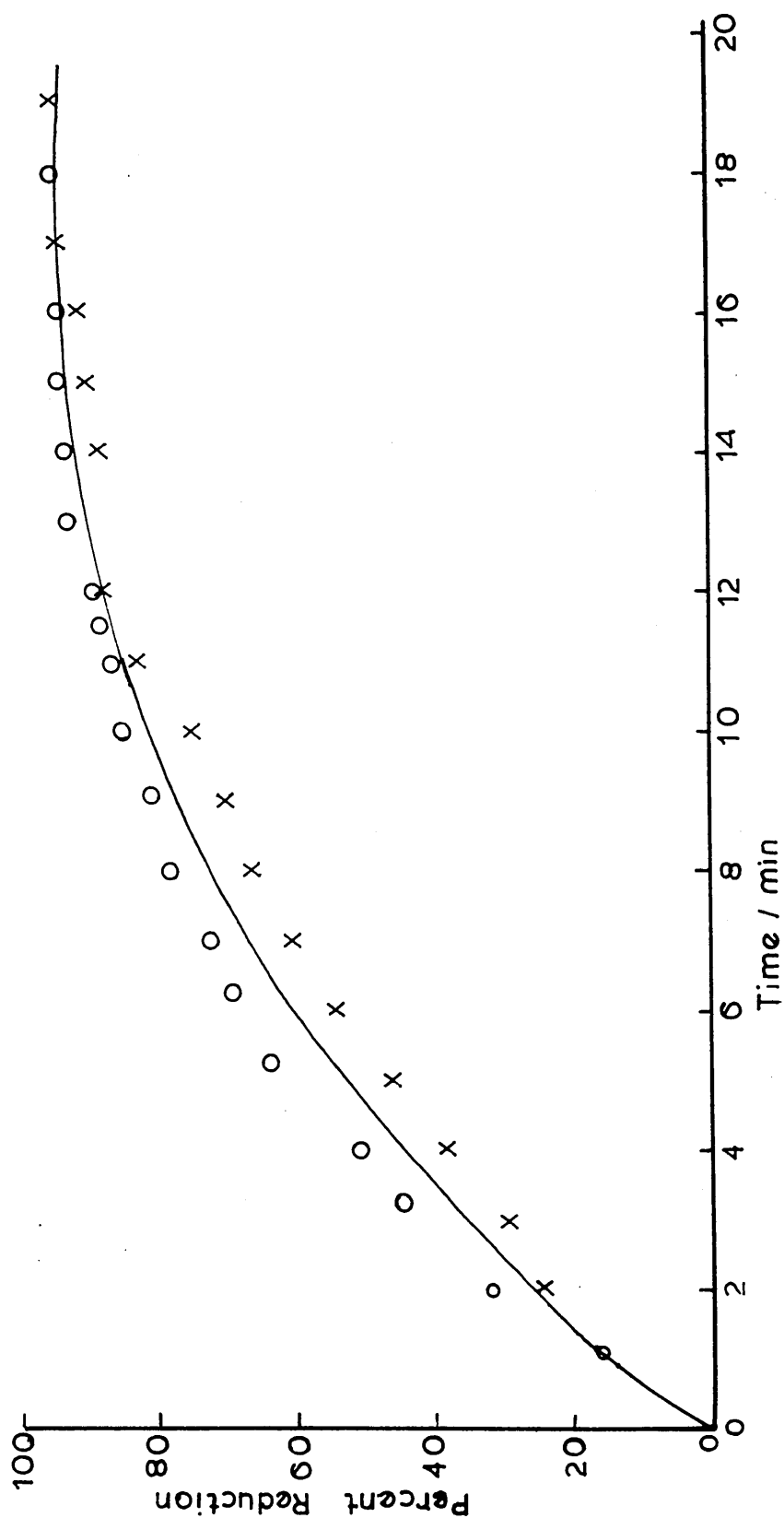


Fig.3.17 Iron oxide pellets containing 1.0% lime and 0.22% silica reduced in hydrogen at 830°C, sintered at 1250°C. (Two different tests carried out under the same reduction conditions).

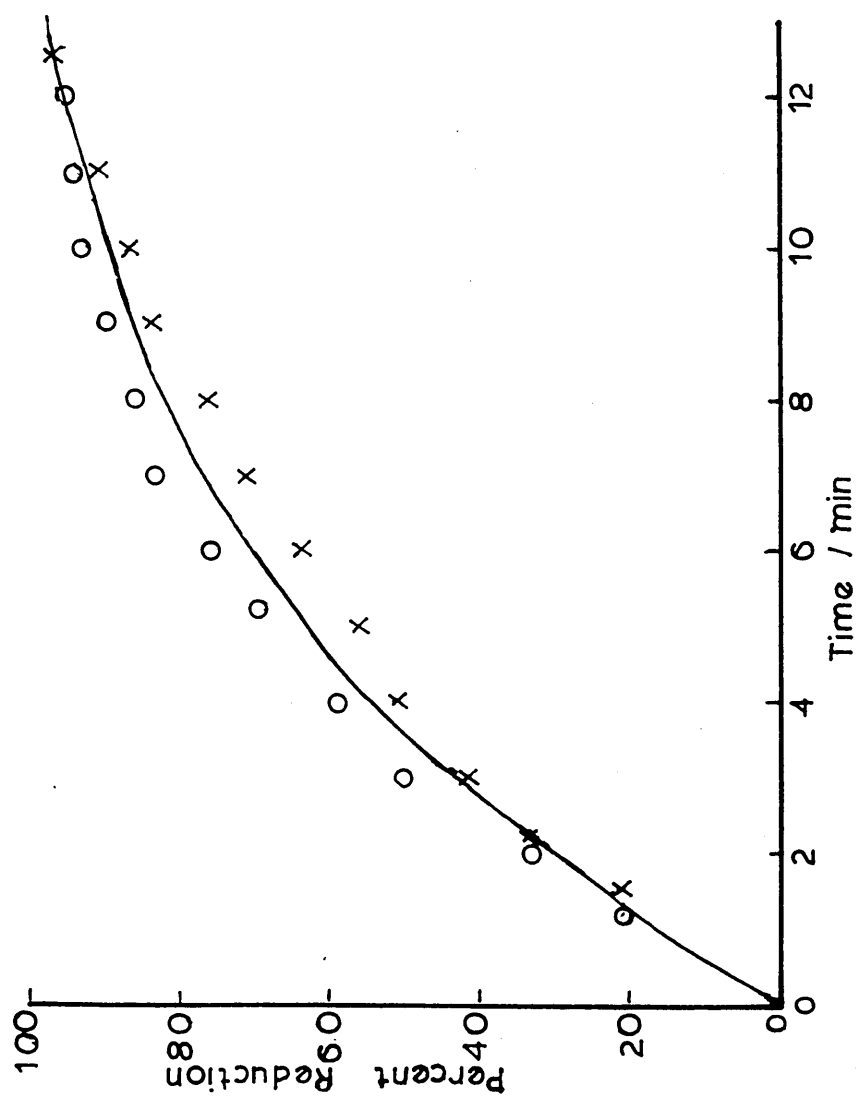


Fig. 3.18 Iron oxide pellets containing 1% lime and 1% silica reduced in hydrogen at 830°C, sintered at 1250°C. (Two different tests carried out under the same reduction conditions).

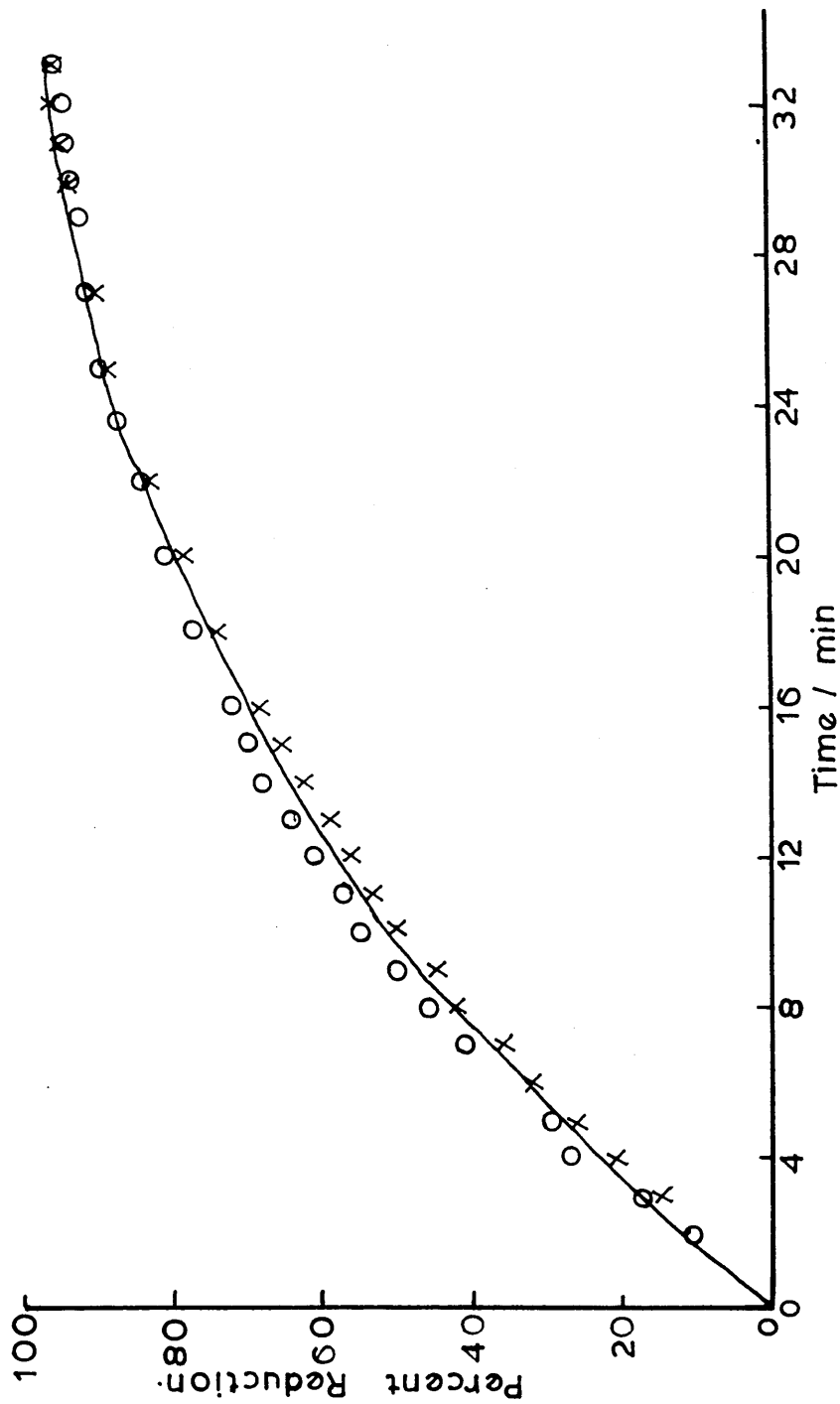


Fig.3.19 Iron oxide pellet containing 5.0% lime and 22% silica reduced in hydrogen at 830°C, sintered at 1250°C. (Two different tests carried out under the same reduction conditions).

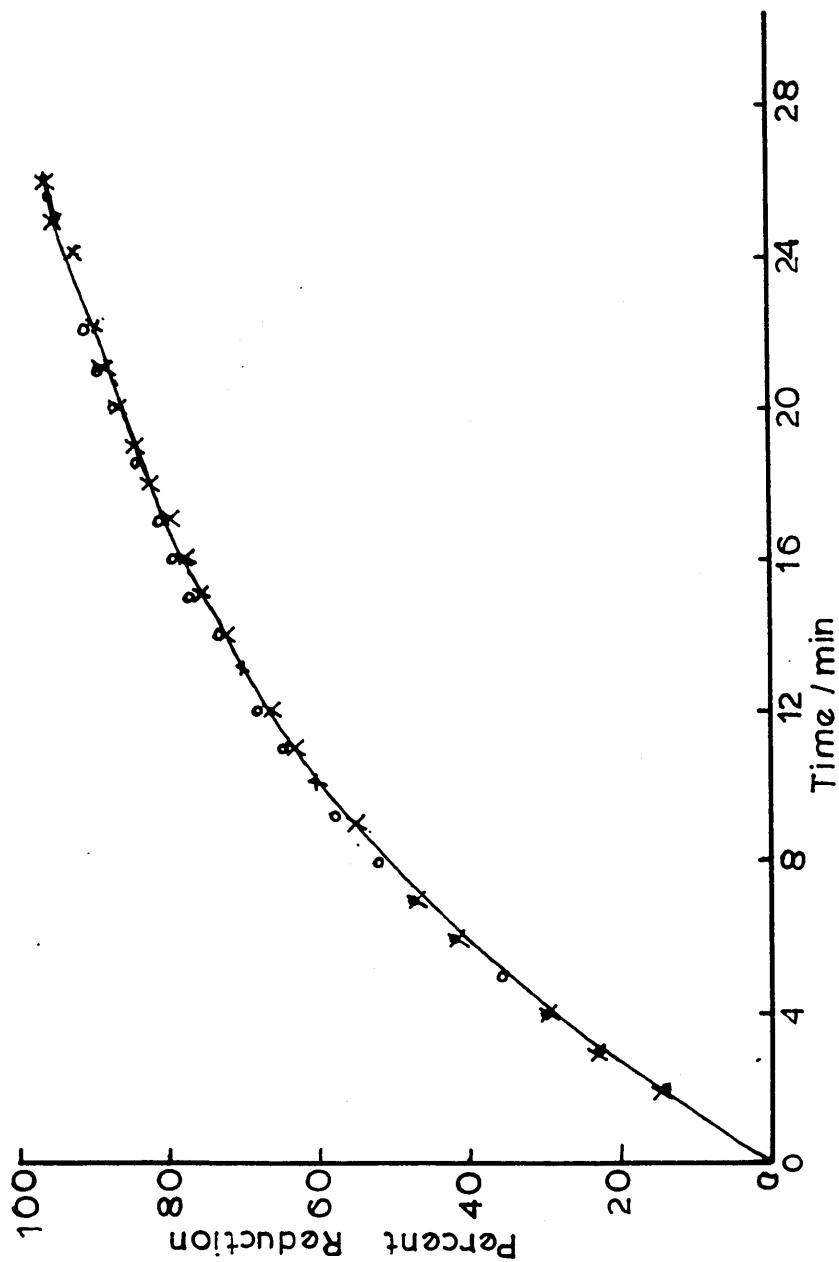
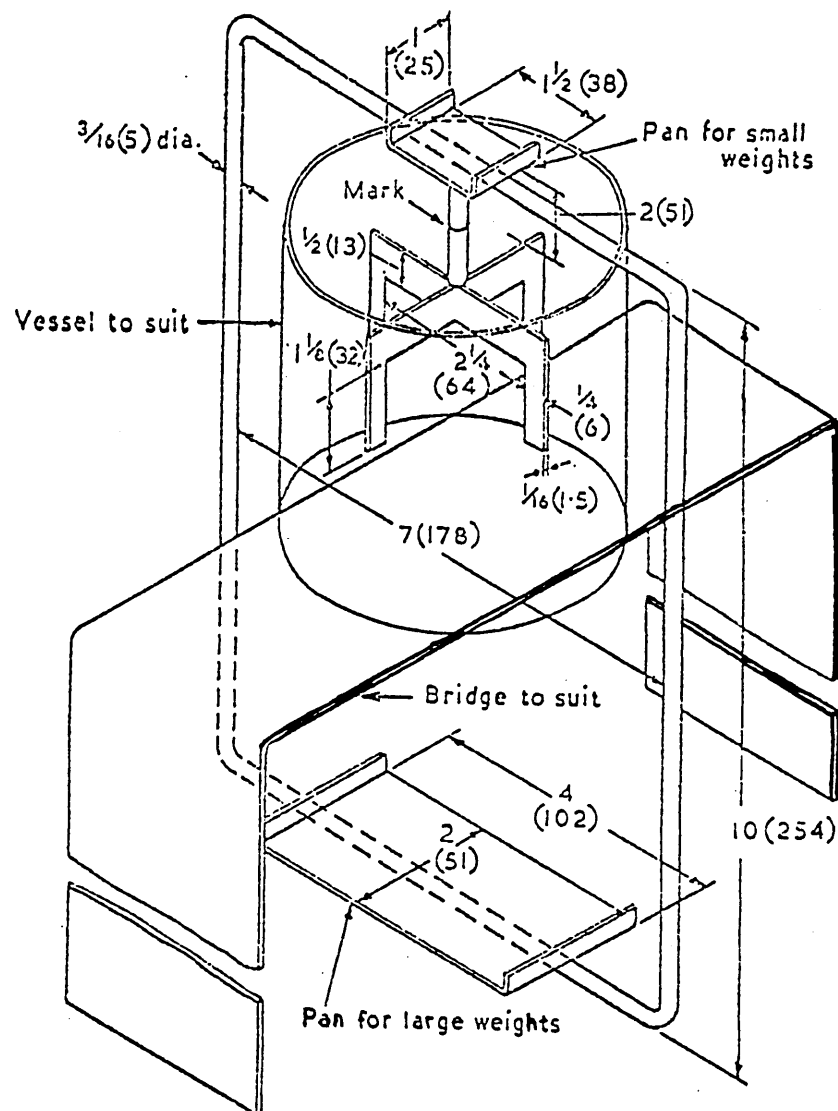


Fig.2.20 Iron oxide pellets containing 5% lime, 1.0% silica reduced in hydrogen at 830°C, sintered at 1250°C. (Two different tests carried out under the same reduction conditions).



Dimensions in inches (millimeters)

Fig 3-21 The mercury balance (B.S.1302 part 1A: 1966)

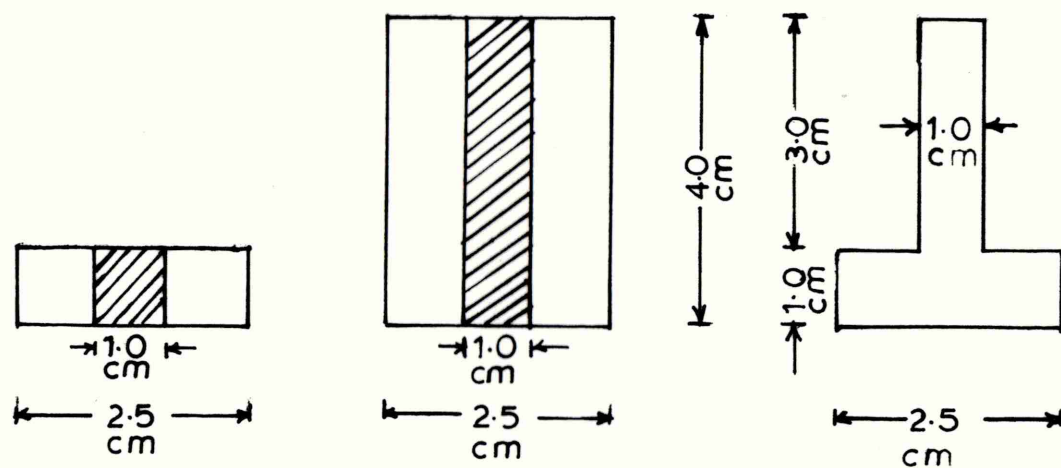


FIG 3.22 DIE FOR NAPHTHALENE CASTING

FIG.4.1. DENSITY OF DIFFERENT IRON OXIDE PELLETS SINTERED AT DIFFERENT TEMPERATURES.

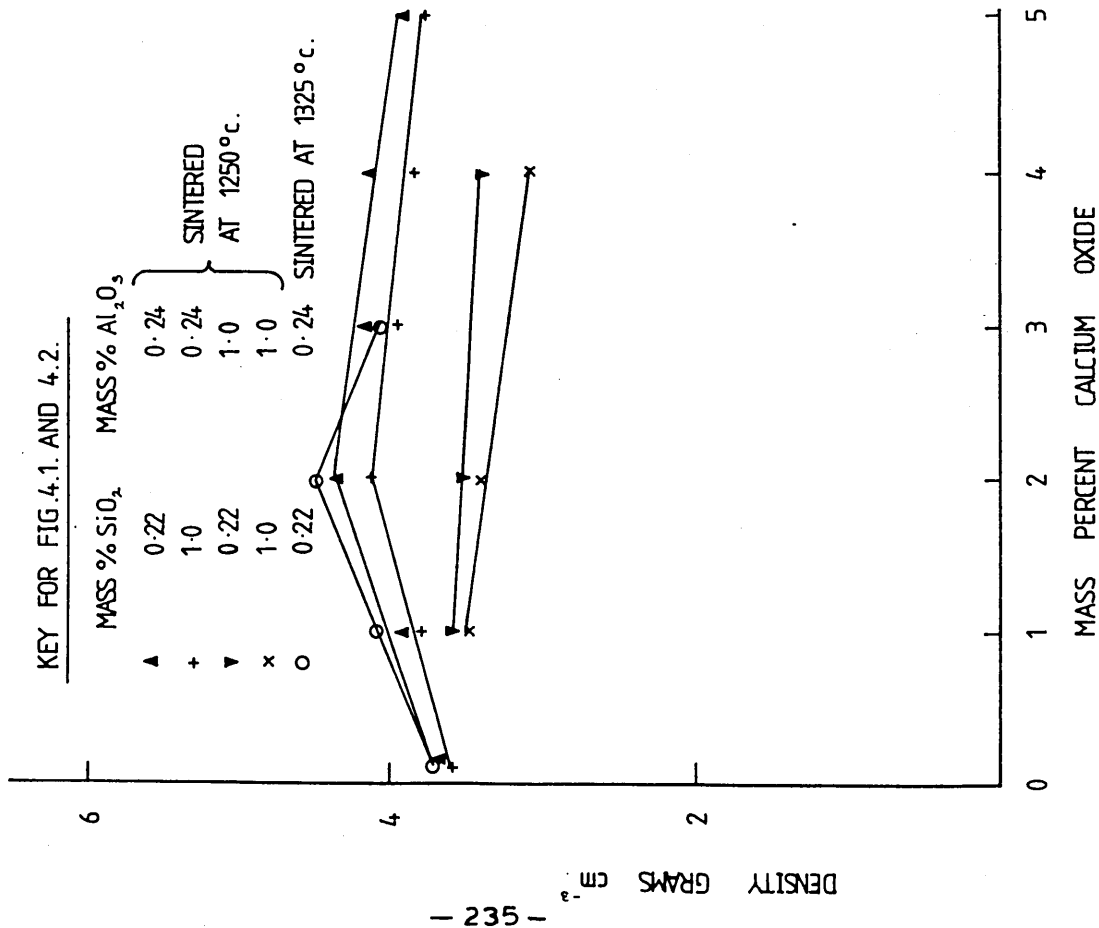
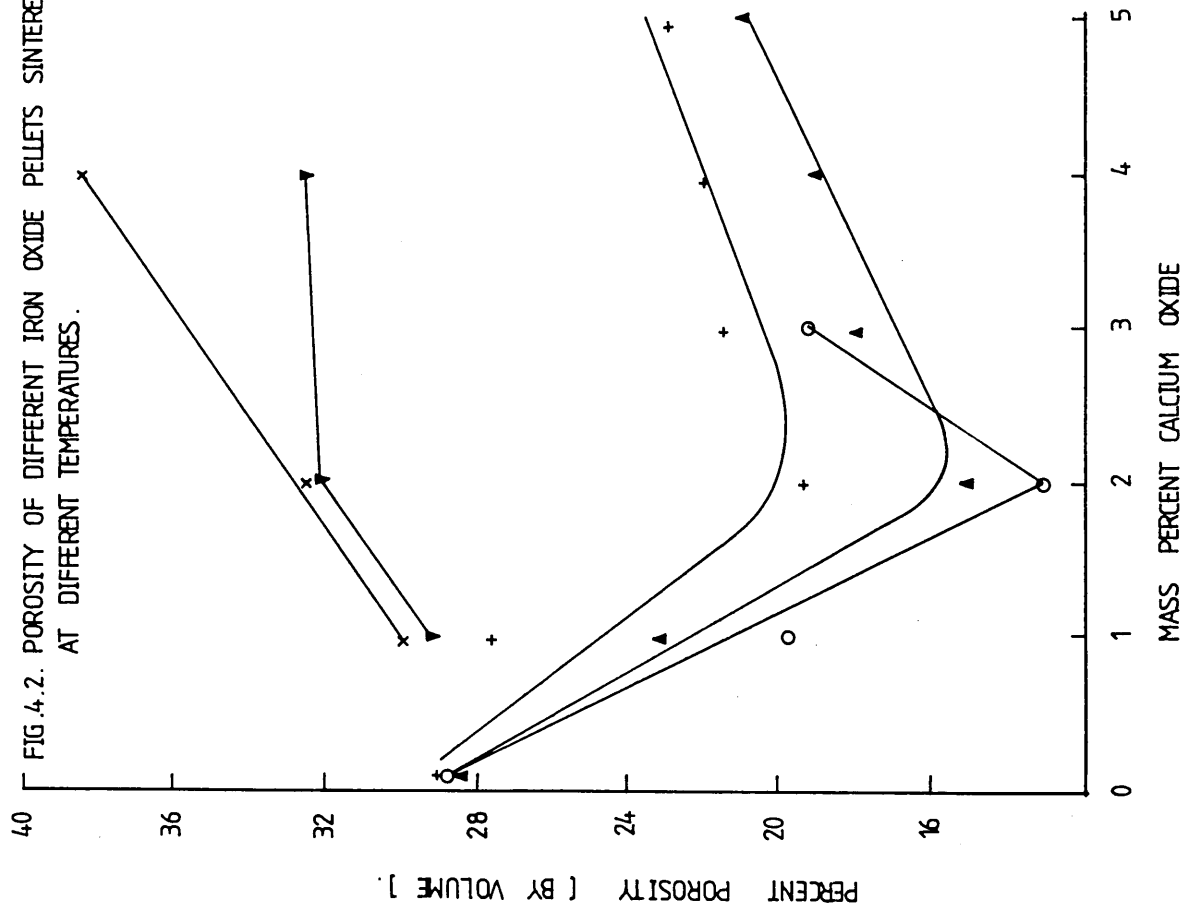


FIG.4.2. POROSITY OF DIFFERENT IRON OXIDE PELLETS SINTERED AT DIFFERENT TEMPERATURES.



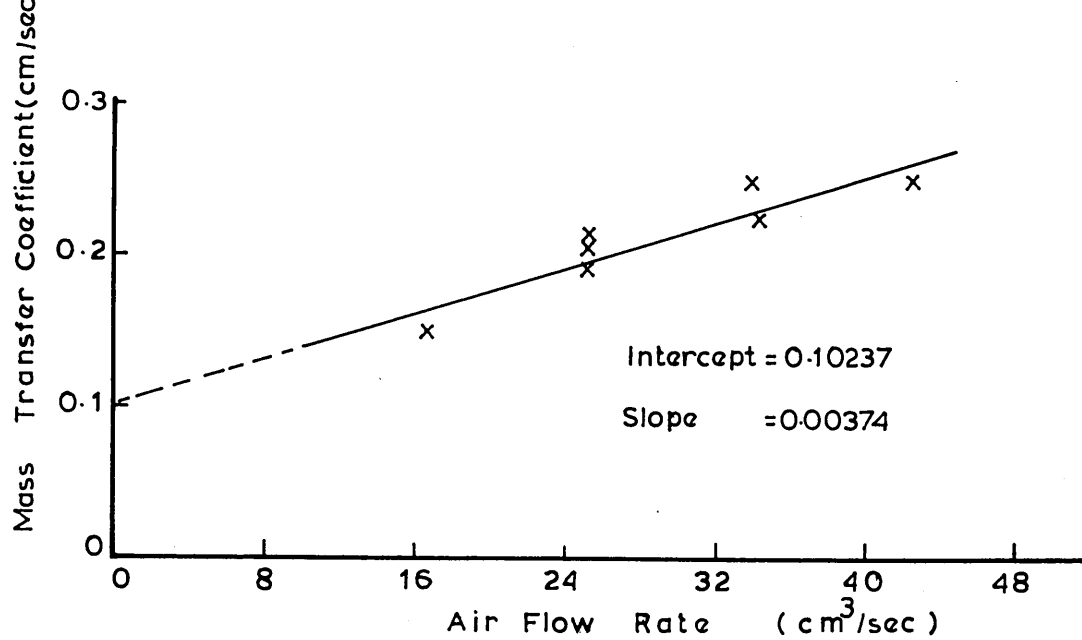


Fig43(a) The effect of air flow rate on the mass transfer coefficient obtained from naphthalene sublimation experiments.

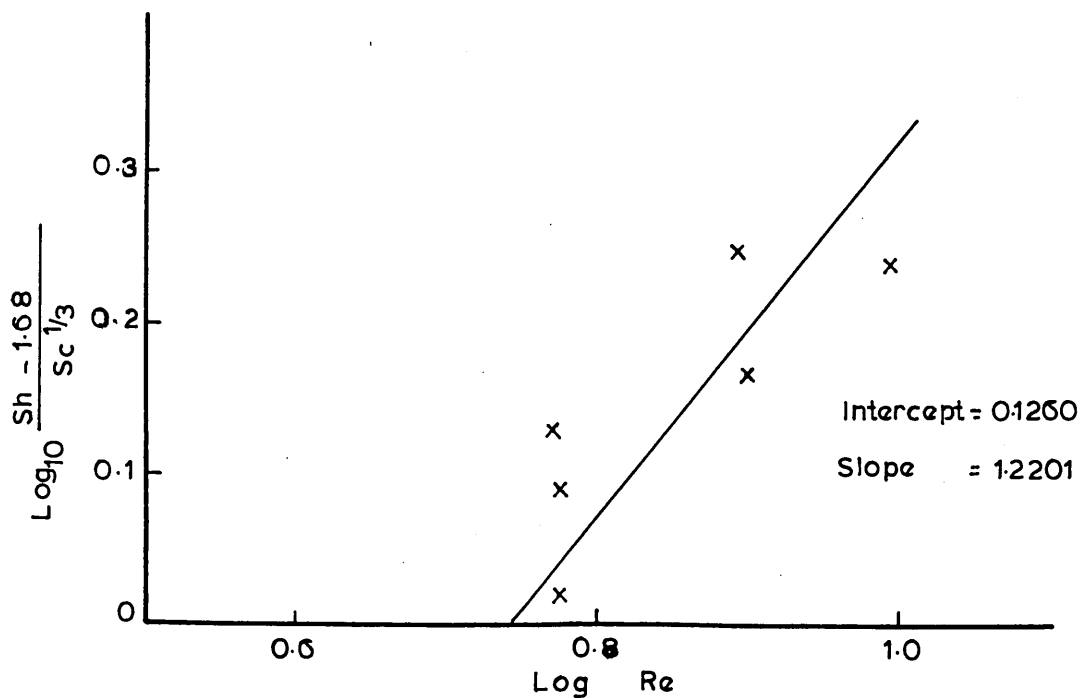


Fig43(b) Graphical presentation of $\log Re$ VS $\log \frac{Sh - 1.68}{Sc^{1/3}}$ relationship for the derivation of the mass transfer correlation for the pellet in the reduction under load apparatus.

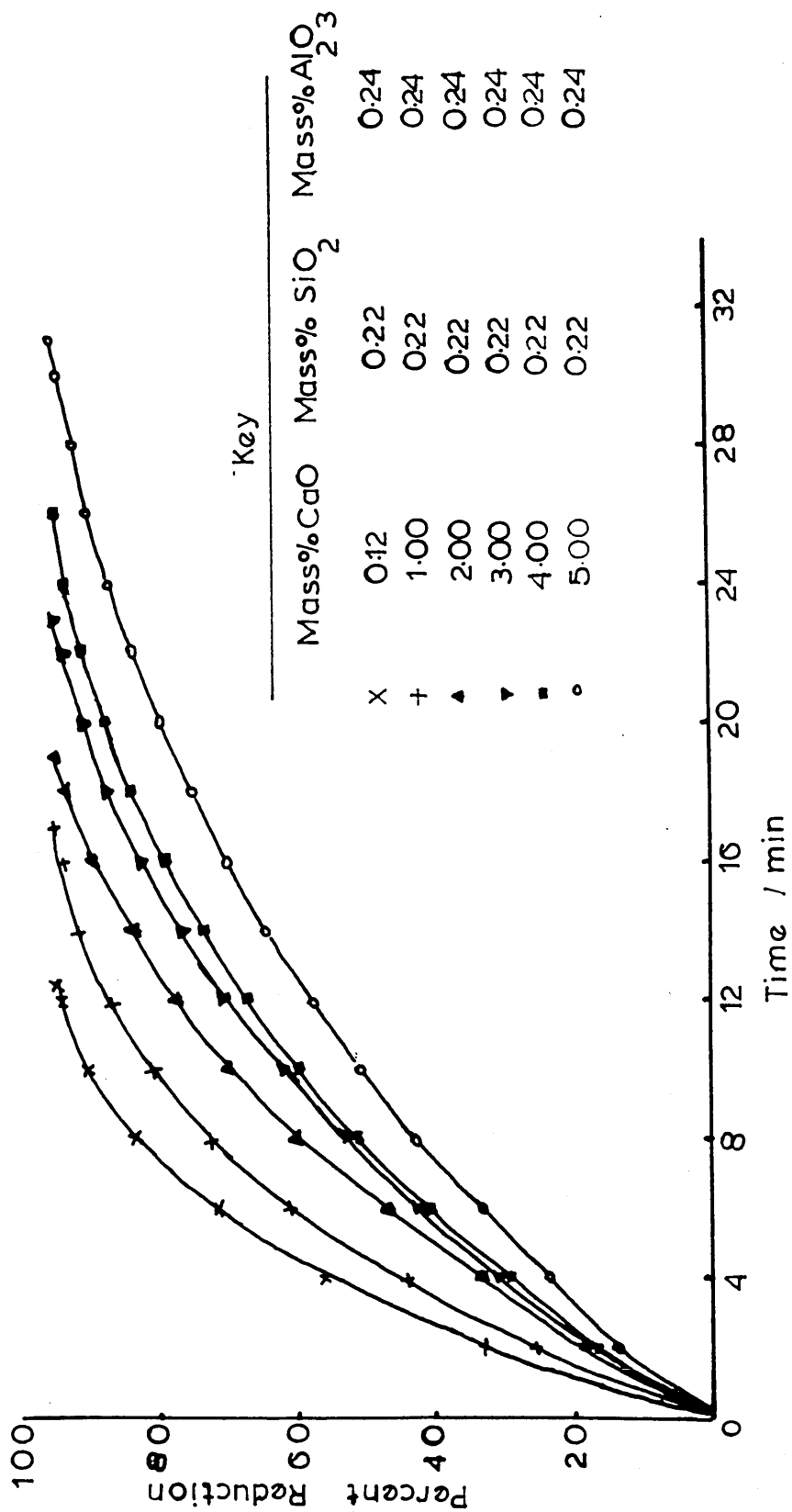


Fig.4.4 Effect of calcium oxide on the reducibility in hydrogen at 830°C of iron oxide at low silica and alumina content (0.22 and 0.24 mass %), sintered at 1250°C.

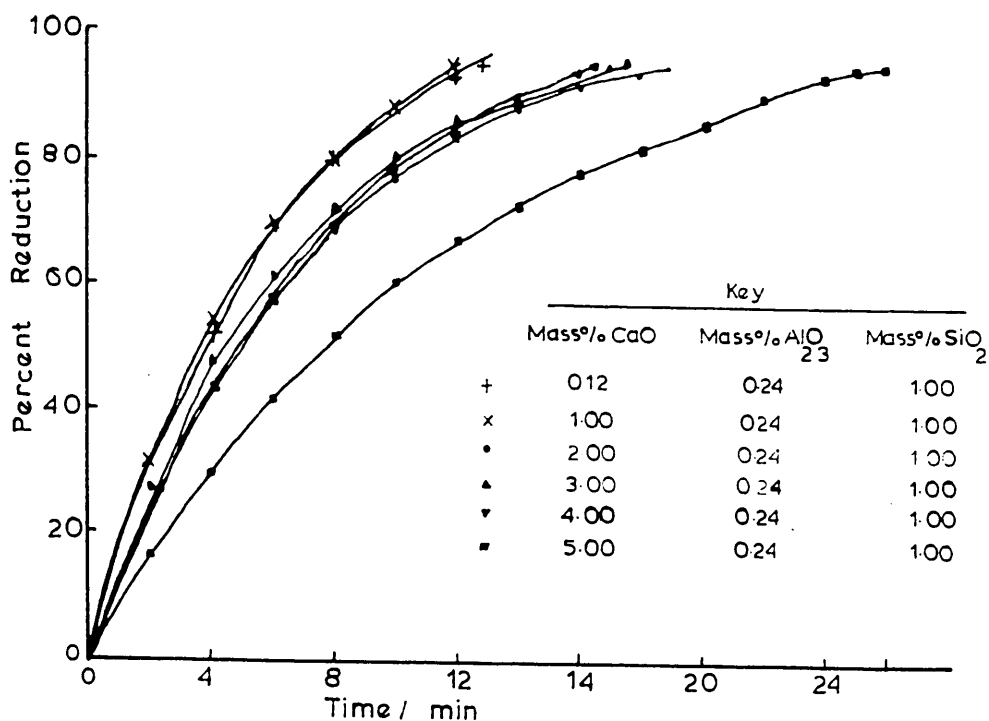


Fig.4.5 Effect of calcium oxide on reducibility at high SiO₂ 1% reduced in H₂ at 830°C (sintered at 1250°C).

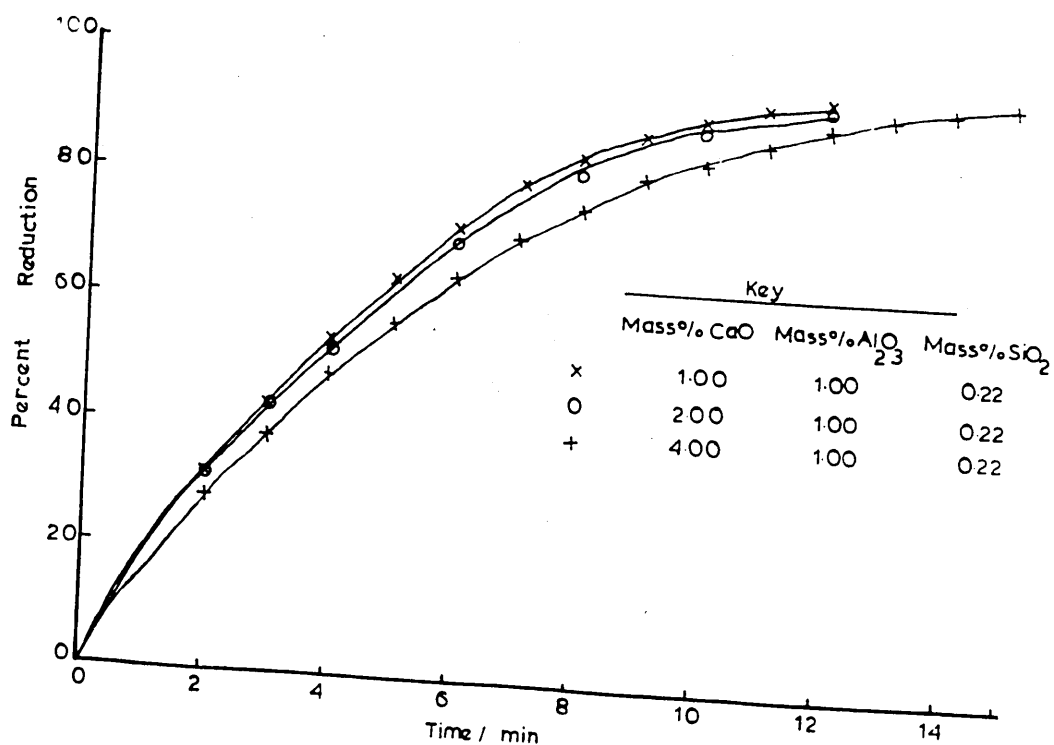


Fig.4.6 Effect of calcium oxide on reducibility of iron oxide pellets at 0.22% SiO₂, 1% alumina reduced in H₂ at 830°C (sintered at 1250°C).

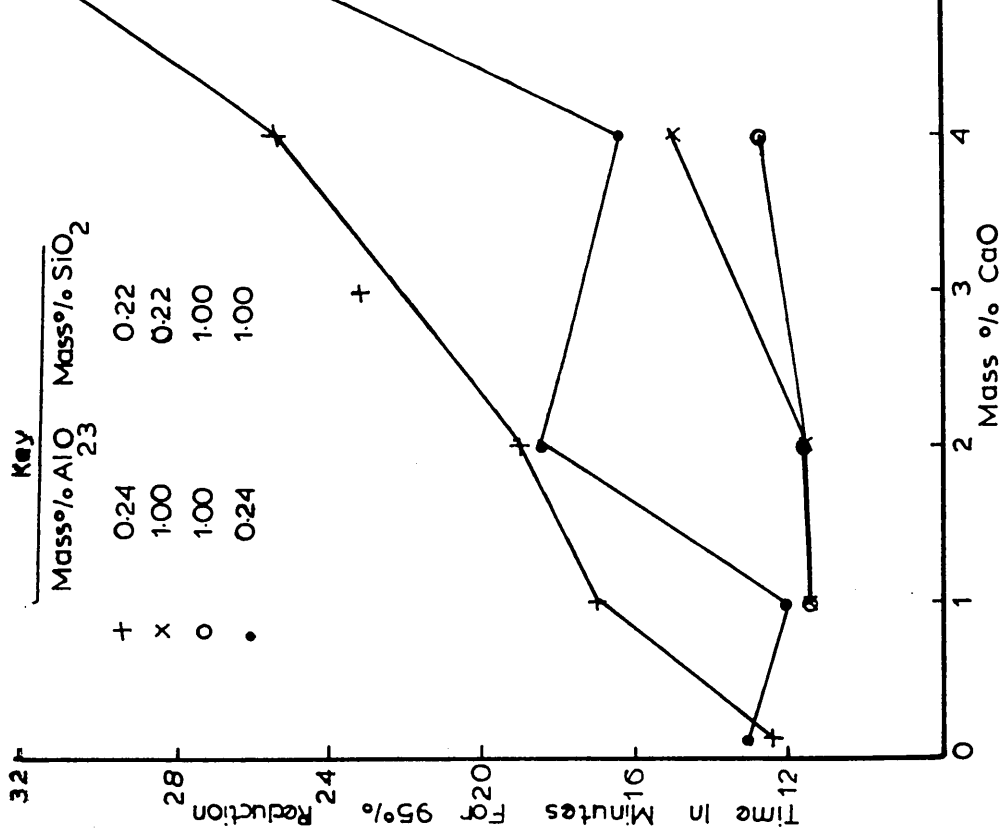


Fig. 4.7 Effect of CaO on reducibility of different iron oxide pellets at high SiO₂ 1% and Al₂O₃ 1% reduced in H₂ at 830°C (sintered at 1250°C).

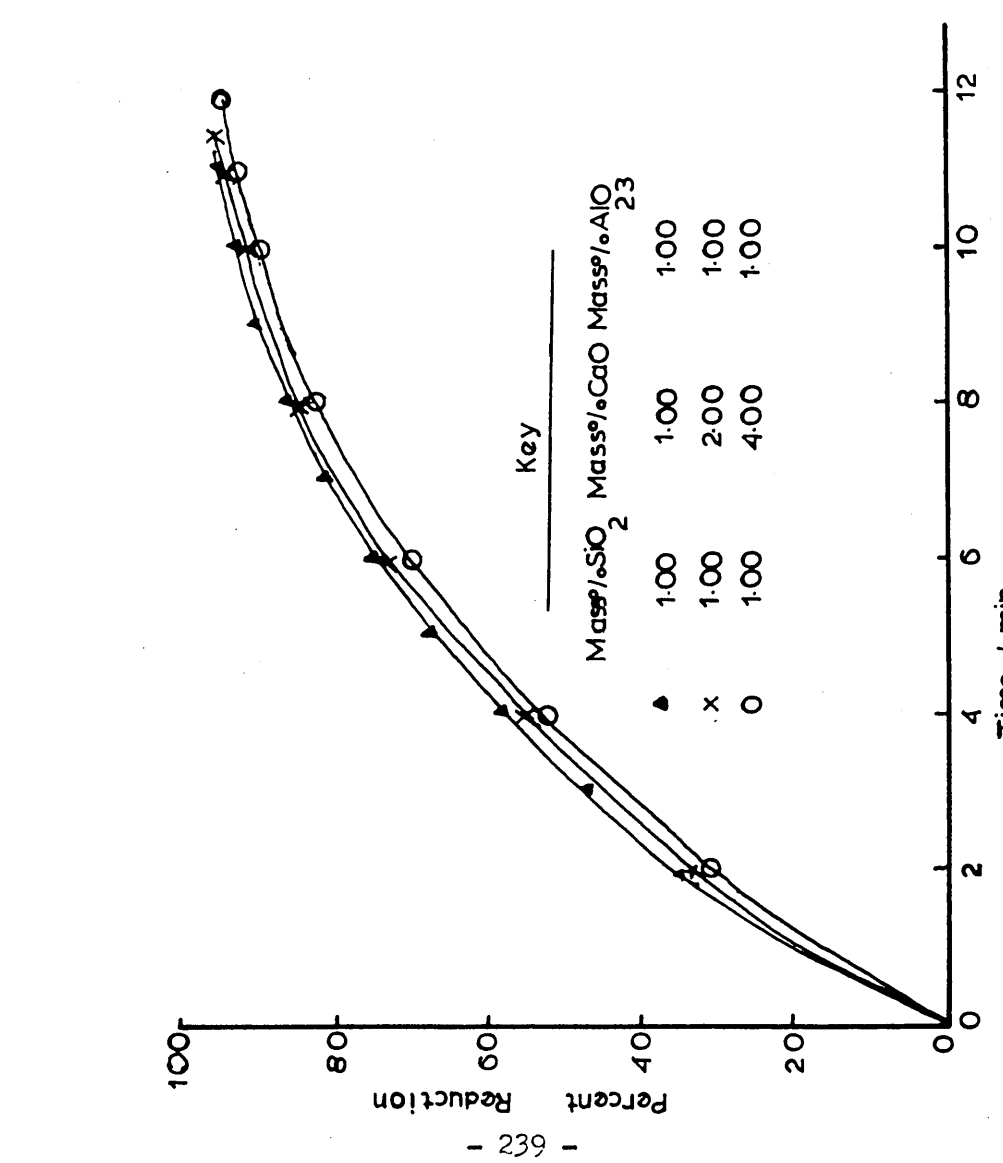


Fig. 4.8 Effect of different doping agent on the time required for 95% reduction of iron oxide pellets reduced in H₂ at 830°C (sintered at 1250°C).

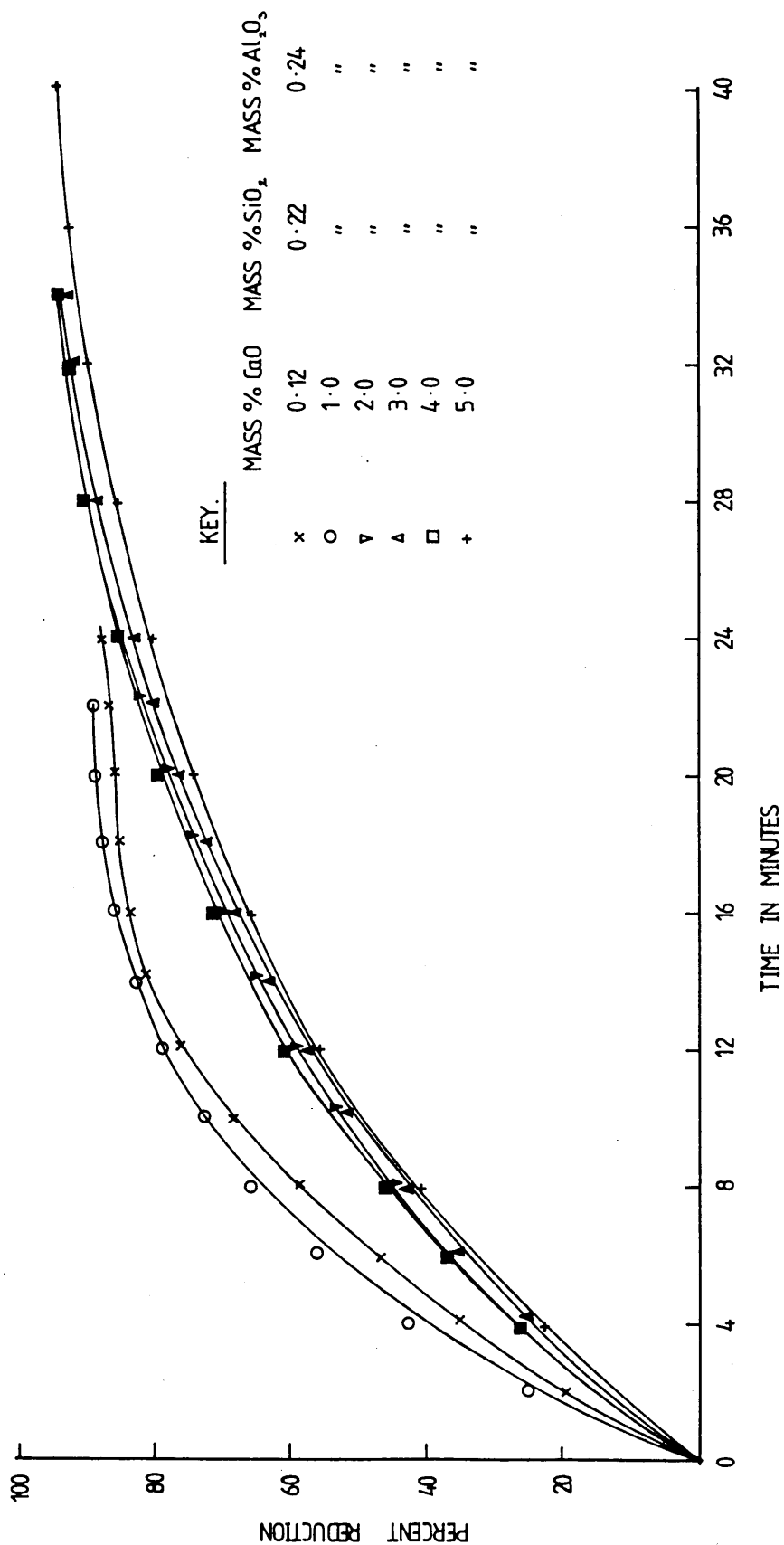


FIG.4-9. EFFECT OF LIME ON REDUCIBILITY OF DIFFERENT IRON OXIDE PELLETS AT LOW SiO₂ 0.22% CONTENT, REDUCED IN (H₂+Co) GAS MIXTURE AT 830 °c (SINTERED AT 1250 °c).

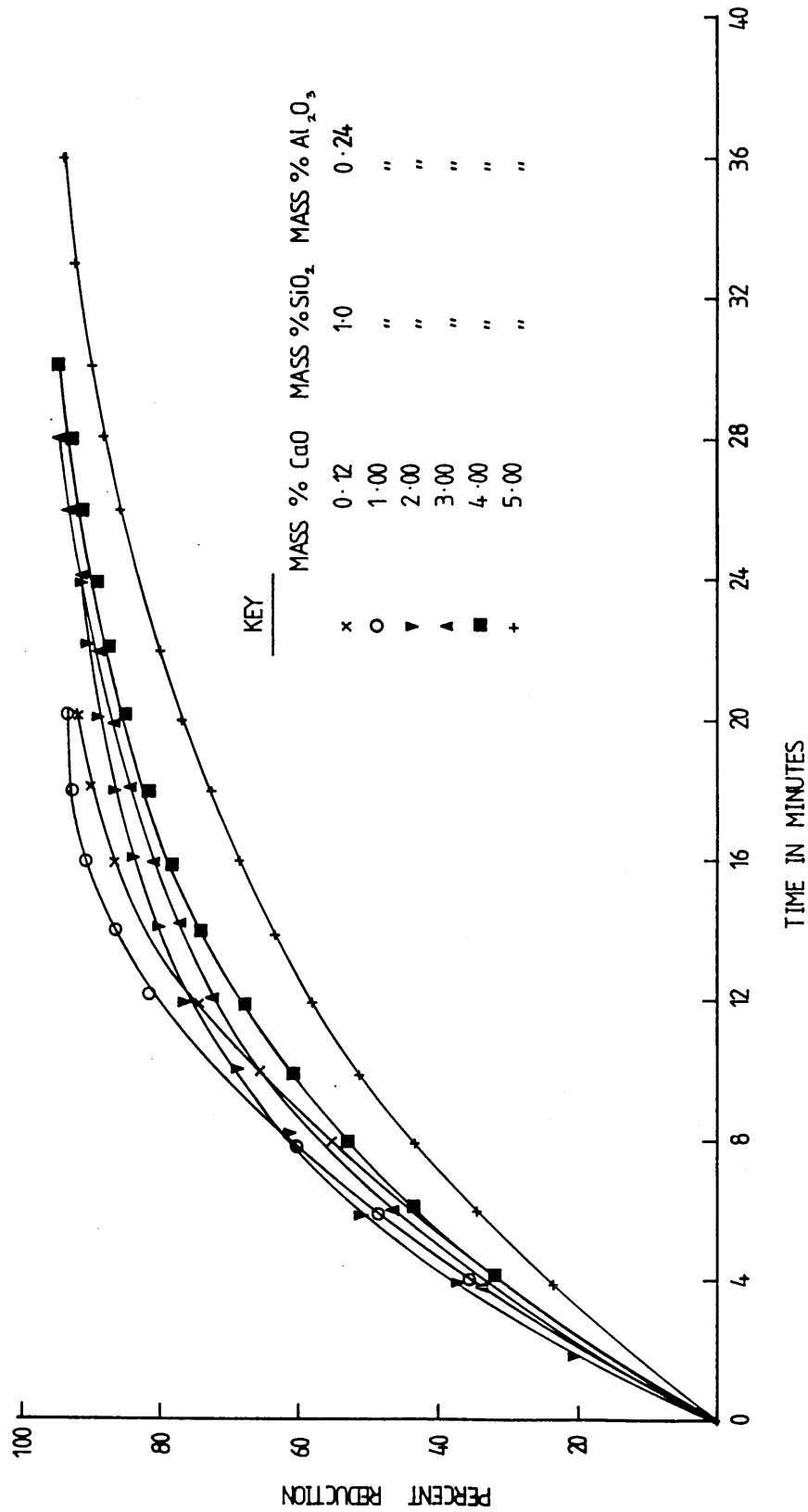


FIG. 4-10. EFFECT OF LIME ON REDUCIBILITY OF DIFFERENT IRON OXIDE PELLETS AT HIGH SiO₂ 1.0% CONTENT, REDUCED IN (H₂+Co) GAS MIXTURE AT 830°C (SINTERED AT 1250°C).

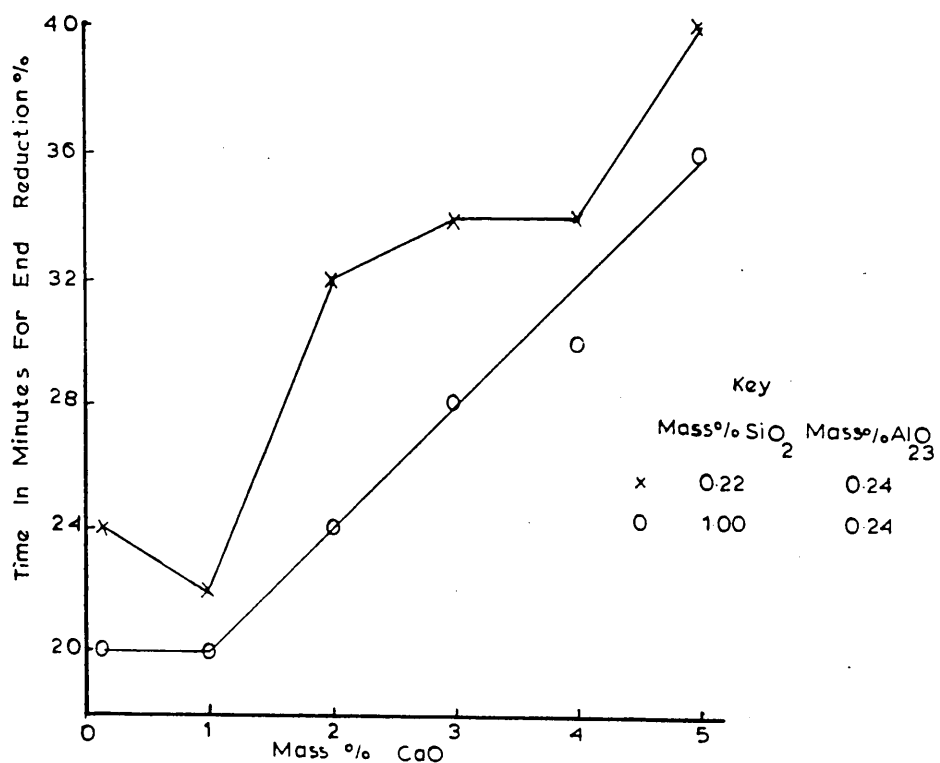


Fig. 4.11 Effect of different doping agent on the time required for end of reduction of iron oxide pellets reduced in (H₂ + CO) gas mixture at 830°C (pellets sintered at 1250°C).

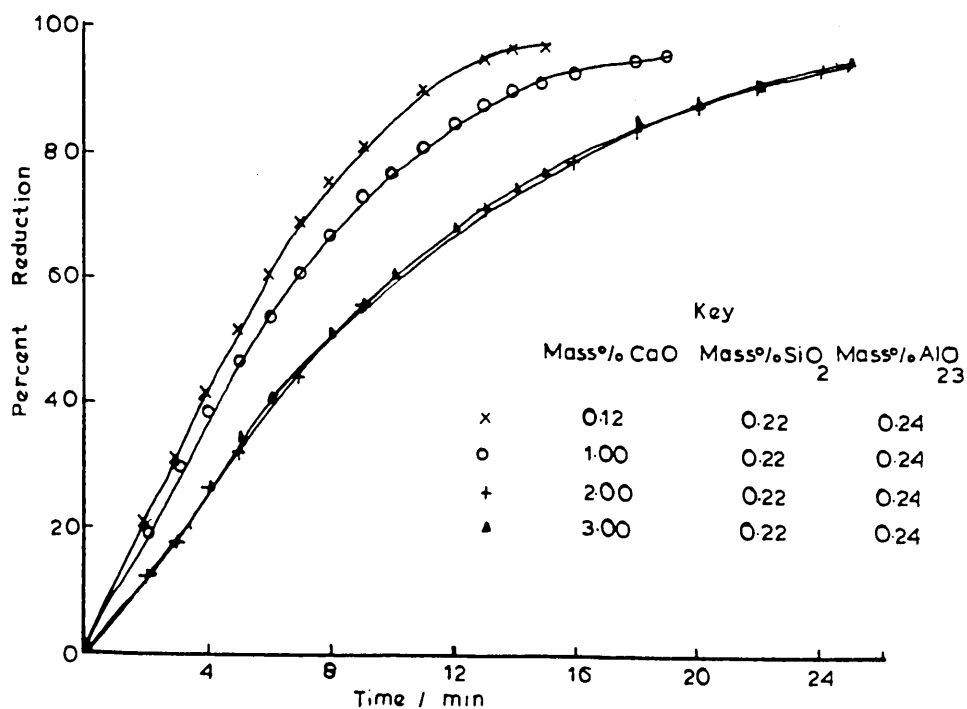


Fig. 4.12 Effect of time on reducibility of different iron oxide pellets reduced in hydrogen at 850°C (sintered at 1325°C).

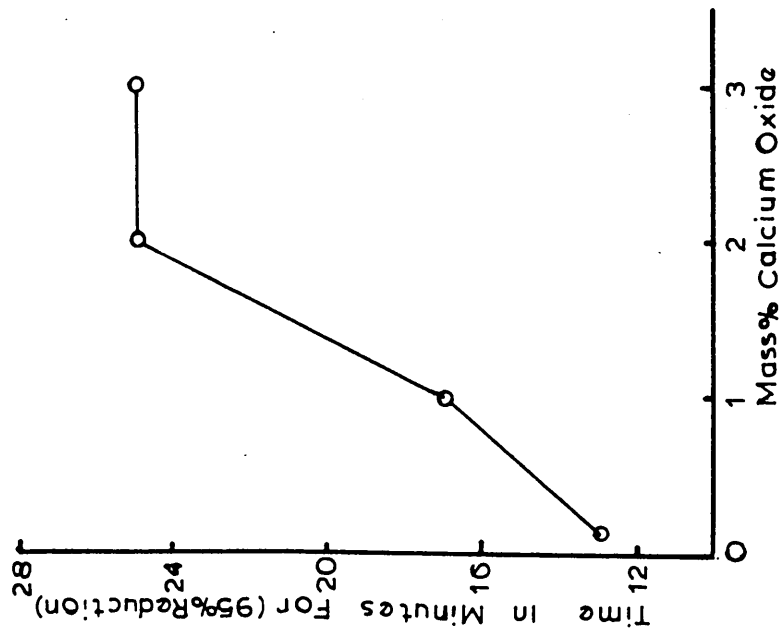


Fig.4.13 Effect of lime on time required for 95% reduction. Reduced in hydrogen at 850°C.

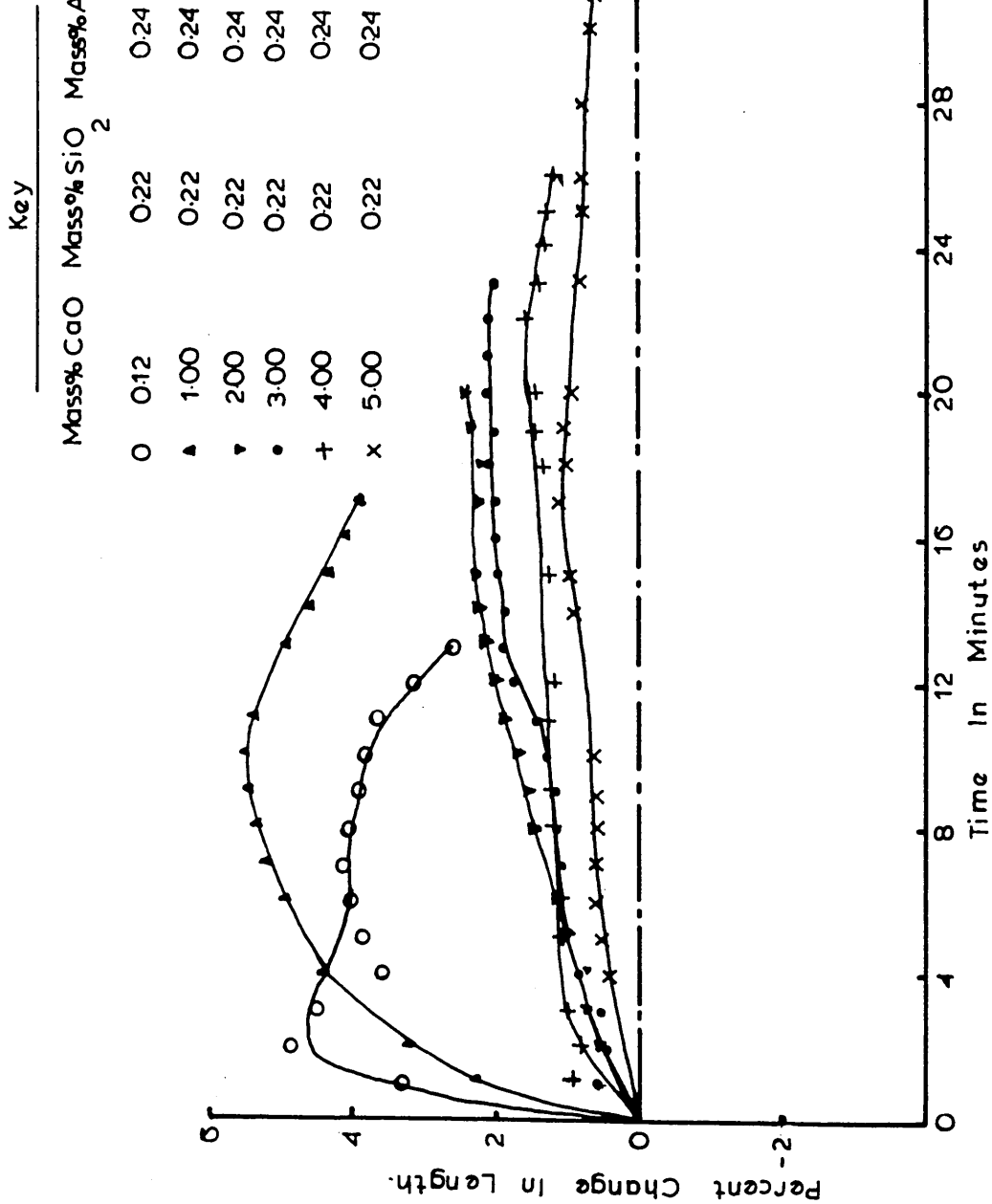


Fig.4.14 Change in length of pellet reduced in H₂ at 830°C and at zero stress (sintered at 1250°C)

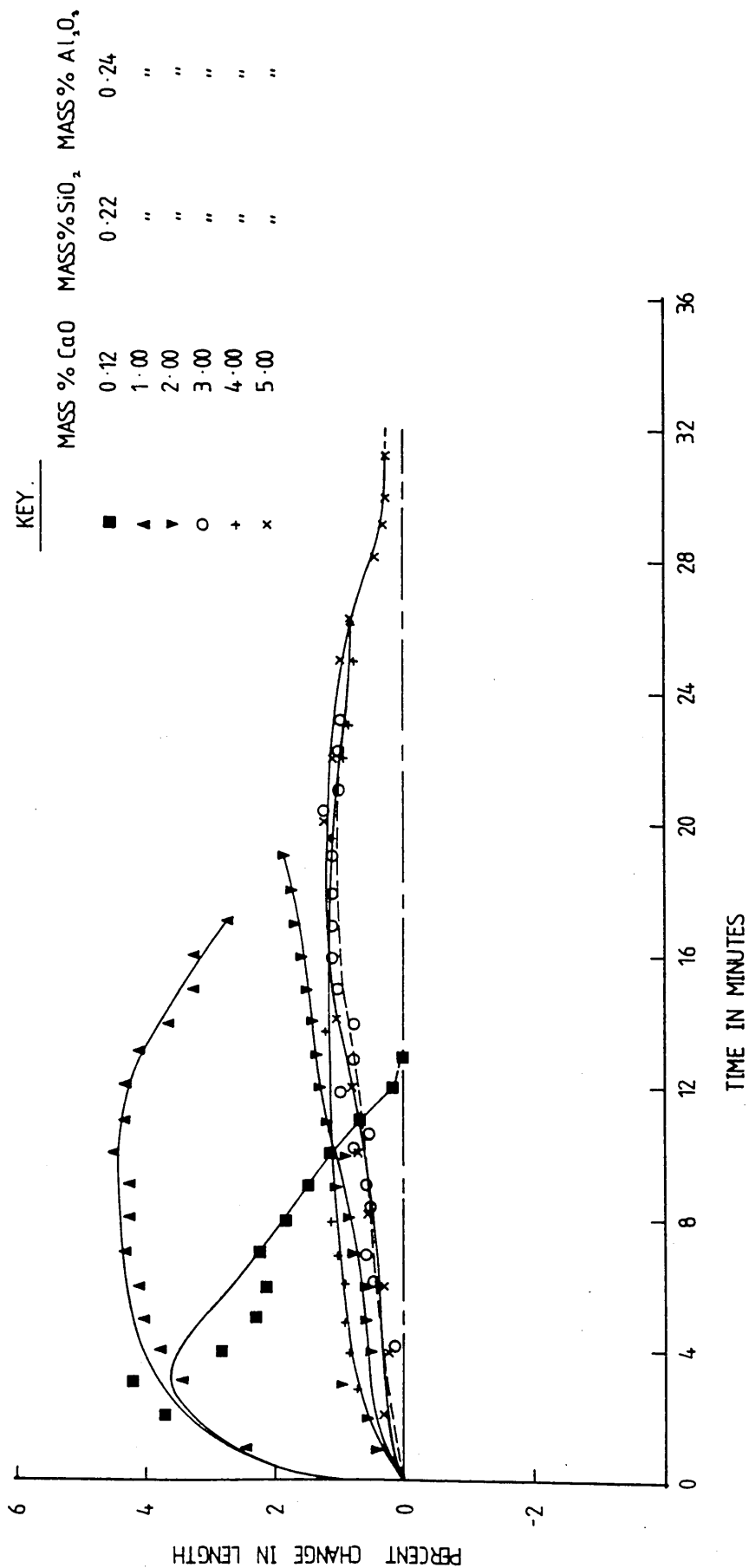


FIG. 4.15. Change in length of pellets reduced in hydrogen at 830°C and at 1.5 kg load (sintered at 1250°C)

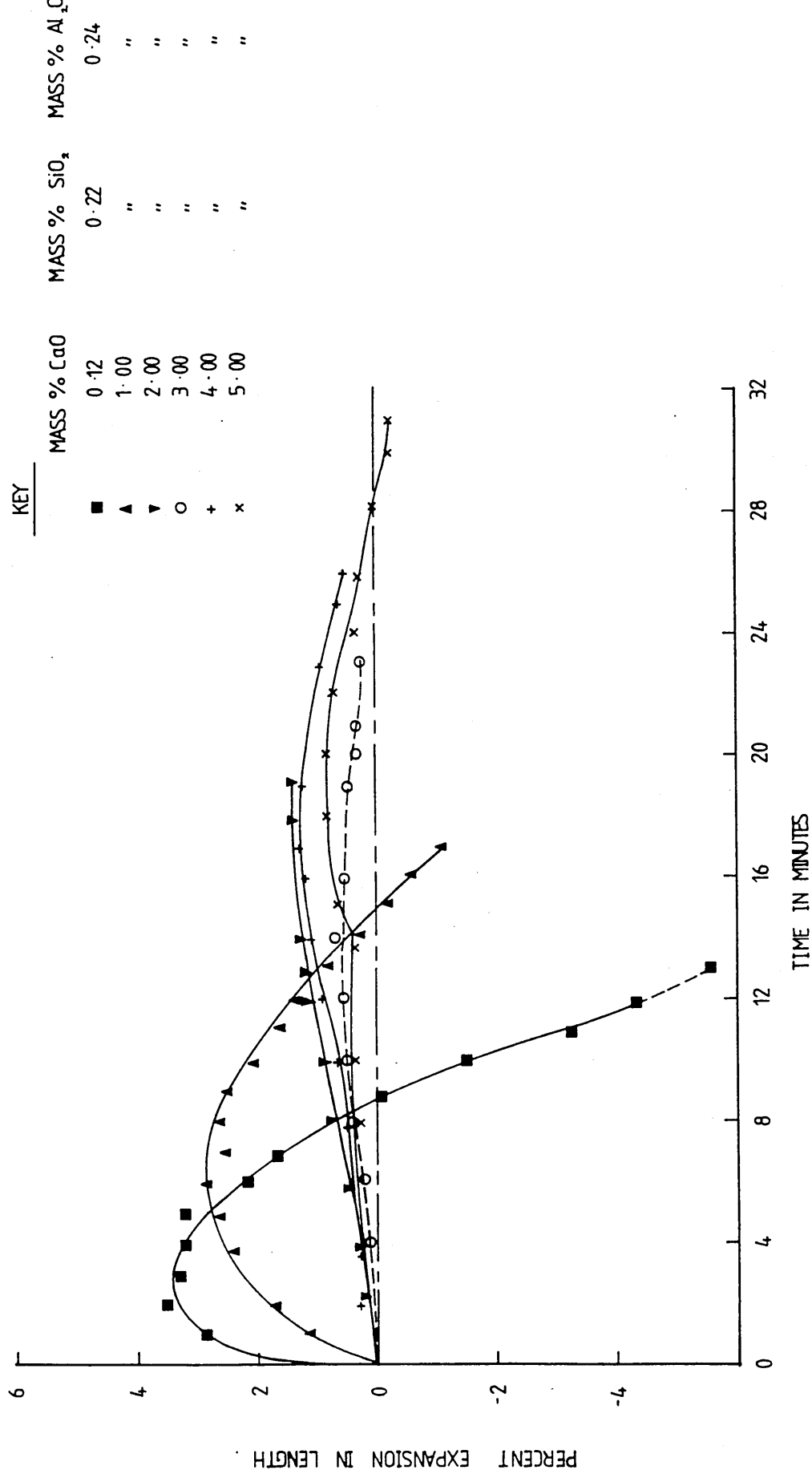


FIG. 4-16. Change in length of pellets reduced in hydrogen at 8300C and at 3.0 kg load (sintered at 12500C)

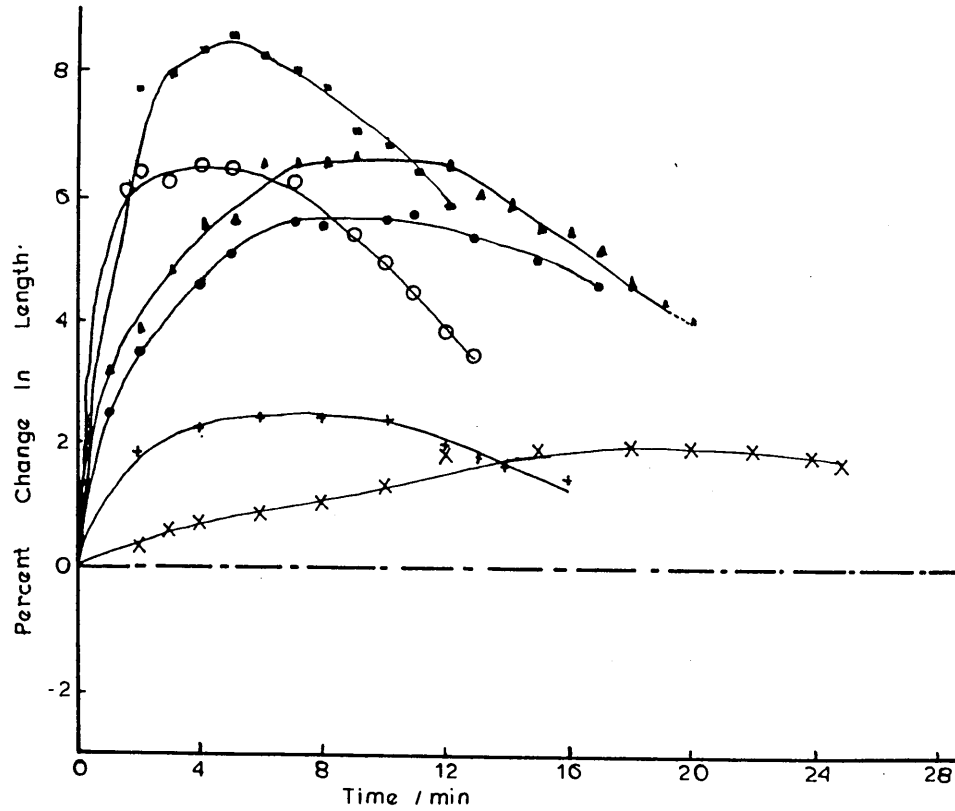


Fig.4.17 Change in length of different pellets reduced in hydrogen at 830°C at zero stress (sintered at 1250°C).

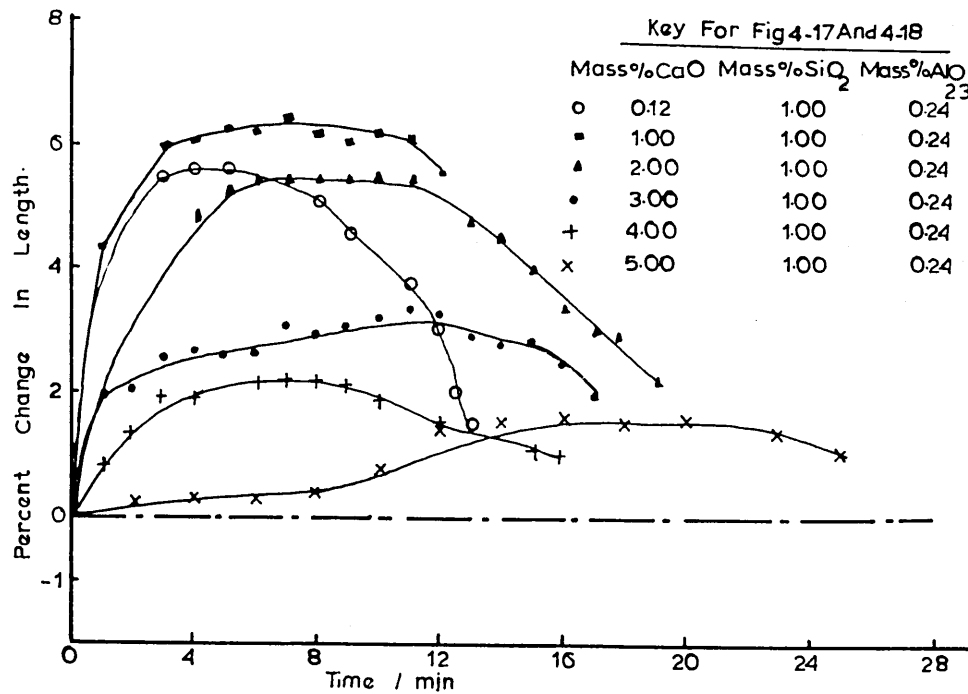


Fig.4.18 Change in length of pellets reduced in hydrogen at 830°C at stress of 1.5 kg cm⁻² (sintered at 1250°C).

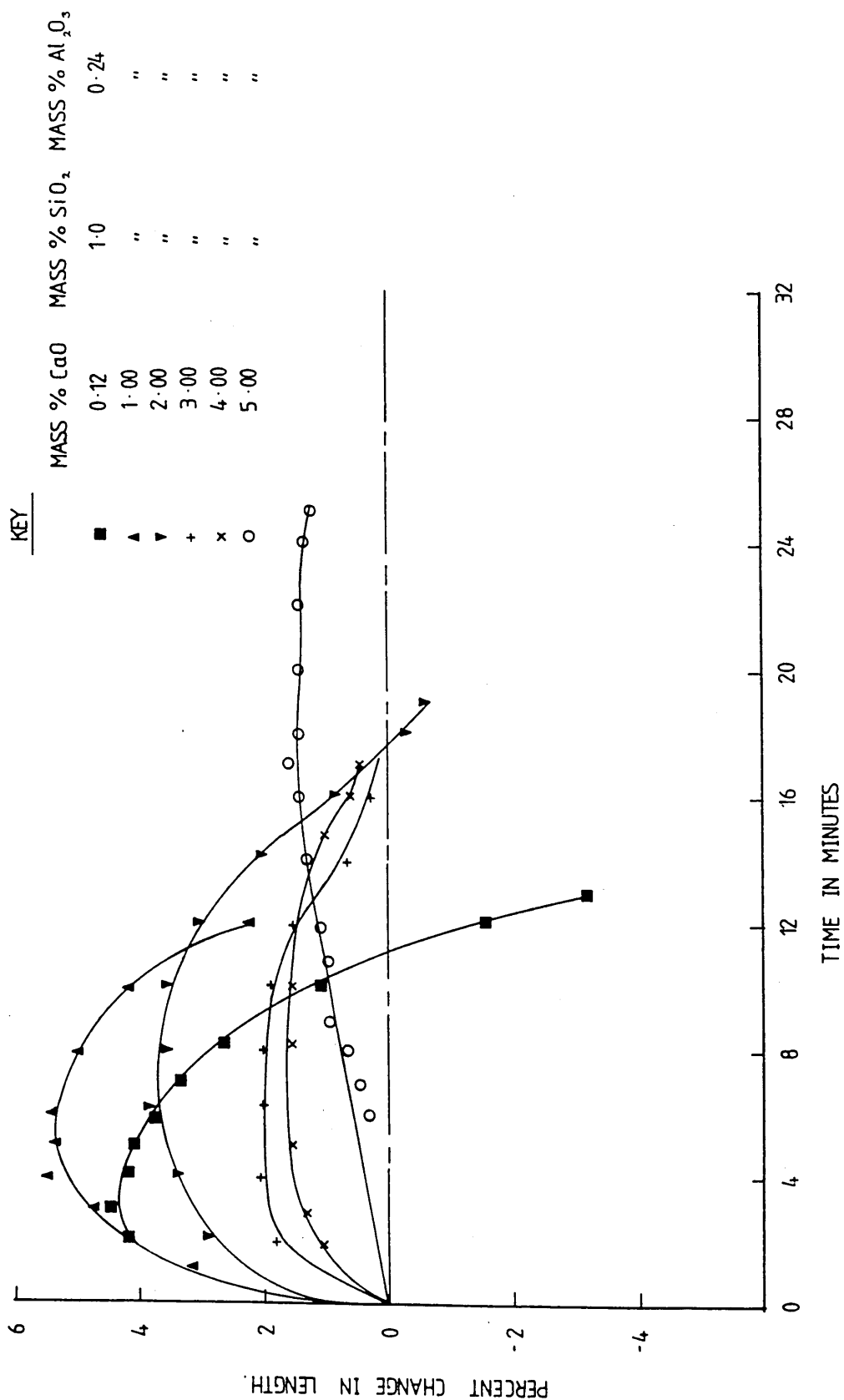


FIG. 4.19. Change in length of pellets reduced in hydrogen at 3 kg cm⁻² load at 830°C (sintered at 1250°C)

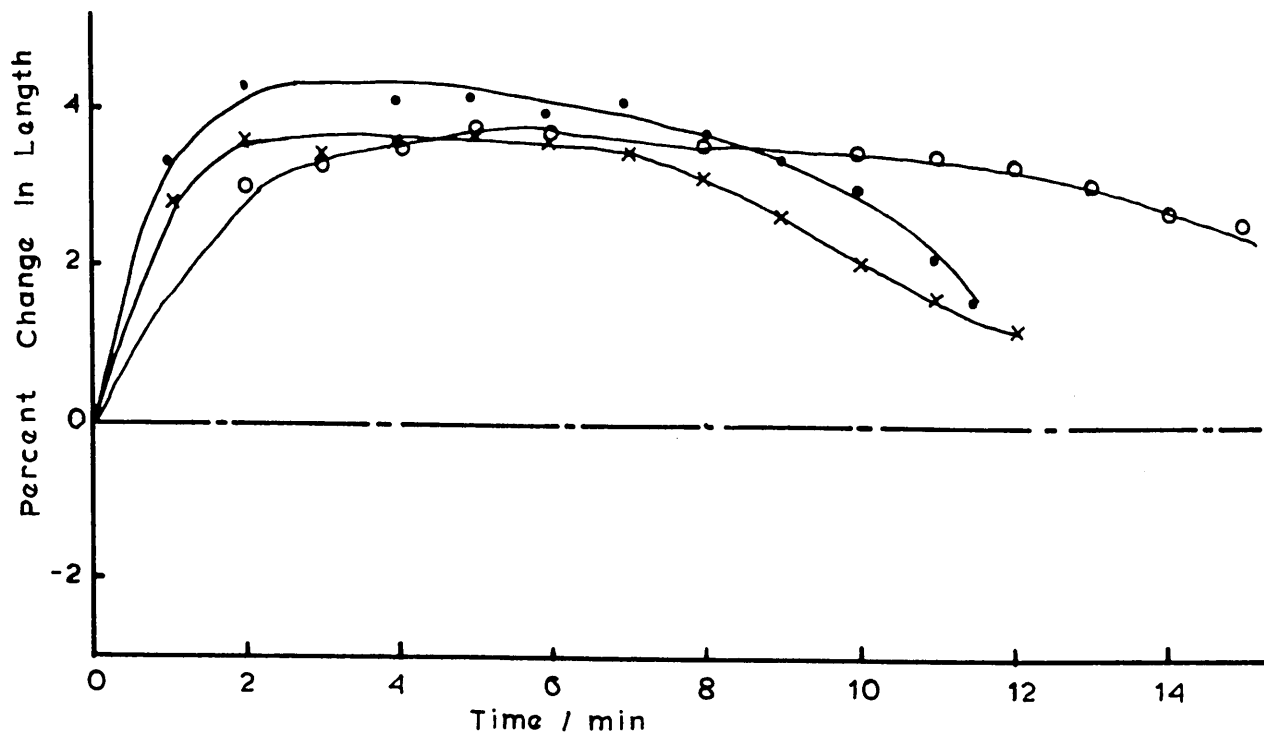


Fig. 4.20 Change in length of pellets reduced in hydrogen at 830°C at zero stress (sintered at 1250°C)

Key For Fig 4.20 And 4.21

	Mass% CaO	Mass% SiO ₂	Mass% AlO ₂₃
•	1.00	0.22	1.00
x	2.00	0.22	1.00
o	4.00	0.22	1.00

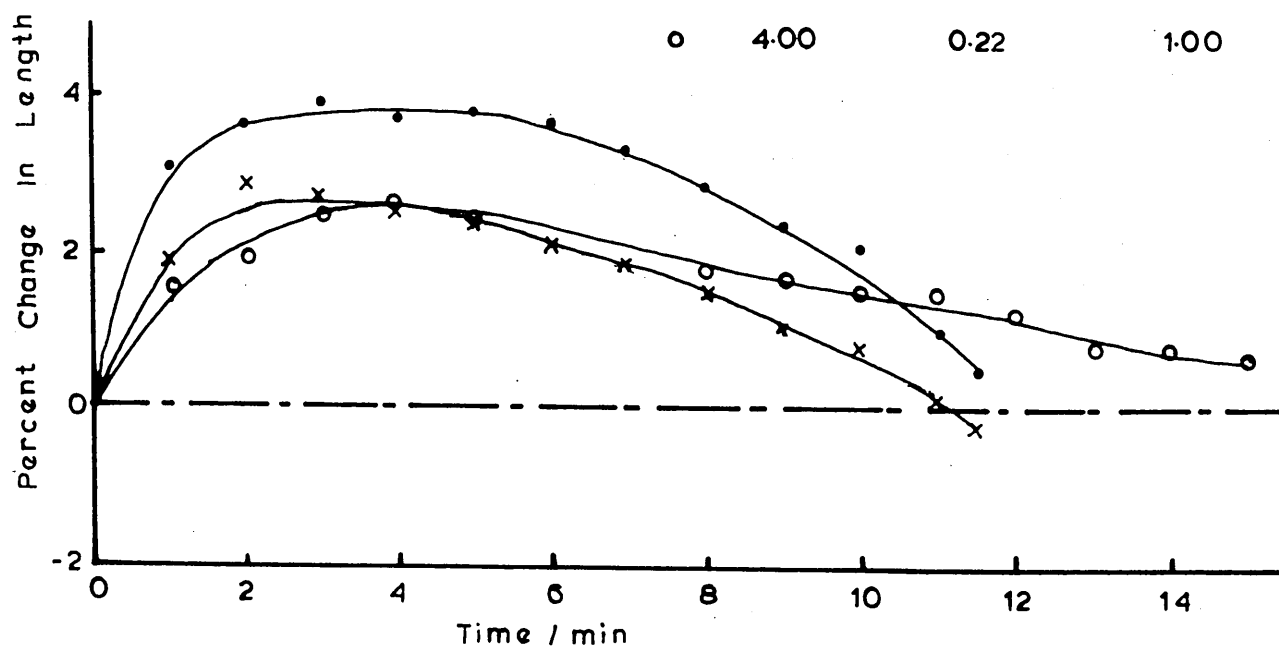


Fig. 4.21 Change in length of pellets reduced in hydrogen at 830°C at stress of 3 kg cm⁻² (sintered at 1250°C)

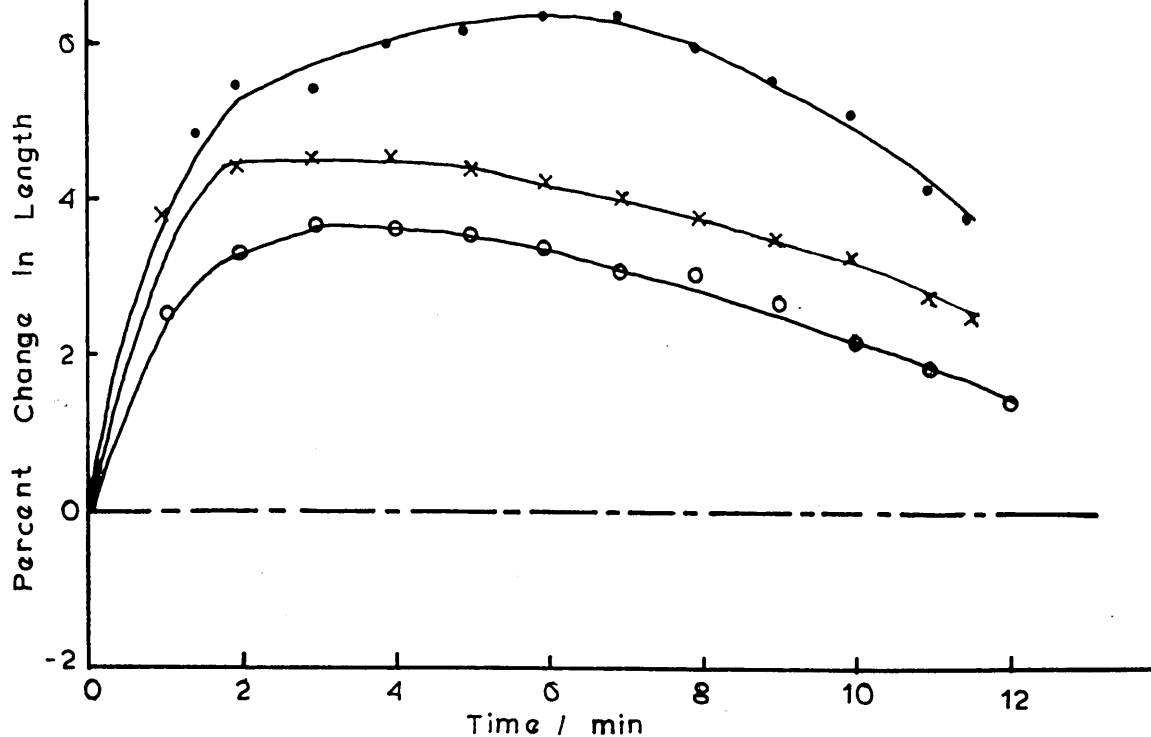


Fig.4.22 Change in length of pellets reduced in hydrogen at 830°C at zero stress (sintered at 1250°C).

Key For Fig 4.22 And 4.23

	Mass% CaO	Mass% SiO ₂	Mass% AlO ₂₃
•	1.00	1.00	1.00
x	2.00	1.00	1.00
o	4.00	1.00	1.00

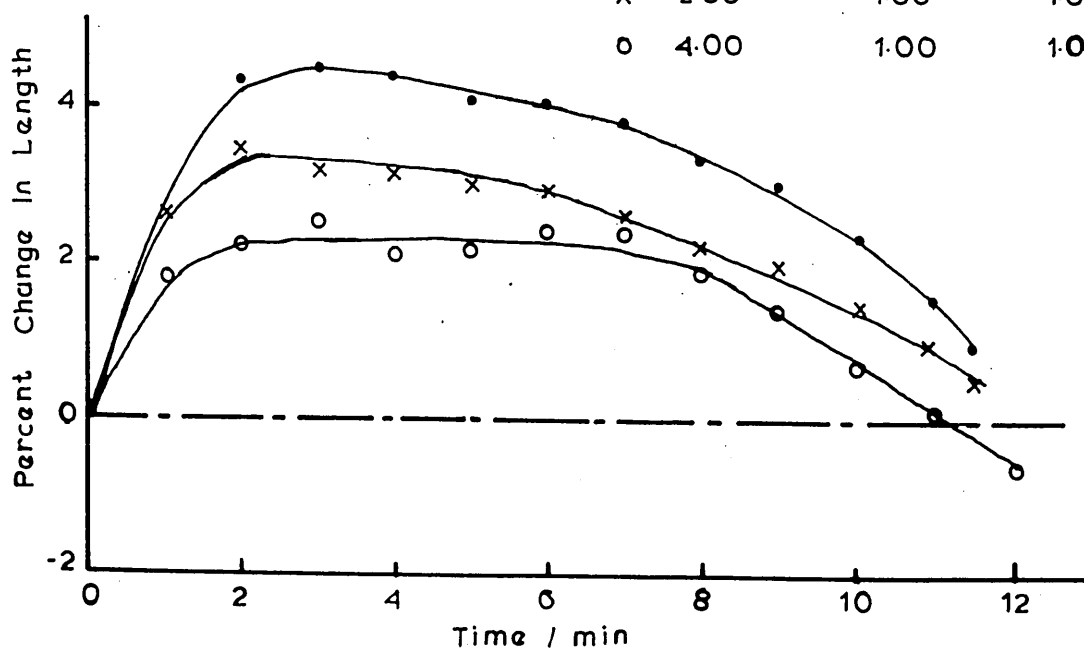


Fig.4.23 Change in length of pellets reduced in hydrogen at 830°C at stresses of 3.0 kg cm⁻² (sintered at 1250°C).

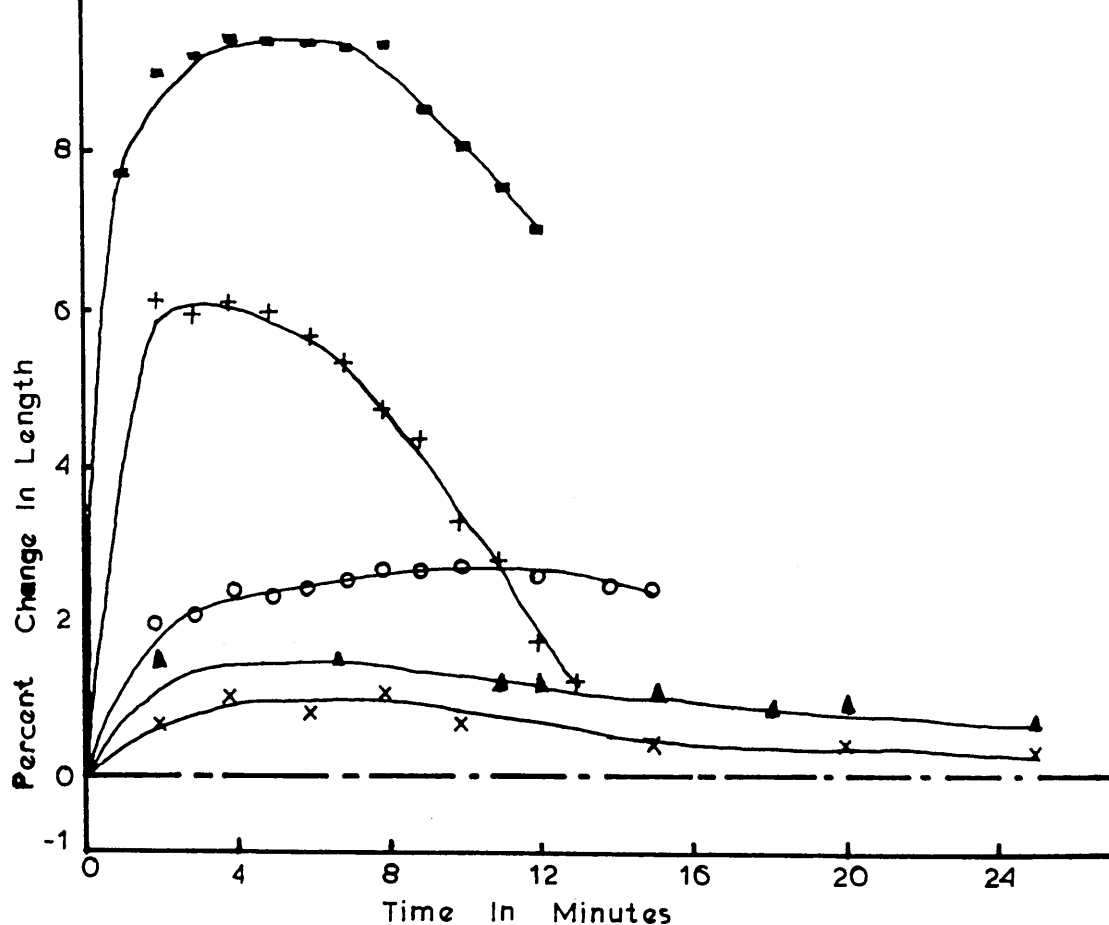


Fig.4.24 Change in length of pellets reduced in hydrogen at 850°C at zero stress (sintered at 1325°C).

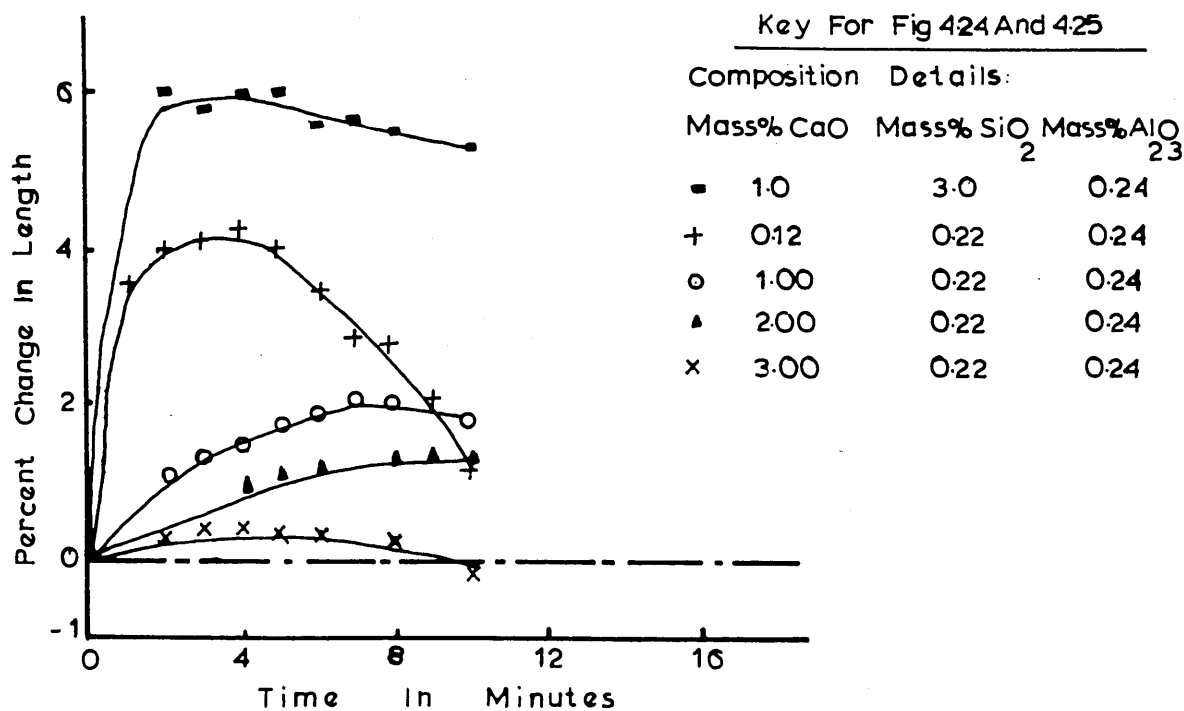


Fig.4.25 Change in length of pellets reduced in hydrogen at 850°C at stresses of 1.5 kg cm⁻² (sintered at 1325°C).

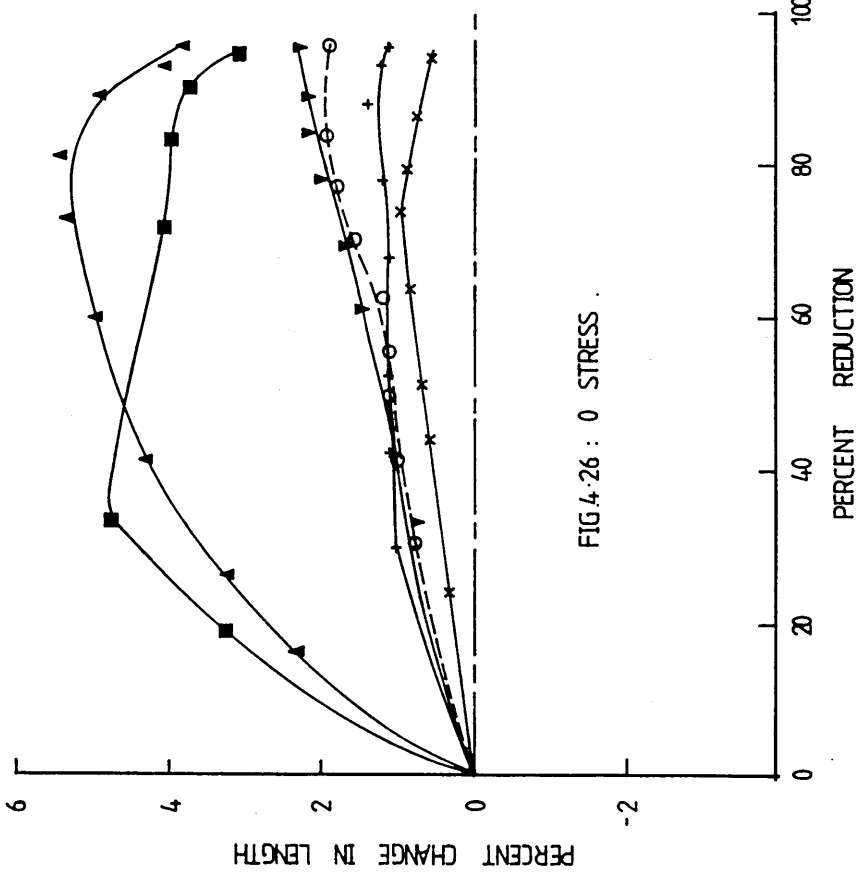


FIG 4-26 : 0 STRESS .

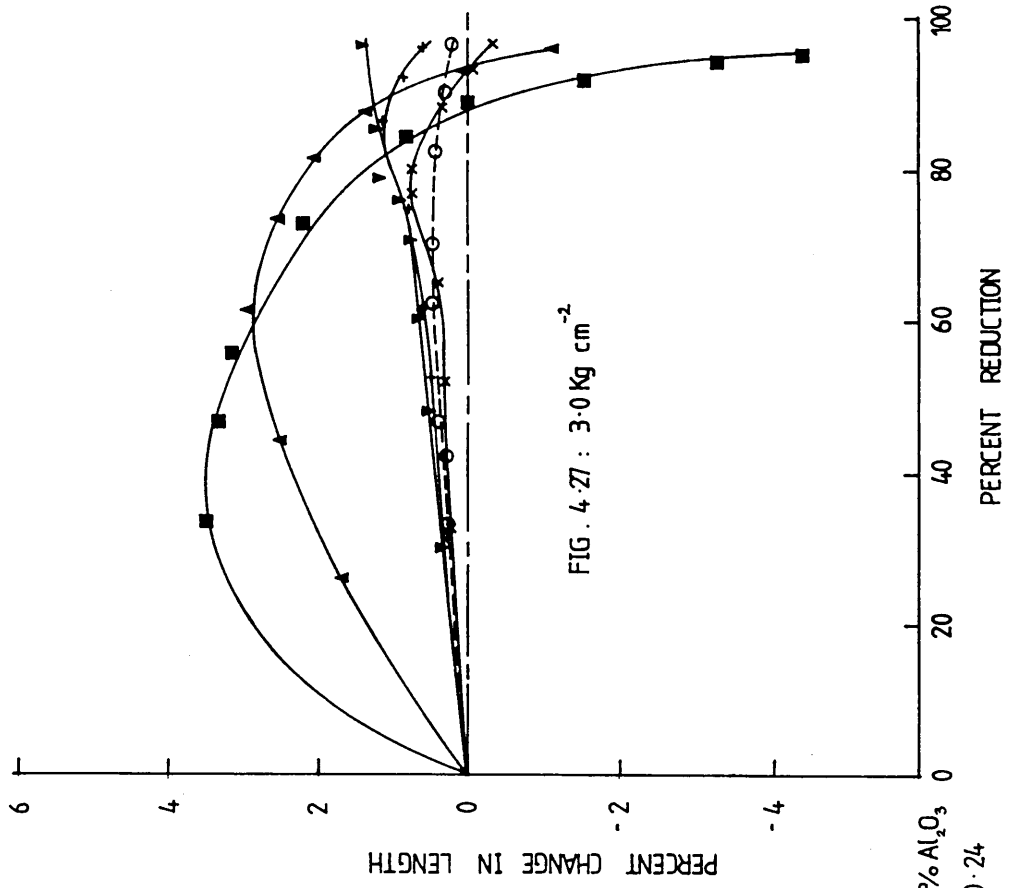


FIG . 4-27 : 3.0 Kg cm⁻²

COMPOSITION DETAILS FOR BOTH FIGURES :-

	MASS % CaO	MASS % SiO ₂	MASS % Al ₂ O ₃	MASS % CaO	MASS % SiO ₂	MASS % Al ₂ O ₃
■	0.12	0.22	0.24	3.0	0.22	0.24
▲	1.0	"	"	4.0	"	"
▼	2.0	"	"	5.0	"	"

FIG . 4-26 AND 4-27. PERCENTAGE CHANGE IN LENGTH VERSES PERCENTAGE REDUCTION FOR IRON OXIDE PELLETS REDUCED IN HYDROGEN AT 830 °c AND AT 0 AND 3.0 Kg cm⁻².

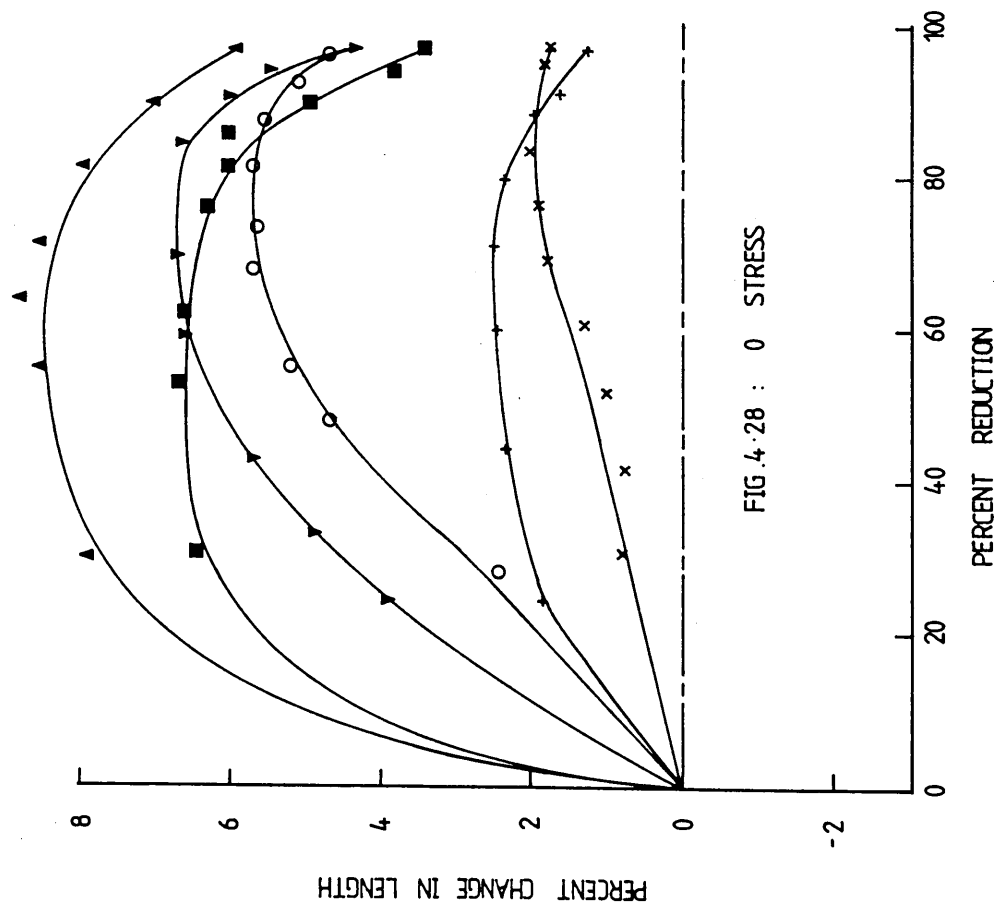
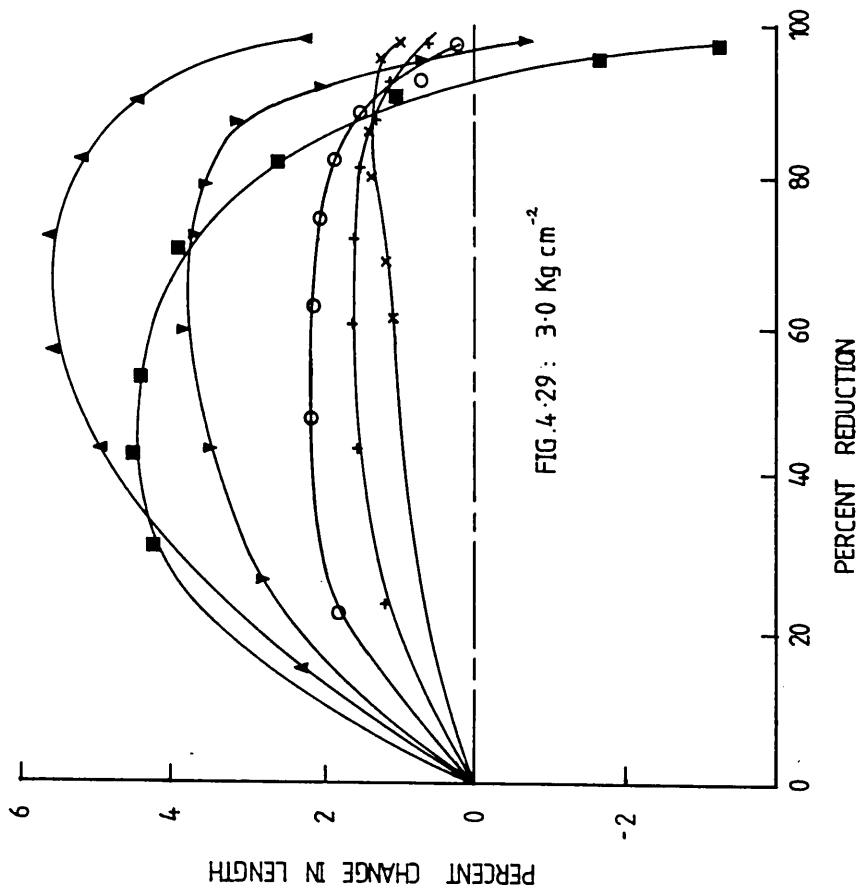


FIG. 4.28 AND 4.29. PERCENTAGE CHANGE IN LENGTH VERSUS PERCENTAGE REDUCTION FOR IRON OXIDE PELLETS REDUCED IN HYDROGEN AT 830 °C AND AT 0 AND 3.0 Kg cm⁻².

Key For Fig 4.30 And 4.31

Mass% CaO	Mass% SiO ₂	Mass% AlO ₂₃
• 1.00	0.22	1.00
x 2.00	0.22	1.00
o 4.00	0.22	1.00

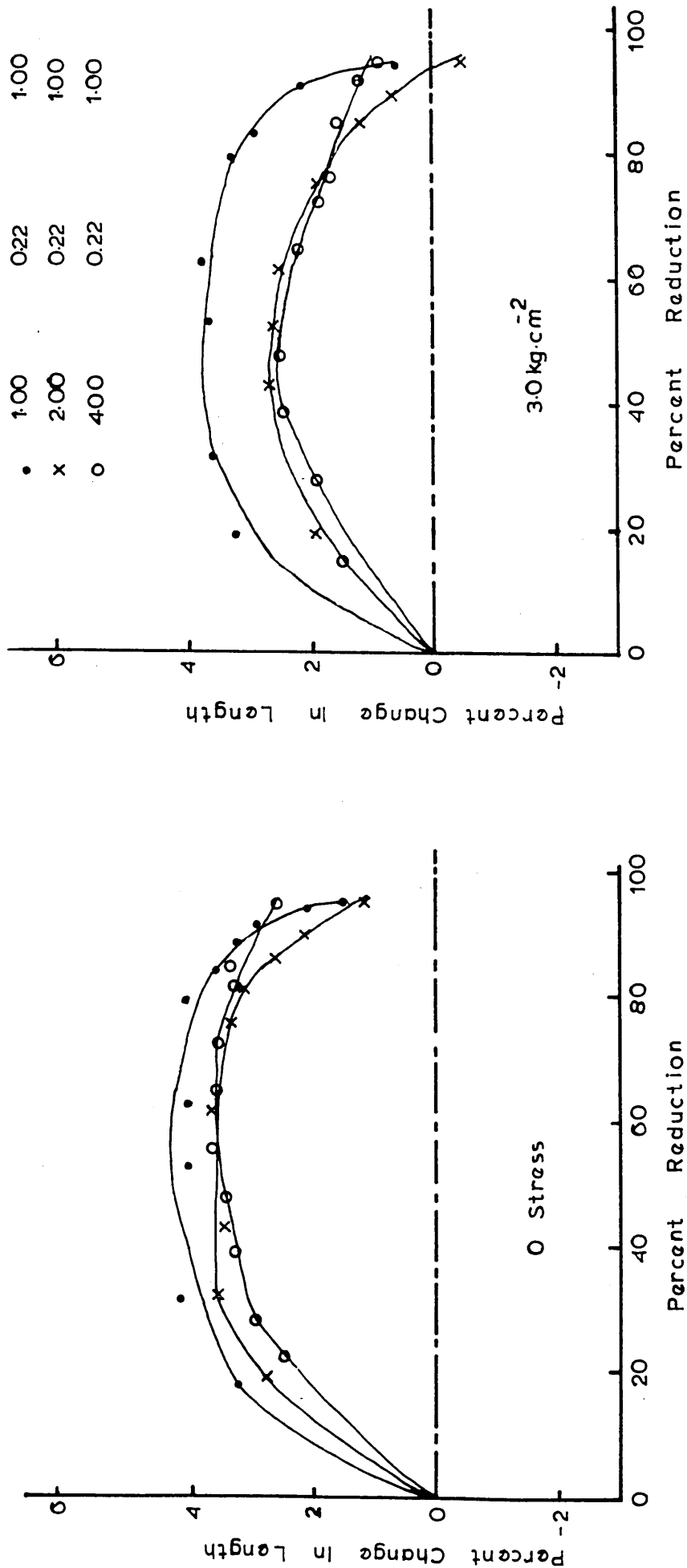


Fig. 4.30 and 4.31 Percentage change in length versus percentage reduction for iron oxide pellets reduced in hydrogen at 830°C and at zero and 3 kg cm⁻² stress. (sintered at 1250°C).

Key For Fig 4.32 And 4.33

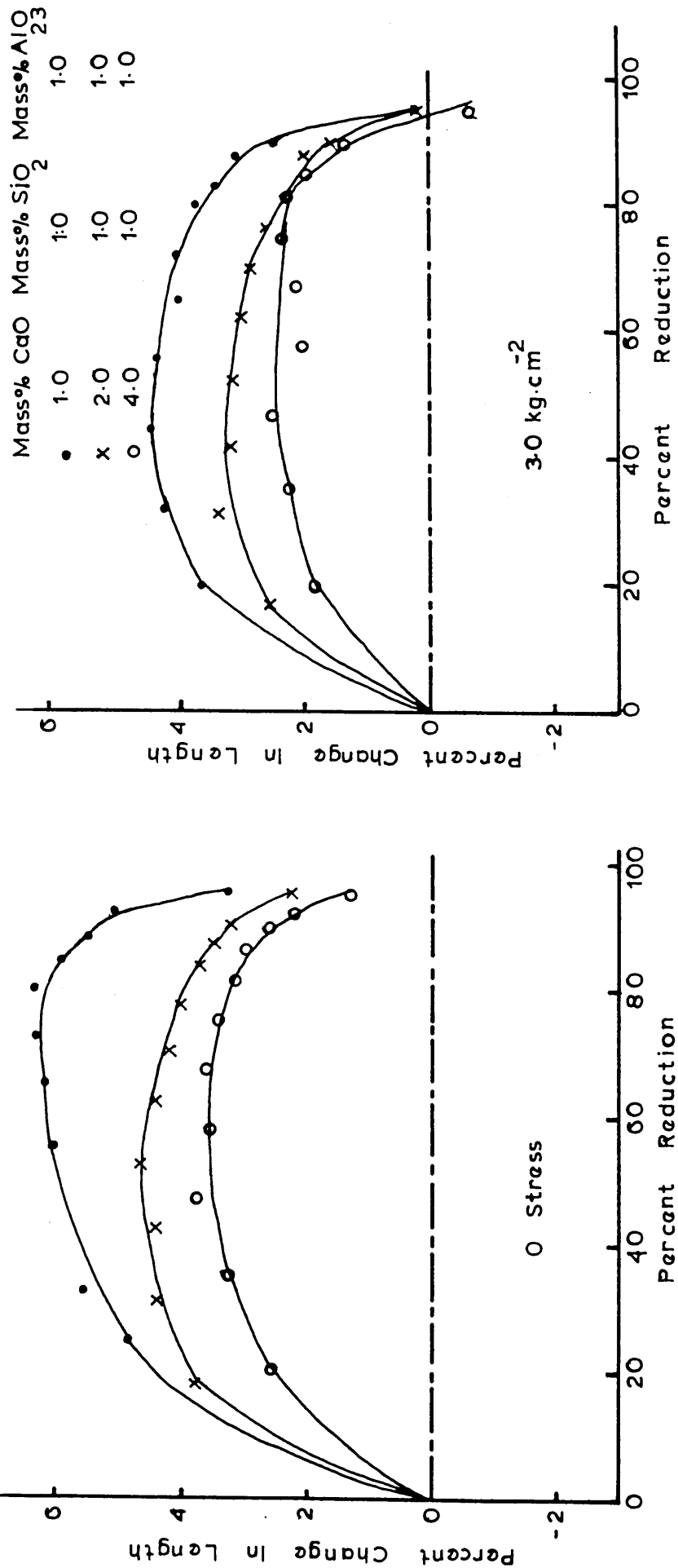


Fig. 4.32 and 4.33 Percentage change in length versus percentage reduction for iron oxide pellets reduced in hydrogen at 830°C at zero and 3 kg cm^{-2} . (sintered at 1250°C).

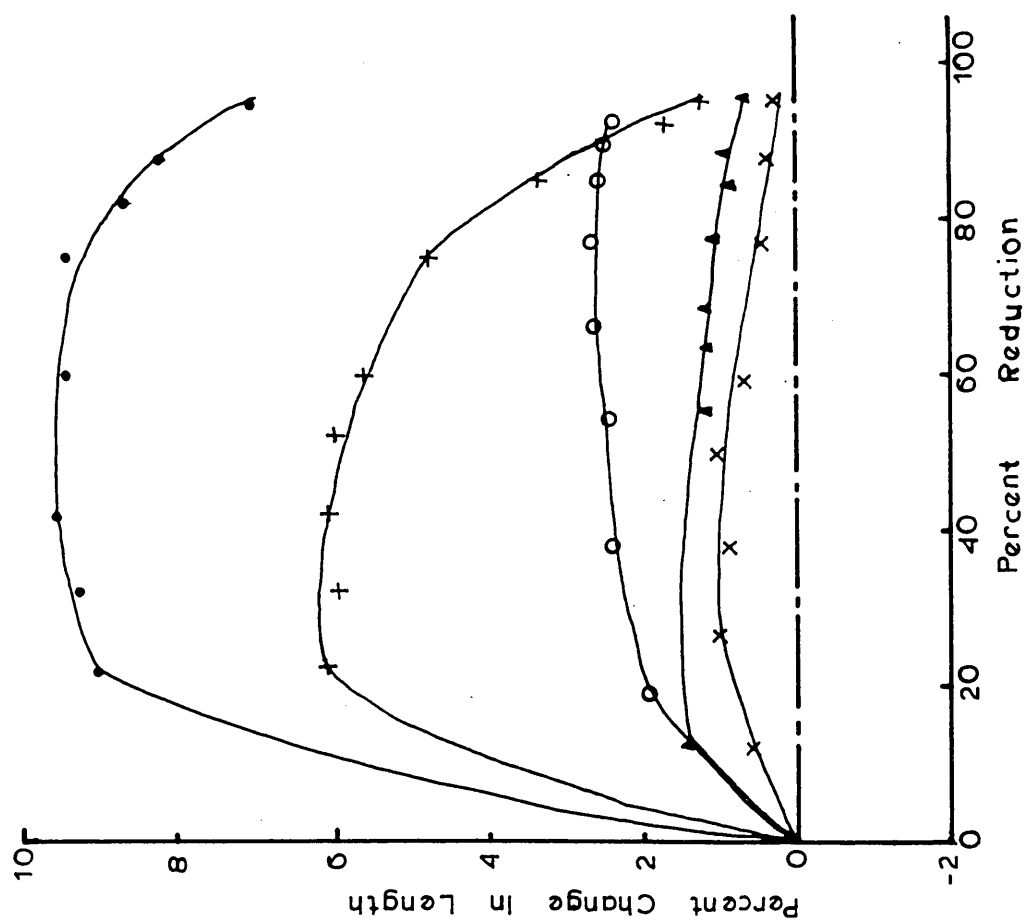


Fig. 4.34 Percentage change in length vs percentage reduction of iron oxide pellets at zero load. Reduced in hydrogen at 850°C. (sintered at 1325°C).

Key For Fig 435 And 436

+	0	Stress
o	15	$\text{kg}\cdot\text{cm}^{-2}$
x	30	$\text{kg}\cdot\text{cm}^{-2}$

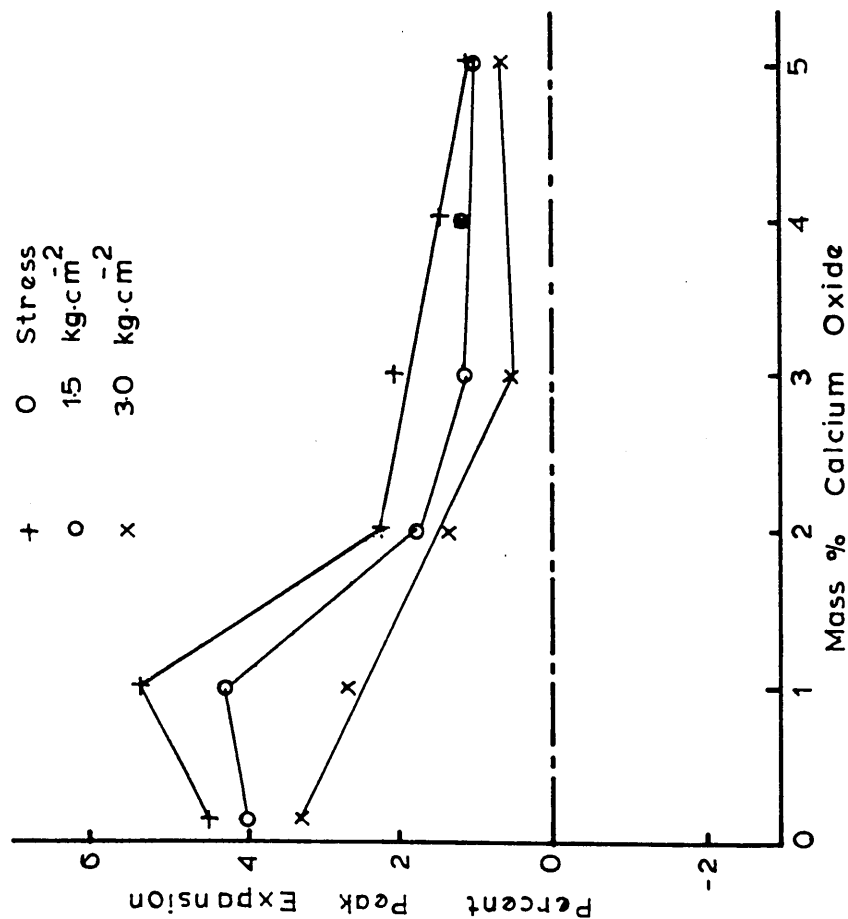


Fig. 4.35 Peak expansion of iron oxide pellets containing CaO at low SiO_2 and 0.24% Al_2O_3 under different stresses, reduced in H_2 at 830°C. (sintered at 1250°C).

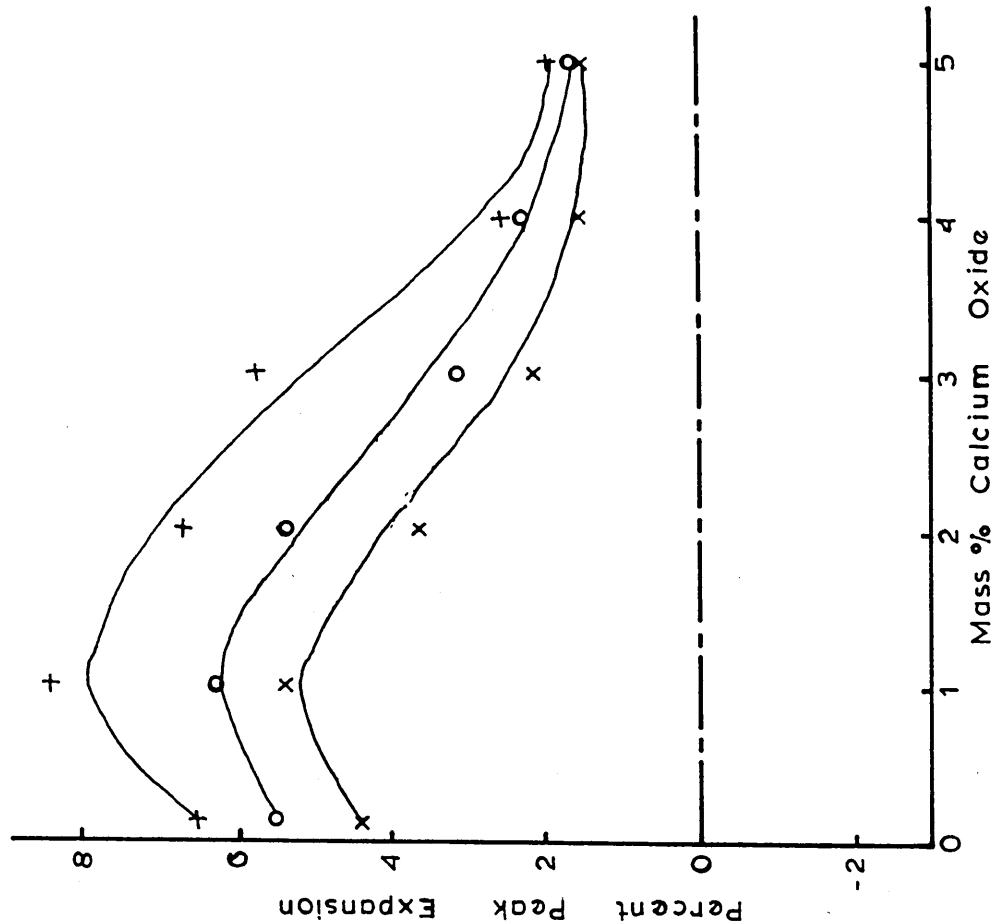


Fig. 4.36 Peak expansion of iron oxide pellets containing CaO at 1.0% SiO_2 and 0.24% Al_2O_3 under different stresses, reduced in H_2 at 830°C. (sintered at 1250°C).

Key For Fig 437 And 438

x O Stress
o 30 kg·cm⁻²

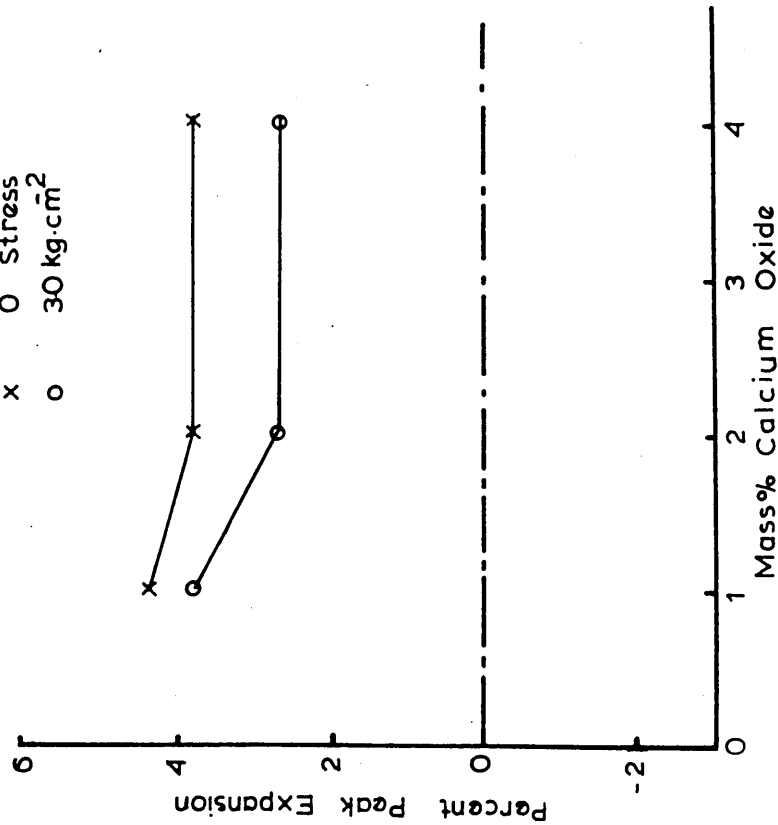


Fig. 4.37 Effect of CaO on peak expansion of iron oxide pellets at high Al₂O₃, 1% and 0.22% SiO₂. Reduced in hydrogen at 830°C. (sintered at 1250°C).

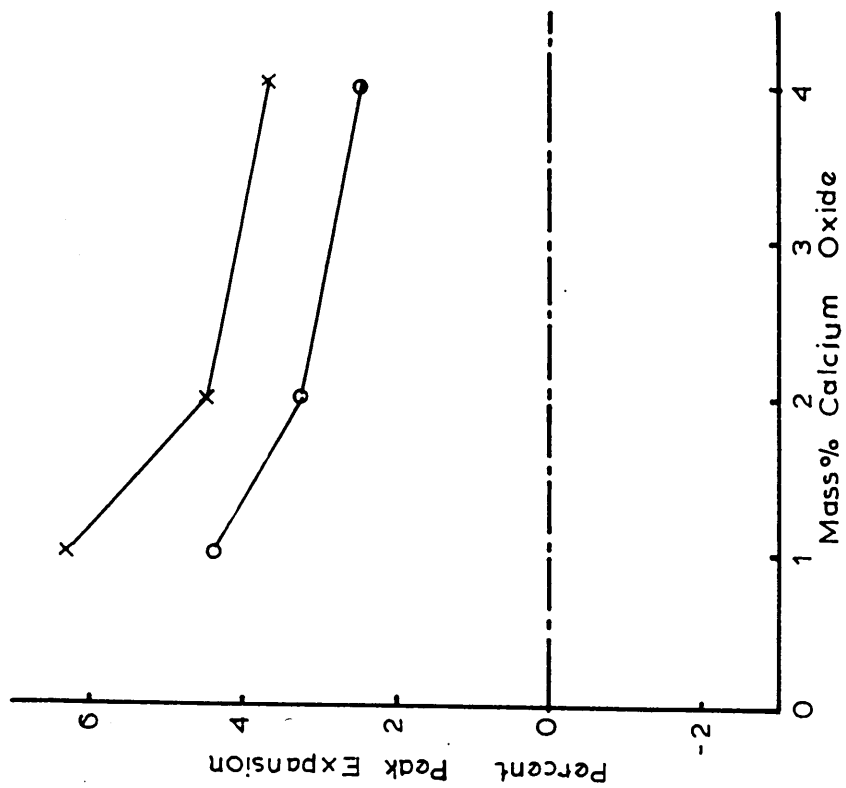


Fig. 4.38 Effect of CaO on peak expansion of iron oxide pellets at high Al₂O₃, 1% and 0.22% SiO₂. Reduced in H₂ at 830°C. (sintered at 1250°C).

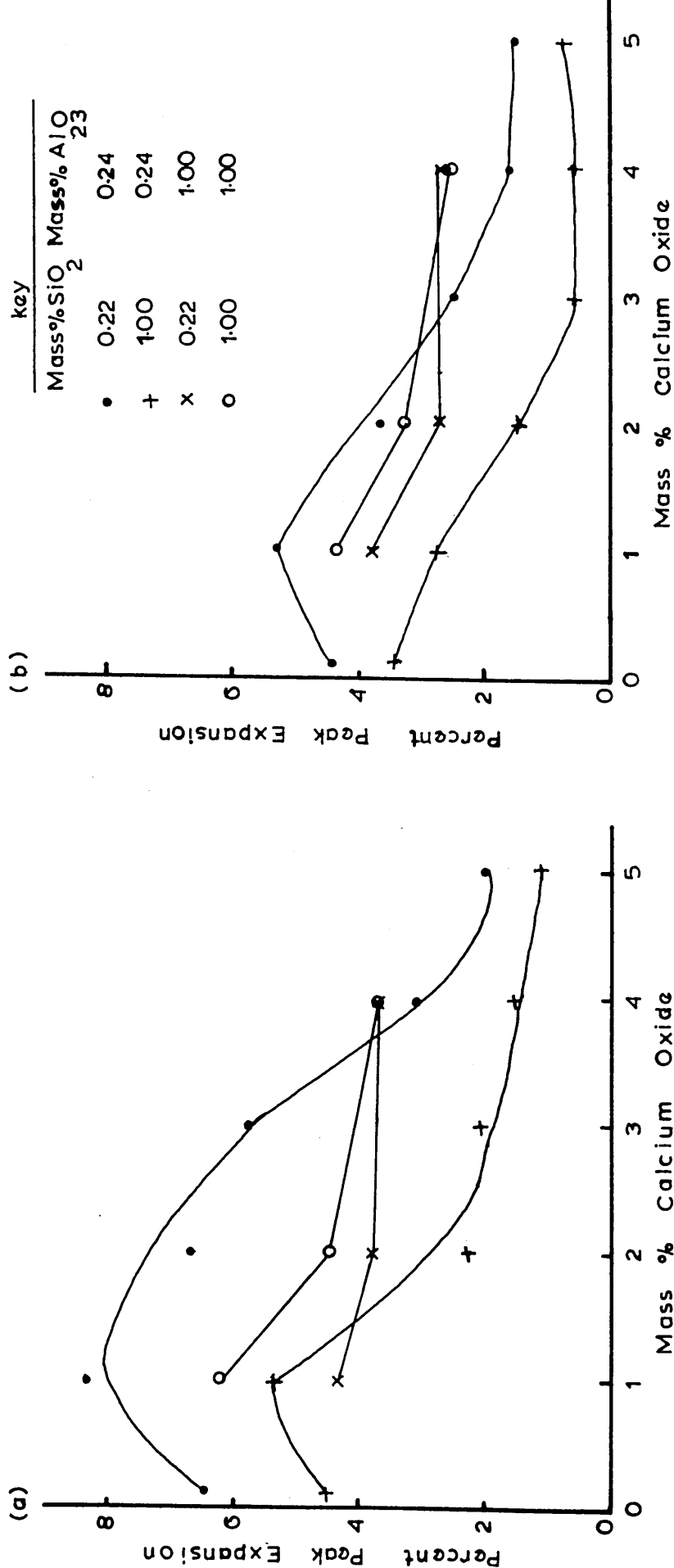


FIG. 4.22 Effect of different doping agents on peak expansion of different iron oxide pellets. Reduced in hydrogen at 830°C. (sintered at 1250°C).

(a) Zero stresses
(b) 3.0 kg cm⁻² stresses

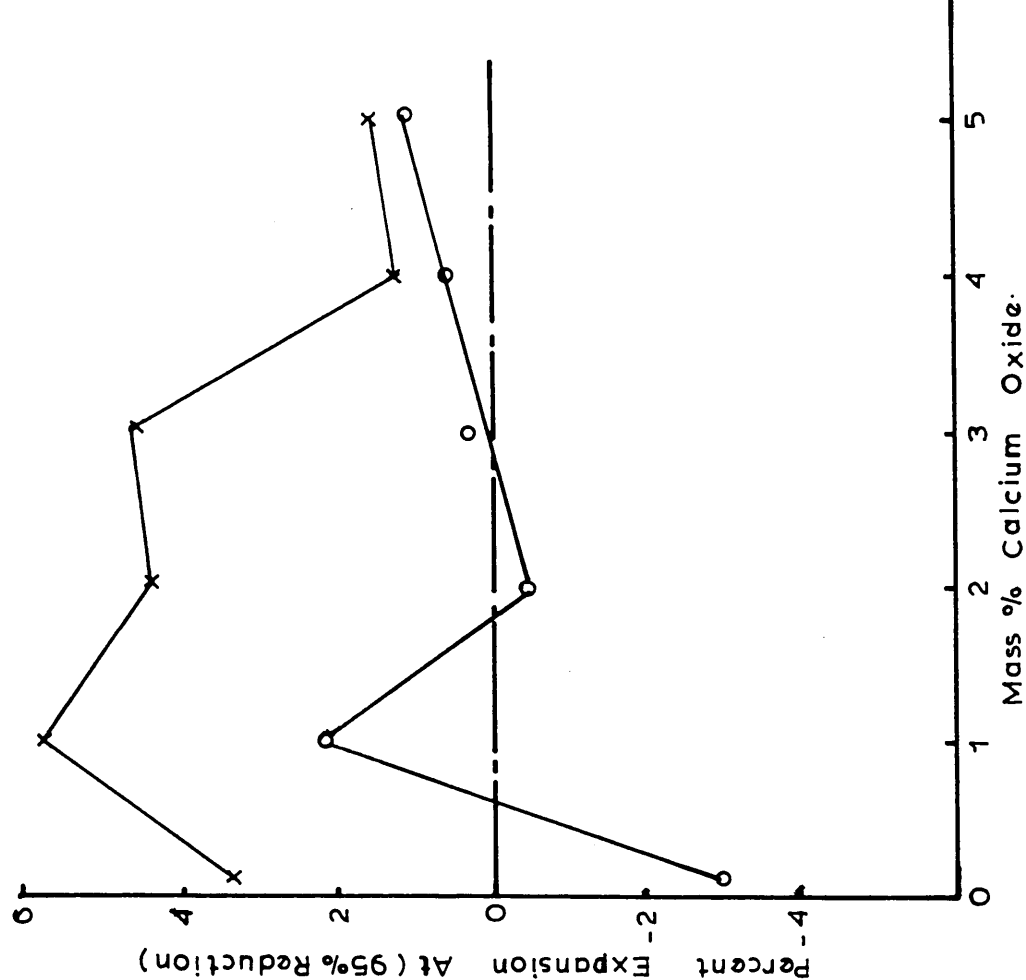


Fig. 4.41 The influence of stress and lime content on the terminal expansion values at 1% SiO₂, 0.24% Al₂O₃ content, reduced in H₂ at 830°C. (sintered at 1250°C).

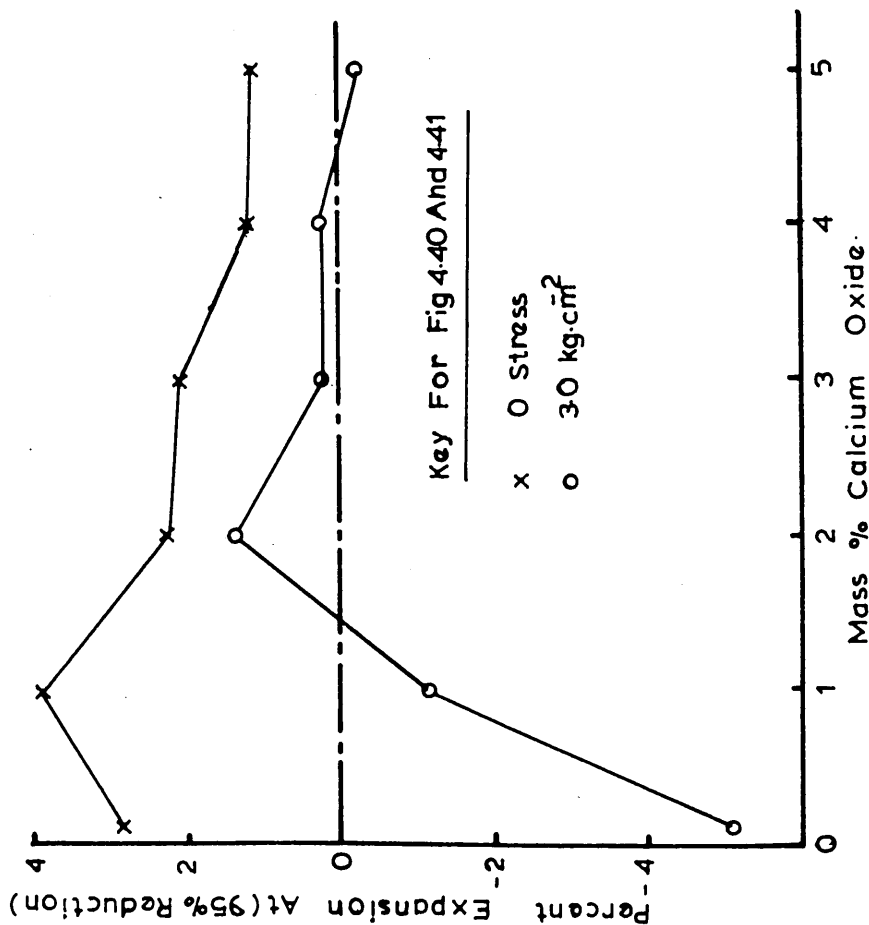


Fig. 4.40 The influence of stress and lime content on the terminal expansion values at 0.22% SiO₂, 0.24% Al₂O₃ content reduced in H₂ at 830°C. (sintered at 1250°C).

Key For Fig 4.42 And 4.43

x 0 Stress
o 30 kg·cm⁻²

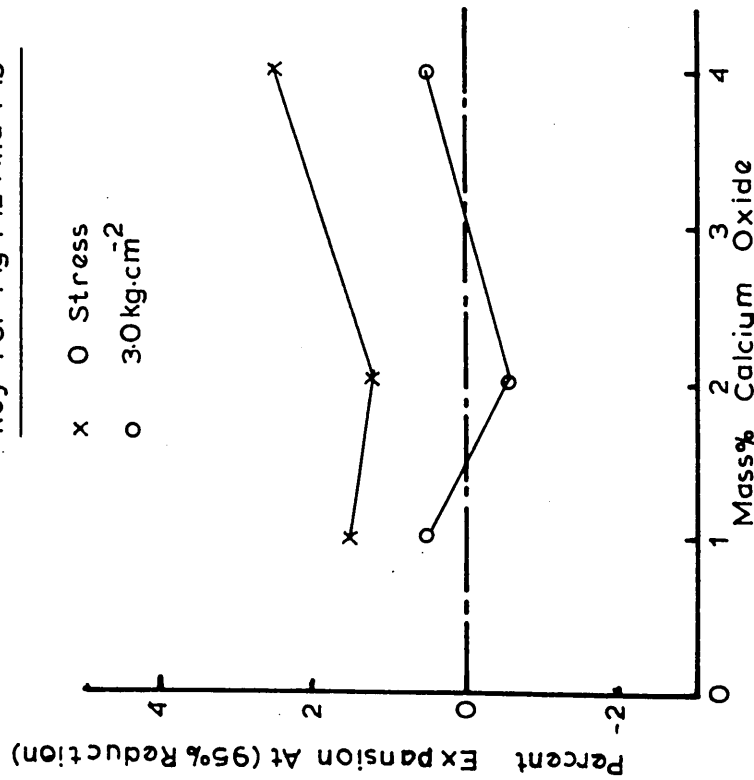


Fig. 4.42

The influence of stress and lime content on the terminal expansion value at 1% SiO₂, 1% Al₂O₃ reduced in hydrogen at 830°C. (sintered at 1250°C).

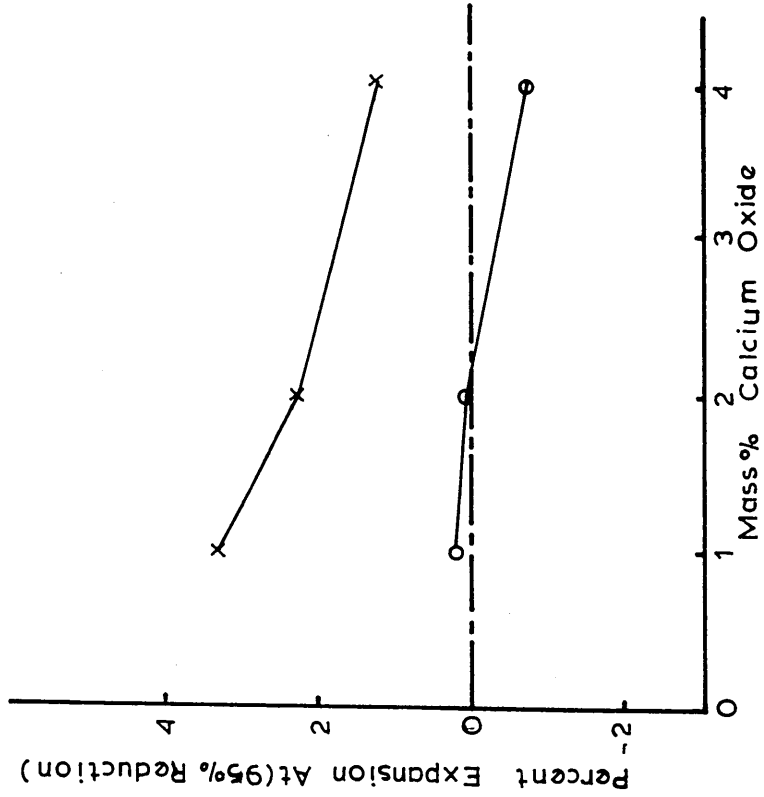


Fig. 4.43

The influence of stress and lime content on the terminal expansion value at 1% SiO₂, 1% Al₂O₃ reduced in hydrogen at 830°C. (sintered at 1250°C).

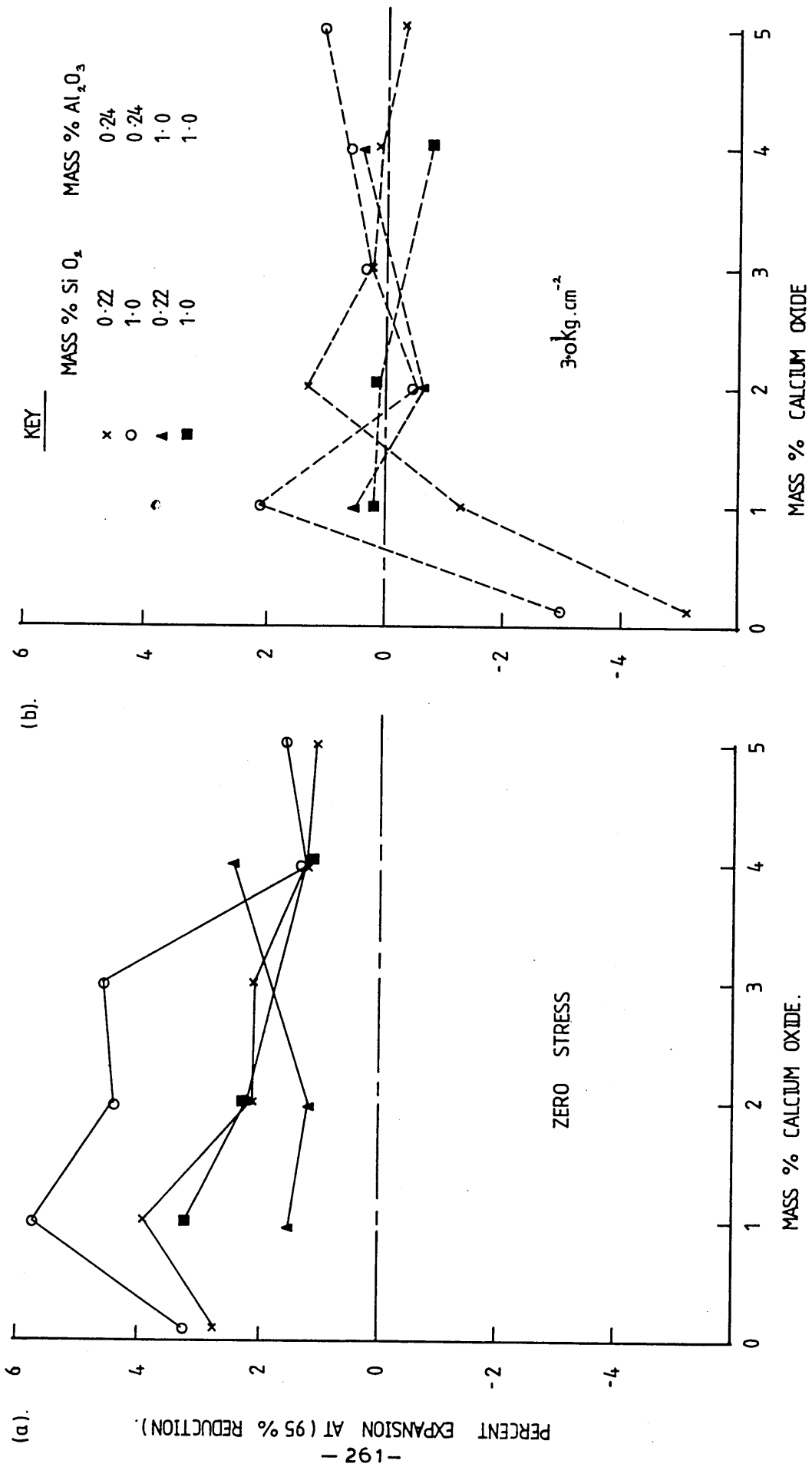


FIG. 4.44 (a). AND 4.44 (b). EFFECT OF DIFFERENT DOPING AGENTS ON PERCENT EXPANSION AT 95% R.

Key For Fig 4.45 And 4.46

	Before Reduction	Mass% SiO_2	Mass% Al_2O_3
x	Before Reduction	0.22	0.24
+	After Reduction	0.22	0.24
o	Before Reduction	1.00	0.24
•	After Reduction	1.00	0.24

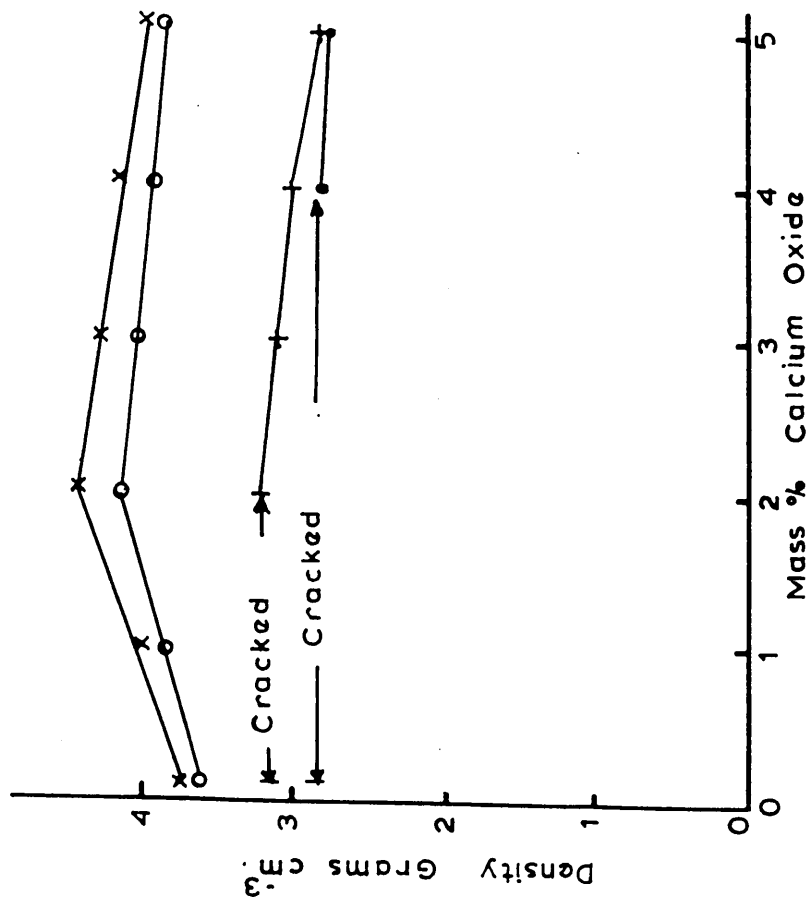


Fig. 4.45 Density of different iron oxide pellets before and after reduction in H_2 at 830°C. (sintered at 1250°C).

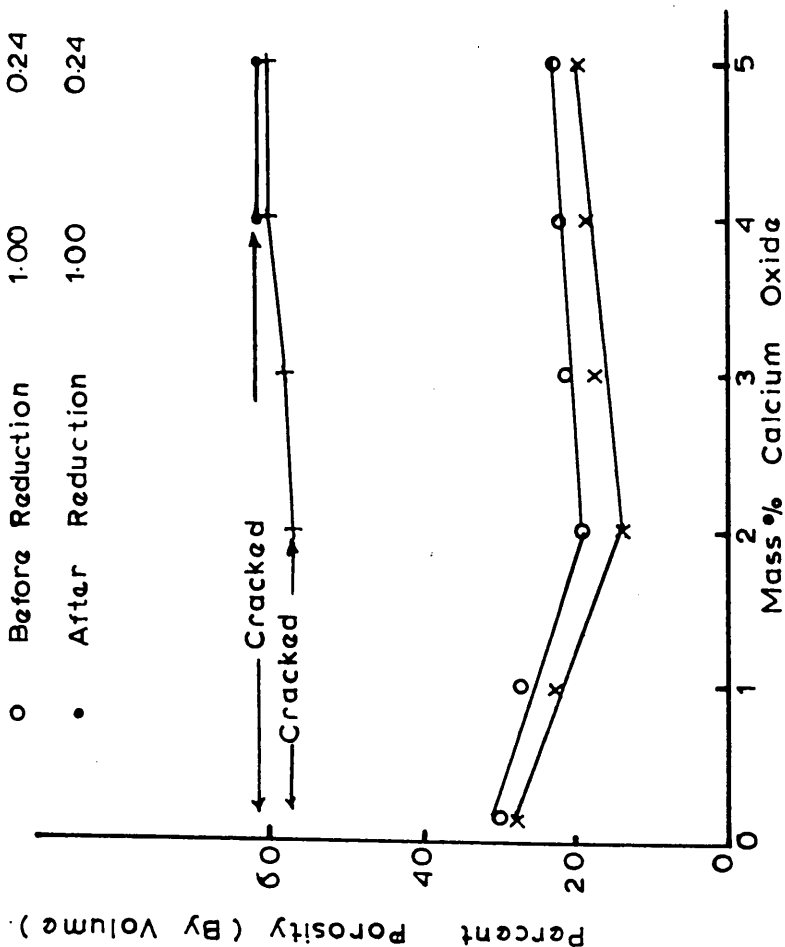


Fig. 4.46 Porosity of different iron oxide pellets before and after reduction in H_2 at 830°C (sintered at 1250°C).

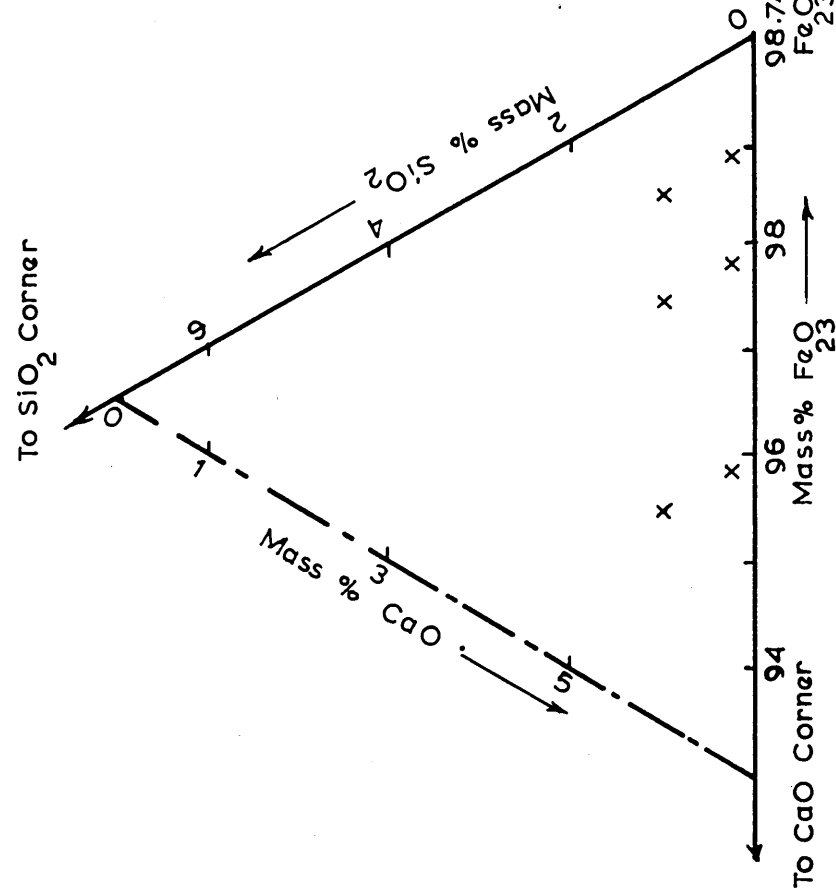


FIG 5:1(b) A SECTION OF TERNARY DIAGRAM
 $\text{CaO-SiO}_2\text{-FeO}_{23}$, SHOWING THE COMPOSITION
 OF CaO AND SiO_2 MASS FRACTIONS IN
 HEMATITE ORE CONTAINING $10\% \text{AlO}_{23}$

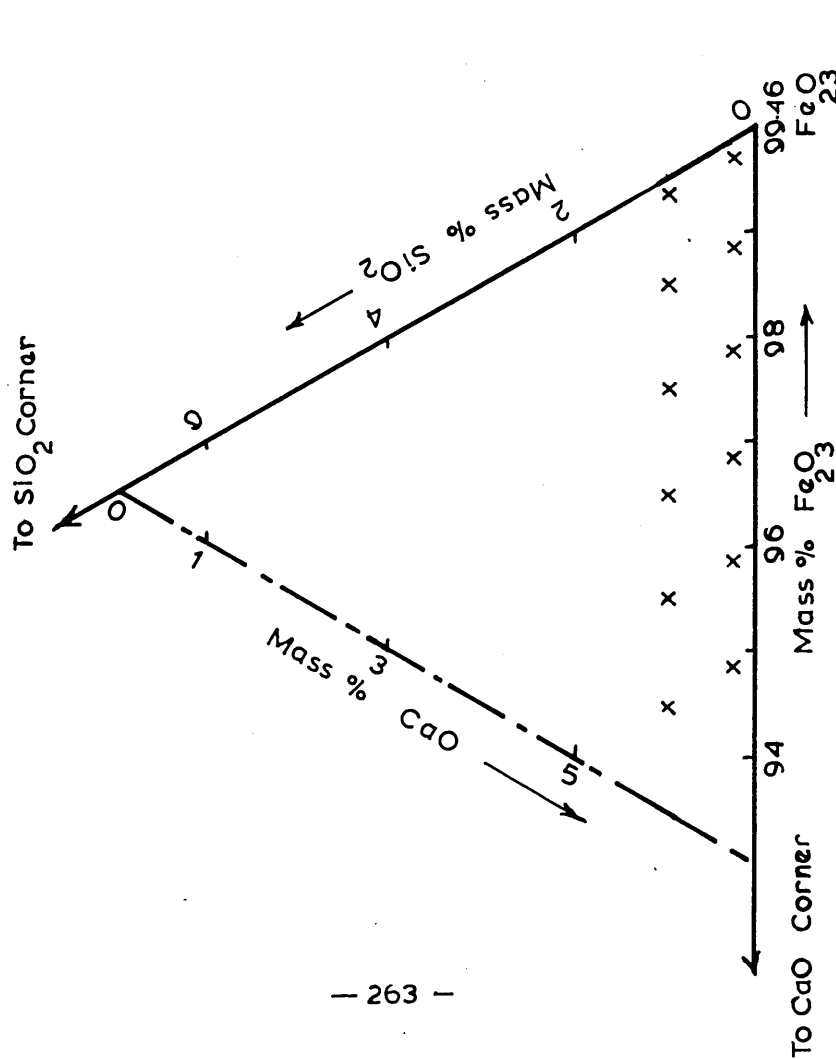
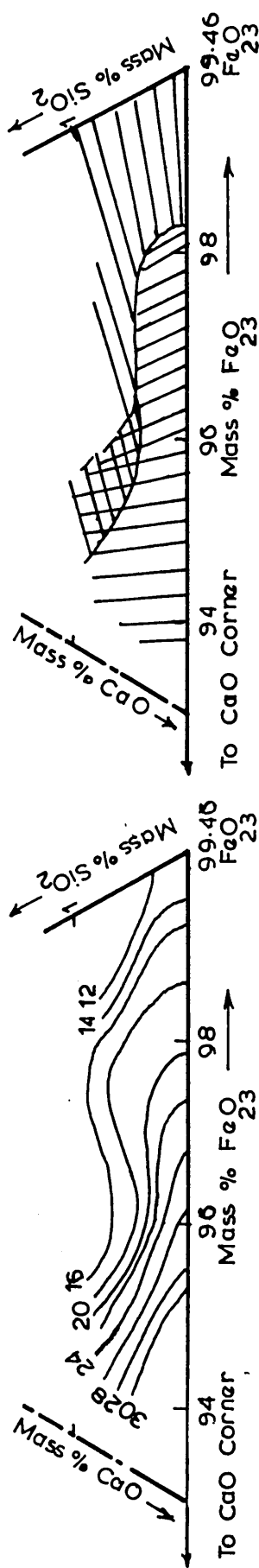
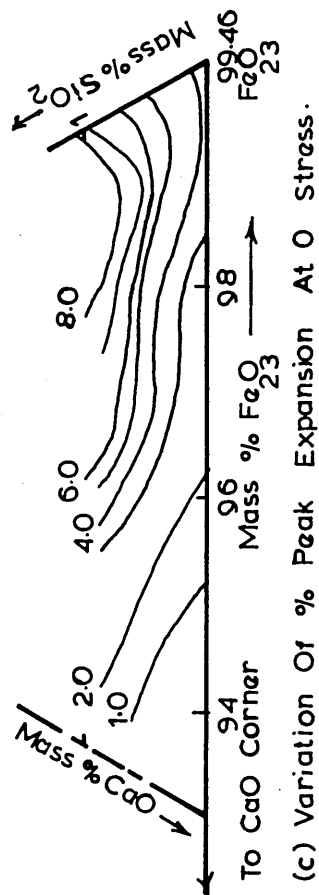


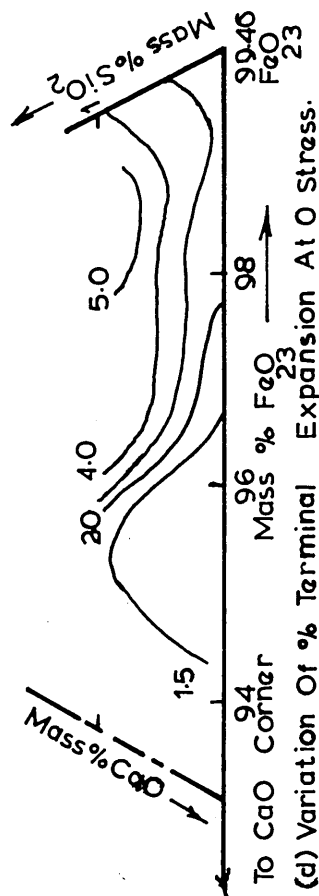
FIG 5:1(a) A SECTION OF TERNARY DIAGRAM
 $\text{CaO-SiO}_2\text{-FeO}_{23}$, SHOWING THE COMPOSITION
 OF CaO AND SiO_2 MASS FRACTIONS IN HEMATITE
 ORE CONTAINING $0.24\% \text{AlO}_{23}$



(a) Time in Minutes for 95% Reduction.

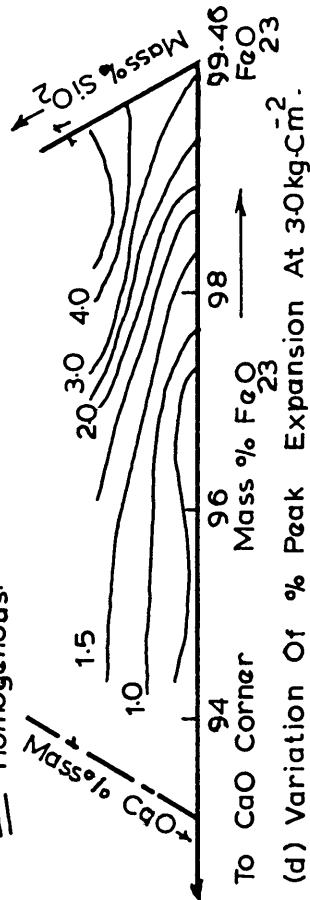


(c) Variation of % Peak Expansion At 0 Stress.

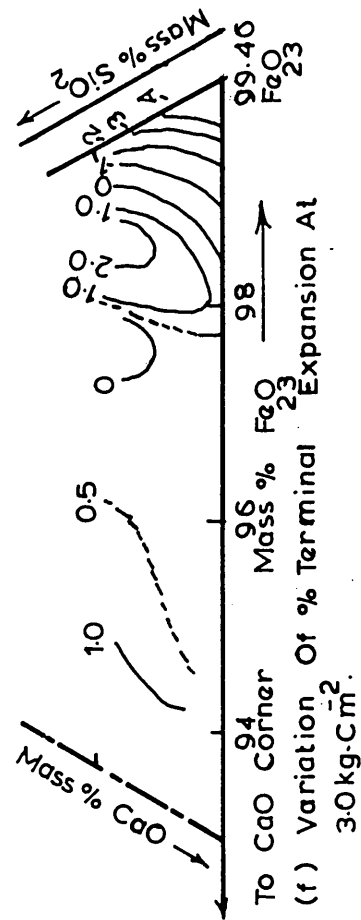


(d) Variation of % Terminal Expansion At 0 Stress.

(b) Mode Of Reduction: $\parallel \parallel \parallel$ Topochemical. $\times \times \times$ Mixed. \equiv Homogenous.



(d) Variation of % Peak Expansion At 30 kg-Cm⁻².



(f) Variation of % Terminal Expansion At 30 kg-Cm⁻².

FIG 52: EFFECT OF VARIATIONS IN CaO AND SiO₂ MASS FRACTIONS IN HEMATITE ORE CONTAINING 0.24% Al₂O₃.

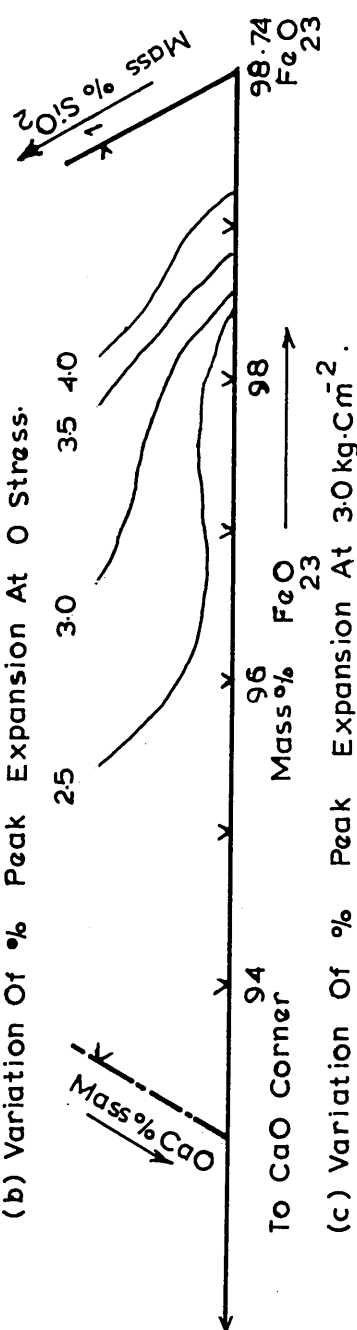
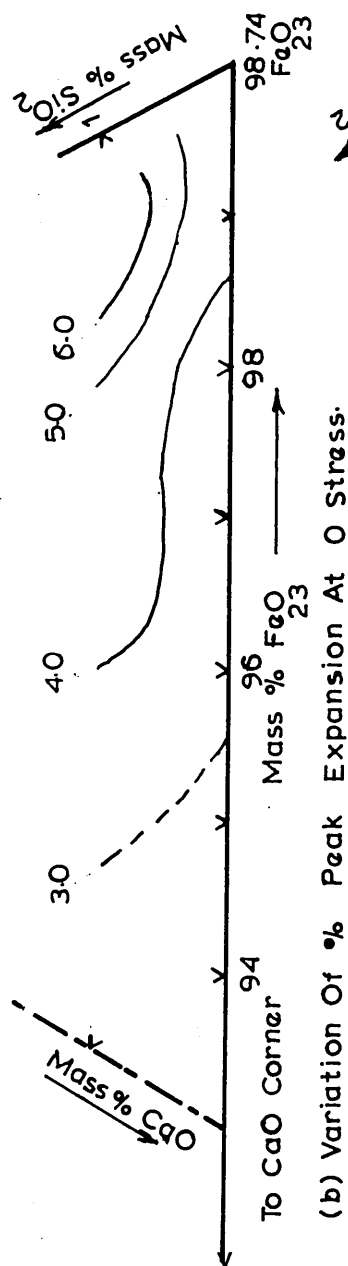
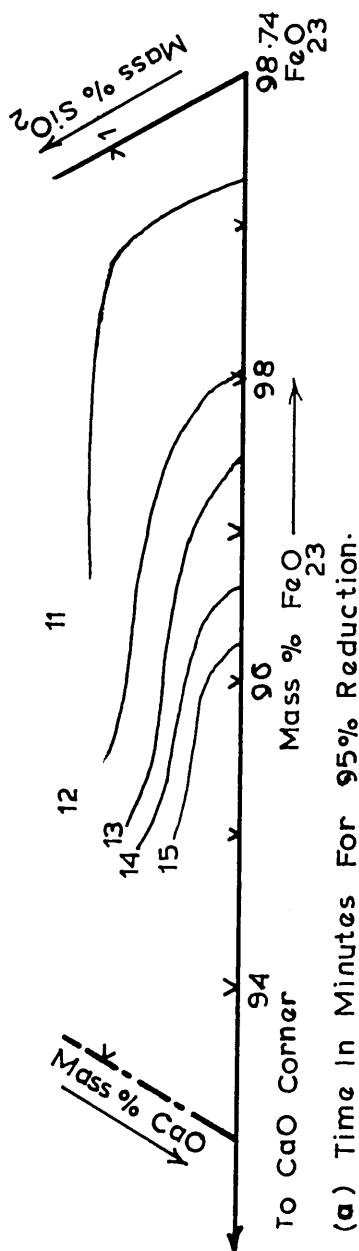


Fig.5.3 Effect Of Variations In CaO And SiO₂ Mass Fractions In Hematite Ore Containing 1.0% Al₂O₃ Reduced In Hydrogen At 830 °C

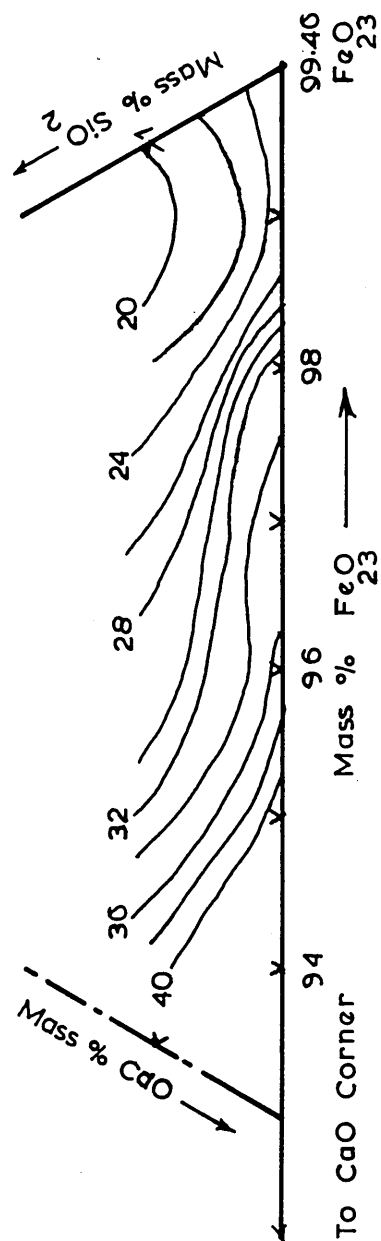
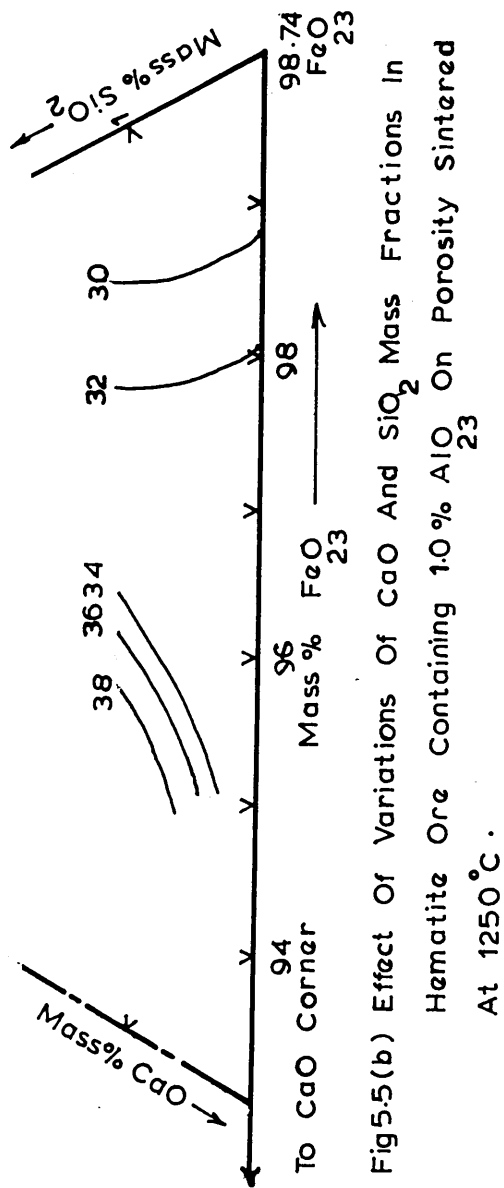
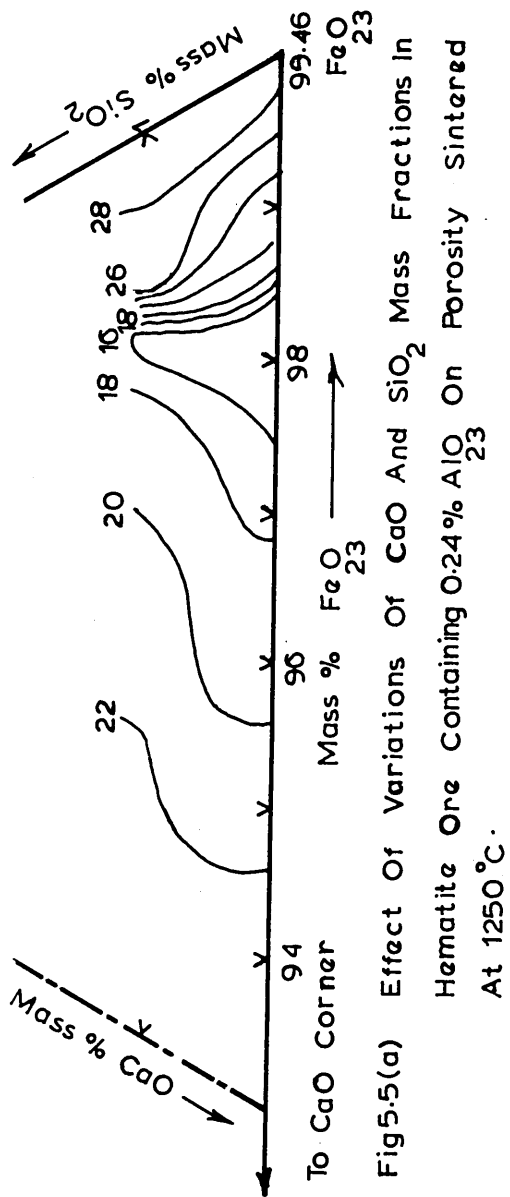


Fig5.4 Time In Minutes For 'End' Of Reduction, Varies With Variations
 In CaO And SiO_2 Mass Fractions In Hematite Ore Containing $0.24\% \text{Al}_2\text{O}_3$
 Reduced In Hydrogen+Carbon Monoxide Gas Mixture At 830°C



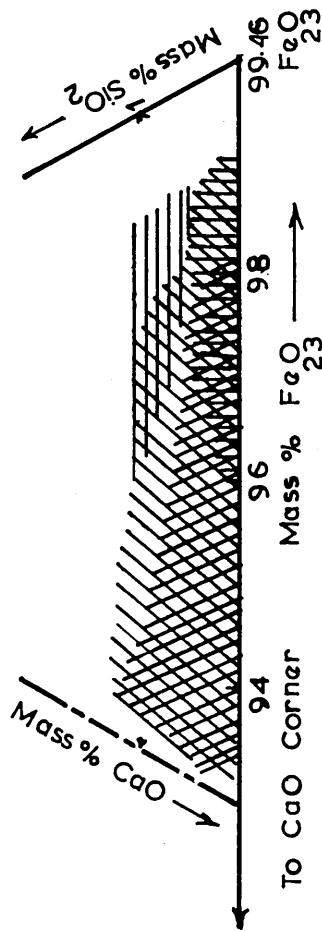


Fig 5.6(a) Variation Of Phases With CaO And SiO₂

Mass Fractions In Hematite Ore Containing

0.24% Al₂O₃

Key

- ||| CF_{3.5} Calcium ferrite
- /// CF₂ Calcium di-ferrite
- \\ CF Calcium mono-ferrite
- ≡ ICS Iron Calcium Silicate

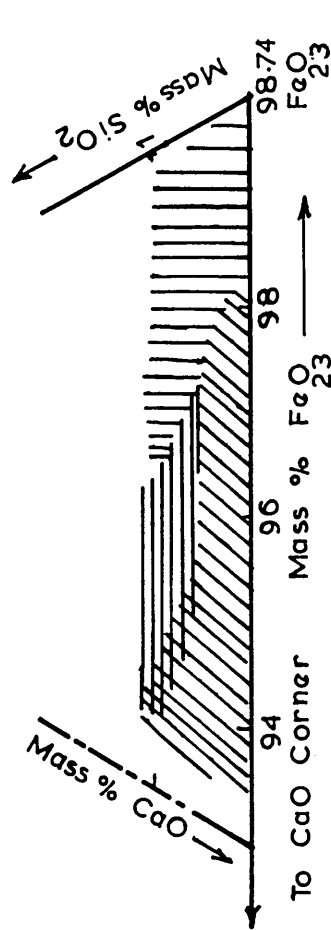


Fig 5.6(b) Morphology Of Phases With CaO And SiO₂

Mass Fractions In Hematite Ore Containing

0.24% Al₂O₃

Key

- ||| Porous Structure, Phases Are Rare
- ≡ Laths, Needles And Porous Calcium ferrite Phases
- /// Closed Pores Structure, Dense Calcium ferrite Phases

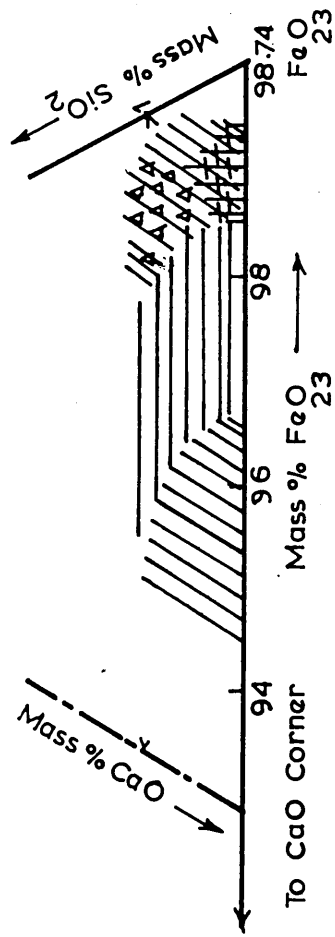


Fig 5.7(a) Variation Of Phases With CaO And SiO₂ Mass Fractions In Hematite Ore Containing 1.0 % AlO₂₃

Key

- /// CF₂ Calcium di-ferrite
- △△ C₂F Di-Calcium ferrite
- ||| AlO₂₃
- + + CaO·AlO₂₃ Calcium-Aluminate
- ≡ Not Analysed

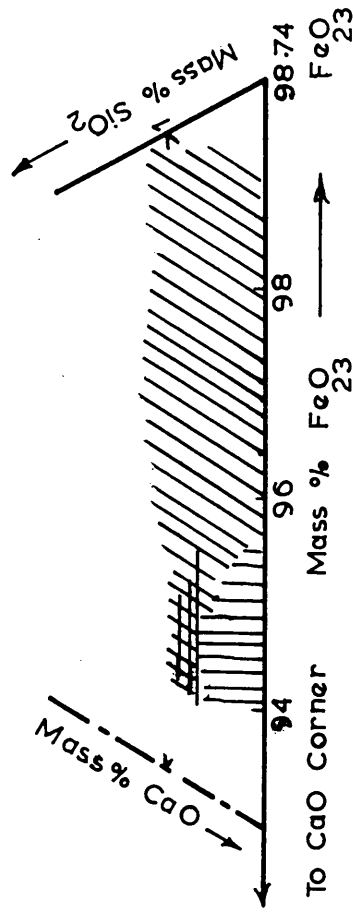


Fig 5.7(b) Morphology Of Phases With CaO And SiO₂ Mass Fractions In Hematite Ore Containing 1.0 % AlO₂₃

Key

- ||| Solid Phases
- ≡ Acicular
- /// Globular And Porous Phases